IN-SITU ALLOYING BASED ADDITIVE MANUFACTURING OF HIGH-PERFORMANCE BETA Ti-Mo ALLOYS

BY

RANXI DUAN



UNIVERSITY OF BIRMINGHAM

A thesis submitted to the University of Birmingham for the degree of

DOCTOR OF PHILOSOPHY

School of Metallurgy and Materials

College of Engineering and Physical Sciences

University of Birmingham

Nov 2021

UNIVERSITY OF
BIRMINGHAM

University of Birmingham Research Archive

e-theses repository

This unpublished thesis/dissertation is copyright of the author and/or third parties. The intellectual property rights of the author or third parties in respect of this work are as defined by The Copyright Designs and Patents Act 1988 or as modified by any successor legislation.

Any use made of information contained in this thesis/dissertation must be in accordance with that legislation and must be properly acknowledged. Further distribution or reproduction in any format is prohibited without the permission of the copyright holder.

ACKNOWLEDGEMENTS

First and foremost, I would like to express my profound gratitude to my supervisor Professor Moataz Attallah for providing me with the opportunity to undertake the presented research and pursue a PhD degree at the University of Birmingham. His immense knowledge and plentiful research experience have encouraged me to keep motivation, diligence, curiosity, and enthusiasm for scientific research. Without his invaluable advice, continuous support, and patience, the completion of this dissertation could not have been possible.

My sincere gratitude extends to my second supervisor Prof.Fuzeng Ren, from Southern University of Science and Technology, for the invaluable supervision, support, and suggestions, especially in shaping my characterisation skills, such as focused ion beam and TEM.

My great appreciation goes to my co-supervisor Dr.Biao Cai, from University of Birmingham, for his timely help and invaluable guidance, especially for guiding me to explore the beauty of materials by using the synchrotron X-ray.

I would like to acknowledge the supports from the Southern University of Science and Technology and University of Birmingham for offering me the PhD scholarship.

It is also pleasure to thank my colleagues, lab mates, and friends for their supportive helps at the University of Birmingham and the Southern University of Science and Technology, in particular to Dr. Sheng Li, Dr. Weiwei Zhu, Prof. Di Wang, Dr. Chaolin Tan, Dr. Cancan Zhao, Dr. Ju Fang, Dr. Minshi Wang, Dr. O.V.Magdysyuk, Dr.Zengbao Jiao, Dr. Junhua Luan, Mr. Kun Sun, Mr. Peng Chen, Mr. Zhi Tao, Ms. Jasi Luo, Mr. Dingshan Liang, Mr. Lu Yang, and Mr. Pengbo Wei.

Finally, I would like to give my sincere gratitude and thanks to my parents and family for their tremendous understanding and never-ending encouragement in the past four years.

ABSTRACT

β Titanium (Ti) alloys have shown outstanding commercial importance, mainly due to their high specific strength, low modulus, and excellent fatigue and corrosion resistance. Considering the difficulties and high cost of manufacturing β Ti alloys, this work applied the novel cost-effective method, in-situ alloying based laser powder bed fusion (LPBF) processing, to fabricate β Ti-Mo alloys, and explored the processing-microstructure-property relations.

For the densification and homogenisation of β Ti-Mo alloys, LPBF parametrical studies were firstly performed to β Ti-12Mo alloy from low-cost elemental powders. When the high laser area energy density (AED) was applied, the refractory Mo powder melted and dissolved into the Ti matrix due to the high temperature of the melt pool and increased cycles of remelting. Additionally, keyhole-induced defects emerged under such high AED, which could be eliminated by optimising laser beam delay (LBD) and island spacing (IS) settings. After that, the metastable β Ti-12Mo and Ti-12Mo-6Zr-2Fe (TMZF) alloys with highly dense and largely chemical homogeneous structures were successfully fabricated by in-situ alloying based LPBF.

Furthermore, it is noticed that applying varied AED during LPBF can significantly control the microstructure and mechanical properties of Ti-Mo alloys. In view of this, a Ti-Mo functional gradient composite (FGC), with great compressive behaviour, was fabricated via alternating AEDs layer-wise, which paved a new opportunity to design and engineer high-performance biomimetic FGCs components.

Moreover, detailed investigations have been performed to understand the influence of scanning strategies (simple and chessboard scan) and post heat treatment on the microstructure-property relations of β TMZF alloys processed by in-situ alloying based LPBF. The specimens processed via simple scanning strategy showed considerably high strength but were brittle. While the TMZF alloys, manufactured using chessboard scanning strategy, possessed an

excellent combination of high yield strength of 1026 MPa, low modulus of 85.7 GPa, and good ductility of 12.7 %. After solution heat treatment, the specimens exhibited a lower modulus of 70.9 GPa, while maintaining high yield strength and ductility. The study revealed that different scanning strategies and post heat treatment could regulate the grain structures, texture, and secondary phases of β Ti alloys, which offered a viable strategy for optimising their mechanical properties.

The metastable β Ti-12Mo alloys typically show low yield strength (< 500 MPa) but good ductility, resulting from twinning-induced plasticity (TWIP) and transformation-induced plasticity (TRIP). The metastable β Ti-12Mo alloy, fabricated by LPBF, showed a significant improved tensile behaviour of high yield strength (725 MPa), excellent strain hardening rates (SHR) and good ductility. The strengthening and deformation mechanisms were understood through the combined usage of in-situ and ex-situ characterisations. The high yield strength mainly resulted from the specific isothermal ω nanoparticles, strengthening the alloy through the dislocation shearing mechanism. The high SHR and good ductility could be attributed to the hierarchical TWIP/TRIP effects, which were operative during the plastic deformation. At the very early stage of plastic deformation (strain < 1.9 %), {332}<113> twinning was the dominant deformation mechanism, while the deformation-induced α" phase was not yet activated. At the later stage of deformation, various primary and secondary twins, and martensite α" phases formed hierarchical structures, contributing to the dynamic Hall-Petch effect.

In this work, the in-situ alloying based LPBF technology is demonstrated to be a promising manufacturing route for the fabrication of high-performance β Ti-12Mo alloy, TMZF alloy and Ti-Mo FGCs, that are hard to process via conventional ways. The novel method can be the desirable candidate for some applications in the biomedical and aerospace industries.

LIST OF PUBLICATIONS

[1] **R. Duan**, S. Li, B. Cai*, W. Zhu, F. Ren*, M.M. Attallah*, A high strength and low modulus metastable β Ti-12Mo-6Zr-2Fe alloy fabricated by laser powder bed fusion in-situ alloying, Addit Manuf. 37 (2021) 101708. https://doi.org/10.1016/j.addma.2020.101708.

Author credits： **R.Duan**: Conceptualization, Methodology, Investigation, Formal analysis, Data curation, Validation, Visualization, Writing original draft. **M.M. Attallah, F. Ren, B. Cai**: Supervision, Conceptualization, Project administration, Resources, Writing review & editing. **S.Li**: Investigation, Methodology, Validation. **W. Zhu**: Investigation.

[2] **R. Duan**, S. Li, B. Cai*, Z. Tao, W. Zhu, F. Ren*, M.M. Attallah*, In situ alloying based laser powder bed fusion processing of β Ti–Mo alloy to fabricate functionally graded composites, Compos Part B Eng. 222 (2021) 109059.

https://doi.org/10.1016/j.compositesb.2021.109059.

Author credits： **R.Duan**: Conceptualization, Methodology, Investigation, Formal analysis, Data curation, Validation, Visualization, Writing original draft. **M.M. Attallah, F. Ren, B. Cai**: Supervision, Conceptualization, Project administration, Resources, Writing review & editing. **S.Li**: Investigation, Methodology. **Z. Tao, W. Zhu**: Investigation.

[3] **R. Duan**, F. Ren*, O.V.Magdysyuk, J. H. Luan, Z. B. Jiao, M. M. Attallah*, B. Cai*, On the hierarchical TWIP/TRIP effects in a high strength metastable β Ti prepared by in-situ alloying based additive manufacturing. (Manuscript to be submitted)

Author credits: **R.Duan**: Conceptualization, Methodology, Investigation, Formal analysis, Data curation, Validation, Visualization, Writing original draft. **M.M. Attallah, F. Ren, B. Cai**: Supervision, Conceptualization, Project administration, Resources, Writing review & editing. **O.V.Magdysyuk, J. H. Luan**, **Z. B. Jiao** : Methodology.

TABLE OF CONTENTS

Chapter 1: Introduction 1

1.1. Additive Manufacturing and Laser Powder Bed Fusion 1
1.2. Applications of β Titanium Alloys 3
1.3. Aims and Objectives 6
1.4. References 8

Chapter 2: Literature Review 10

2.1. Laser Powder Bed Fusion 10
2.1.1. Introduction 10
2.1.2. Physical aspects 11
2.1.3. Commonly observed defects and eliminating methods. 15
2.2. Metallurgy of β Ti Alloys 19
2.2.1. Chemical composition 19
2.2.2. Conventional preparation methods 23
2.2.3. Phase transformations 25
2.2.4. Strengthening strategies 39
2.2.5. Deformation modes 46
2.2.6. Typical heat treatments 49
2.3. Laser Powder Bed Fusion of β Ti Alloys 52
2.3.1. LPBF using pre-alloyed powders 52
2.3.2. LPBF using blended elemental powders (in-situ alloying) 54
2.3.3. Microstructural evolutions of β Ti alloys 60
2.3.4. Controlling elastic modulus of β Ti 64
2.3.5. Creating functional gradient structures by LPBF 68
2.4. Summary of the Literature and Knowledge Gaps for Further Investigations. 70
2.5. References 71

Chapter 3: Materials and Experimental Methods 91

3.1. Feedstock Powders 91
3.2. LPBF Processing and Post-treatments 91
3.3. Microstructure Characterisation 93

3.4. In-situ Synchrotron X-Ray Diffraction 96
3.5. Mechanical Properties 97
3.6. References 98

Chapter 4: In-situ Alloying Based LPBF Fabrication of β Ti-12Mo Alloy and Its Functionally Graded Composites 100

4.1. Introduction 101
4.2. Experimental 104
4.2.1. Powders 104
4.2.2. LPBF process 105
4.2.3. Microstructural characterisation 107
4.2.4. Mechanical testing 108
4.3. Results and Discussion 108
4.3.1. Melting and homogenisation 109
4.3.2. Keyhole-induced defects 114
4.3.3. Microstructure of the Ti-12Mo alloy 122
4.3.4. Fabrication of the Ti-Mo FGC 123
4.3.5. Microstructure of the Ti-Mo FGC 124
4.3.6. Macro and micro mechanical behaviours. 130
4.3.7. Post-deformation characterisation 134
4.4. Outlook and Challenges 137
4.5. Conclusions 138
4.6. References 139

Chapter 5: In-Situ Alloying Based LPBF Fabrication of A High Strength and Low Modulus β Ti-12Mo-6Zr-2Fe Alloy 145

5.1. Introduction 146
5.2. Experimental 149
5.2.1. Powders 149
5.2.2. LPBF processing and heat treatment 149
5.2.3. Microstructural characterisation 151
5.2.4. Mechanical tests 153
5.3. Results 153

5.3.1. Mechanical properties 153
5.3.2. Chemical homogeneity 155
5.3.3. Melt pool microstructure 158
5.3.4. Grain structure 159
5.3.5. Phase identification 162
5.3.6. Heat treatment response 170
5.4. Discussion 171
5.4.1. Chemical homogenisation 171
5.4.2. Second phases 173
5.4.3. Elastic modulus 175
5.4.4. Strengthening mechanisms 177
5.5. Conclusions 181
5.6. References 182

Chapter 6: Deformation Mechanisms of β Ti-12Mo Alloy with High Strength and High Strain Hardening Rate Prepared by In-situ Alloying Based LPBF 189

6.1. Introduction 190
6.2. Materials and Methods 193
6.2.1. Materials processing 193
6.2.2. In-situ X-ray diffraction and tensile tests 195
6.2.3. Microstructural characterisation 196
6.3. Results 199
6.3.1. Tensile behaviour 199
6.3.2. Microstructural analysis 201
6.3.3. Synchrotron X-ray analysis 211
6.3.4. Microstructural investigations after 1.4 % strain 216
6.3.5. Microstructural investigations after 5 % strain 219
6.3.6. Microstructural investigations after 11 % strain 228
6.3.7. Microstructural investigations after 17 % strain 232
6.4. Discussion 233
6.4.1. Strengthening contribution to the yield strength 234
6.4.2. Mechanisms and sequence of plastic deformation 237
6.5. Conclusion 242

6.6. References 243

Chapter 7：Conclusions & Future Work 251

7.1. Summary and Conclusions 251

7.1.1. Parametrical studies for densification and homogenisation 251

7.1.2. Influence of energy density and the FGC material 252

7.1.3. Influence of scanning strategies 253

7.1.4. Influence of solution heat treatments 255

7.1.5. The deformation mechanisms 256

7.2. Future Works 257

TABLE OF FIGURES

Fig. 1.1. The applications of Additive Manufacturing of metals, modified from [2,4]. 2
Fig. 1.2. The schematic shows the elastic modulus of different implant materials, inserted with the X-Ray computed tomography (XCT) image, exhibits the stress shielding phenomenon, modified from [12,13]. 4
Fig. 1.3. The yield strength and fracture toughness of various Titanium alloys were tested at room temperature (Modified from [14]). 5
Fig. 2.1. The schematic image shows the procedure of LPBF processing. (Modified from [3]). 11
Fig. 2.2. The 3D model of melt flow effects with the increase of temperature-dependent physics fidelity. (Modified from [11]) 14
Fig. 2.3. The morphologies of lack of fusion porosities in Ti6Al4V alloys processed by LPBF: (a) the optical microscopy image; (b) the SEM image. (Modified from [8,18,19]) 15
Fig. 2.4. The porous morphologies, including gas porosities and LOF, in AM Ti6Al4V alloy, are characterized by synchrotron XCT. (Modified from [21]) 17
Fig. 2.5. Melt pool and vapour depression's evolutions under continuous laser irradiation. (Modified from [24]).....17
Fig. 2.6. The morphology of solidification cracks in Ti-40Al-9V-0.5Y alloys processed by LPBF. (Modified from [31]) 18
Fig. 2.7. The phase diagram of Ti-Mo alloy. (Modified from [37]) 20
Fig. 2.8. The phase diagram of Ti-Cr alloy. (Modified from [37]) 21
Fig. 2.9. The schematic shows the Mo_{eq} values and classifications of various β Ti alloys. (Modified from [41]).....22
Fig. 2.10. Pure metallic elements and their biocompatibility. (Modified from [42–44]).....23
Fig. 2.11. Crystal structure of α, β and ω phases. (Modified from [39,53,54]).....26
Fig. 2.12. The time-temperature-transformation (T.T.T) diagram for Ti-12Mo. (Modified from [55]).....27
Fig. 2.13. The T.T.T diagram for Ti-15Mo, and the microstructural evolution during the isothermal ageing treatment at 450 and 650 ℃. (Modified from [55]) 28
Fig. 2.14. The schematic shows the β/α phases transformations. (Modified from [38]).....29
Fig. 2.15. (a) The inverse pole figure (IPF) maps of β+α phases in Ti-5553 alloy after solution heat treated and aged at 600 ℃. (b) The IPF map of α phases with only three variants. (c) The microstructure of the Ti5553 alloy is processed by double ageing (2h 350 ℃ + 2h 600 ℃): the IPF map of α phases with five variants (Modified from [61]). 30
Fig. 2.16. The schematic shows the pathway from ω transform to α phase during isothermal ageing treatments. (Modified from [64]) 31
Fig. 2.17. X-ray energy dispersive spectrometry (XEDS) maps (a,b) and its high angle annular dark-field scanning transmission electron microscopy (HAADF-STEM) image (c) show the nucleation of α phases assisted by the isothermal ω phases. (Modified from [67]).....32
Fig. 2.18. The phase diagram shows the equilibrium and the non-equilibrium phases transformations in metastable β Ti alloys. (Modified from [36]) 34
Fig. 2.19. (a-e) The HAADF-STEM images of the interfaces between the β/α" or β/α under different ageing temperatures. (f) S values under different conditions. (g) The Nb concentrations across the interface of phases. The EDS mapping of the phase boundaries (h) and its line profile (i). (Modified from [83]). 35

Fig. 2.20. The SEM image shows the martensite α" plate in the Ti-6%Mo alloy. (Modified from [79]).....36
Fig. 2.21. (a) The HAADF-STEM images reveal the ω and O' phases in Ti-18Mo alloy. the lattice structures. (b) The high magnification HAADF-STEM image shows the lattice shuffle in O' phases. (c) The schematic showing the {110}<110> lattice shuffle from β to O' phases (Modified from [90]).....37
Fig. 2.22. The schematic shows the lattice transformations of the three different non-equilibrium phases in metastable β Ti alloys: (a) α'/α" phase; (b) O' phase; (c) ω phase. (Modified from [95]).....38
Fig. 2.23. The schematic figure shows the nonequilibrium phases of metastable β Ti alloys and their lattice transformations. (Modified from [90]).....38
Fig. 2.24. The optical microscopy images of (A) pure Ti, (B) Ti-0.05Be, (C) Ti-0.1Be, and (D) Ti-0.2Be. (Modified from [106]).....42
Fig. 2.25. The TEM bright field images show: (a, c) the coarse grain boundary α; (b, d) plate-like primary intragranular α, and nano-sized secondary intragranular α phases. (Modified from [121]).....44
Fig. 2.26. (a) The schematic shows the details of heat treatment procedures. (b-f) The backscattered electron (BSE) images show the evolution of microstructures after different low-temperature holding times. (Modified from [125]). 46
Fig. 2.27. The deformation modes in varied β Ti alloys are divided by Mo_{eq}. (Modified from [36,131]).....47
Fig. 2.28. The $Bo - Md$ map conclude the chemical stabilities and deformation modes of various β Ti alloys. (Modified from [42,96]).....48
Fig. 2.29. The phase diagram shows the typical heat treatments of β Ti alloys. (Modified from [38]).....51
Fig. 2.30. The BE powders' BSE images (Ti, Al and V) and the laser beam's interaction schematics using conventional mixing (a) and satellited blending (b). (Modified from [30]).....55
Fig. 2.31. (a) The BSE image shows the microstructure of in-situ alloyed Ti64-Mo. (b) The 3D XCT images of in-situ alloyed Ti-26Nb. (Modified from [179,180]) 56
Fig. 2.32. (a) Area percentage of residual Ta particles in in-situ alloyed Ti-Ta using varied scanning speeds and melting strategies. (b) The BSE image shows the microstructure of the specimen fabricated using the single melt strategy. (c) The BSE image shows the microstructure of the specimen fabricated using remelt strategy. (Modified from [170]) 57
Fig. 2.33. The 3D XCT results show the evolution of porosity and residual Nb particles in the Ti34Nb samples with the increase of laser energy from 350w to 950w. (Modified from [181]).....57
Fig. 2.34. (a) The influence of G and R on the morphology of solidification microstructure. (b) The solidification map of Ti6Al4V alloy. (Modified from [8,191]).....61
Fig. 2.35. The OM images show the grain structure of Ti6Al4V (a) and Ti-8.5Cu (b) alloys processed by LPBF, respectively. (c) The grain growth mechanisms of the above two alloys, where TA and TE are the profile of the melt temperature and equilibrium liquidus temperature, respectively. The value of ΔTCS is equal to $TE - TA$, and ΔTn is regarded as the magnitude of the length bar. (Modified from [104]) 63
Fig. 2.36. Microstructures of Ti-25Ta alloys after laser remelt and the corresponding selected area diffraction (SAED) patterns from different regions (The SAED patterns of A, B, C, D, and E were acquired from the position A, B, C, D, and E, respectively). (Modified from [170]).....64

Fig. 2.37. The V and Nb contents' dependence of Young's modulus in Ti-V (a) and Ti-Nb (b) binary systems, respectively. (Modified from [135]) 65
Fig. 2.38. The textures of as-SLMed Ti-15Mo-5Zr-3Al alloys are processed by different scan strategies (Modified from [199]). 66
Fig. 2.39. (a) The LPBF processed porous Ti6Al4V alloys with varied triply periodic minimal surfaces design. (b) A Ti implant combined with solid and porous structures fabricated by LPBF. (Modified from [205–207]) 68
Fig. 2.40. (a) The schematic shows the repetitive laser scan process with varied laser energy. (b) The as-fabricated gradient NiTi specimens. (Modified from [215]).....69
Fig. 3.1. The microstructure characterisations and mechanical properties tests have been employed to the β Ti alloys prepared by in-situ alloying based LPBF. 93
Fig. 3.2. (a) The schematic shows the interaction of incident beam and specimen during the TKD characterisations, where the structure of on-axis and off-axis detectors are also illustrated. (b) The photograph of the chamber of the off-axis TKD test. (Modified from [5,6]).....95
Fig. 4.1. (a) The particle size distributions of Ti and Mo elemental powders; (b) the schematic of the powder blending process; (c) BSE micrograph of Ti12Mo blended powder; (d) the schematic of LPBF in situ alloying processing; (e) as-fabricated samples with different scanning parameters; and (f) schematic illustration of the scanning strategies depicting the island spacing, and beam delay settings. 106
Fig. 4.2. (a) BSE images of as-fabricated Ti-12Mo specimens (values on the images are the AED); (b) effect of AED on the percentage of un-melted Mo and density; (c) XRD patterns of as-fabricated Ti-12Mo cube specimens; (d) BSE micrograph of Ti-12Mo sample; (e) and (f) are EDS elemental maps of Ti and Mo, respectively; (g) high magnification BSE micrograph (black dotted lines indicated the melt pool boundaries); (h) and (i) are the EPMA maps of Ti and Mo, respectively (Black arrows indicated the chemical segregations).....110
Fig. 4.3. (a)–(c) are side-view BSE micrographs of the as-fabricated Ti-12Mo sample under different processing conditions: (a) low AED (1.7 J/mm^2), (b) middle AED (2.2 J/mm^2), and (c) high AED (4 J/mm^2); (d) and (e) are the side-view BSE images of the top layer of the samples fabricated using the AED of 1.7 and 2.2 J/mm^2, respectively; (f) the side-view optical micrograph of the top layer of the sample fabricated using AED of 4 J/mm^2; (g) the schematic illustration shows the remelting process of Mo particles during LPBF. 112
Fig. 4.4. The linear correlation between the melt pool depth (μm) and AED (J/mm^2).....112
Fig. 4.5. The BSE image of the Ti-12Mo sample was fabricated using the AED of 5 J/mm^2. 115
Fig. 4.6. (a) Optical micrograph of the full side section of the chessboard-scanned Ti-12Mo sample fabricated using AED of 4 J/mm^2, and high LBD settings; (b) and (c) are side-view optical micrographs of the keyholes of the chessboard-scanned Ti-12Mo alloy: (b) top layer; and (c) middle layer; and (d) the schematic illustration of the formation of keyholes defects. 117
Fig. 4.7. The OM microstructures of the specimens were fabricated using the simple scanning strategy with high (a) and low (b) LBD settings, respectively, of which the other scanning parameters are the same. 118
Fig. 4.8. The OM images of the specimens were processed using chessboard scanning strategy with high LBD (a) and low LBD (b), respectively (Red lines indicate the scanning directions of the top layer, the white lines present some melt pool boundaries,

and the blue lines indicate the spacing between the keyholes along the build direction). (c) Schematic illustration of the scanning speed variations during the single scanning trace and the corresponding melt pool shape; (d) scanning traces (red lines) of chessboard-scanned samples (the blue circle marks the single scanning trace, while the green circles indicate the overlap points between the neighbouring island); (e) schematic illustration of the definition of IS parameters and LBD settings; (f) the relationship between the samples' relative density fabricated using 4 J/mm^2 with different IS and LBD settings (inset is the BSE micrograph of the Ti-12Mo alloy fabricated using low LBD and 0.06 IS settings). 120
Fig. 4.9. The side-view optical images of the samples for the optimisation of LBD and IS. 121
Fig. 4.10. (a)–(c) are the XRD pattern, low magnification and high magnification BSE images of Ti-12Mo alloy fabricated using a low AED of 1.6 J/mm^2, respectively; (d)–(f) are the XRD pattern, low magnification and high magnification BSE images of Ti-12Mo alloy fabricated using a high AED of 4 J/mm^2, respectively. 123
Fig. 4.11. (a) Schematic of the Ti-12Mo FGC with two designed low energy input layers; (b) the merged BSE micrograph of the FGC and the corresponding EDS elemental maps of Ti (c) and Mo (d). 124
Fig. 4.12. The microstructure of the interdiffusion area: (a) an EBSD IPF map of β phase; (b) KAM map of the β Ti matrix; (c) the phase distributions map of α" and β; (d) and (e) are the EDS elemental maps of Ti and Mo, respectively; (f) EDS line profiles of Ti and Mo elements' concentration along the solid white lines in (d) and (e); (g)–(i) are the BSE micrographs of the regions selected in (c), respectively. 125
Fig. 4.13. Elemental distribution across the interdiffusion region. (a) and (b) are the EDS elemental maps of Ti and Mo, respectively; (c) is EDS line profiles along the solid white line in (a) and (b). 126
Fig. 4.14. The side-view BSE image of the top layer of the LE sample shows the melt pools' depth. 127
Fig. 4.15. The microstructure of the matrix of the Ti-12Mo alloy fabricated using a high AED of 4 J/mm^2 (HE layer in FGC). (a) SEM micrograph shows the selected site for FIB milling with the inset showing the morphology of FIB lamella; (b) the HAADF-STEM image; (c) the bright-field TEM image (magnified from selected region in (b)) and corresponding SAED pattern; (d) and (e) are the dark-field TEM images show ω1 and ω2 phases, respectively. 128
Fig. 4.16. The microstructure of the matrix of the Ti-12Mo alloy was fabricated using a low AED of 1.6 J/mm^2 (LE layer in FGC). (a) SEM micrograph shows the selected site for FIB milling with the inset showing the morphology of FIB lamella; (b) and (c) are the bright-field TEM image and corresponding SAED pattern, respectively; (d) and (e) are the bright-field TEM image, and corresponding SAED pattern from another region; (f)–(h) are the HAADF-STEM image and corresponding EDS elemental maps of Ti (g) and Mo (h), respectively. 129
Fig. 4.17. The microhardness profile across the Ti-Mo FGCs along the build direction (The interval between adjacent hardness tests is 0.1 mm). 131
Fig. 4.18. (a) The engineering (solid lines) and true (dotted lines) stress-strain curves of the LE, HE and FGC samples; (b) the strain-hardening rates of LE, HE and FGC samples. 132
Fig. 4.19. The superimposed images of the samples' surfaces and the strain field during compression test: (a) LE sample; (b) HE sample; and (c) FGC sample. 132
Fig. 4.20. Compressive behaviours of the micropillars in LE and HE layers of FGC. (a) The engineering stress-strain curves; (b, c, d) the SEM image of the micropillar of LE: (a) as-

milled, (c and d) after compression; (e, f, g) the SEM image of the micropillar of HE:(e) as-milled, (f and g) after compression. 133
Fig. 4.21. (a) The BF TEM image shows the microstructure of the FIB thin film, lifted out from the HE area in FGC specimens, which aligned with the compressive direction. (b) The BF TEM image, magnified from (a), and the corresponding SAED pattern (c). (d) The DF TEM image shows the distribution of ω phases. 135
Fig. 4.22. (a) The BF TEM image shows the microstructure of the FIB thin film, lifted out from the LE area in FGC specimens, which aligned with the compressive direction. (b) The BF TEM image, magnified from (a), with the SAED pattern inserted. (c) The HAADF STEM image shows high-density dislocations. 136
Fig. 5.1. (a) The schematic of the powders blending processing. (b) and (c) are the BSE image and the corresponding EDS elemental map of Ti-12Mo-6Zr-2Fe blended powder. (d) Schematic of the LPBF processing of the blended powders. (e) Schematic of scanning strategies for the fabrication of tensile bars, where the TD, build direction (BD), and their normal direction (ND) were indicated by the black arrows. (f) Optical micrograph of the side section of as-fabricated TMZF alloy..... 151
Fig. 5.2. (a) The engineering (solid lines) and true (dotted lines) stress-strain curves of AF-SS, AF-CS, and ST-CS TMZF alloys. (b) A comparison of the present TMZF alloys with other biomedical Ti alloys in yield strength and the ratio of yield strength to the Young's modulus. (c)-(e) are the fracture morphology of AF-SS, AF-CS, and ST-CS TMZF alloys, respectively. 155
Fig. 5.3. The contour mapping shows the distributions of (a) Ti, (b) Mo, (c) Zr and (d) Fe elements in the side section of the AF-CS TMZF sample plane, parallel with the build direction. 157
Fig. 5.4. BSE images and elemental distributions of the cross-section of AF-CS TMZF alloy. (a) A low magnification BSE image; (b)–(e) EDS elemental maps of Ti, Mo, Zr, and Fe, respectively; (f) a higher magnification BSE image (Yellow dotted lines indicated the melt pool boundaries); (g)–(j) EMPA elemental maps of Ti, Mo, Zr, and Fe, respectively. 158
Fig. 5.5. SEM micrographs of the melt pool morphology of the AF-CS TMZF alloy, including the top layer (a), the middle layer after several heat cycles (b), and the thin region along the melt pool boundaries (c). The white dotted lines, white arrows, white solid lines and red dotted lines marked the cellular sub-grains, cellular solidification direction, grains boundaries, and the thin region of cellular structure, respectively. 159
Fig. 5.6. EBSD inverse pole figure (IPF) maps (left column) and the grain size distributions (right column) of β phase in the middle layer of AF-SS (a, b), AF-CS (c, d) (the white dotted lines indicated the melt pool boundaries), and ST-CS (e, f) TMZF alloys (IPF Z-axis along the TD). The insets in (b, d, and f) are (100) pole figures. 160
Fig. 5.7. Melt pool microstructure of the cross-section (perpendicular to BD) of AF-CS TMZF alloy: (a) an EBSD IPF map; (b) the EBSD band contrast map with superimposed LAGBs and HAGBs. 161
Fig. 5.8. Rietveld refinement analysis of the XRD patterns obtained from the planes perpendicular to TD, and parallel with BD, of (a) AF-SS, (b) AF-CS, and (c) ST-CS TMZF alloys (The different positions were magnified to label the peaks of α" phase, which were indicated by yellow or green dotted circles, respectively). (d) The Young's modulus and the peak intensity ratios of $(200)_{\beta}$ to $(110)_{\beta}$ of the three groups of samples in different processing conditions. 163
Fig. 5.9. The microstructure of the AF-SS TMZF alloy. (a) EBSD IPF map of the α" phase in

the plane perpendicular to TD; (b) SEM image; (c) HAADF-STEM image of the α" phase; (d)-(g) EDS elemental maps of Ti, Mo, Zr, and Fe collected from the yellow dotted square in (c), respectively; (h) bright-field TEM image of a selected area containing α" phase; (i) the SAED pattern along the $[111]_\beta$ zone axis collected from the black dotted circle in (h) shows the orientation relationship of $[110]_{\alpha''}//[111]_\beta$; (j) a HAADF-STEM image shows the β matrix and α" phases; (k) SAED pattern along the $[011]_\beta$ zone axis collected from the area without α" phase; and (l) dark-field TEM image selected from the ω reflections as indicated by the white circle in (k).....166
Fig. 5.10. The microstructure of the AF-CS TMZF alloy. (a) EBSD IPF map of β and α" phase; (b) EBSD IPF map only showing the α" phase; (c) KAM map of the β Ti matrix; (d) bright-field TEM image shows the grain boundaries clustering α" phases with the inserted SAED pattern along the $[113]_\beta$ zone axis collected from the area without α" phases; (e) bright-field TEM image shows the α" variants inside some grains; (f) bright-field TEM image magnified from the selected area (white dotted square) of (e); (g) SAED pattern along the $[131]_\beta$ zone axis collected from the white dotted circle in (f); (h) a HAADF-STEM image shows the β matrix and α" phases in the AF-CS TMZF alloy; and (i)-(l) EDS elemental maps of Ti, Mo, Zr, and Fe, respectively.....167
Fig. 5.11. The microstructure of the ST-CS TMZF. (a) the EBSD IPF map of β phase; (b) the EBSD IPF map only showing the α" phase; (c) the KAM map of the β Ti matrix; (d) a low magnification bright-field TEM image; (e) a higher magnification bright-field TEM image which clearly illustrates the dislocation tangles inside the α" phase; (f) SAED pattern along the $[011]_\beta$ zone axis collected from the interface of β and α" phases as indicated by the black circle in (e); (g) a HAADF-STEM image shows the β matrix and α" phases; and (h)-(k) EDS elemental maps of Ti, Mo, Zr, and Fe, respectively.....169
Fig. 5.12. DSC results of AF-CS Ti12Mo and TMZF. 171
Fig. 5.13. (a) The optical microscopy image of the side section of the TMZF alloy manufactured by the chessboard scanning strategy shows the melt pool morphologies of the top layer. (b) The schematic represents the homogenisation mechanism during the laser remelts. 173
Fig. 5.14. (a) The contributions from CRSS of pure Ti ($\sigma 0$), solid solution strengthening (σSS), grain boundary strengthening (σHP), dislocation strengthening (σDS), and precipitation strengthening (σPS) of AF-SS, AF-CS and ST-CS TMZF alloys. (b) The precipitation strengthening (σPS) and the volume fraction of α" phases in AF-SS, AF-CS and ST-CS TMZF alloys.....180
Fig. 6.1. (a) Schematic diagram shows the LPBF in-situ alloying process of Ti-12Mo blended powders. (b) schematic diagram shows the synchrotron experimental set-up of the tensile specimen, incident monochromatic X-ray beam, and the Debye-Scherrer rings represented in 2D area detector. The Debye-Scherrer ring is recorded at load 1440 N. Three 15º ranges (±7.5º) of azimuthal integration are shown: 0 º - diffraction in the tensile direction (loading direction), 90 º - diffraction in the Poisson direction, and 45 º - diffraction in the diagonal direction. 198
Fig. 6.2. (a) Engineering stress-strain curves of the standard tensile tests and in-situ tensile test of AF-CS and ST-CS Ti-12Mo alloy. (b) True stress-strain curves and strain-hardening rates ($d\sigma Ture/d\varepsilon Ture$) of the ST-CS Ti-12Mo and conventional Ti-12Mo prepared by arc melting [8]. (c) Ultimate tensile strength (UTS), accompanied with elongation of the ST-CS Ti-12Mo samples, compared with other Ti alloys prepared by additive manufacturing. 201
Fig. 6.3. The EDS elemental maps of Ti (a) and Mo (b). (c) The detailed weight percentage of

Ti and Mo concentrations in 6 random areas. 202
Fig. 6.4. The XRD patterns of AF-CS and ST-CS Ti-12Mo alloys 203
Fig. 6.5. 3D EBSD figures show the grain structure of AF-CS (a) and ST-CS (c) Ti-12Mo specimens, where the build direction, tensile direction and incident X-ray beam direction are presented; (b and c) the grain size distributions in AF-CS (b) and ST-CS (d) Ti-12Mo specimens (inserted: the (100) pole figure of X-Y plane, which is perpendicular to the build direction). 204
Fig. 6.6. The microstructure of AF-CS Ti-12Mo alloy: (a) the bright-field (BF) TEM micrograph (the SAED pattern and line intensity profile along the [121] direction; (b) the dark-field (DF) TEM image of ω particles; (c) the HR-TEM image and (d-e) the corresponding inverse fast Fourier transformation (FFT). The diffraction streaks in (d) demonstrate the presence of high-density stacking faults in ω laths. 205
Fig. 6.7. (a) XRD pattern of the ST-CS Ti-12Mo sample. (b) The bright-field (BF) TEM micrograph and its selected area electron diffraction (SAED) pattern (c). The average size distributions of ω phase (d) and the dark-field (DF) TEM micrographs(e-f) derived from the ω diffraction spots in green and yellow circles in the SAED pattern of (c). (g) Reconstructed atom probe tomographic micrograph shows the morphology and distribution of ω particles. (h) Two-dimensional cross-sectional atom map derived from the APT with 92 at% Ti iso-concentration surfaces. (i) Concentration profiles of Ti and Mo elements with the blue arrow indicating its location in (h). (j) Proximity histograms of the mean concentrations of Ti, Mo, and O elements as a function of distance across the β/ω interface. 207
Fig. 6.8. (a) BF TEM image of the region in the ST-CS Ti-12Mo sample with some α" precipitates. (b) high-resolution TEM (HRTEM) image observed inside the α" precipitates. (c) Fast Fourier Transformation (FFT) derived from the dotted square in (b). (d) HRTEM image shows the phase boundary between the α" and β phases. (e) geometric phase analysis (GPA) conducted on the phase boundary of (d). (f) inverse FFT image derived from (d), and the applied mask was inserted. (g) high-angle annular dark-field (HAADF) STEM image and the corresponding energy dispersive spectroscopy (EDS) mapping of Ti (h) and Mo (i) elements. (j) The line intensity profiles of HAADF, Ti and Mo elements along the solid arrow lines in (g-i). 210
Fig. 6.9. (a) Evolution of lattice strain along the LD, 45 º to LD and PD. (b) Evolution of lattice parameter of β Ti along the LD, 45 º to LD and PD. 213
Fig. 6.10. Color-coded 3D plots derived from the XRD patterns during the deformation: (a) Loading direction (LD); (b) Poisson direction (PD). 214
Fig. 6.11. (a) XRD patterns maximised from selected two theta range show the reflections' evolution of β, α" and ω phases. (b) Color-coded 2D plots are corresponding to the reflections of β and α" phases. (c) Evolution of the volume fraction of SIM α" phase during the tensile deformation. 216
Fig. 6.12. Microstructures of the tensile specimen at 1.4 % true strain (just after yielding): (a) SEM image shows the position where the FIB lamellar was lifted out. (b) BF TEM image. (c) SAED pattern from the selected area 1. (d) SAED pattern from the selected area 2. (e) BF TEM image of matrix and twin boundary. (f-g) DF TEM micrograph derived from the ω diffraction spots in green and yellow circles in the SAED pattern of (d), where the HRTEM was inserted. (h) SAED pattern from the selected area 3. (i) BF TEM image of twin and twin boundary, where the slip traces were marked by red dotted lines. (j-k) DF TEM micrograph derived from the ω diffraction spots in green and yellow circles in the SAED pattern of (h). 218

Fig. 6.13. Microstructures of the tensile specimen at 5 % true strain: (a) SEM image (the inserted figure is the band contrast image superimposed with CSL 11 boundaries). (b) EBSD inverse pole figure (IPF) of β Ti matrix from the red square in (a) and corresponding IPF map showing the distribution of SIM α" phase (c). (d) pole figures of β matrix and SIM α" in (b) and (c) (dotted circle means the common poles in selected pole figures, and the solid square and circle represents the several corresponding poles in the selected pole figures of β and α" phases). (e) EBSD IPF map of β Ti matrix from the green dotted square in (a). (f) Schmid factor (0.4< SF < 0.5) distribution of {332}<113> twinning system along tensile direction. (g) The band contrast image superimposed with CSL 11 boundaries. (h) The GROD (grain-based misorientation parameter) map. (i) Schmid factor (0.4 < SF < 0.5) distribution of SIM α" transformation along tensile direction. (j) IPF map shows the distribution of SIM α" phase 221
Fig. 6.14. Microstructures of the tensile specimen at 5 % true strain: (a) BF TEM image of the FIB lamellar lift out from Area 1 in (b). (b) Backscattered electron (BSE) micrograph of the ST-CS Ti-12Mo sample at the true strain of 5 % (the squares in white contrast show the locations of FIB lift-out). (c) BF TEM image of the FIB lamellar lift out from Area 2 in (b).....222
Fig. 6.15. Microstructures of area 1 in Fig.9b: (a) BF TEM micrograph shows the primary β twin. (b) BF TEM micrograph magnified from (a). (c) SAED pattern collected from region 1 in (a). (d) SAED pattern collected from region 2 in (a), and the corresponding DF TEM images showing the location of ω lath (e), secondary β twin and lath (f) inside the composite band. (g) The DF STEM image shows the slip traces inside the primary β twin, where the high-density dislocations were observed. (h) Simulated SAED pattern of (d).....223
Fig. 6.16. Microstructures of area 2 in Fig.9b: (a) BF TEM image. (b) BF TEM image magnified from (a). (c) SAED pattern collected from a dotted circle in (b), and the corresponding DF TEM images showing the ω phases (d) in the primary β twin, and the boundary SIM α" phase (e). (f) simulated SAED pattern of (c). 224
Fig. 6.17. Crystallographic orientations of β and α" phases represented using the stereographic projections to analyse the burgers orientation relationship (BOR) between the primary β matrix, β twin, secondary β twin and SIM α" phases in area 1 (a-d) and 2 (e-g) from Fig.6.15 and Fig.6.16, respectively. 226
Fig. 6.18. Microstructures of the tensile specimen at 5 % true strain: (a) HAADF-STEM image, EDS mapping of Ti (b) and Mo elements (c). (d) BF TEM image under the two-beam condition of g = [110]. (e) weak beam dark field (WBDF) image (g-3g). (f) The magnified WBDF image.....228
Fig. 6.19. TKD micrographs show the microstructure of ST-CS Ti-12Mo at 11 % true strain: (a) IPF EBSD map of β and α" phases; (b) the distributions of β and α" phases;(c) band contrast (BC) map superimposed with the twin boundaries of CSL 3 and 11. (d) IPF EBSD map of a single primary β twin and the corresponding line intensity profile (e) across the solid black line. (f) BF TEM image shows the boundary α" phases. (g) pole figures of β and SIM α" phases (dotted circle means the common poles in selected pole figures, and the solid square and circle represent the several corresponding poles in the selected pole figures of β and α" phases).....231
Fig. 6.20. Microstructures of ST-CS Ti-12Mo at 17 % true strain (the endpoint of uniform deformation): (a) phase map shows the distributions of β and α" phases; (b) IPF EBSD map of β phases; (c) IPF EBSD map of α" phase. (d) pole figures of β and SIM α" phases (dotted circle means the common poles in selected pole figures, and the solid square and

circle represent the several corresponding poles in the selected pole figures of β and α" phases). (e to g) TKD micrographs show the microstructures in unindexed region: (e) distributions of β and α" phases; (f) IPF EBSD map of β phases; (g) IPF EBSD map of α" phase. 233
Fig. 6.21. (a) GND map and (b) distribution of GND density. 235
Fig. 6.22. (a) EBSD IPF maps of the twinning structures after different levels of true strain. (b) The relationship between the true strain with the volume fraction of twins and α". .238
Fig. 6.23. Schematic shows the evolution of the microstructure of ST-CS Ti-12Mo alloy during the tensile deformation. 241

LIST OF TABLES

Table 2.1. The laser absorption coefficient of various materials [9]. 13
Table 2.2. The shear moduli (μ), Seitz radius(R), misfit parameter ($\boldsymbol{\lambda}_i$) and the coefficient of SSH (B_i) of the primary solutes in the β Ti alloys [99,100]..... 39
Table 2.3. The $Ml(k-1)$ values of varied elements in Ti matrix [106]. 41
Table 2.4. The mechanical properties of LPBF processed β Ti alloys. 58
Table 3.1. LPBF processing parameters in five levels using the simple scanning strategy. ... 92
Table 4.1. Characteristics of pure Ti and Ti-12Mo blended powders. 104
Table 4.2. Scanning parameters of the Ti-12Mo alloy using LPBF. 106
Table 4.3. Scanning parameters of the Ti-Mo FGC using LPBF. 122
Table 5.1. Optimised in-situ alloying based LPBF processing parameters for the fabrication of TMZF alloy. 151
Table 5.2. The mechanical properties of the AF-SS, AF-CS, and ST-CS TMZF alloys..... 155
Table 5.3 The microstrain, dislocation density, β phase lattice parameters and phase constitutions of the three groups of TMZF alloys calculated by the Rietveld method.... 163
Table 5.4. Quantitative EDS analysis of the contents of Ti, Mo, Zr, and Fe in the α" and β phases of the fabricated TMZF alloys. 169
Table 5.5. The contributions from CRSS of pure Ti ($\sigma 0$), solid solution strengthening (σSS), grain boundary strengthening (σHP), dislocation strengthening (σDS), precipitates strengthening (σPS) ,and σy of AF-SS, AF-CS and ST-CS TMZF alloys 180
Table 6.1. Optimised in-situ alloying based LPBF processing parameters for the fabrication of Ti-12Mo alloy. 194
Table 6.2. The tensile mechanical properties of LPBF processed Ti-12Mo, compared with the conventional Ti-12Mo prepared by arc melting. 201
Table 6.3. The average Ti, Mo and O concentrations of the β matrix and ω phases， based on the APT results..... 207
Table 6.4. The Young's modulus of the ST-CS Ti-12Mo alloy and the elastic modulus and Poisson ratio (ν) along the different crystallographic families..... 213
Table 6.5. The measured *l, e* and the calculated *F* after several true strains of the ST-CS Ti-12Mo samples. 238

NOMENCLATURE

Term	*Description*
AED	Area energy density
AF	As fabricated
AM	Additive manufacturing
APT	Atomic probe tomography
BCC	Body-centred cubic
BD	Build direction
BE	Blended elemental
BF-TEM	Bright-field TEM
BOR	Burger's orientation relationship
BSE	Backscattered electron
CET	Columnar to equiaxed transformation
CRSS	Critical resolved shear stress
CS	Chessboard scanning strategy
DF-TEM	Dark-field TEM
DIC	Digital image correlation
DSC	Differential scanning calorimetry
EBSD	Electron backscattering diffraction
EDS	Energy dispersive X-Ray spectroscopy
EPMA	Electron probe microanalysis
FFT	Fast Fourier transformation
FGC	Functional gradient composite
FIB	Focused ion beam
GNDs	Geometrically necessary dislocations
HAADF-STEM	High-angle annular dark-field scanning TEM
HR-TEM	High-resolution TEM
HCP	Hexagonal close-packed
HIP	Hot isostatic pressing
HP	Hall-Petch
IPF	Inverse pole figure

Term	*Description*
IS	Island spacing
KAM	Kernel average misorientation
LBD	Laser beam delay
LOF	Lack of Fusion
LPBF	Laser powder bed fusion
Mo_{eq}	Mo equivalent
ND	Normal direction
OM	Optical microscopy
PA	Pre-alloyed
PD	Poisson direction
PM	Powder metallurgy
SAED	Selected area electron diffraction
SE	Secondary electron
SEM	Scanning electron microscopy
SHR	Strain hardening rate
SIM	Stress-induced martensitic
SS	simple scanning strategy
SSH	Solid-solution hardening
ST	Solution heat treatment
T.T.T	Time-temperature-transformation
TD	Tensile direction
TEM	Transmission electron microscopy
Ti	Titanium
TKD	Transmission Kikuchi diffraction
TMZF	Ti-12Mo-6Zr-2Fe
TRIP	Transformation-induced plasticity
TWIP	Twinning-induced plasticity
UTS	Ultimate tensile strength
XRD	X-ray diffraction

*For the abbreviations used more than three times.

Chapter 1: Introduction

This chapter presents an overview of Additive Manufacturing and Laser powder bed fusion technology and the related applications of β Titanium (Ti) alloys. Finally, the overall research aims, and objectives of this thesis are presented.

1.1. Additive Manufacturing and Laser Powder Bed Fusion

Additive manufacturing (AM), also referred to as three-dimensional (3D) printing or rapid prototype, is a revolutionary technology that produces components near to their complete form (near net shape) [1,2]. This technique offers an alternative to traditional manufacturing procedures for high-complexity, low-waste components [3]. In recent years, AM has shown the ability to revolutionise industries and generate considerable cost and energy savings, which is proven by being used in a wide variety of applications and industries, as shown in Fig.1.1. The repairing and remanufacturing of more complicated components utilising various sophisticated materials is also demonstrated using AM [2,4].

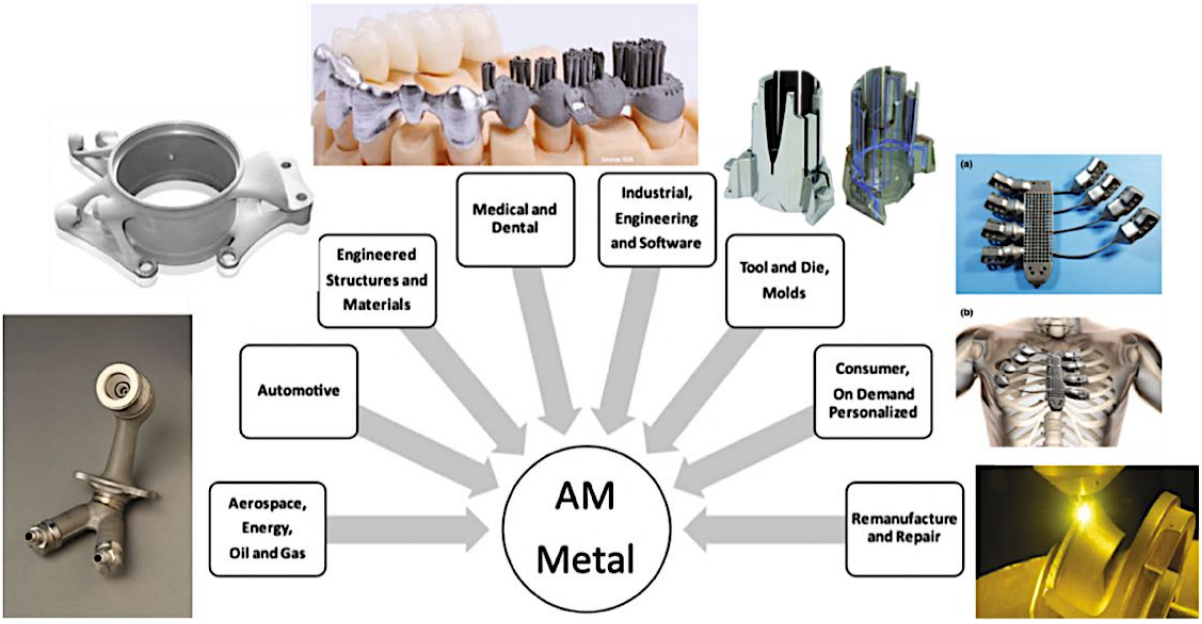


Fig. 1.1. The applications of Additive Manufacturing of metals, modified from [2,4].

The laser powder bed fusion (LPBF) process, alternatively referred to as selective laser melting or laser beam melting, is one of the most widely used AM technologies. Based on the 3D models, the LPBF applied a highly intensive laser beam to scan and melt the particular region of the powder bed through a layer-by-layer strategy, enabling it to overcome the geometric constraints and costly tooling needs associated with the subtractive manufacturing process. As a result, the LPBF technology shows enormous promise in the medical, aerospace, and automotive sectors (Fig.1.1). The advantages of using LPBF to process metallic components can be concluded as follow:

- The customisable computer aid design (CAD) models enable the high flexibility of LPBF fabrications, which also benefits from the elevated geometrical precision due to the highly concentrated laser beam.
- The LPBF offers the opportunities to combine several parts to reduce or eliminate subsequent assembly, even change material during the process to integrate multiple phases and thermal physics systems.
- The LPBF break out the constraints from the metal shape and some conventional post-processing treatments. In the meantime, it can reduce material waste caused by machining or forming.
- The ability to build complex porous/interconnected structures/lattice for lightweight purposes or requirements from specific mechanical or thermal physical properties.
- The LPBF paves the way to process materials that are hard to manufacture due to high melting temperature and/or low tooling rate.

1.2. Applications of β Titanium Alloys

In recent years, the β Ti alloys have shown their outstanding commercial importance, especially for the aerospace applications, biomedical and healthcare industry, mainly due to their high specific strength, low modulus, and excellent fatigue and corrosion resistance. Due to these, β Ti alloys become the most versatile class of titanium alloys.

Recently, the need for implantations and replacement surgeries are proliferating [5]. There are interests in discovering long-term biomedical implants materials [5,6], since most of the market implants use pure Ti or Ti6Al4V alloys [7,8], due to their good corrosion resistance and biocompatibility. However, many studies have illustrated that V and Al are slowly released in vivo, which may cause long-term harmful effects, including Alzheimer's and neuropathy [9]. On the other hand, the elastic modulus of CP Ti and Ti6Al4V is about 110GPa, which is much higher than cortical bone modulus (20~40 Gpa), resulting in stress shielding that can lead to bone loosening and resorption [5], as shown in Fig.1.2.

To avoid the two problems, the materials used for implants should be non-toxic and have low elastic modulus [5,6]. Compared with the hexagonal close-packed (HCP) α Ti alloy, the body-centred cubic (BCC) β Ti alloys containing Mo, Nb, Ta, Zr, Fe, Sn et al. elements have attracted considerable attention. This is mainly because of their excellent combination of low modulus, no long-term toxicity, no allergic reactions, and outstanding corrosion resistance [9]. Some elements can even raise the biocompatibility and cell viability of titanium alloys[10]. For example, Ti-12Mo-6Zr-2Fe (weight per cent and hereafter) alloy, known as TMZF alloy, has been used as a femoral stem in total hip replacement since the early 2000s with outstanding biocompatibility and corrosion resistance [11]. Moreover, previous works have reported that very low elastic modulus could be obtained by altering the β stabilising elements in Ti alloys (Fig.1.2) [12]. Thus, the β Ti alloys become the possible candidates for developing absolute

safe Ti implants with a combination of excellent biological passivity and reduced modulus.

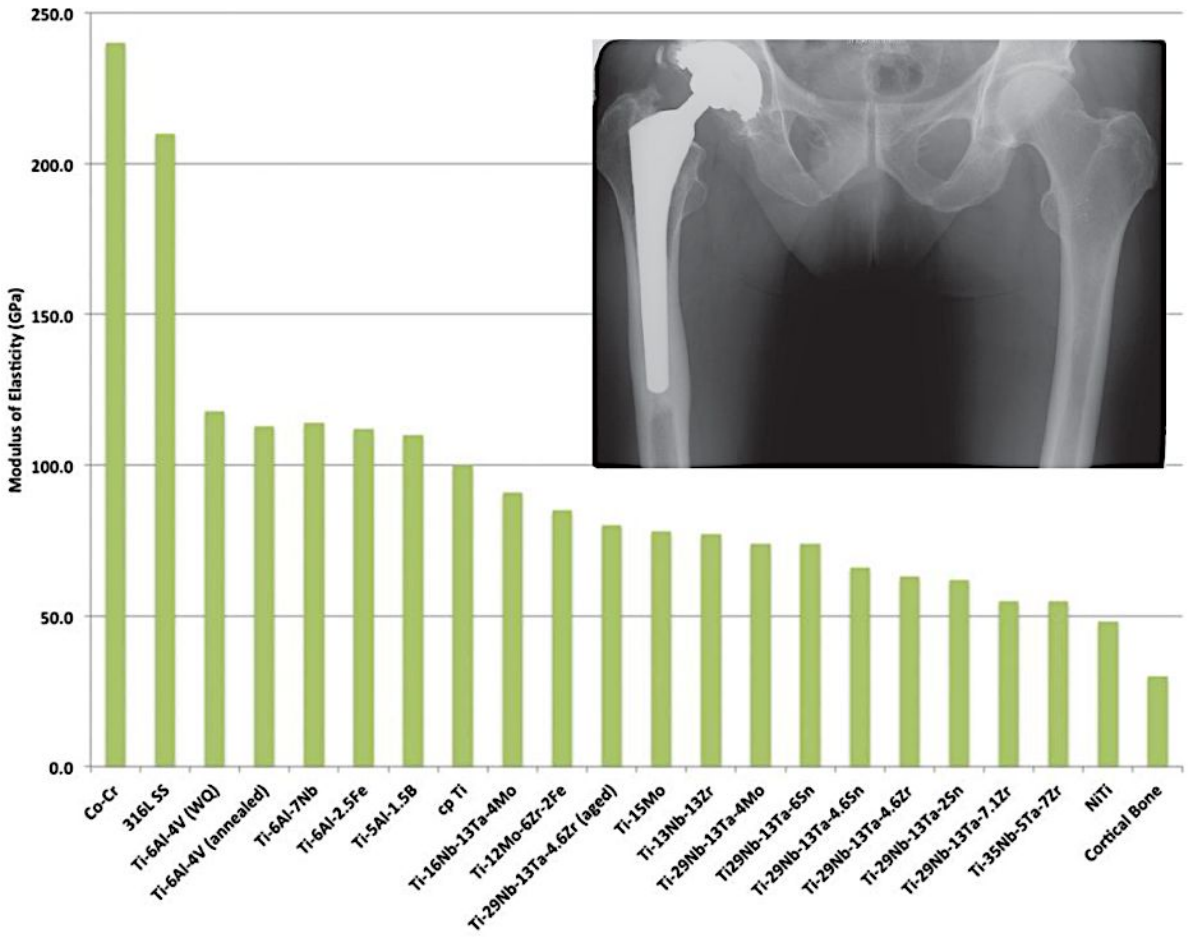


Fig. 1.2. The schematic shows the elastic modulus of different implant materials, inserted with the X-Ray computed tomography (XCT) image, exhibits the stress shielding phenomenon, modified from [12,13].

As shown in Fig 1.3, the β Ti alloys have exhibited exceptional high yield strength and excellent fracture toughness, which promote commercial success in aerospace structural applications [14]. With the purpose to use the β Ti alloys at an elevated high temperature, the Beta 21S (Ti-15Mo-3Al-3Nb) has been developed [14,15]. The alloy's particular combination of production, high ambient strength, remarkable high-temperature characteristics, and exceptional resistance to environmental degradation has proved beneficial for military and civil aero-engine exhaust components throughout the past centuries.

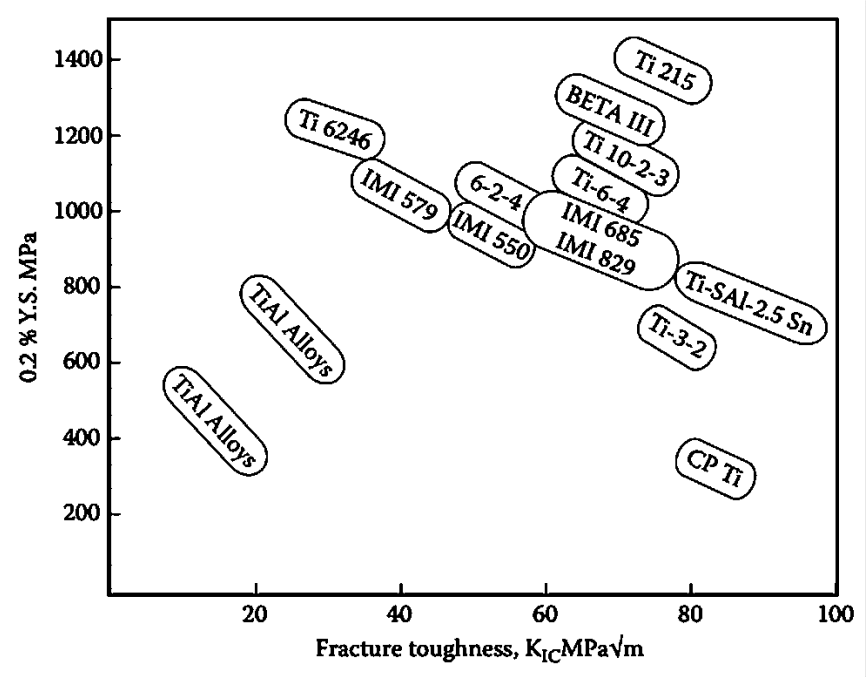


Fig. 1.3. The yield strength and fracture toughness of various Titanium alloys were tested at room temperature (Modified from [14]).

In summary, the β Ti alloys are indeed an excellent class of alloys used in high-stress or low-modulus applications, including aircraft structures and engines, as well as medical and orthopaedic implants. Whereas the considerable disadvantage of β Ti alloys is the high cost, mainly due to processing costs, which were concluded below[16]:

- Many alloying elements are expensive and refractory, thus higher formulation costs compared with conventional α+β alloys.
- More complex processing routes and narrower processing windows due to reduced β transus temperature.
- Thermal instabilities in the microstructure become more pronounced when treating components with variable cross-sections or massive dimensions.
- The low thermal conductivity reduces the heat diffusion between the tool and workpiece, yields short tool life and is hard to machine.

- Long processing cycles are needed to produce homogeneous microstructure because some alloying elements are refractory and have an extremely low interdiffusion rate in Ti.

Thus, investigating proper and cost-effective processing methods is critical for the effective use of β Ti alloys. Additionally, systematic relationships between processing, microstructure, and characteristics must be established to determine a technically feasible and appropriate processing window.

1.3. Aims and Objectives

Since a variety of research is interested in manufacturing high-performance β Ti alloys for applications in biomedical or aerospace industries. Considering the difficulties and high cost of manufacturing β Ti alloys, this work applied a novel cost-effective method, in-situ alloying based LPBF processing, to fabricate the β Ti-Mo alloys. The method will also be demonstrated to create biomimetic functional gradient composite materials. The results will advance our understanding of the interaction between processing optimisations, microstructural evolutions, mechanical properties, strengthening and deformation mechanisms of β Ti alloys.

The main aim is to **develop, process and evaluate high mechanical performance β Ti-Mo based alloys manufactured using in-situ alloying based LPBF technology**. The specific objectives are summarised as follows:

- **Fabrication of near fully dense and chemical homogeneous Ti12Mo alloy by in-situ alloying based LPBF (Chapter 4):**
  1) To eliminate residual Mo particles by optimising the processing parameters of LPBF, achieve largely homogeneous microstructures and investigate the mechanisms of chemical homogenisation resulted from laser remelting.

2) To reveal the formation mechanisms of defects and propose effective methods for the elimination.

- **Creation of Ti-Mo functional gradient composite (FGC) materials (Chapter 4):**
  1) To investigate the microstructures of different specimens produced using various laser energy inputs during LPBF processing.
  2) To explore the fabrication of Ti-Mo FGC materials by in-situ alloying based LPBF, evaluate the mechanical properties, reveal the microstructures and deformation mechanisms.
- **Fabrication of a biocompatible β Ti-12Mo-6Zr-2Fe (TMZF) alloy by in-situ alloying based LPBF (Chapter 5):**
  1) To evaluate the printability and chemical homogeneity of as-build TMZF alloy.
  2) To investigate the microstructural evolutions, including grain structures, textures, and precipitations of the specimens processed by varied scanning strategies and post-heat treatments. And conclude the relationship between the processing condition, microstructures, and mechanical behaviours.
  3) To quantify the strengthening effects from solid solution, grain boundaries, dislocation density and precipitations by dislocation slip system driven modelling.
- **Systematical investigations on strengthening mechanisms and deformation behaviours of LPBF processed β Ti12Mo alloys (Chapter 6):**
  1) To determine the effect of post-heat treatments on the microstructural developments and mechanical properties of β Ti12Mo alloys.
  2) To study twinning-induced plasticity (TWIP) and transformation-induced plasticity (TRIP) and conclude the deformation sequence of Ti-12Mo alloys during tensile using in-situ and ex-situ characterisation methods.

1.4. References

[1] L. Choisez, L. Ding, M. Marteleur, H. Idrissi, T. Pardoen, P.J. Jacques, High temperature rise dominated cracking mechanisms in ultra-ductile and tough titanium alloy, Nat Commun. 11 (2020) 2110. https://doi.org/10.1038/s41467-020-15772-1.

[2] J.O. Milewski, Additive Manufacturing of Metals, From Fundamental Technology to Rocket Nozzles, Medical Implants, and Custom Jewelry, 2017. https://doi.org/10.1007/978-3-319-58205-4.

[3] D. Zhang, D. Qiu, M.A. Gibson, Y. Zheng, H.L. Fraser, D.H. StJohn, M.A. Easton, Additive manufacturing of ultrafine-grained high-strength titanium alloys, Nature. 576 (2019) 91–95. https://doi.org/10.1038/s41586-019-1783-1.

[4] T. DebRoy, H.L. Wei, J.S. Zuback, T. Mukherjee, J.W. Elmer, J.O. Milewski, A.M. Beese, A. Wilson-Heid, A. De, W. Zhang, Additive manufacturing of metallic components - Process, structure and properties, Prog. Mater. Sci. 92 (2018) 112–224. https://doi.org/10.1016/j.pmatsci.2017.10.001.

[5] L. Kunčická, R. Kocich, T.C. Lowe, Advances in metals and alloys for joint replacement, Prog Mater Sci. 88 (2017) 232–280. https://doi.org/10.1016/j.pmatsci.2017.04.002.

[6] K.A. Nazari, A. Nouri, T. Hilditch, Mechanical properties and microstructure of powder metallurgy Ti–xNb–yMo alloys for implant materials, Mater Design. 88 (2015) 1164–1174. https://doi.org/10.1016/j.matdes.2015.09.106.

[7] M.A.-H. Gepreel, M. Niinomi, Biocompatibility of Ti-alloys for long-term implantation, J. Mech. Behav. Biomed. Mater. 20 (2013) 407–415. https://doi.org/10.1016/j.jmbbm.2012.11.014.

[8] M.J. Runa, M.T. Mathew, M.H. Fernandes, L.A. Rocha, First insight on the impact of an osteoblastic layer on the bio-tribocorrosion performance of Ti6Al4V hip implants, Acta Biomater. 12 (2015) 341–351. https://doi.org/10.1016/j.actbio.2014.10.032.

[9] Y.L. Hao, S.J. Li, R. Yang, Biomedical titanium alloys and their additive manufacturing, Rare Metals. 35 (2016) 661–671. https://doi.org/10.1007/s12598-016-0793-5.

[10] Q. Chen, G.A. Thouas, Metallic implant biomaterials, Mater. Sci. Eng. R. 87 (2014) 1–57. https://doi.org/10.1016/j.mser.2014.10.001.

[11] X. Zhao, M. Niinomi, M. Nakai, J. Hieda, Beta type Ti–Mo alloys with changeable Young's modulus for spinal fixation applications, Acta Biomater. 8 (2012) 1990–1997. https://doi.org/10.1016/j.actbio.2012.02.004.

[12] R.P. Kolli, A. Devaraj, A Review of Metastable Beta Titanium Alloys, Metals-Basel. 8 (2018) 506. https://doi.org/10.3390/met8070506.

[13] H. Bodén, P. Adolphson, M. Öberg, Unstable versus stable uncemented femoral stems: a radiological study of periprosthetic bone changes in two types of uncemented stems with different concepts of fixation, Arch Orthop Traum Su. 124 (2004) 382–392. https://doi.org/10.1007/s00402-004-0666-5.

[14] V.A. Joshi, Titanium Alloys An Atlas of Structures and Fracture Features, CRC, Boca Raton, 2006. https://doi.org/10.1201/9781420006063.ch6.

[15] J.C. Fanning, S.P. Fox, Recent developments in metastable β strip alloys, J Mater Eng Perform. 14 (2005) 703–708. https://doi.org/10.1361/105994905x75484.

[16] R. Boyer, G. Welsch, E.W. Collings, Materials Properties Handbook: Titanium Alloys, ASM International, USA, 1994.

Chapter 2: Literature Review

In this chapter, the main contents cover the relevant aspects of LPBF technology and the applications on processing β Ti alloys. The physical aspects, typical defects and eliminating methods in LPBF processing were first introduced. Relevant literature regarding β Ti alloys' metallurgy is also covered, highlighting the specific phase transformations, strengthening and deformation mechanisms that can be achieved in β Ti alloys. The final section concludes the development of β Ti alloys processed using LPBF and some interesting aspects utilised the advantages of LPBF.

2.1. Laser Powder Bed Fusion

2.1.1. Introduction

The LPBF enables near-net-shape fabrications starting with the CAD files meshed into two-dimensional (2D) stacked layers [1]. At the beginning of the LPBF processing, the raw powders are spread over the chosen substrate with a powder thickness between 20 and 100 microns [1,2]. After levelling a layer of powder, a laser beam is then direct scanning it and raster over the powder surface in a pattern to fill the region specified by one slice of the desired 3D model [2,3]. Fig.2.1 illustrates the interaction between the laser and powder bed during the LPBF process [3]. The near-net-shape technology, LPBF, shows great potential on the fabrication of complex integrational structure for biomedical or aerospace applications, without any expensive traditional tooling or machining like punch, dies or casting moulds, due to its high precision dimension, good fabrication flexibility, high material utilization, and the ability to build highly interconnected designed structure [2,3]. However, the applications of LPBF in

the industry is still rare, mainly due to the limited choice of materials. Some well-known materials for LPBF, such as 316L, Ti6Al4V and Inconel 718 alloys, were initially designed for conventional forming methods [3–5]. Another main challenge is the elimination of defects. When exploring new materials using LPBF, the consideration of porosity, cracks, surface roughness, and residual stress et al., are inevitable for some alloying systems, which need to be thoroughly understood and improved [2,6]. Here we firstly investigate some relative physical aspects during laser processing.

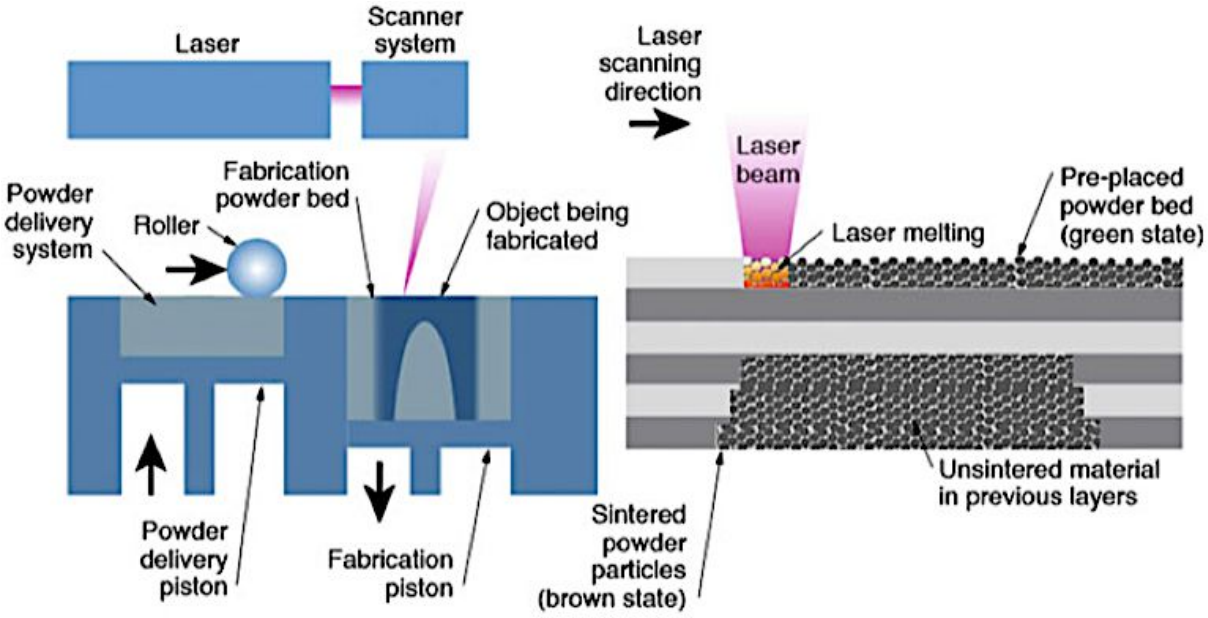


Fig. 2.1. The schematic image shows the procedure of LPBF processing. (Modified from [3]).

2.1.2. Physical aspects

LPBF entails various physical characteristics, including laser absorption and reflection, heat exchange, evaporation, melt flow, and even chemical reactions[1,7]. Meanwhile, physical transformations from powder to liquid and then solid occurred. It is critical to understand these physical phenomena and their relationships to optimal LPBF production of defect-free components.

(1) Absorption and reflection

During the LPBF, heat absorptions and reflections happen continuously when the laser interacts with the powder bed [7]. In the meantime, the photons emission from the laser beam is reflected many times[2]. The amount of energy absorption is affected by the temperature profiles, physical properties of feedstock materials and heat source [2,7]. Typically, three kinds of laser profiles are used in the LPBF systems, including Gaussian, top-hat, and doughnut-shaped profiles [8]. The heat source's radius and power density distribution are critical features for the laser using the Gaussian profile. The power density distribution follows axisymmetric Gaussian distribution can be described as following [8]:

$$P_d = \frac{fP}{\pi r_b^2} \exp\left(-f\frac{r^2}{r_b^2}\right) \tag{2.1}$$

In Eq. 2.1, f represents the distribution coefficient, P denotes the heat source's total power, r indicates the radial spacing between any points and the heat source's axis, and r_b is the heat source's radius. The equation depicts the heat source's power density (P_d) distribution on the feedstock's surface. When the value of f increases, the greater the power density along the heat source's axis; the lower value of r, the higher the power density in all radial directions [5].

Furthermore, the feedstocks in the physical state of powders are well-reported to have higher energy absorption than bulk during the interaction with laser [7]. This is due to the number of reflections through the interparticle gaps, ensuring the radiations penetrate deep into the powder bed. The size distributions and morphology of the feedstock powders can influence the absorption of the heat source [8]. In addition, the absorption of energy is also affected by the laser absorption coefficient of the various materials. Table 2.1 has compared the laser absorption coefficient of different metallic bulk samples during the interaction with a CO_2 laser at a wavelength of 10.6 μm, which shows the higher energy absorption on the rough surface [9].

Table 2.1. The laser absorption coefficient of various materials [9].

Material	Unpurified and unpolished surface	Polished surface
Stainless 316 steel	0.39	0.09
Stainless 416 steel	0.42	0.10
Aluminum	0.12	0.02
Copper	0.12	0.02
4130 steel	0.85	-
Molybdenum	0.12	0.03
Tantalum	0.21	0.04
Titanium	0.25	-
Silver	-	0.01
Gold	-	0.01
Rhodium	-	0.04

(2) Melt flow

During the heat transfer between the laser and powder bed, the conduction, convection, and heat radiation happened within melt flow [5,8]. The features of buoyancy, liquid gravity, vaporization, and Marangoni flow were utilised to understand the evolution of melt flow[9,10]. Meanwhile, some works have demonstrated the significance of Marangoni flow and vaporization for the processing of LPBF [5,8]. Thus, we mainly discuss their effects on the melt flow during LPBF.

Based on the 3D model of melt flow proposed by Saad et al.[11,12], the physical characteristic of melt flow can be well understood. In the beginning, the heat concentrates at the surface of the powder after being hit by a laser. Then the energy would diffuse into the particle uniformly. The heat dissipation and wetting contact amplified rapidly. The laser ray can create shadows, as shown in Fig.2.2a. Furthermore, the balling effect was observed, caused by the tendency to minimize the surface tension (Fig.2.2b), which suggested it was driven by buoyancy. The surface tension can be estimated using Eq.2.2 [11]:

$$\sigma(T) = 3.282 - 8.9e^{-4}T \quad (2.2)$$

T represents the Kelvin temperature. The strong temperature gradient can generate the Marangoni force, as shown in Fig.2.2c, which pull the low surface tension liquid to the high surface tension part. The effects recirculate the melt flow from hot laser to the cold rear, and then deeper the melt pool. In the meantime, some spatters are also created. Moreover, the increment of energy absorption can quickly induce the boiling of the materials. Then the additional recoil pressure joins the interaction with Marangoni force (Fig.2.2d). The recoil pressure (P) is also dependent on the temperature[11,13,14]:

$$\boldsymbol{P(T)} = 0.54\boldsymbol{P_a} exp\left(\lambda/\boldsymbol{K_B}(1/\boldsymbol{T} - \boldsymbol{1}/\boldsymbol{T_b})\right) \quad (2.3)$$

Where P_a is the ambient pressure, λ is the vaporization energy for each powder; K_B is the Boltzmann constant. T is the actual temperature, and T_b is the boiling temperature. Finally, the melt pool depth increased obviously, which was simultaneously influenced by Marangoni effects and vaporization.

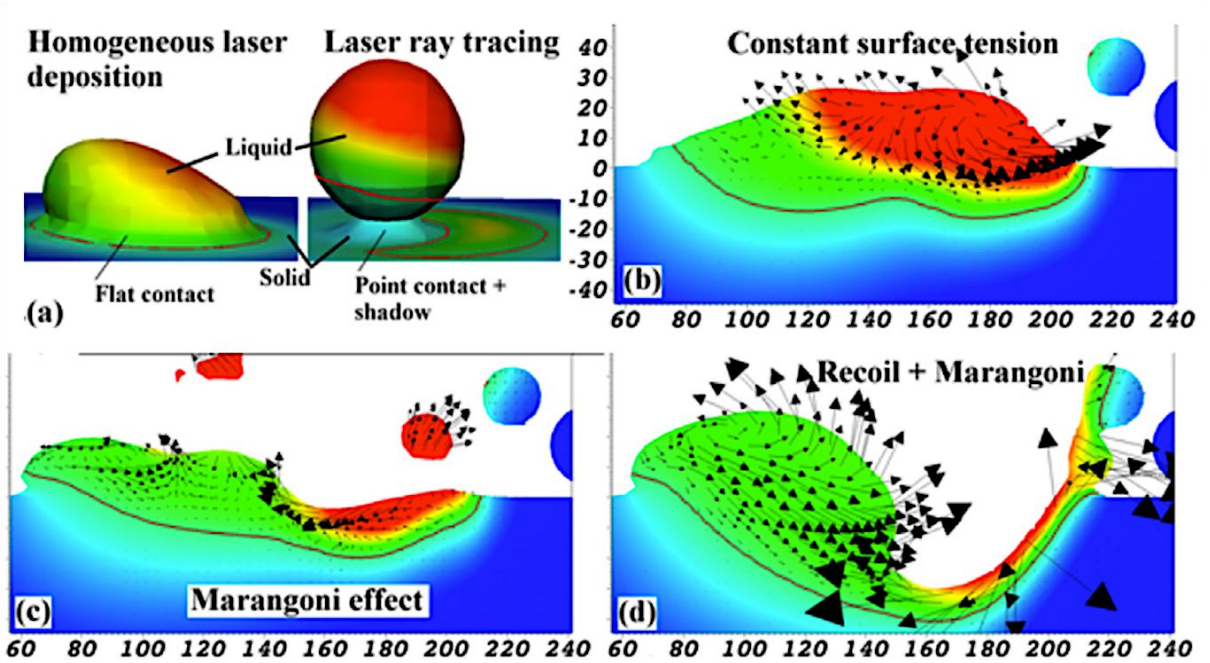


Fig. 2.2. (a-d) The 3D model of melt flow effects with the increase of temperature-dependent physics fidelity. (Modified from [11])

2.1.3. Commonly observed defects and eliminating methods.

(1) Lack of Fusion (LOF)

Lack of fusion pores are irregular and elongated, which is general porosity in AM parts arising due to incomplete particle consolidation[8,15], as shown in Fig.2.3a-b. When the energy density is low, there is insufficient energy to melt the powders fully. Thus the partial sintering occurred, resulting in higher porosity due to lack of fusion.

These voids are relatively large and are easily identified by their sharp edges. Mukherjee et al. [4] used "lack of fusion index" (LFI) to correlate the size of voids: LFI equals the depth of the molten pool divided by the thickness of the powder layer. A deeper melt pool that penetrates enough into the previously sintered layers can effectively bond and reduce the presence of LOF voids [5,16]. As a result, the voids are minimized when an AM process with a high LFI value. Moreover, raising the melt pool depth needs higher energy input density, defined as the ratio of laser power to scanning speed[17]. On the contrary, higher scanning speed significantly reduces the melt pool's depth, which increases the likelihood of developing the LOF porosities. Thus, enhancing laser power can substantially reduce porosity by increasing the size and depth of the melt pool.

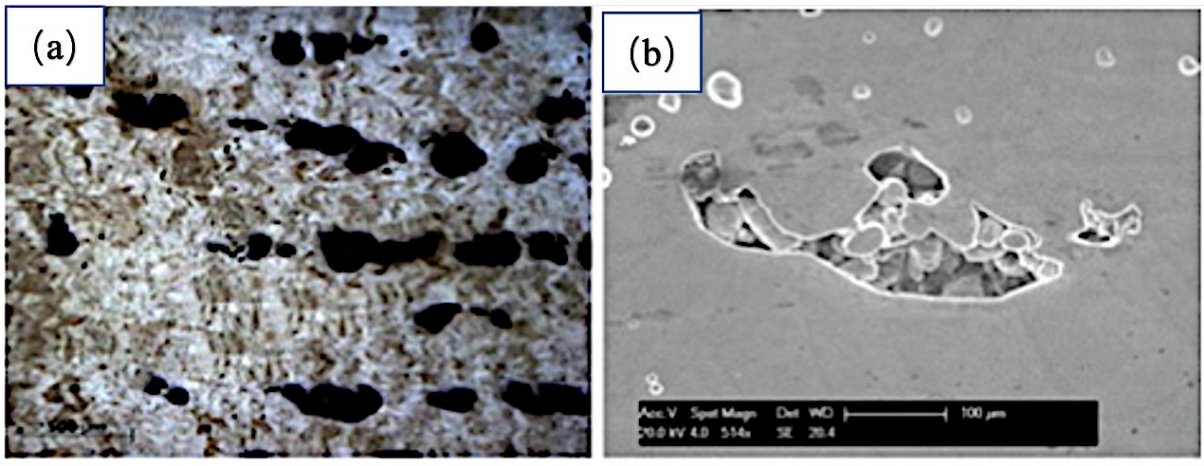


Fig. 2.3. The morphologies of lack of fusion porosities in Ti6Al4V alloys processed by LPBF:

(a) the optical microscopy image; (b) the SEM image. (Modified from [8,18,19])

(2) Gas porosity

The gas porosities are in the shape of near-perfect spherical, which are randomly distributed across the as-fabricated samples[20,21], as exhibited in Fig.2.4. The size and shape of the gas porosity are relatively close to the porous that already existed in the as-received feedstock powders[22]. It suggests that some of them may be inherited from the initial particles formed during atomization. Moreover, other gas porosities are subjected to the interaction of Marangoni force and recoil pressure in the melt flow [20,22]. If the porosities were entrapped from the surrounding atmosphere, which did not have enough time to escape, they were rested inside the LPBF components. Therefore, gas entrapment can arise from atomisation or the processing atmosphere. To remove the gas porosities, hot isostatic pressing (HIP) can effectively eliminate large gas porous[23]. More detailed optimizations of LPBF processing parameters should be needed for further release and eliminations of gas porosities.

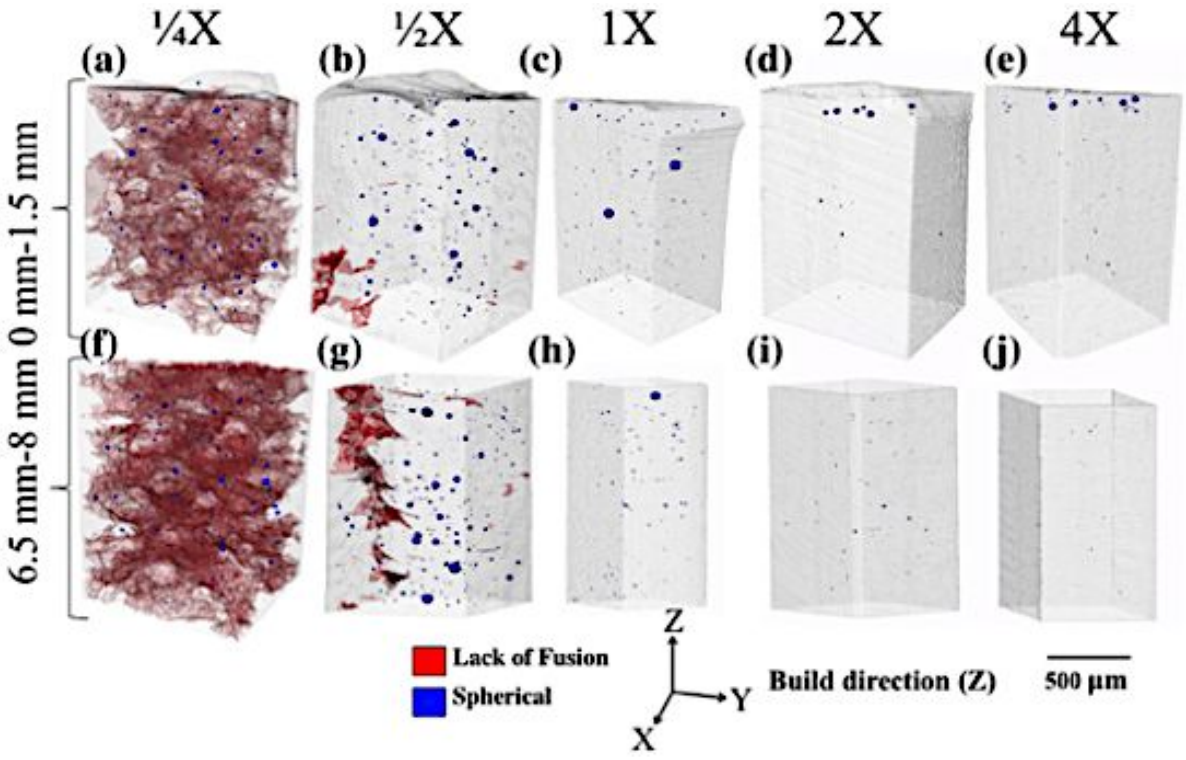


Fig. 2.4. The porous morphologies, including gas porosities and LOF, in AM Ti6Al4V alloy, are characterized by synchrotron XCT: (a-e) the top 0-1.5 mm region of the specimen; (f-j) the 6.5-8 mm region of the specimen. (Modified from [21])

(3) Keyhole

Keyhole-induced defects in the LPBF parts can lead to low fatigue strength and premature failure [24]. Therefore, the reduction of keyhole defects is essential for the structural integrity of the printed components. When the energy input increases, the melt pool transfers from a shallow and semicircular shape to a narrow and deep shape, easily forming the keyhole [24]. Although the keyhole might facilitate the absorption of laser and energy efficiency relatively, it could be trapped in the components due to the multiple reflections of rays inside the keyhole [25]. Recently, the high-speed synchrotron X-ray radiographic observations [24] revealed that keyholes formation followed the sequence of vaporization, suppression of the liquid surface, instability, and pore formation, as shown in Fig.2.5. The suppression of the liquid surface was caused by the recoil pressure [26], which formed as a result of vaporization [27]. The acoustic waves generated by the keyhole instability are also a critical driving force [28]. The optimization of scanning parameters is the essential way to eliminate keyhole defects. The keyholes can also be closed within the range from 10 to 50 μm by post-processing of HIP.

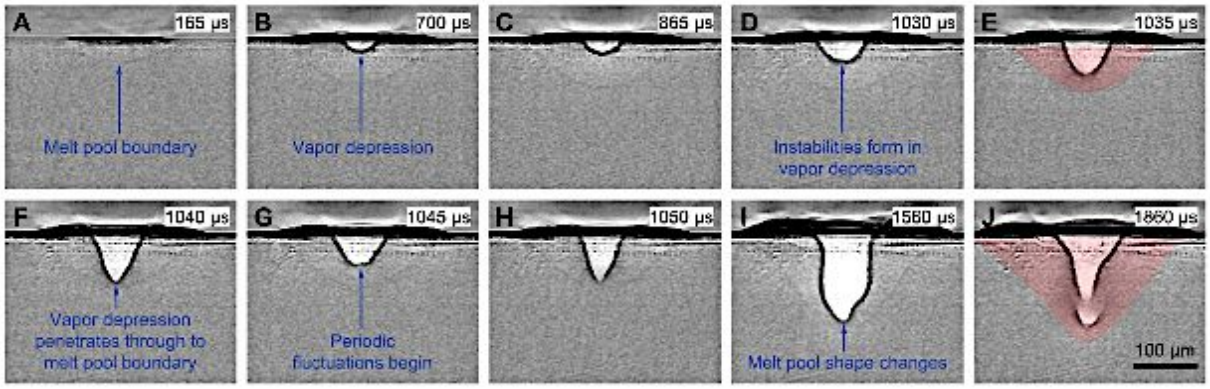


Fig. 2.5. (A-J) Melt pool and vapour depression's evolutions under continuous laser irradiation.

(Modified from [24])

(4) Cracking

Two kinds of cracks were previously observed in the LPBF components: solidification cracking and solid-state cracking[23]. There are two factors for solidification cracking: the local strain and susceptible microstructure[29]. During the fast cooling of LPBF, the high inner stress and local mechanical strain cannot be avoided [8,23]. Moreover, it is known that the solidification temperatures were varied between different alloy systems[30]. The alloys with wide-range solidification temperatures are susceptible to solidification cracking because of the accumulated thermal strain [8]. Such solidification cracking was reported in Ti-Al alloys prepared by LPBF due to the extremely high cooling rate and brittle B_2 phase, which is susceptible to cracking, as shown in Fig.2.6[31]. The effective method to avoid solidification cracking is to reduce the thermal gradient and eliminate the sensitive precipitations[8,23].

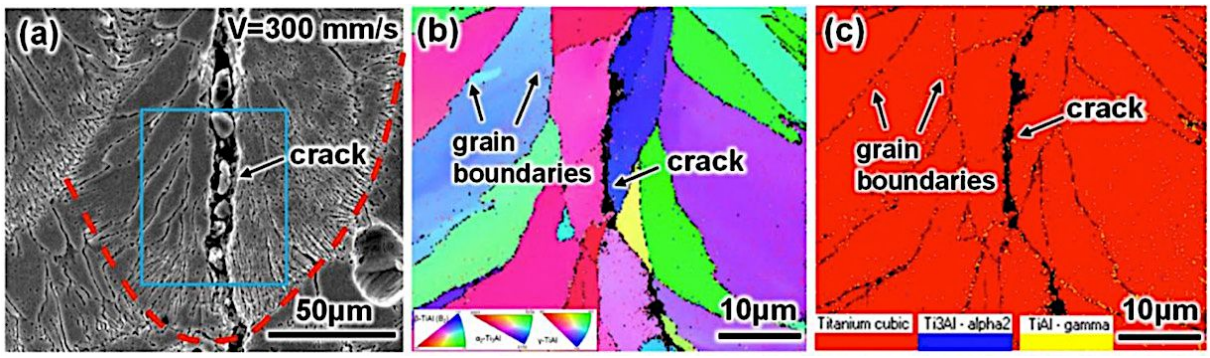


Fig. 2.6. The morphology of solidification cracks in Ti-40Al-9V-0.5Y alloys processed by LPBF: (a) the SEM micrograph; (b) the EBSD IPF image; (c) the EBSD phase map. (Modified from [31])

The solid-state cracking mainly includes ductility-dip cracking (DDC) and post-weld heat treatment cracking (PWHT)[32]. The rapid reduction of ductility was reported primarily on Nickel, Aluminium, and copper-based alloys, which cause the DDC during the rapid cooling of LPBF [23,32]. The influence factors of the DDC cracking are composed of grain boundaries,

chemical composition, temperature, et al. The PWHT happens during the post-processing of machining or stress relief. The materials that have strong precipitation reactions are sensitive to PWHT cracking [33]. The conventional ways to prevent the PWHT during LPBF are to control the scanning parameters, chemical composition, residual stress, and the method of stress relief [23,34].

2.2. Metallurgy of β Ti Alloys

Previous works [35,36] about β Ti alloys focused on their β phases' stability, biocompatibility, phases transformations, mechanical performance, deformation mechanisms and post-treatment for biomedical applications or aircraft engineering. This section will cover the strongly related scopes of the thesis, including the extensive review of recent developments of β Ti alloys.

2.2.1. Chemical composition

To attain metastable or stabled β Ti phase after quenching from the β region of the phase diagram, higher β phase stability and reduced phase transformation temperature are required [37,38]. Usually, introducing sufficient β stabilizers is the effective method to increase the β phase stability [38]. In the meantime, it can suppress the metastable phase transformations of α', α" or athermal ω phases during fast cooling [38]. There are two types of β stabilizer elements, involving isomorphous and eutectoid, which depend on the Ti matrix's precipitation reactions[36,39]. According to the binary phase diagram, some isomorphous elements do not show a miscibility gap during the alloying with Ti, like tantalum (Ta) and niobium (Nb). Other isomorphous elements like molybdenum (Mo) and tungsten (Ta) exhibit the monotectoid reaction, as shown in Fig.2.7.

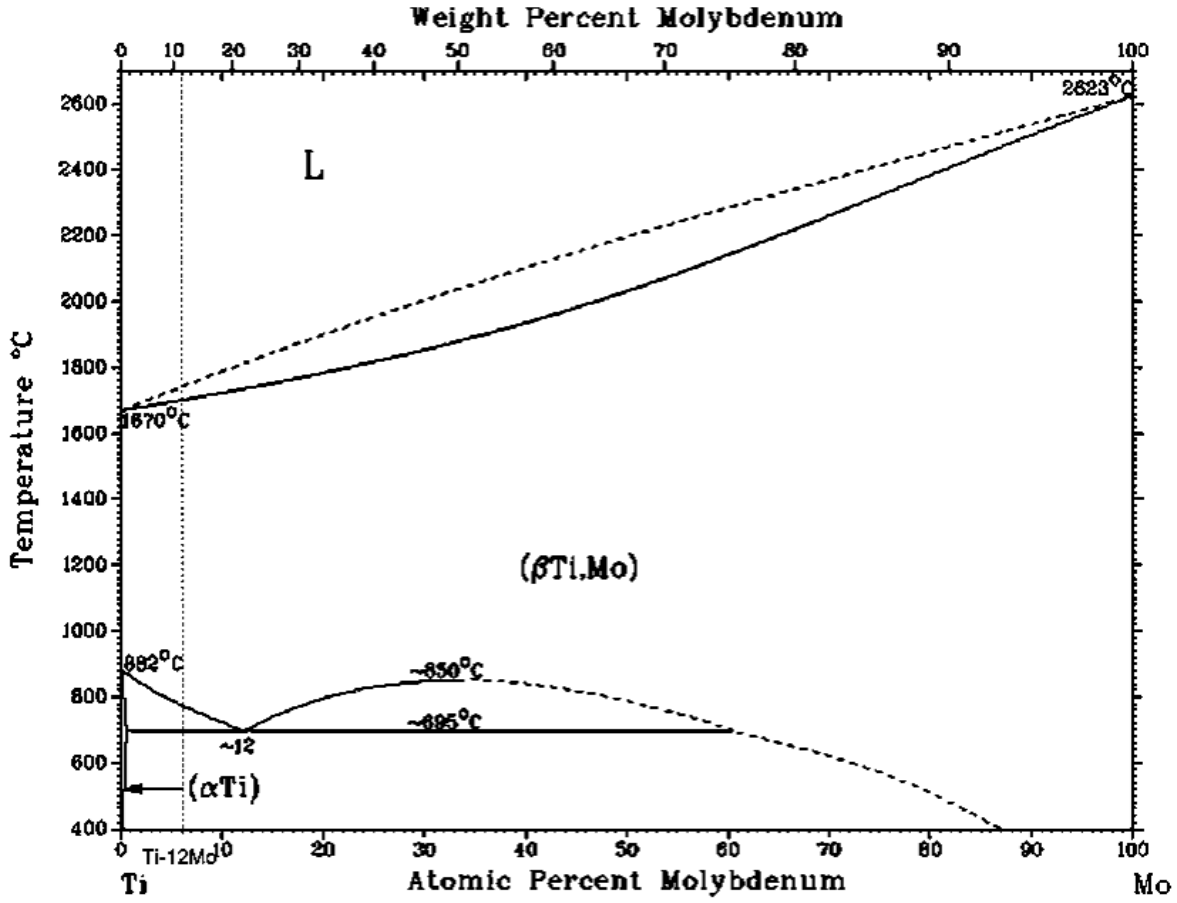


Fig. 2.7. The phase diagram of Ti-Mo alloy. (Modified from [37])

On the other hand, the eutectoid elements, such as iron (Fe), copper (Cu), chromium (Cr, Fig.2.8), manganese (Mn), have shown limited solubility (12 at.% Fe, 7 at.% Cu, 12 at.% Cr and 17 at.% Mn) in Ti. Therefore, some intermetallic compounds can form during the eutectoid reaction with Ti [37]. These isomorphous and eutectoid elements can increase the β phase stability and reduce the β transus temperature. On the contrary, other works summarize α phase stabilizers [36], like aluminium (Al), oxygen (O), and nitrogen (N), and the neutral elements contain zirconium (Zr) or tin (Sn).

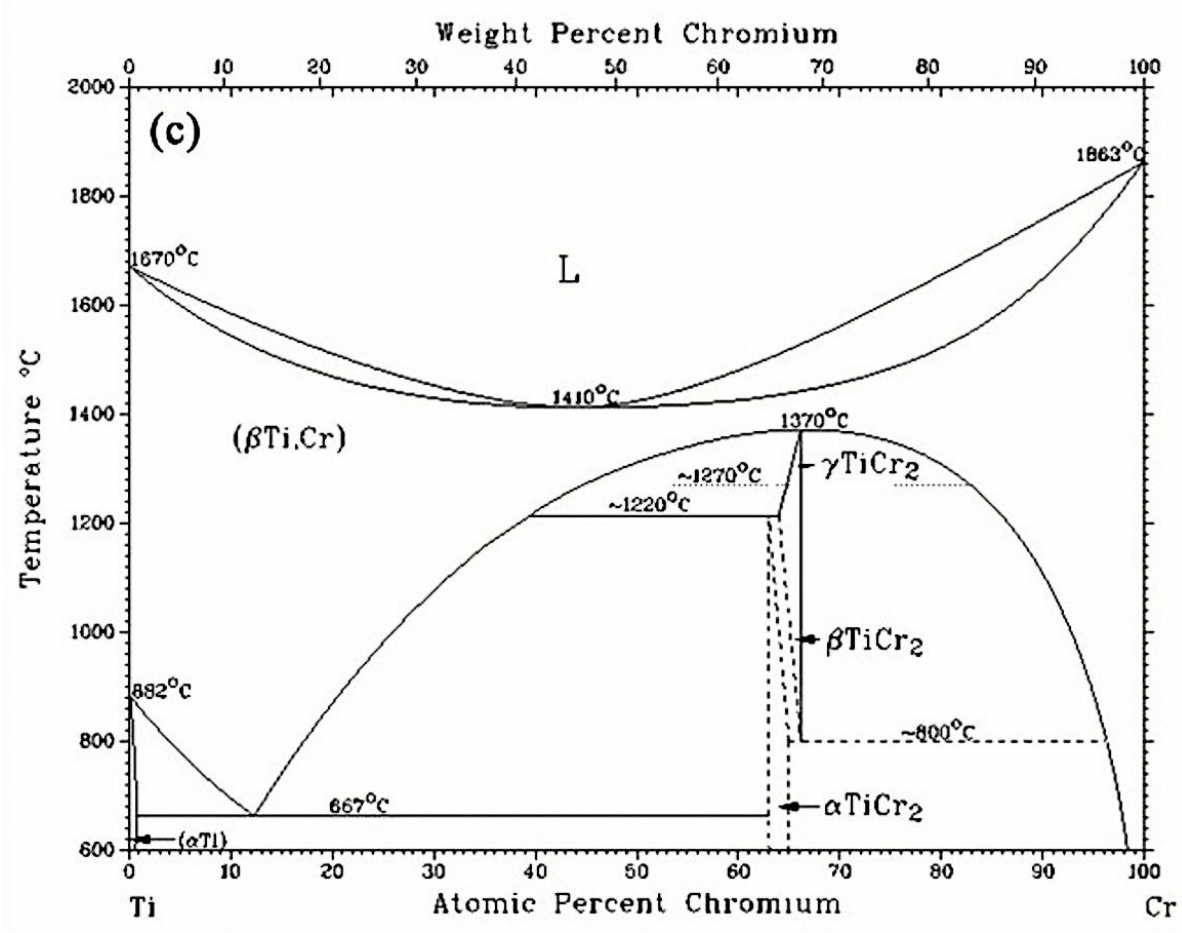


Fig. 2.8. The phase diagram of Ti-Cr alloy. (Modified from [37])

A valuable and well-known method to evaluate the β phase stabilities is the Mo equivalent (Mo_{eq}), which used Mo element as the baseline [36,40]:

$$Mo_{eq} = 1.0Mo + 0.74V + 1.01\,W + 0.23Nb + 0.30Ta + 1.23Fe + 1.10Cr + 1.09Cu + 1.67Ni + 1.81Co + 1.42Mn + 0.38Sn + 0.34Zr + 0.99\,Si + 0.57\,Al\ (at.\ Pct) \quad (2.4)$$

Generally, the Mo_{eq} is used to divide the classifications of β Ti alloys. There are four categories of β Ti alloys[36]: β-rich Ti alloys, near-β Ti alloys, metastable β Ti alloys and stable β Ti alloys. The β-rich Ti alloys, so-called α+β Ti alloys, have the Mo_{eq} less than 5.0, while the near-β Ti alloys are within the range: $5.0 < Mo_{eq} < 10.0$. The metastable β Ti alloys' Mo_{eq} is between 10.0 and 30.0. After that, the stable β Ti alloys have the Mo_{eq}, which is higher than 30. The detailed Mo_{eq} values of different β Ti alloys can be seen in Fig.2.9.

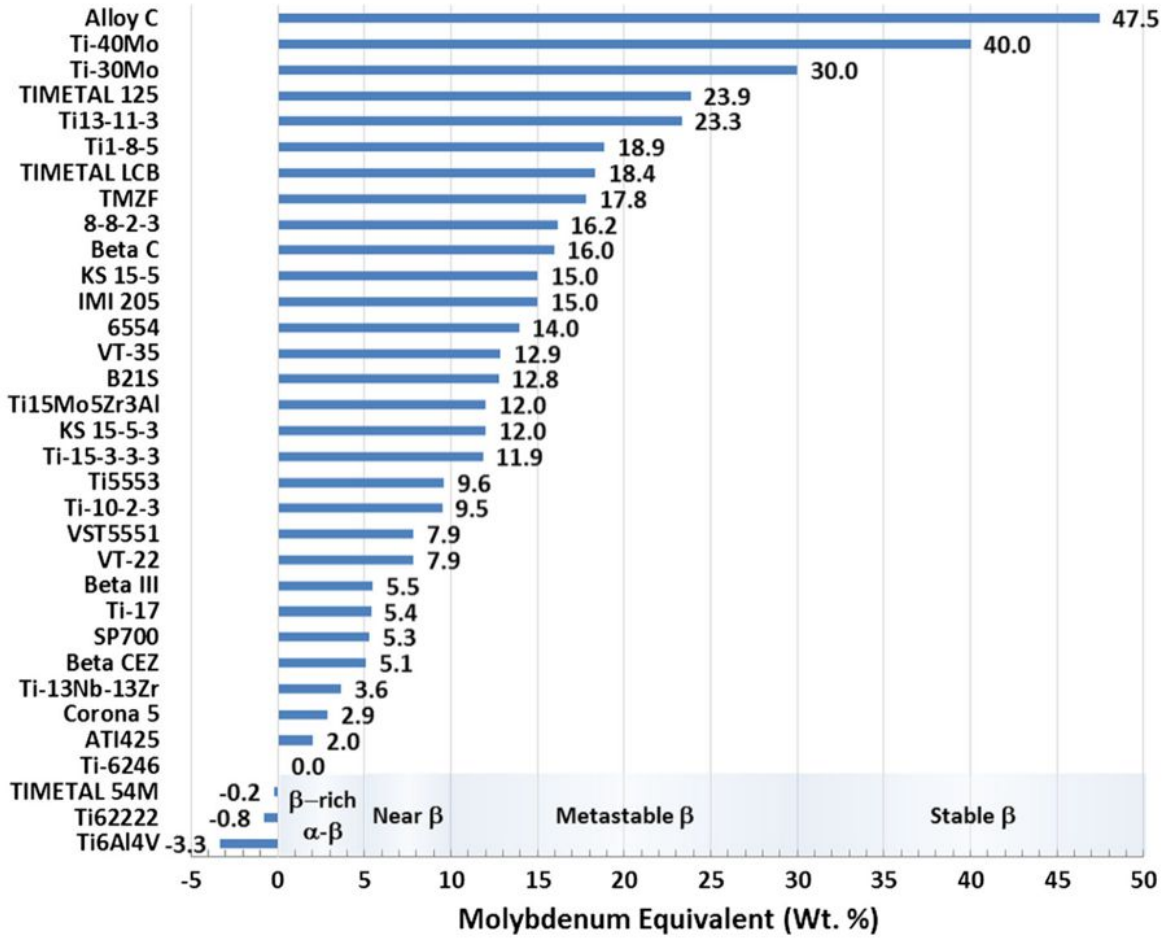


Fig. 2.9. The schematic shows the Mo_{eq} values and classifications of various β Ti alloys. (Modified from [41])

For the applications in biomedical implants, some researchers have distinguished the toxicity of different elements based on the cell reactions [42–44], as shown in Fig.2.10. The results show Al, V, Ni and Co are toxic elements, while Ti, Mo, Nb, Ta, Pb and Zr have good biocompatibility. Al and V elements are related to Alzheimer's disease and some allergic reactions[45]. Park et al. [46] studied the cytotoxicity of a series of elements, through alloying with Ti. They found that the Ti-xMo and Ti-xNb system alloy show high cell viability. Mo can also balance the PH in the human body[47]. On the other hand, Mo element exhibits much higher efficiency than Nb element to retain the stable β phase in Titanium alloys, according to Mo_{eq}. Therefore, the Ti-xMo based β Ti alloys show great potential to be applied as biomedical

implant material.

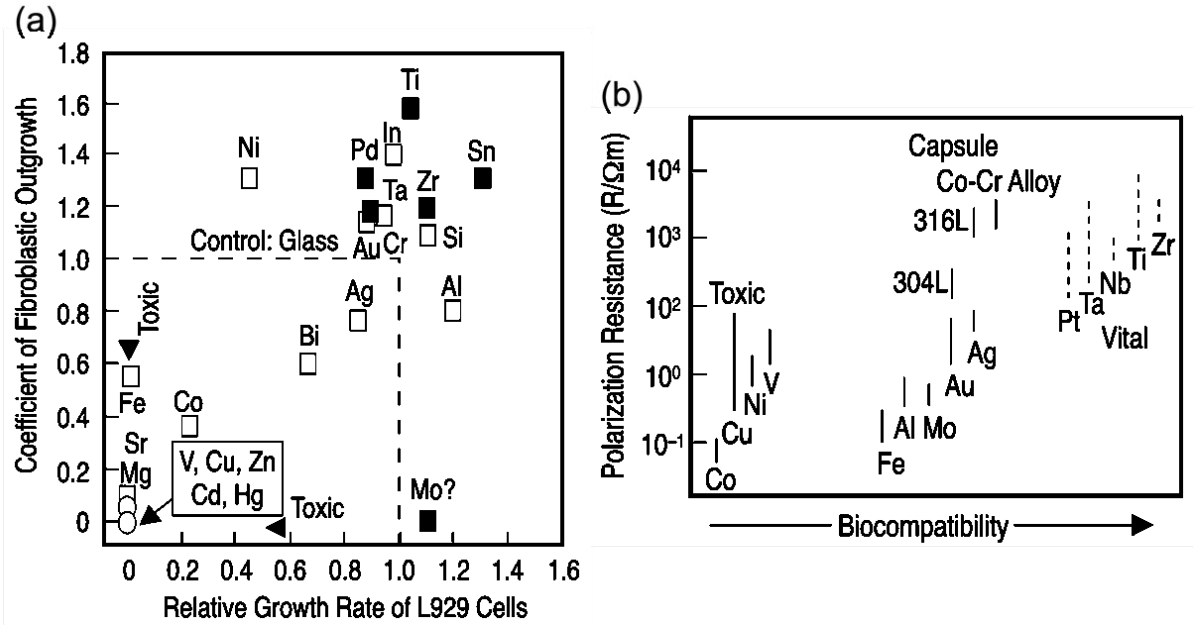


Fig. 2.10. The cytotoxicity of pure metallic elements (a) and their biocompatibility (b). (Modified from [42–44]).

2.2.2. Conventional preparation methods

(1) Melting

Within the melting processing technologies, vacuum arc remelting (VAR) is primarily applied in producing Ti alloys [37,39,41]. The VAR method has been successfully utilised to produce bigger ingots over time, thus significantly reducing production costs [35,39]. For the VAR processing of β Ti alloys, controlling chemical segregations and obtaining the homogeneous microstructure are the most challenging jobs, requiring careful adjustment of melting procedures [37]. Whereas controlling the remelting of VAR is empirical and equipment dependent, which limits the development of VAR technology. As mentioned previously, most β stabilizer elements (Mo, Ta, Fe, and Cr et al.) typically possess low solidification temperatures, which leads to a wide range of temperatures to freeze and increased constitutional

supercooling [41]. Therefore, the situation leads to severe solute segregation during the solidification of ingots, which cannot be addressed rationally by homogenization.

(2) Casting

The use of Ti casting products has increased considerably during the last decades. Ti casting components' production benefits from the improvements of near-net-shape casting methods and hot isostatic pressing (HIP), which significantly optimized the microstructure and eliminated the inner defects in the casting parts [39,48]. Currently, two main methods are used to prepare β Ti casting alloys: one uses rammed graphite as the mould materials; the other is investment casting, which uses the wax as the mould materials [38]. When using the rammed graphite, the casting parts can obtain a good surface finishing due to the low tendency of the reaction between the Ti and graphite [39]. Moreover, the investment casting can generate complex forms with a net-shape appearance, and it allows cooling under specific control, which minimizes the formation of shrinkage pores [10,38]. However, the ability to process the highly complex structure is still limited, depending on the size of wax walls, and it is impossible to build inter-connected pores by investment casting [39]. The removable of wax is also a big challenge for the complex structure in micron size. Furthermore, the chemical inhomogeneous across the component also need to be concerned due to the refractory elements of β stabilizers in β Ti alloys. Some elements even possess extremely low diffusion rates in the Ti matrix, requiring long-time homogenisation heat treatment [49,50].

(3) Powder metallurgy

Powder metallurgy (PM) technology is a consolidation method of powders to produce solid samples with refined microstructures. The main advantages of PM include highly efficient usage of raw powders, good fabrication flexibility and reduced processing steps [39,51]. Thus, PM is a cost-effective way for forming β Ti components. According to the different feedstock

powders, PM can be divided into two groups: pre-alloyed (PA) powders and blended elemental (BE) powders [48]. Traditional PA technology involves the HIP, powder injection moulding and so on. Moreover, the BE typically uses cold pressing and sintering, which have lower producing costs than PA. The other advanced technology of AM to create the components using PA or BE will be discussed in the next section.

Most previous studies of PM for the high-ending needs, like aerospace applications, used PA powders [48,51]. The PM components' mechanical properties using PA are much better than BE, especially the fatigue property. However, the PA powders usually require long processing cycles, including preparing homogeneous ingots and atomization processes. For β Ti alloys, the most efficient elements for β phase stabilization are refractory, with high melting points and low interdiffusion rates in Ti-based alloys [49,50]. These features made the atomization of high-quality PA powders of β Ti alloys to be difficult and expensive.

β Ti alloys formed by arc melting, casting, and even some PM technologies still have limitations on structure complexity and flexibility of the components. Moreover, β Ti alloys are hard to machine mainly because of the low thermal conductivity, reducing the heat diffuse between the tools and materials, and decreasing the tooling life [52]. As a result, developing new forming technologies, like AM, to produce β Ti alloys raises researchers' concerns.

2.2.3. Phase transformations

In the thesis, we mainly investigate the microstructure, mechanical performance, and applications of metastable β Ti, including Ti-12Mo and TMZF alloys. Thus, we will focus on the phase transformations of metastable β Ti alloy in this section.

(1) Equilibrium phases

In the metastable β Ti alloys, with the Mo_{eq} between 10.0 and 30.0, can have two

equilibrium phases (β and α), and one meta-equilibrium phase of ω[48]. Metastable β Ti alloys undergo phase transitions from a high-temperature β phase with a body-centred cubic (BCC) structure to close-packed hexagonal (HCP) α and HCP ω phases at a lower temperature, as exhibited in Fig.2.11 [39,53,54]. The transformation temperature is highly dependent on the alloy composition, and a range of phase transitions is conceivable [39].

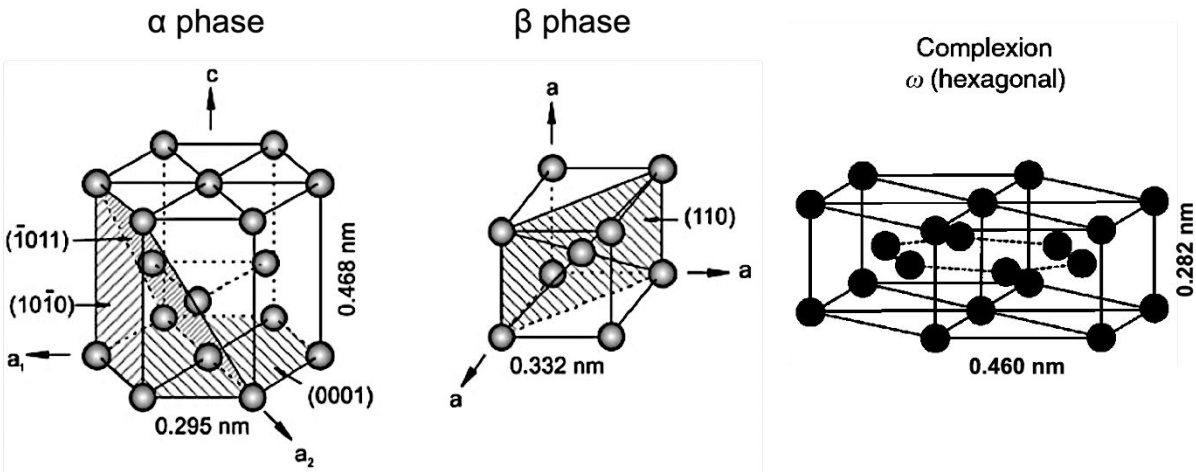


Fig. 2.11. Crystal structure of α, β and ω phases. (Modified from [39,53,54]).

According to the time-temperature-transformation (T.T.T) diagram of the metastable β Ti-12Mo alloy (Fig.2.12), the α and ω phases can form in β matrix during ageing treatment under varying temperatures or annealing with different cooling rates [39,55,56].When Ti-12Mo alloys fast cooling from β transus, the β → β + ω transformation happened. After slowing down the cooling rate, the phase transformations will be β → β + ω + α and then β → β + α. It is reported that the contractions occur when the ω phase is precipitating during ageing treatment. When the predominant phase transformations move to β → β + α, the alloy starts to expand.

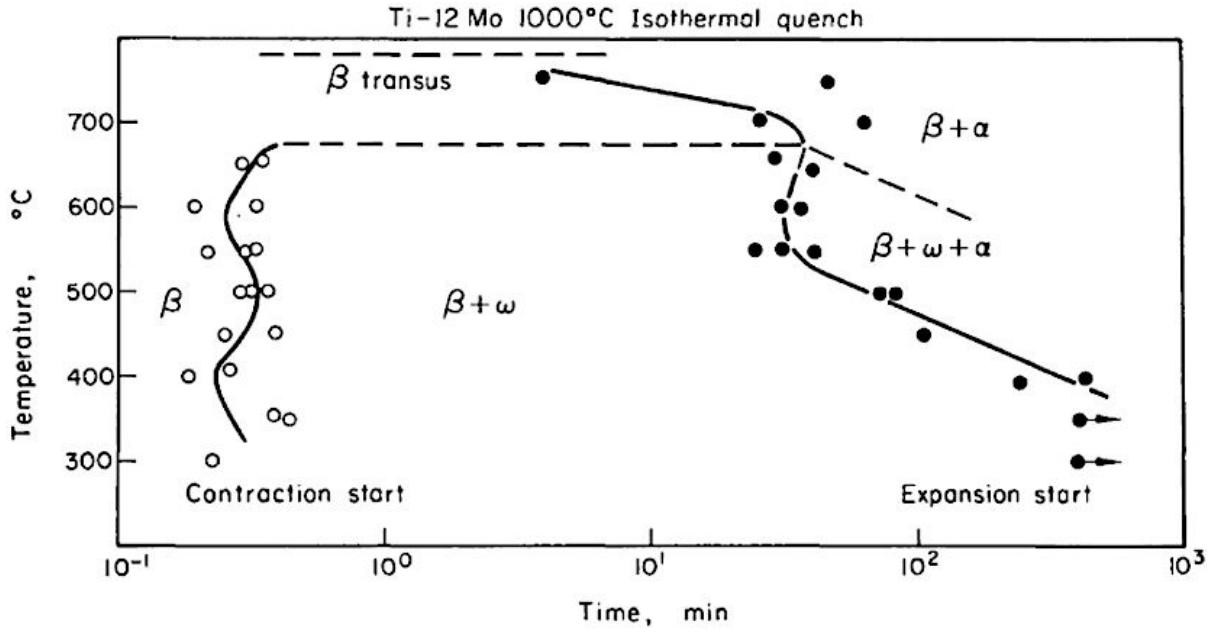


Fig. 2.12. The time-temperature-transformation (T.T.T) diagram for Ti-12Mo. (Modified from [55])

As shown in Fig.2.13, the β → β + ω → β + ω+ α transformations happened during long-time isothermal ageing treatment at 450 ℃, and the α phases were formed uniformly. However, the β → β + α reaction happened when the ageing treatment was performed at 650 ℃. The α phase seems not easy to form by the reaction of β → β + α, because it was mainly precipitated along the β phases' grain boundaries even under high temperature [39,55,57].

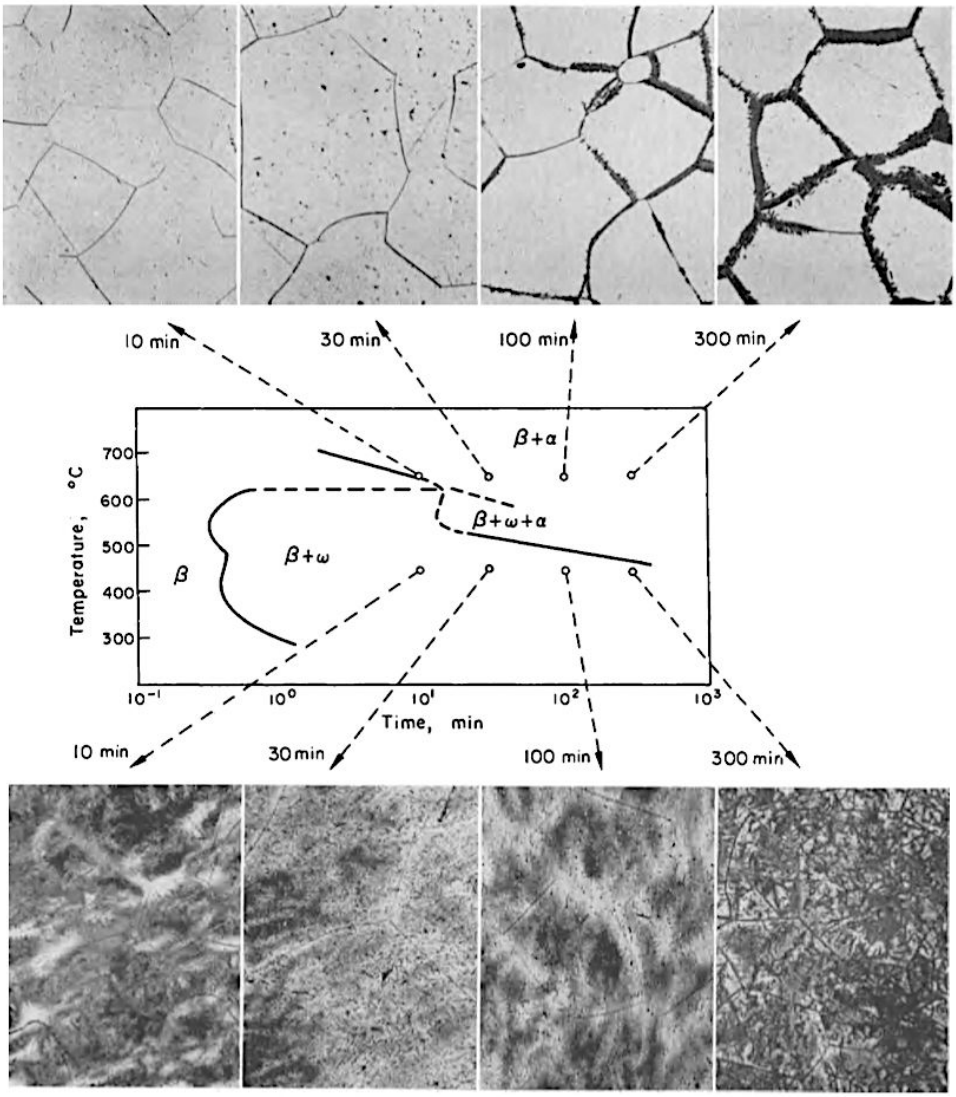


Fig. 2.13. The T.T.T diagram for Ti-15Mo, and the microstructural evolution during the isothermal ageing treatment at 450 and 650 ℃. (Modified from [55])

During the phase transformations, the dense-packed plane {110} of BCC β matrix in metastable β Ti alloys can correspondingly transform to the basal plane {0001} of HCP α phases. They follow the Burgers orientation relationship (BOR) [37,58]:

$$\{110\}_{\beta} // \{0001\}_{\alpha}$$

$$<111>_{\beta} // <1120>_{\alpha}$$

The basal plane's *d* spacing of α phase is larger than that of the {110} plane of β, as indicated in Fig.2.14. Thus, the slight atomic distortion during the β → β + α transformation

causes the specimens' slight expansion, consistent with the T.T.T diagram [38,57].

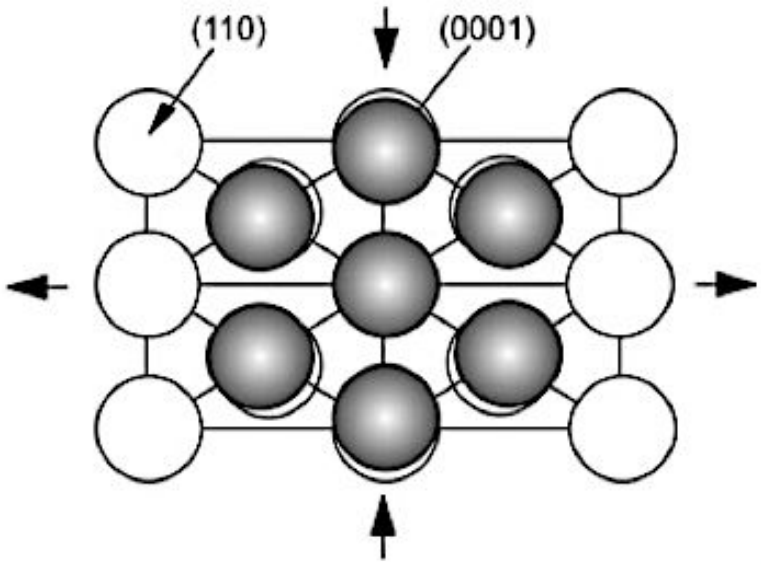


Fig. 2.14. The schematic shows the β/α phases transformations. (Modified from [38])

The BCC β phase consists of six slip planes each with two slip directions, giving 12 possible slip systems in the BCC unit cell [38]. During the β → α reaction, the HCP α plates would nucleate from the priory β grains and growth along the 12 slip systems [59,60]. Thus, the maximum 12 possible variants of α can form from the β Ti alloys during isothermal heat treatments. However, only limited variants of the α phase can be obtained in the β Ti alloys. Nag et al. [61] have compared the α variants in the Ti5553 specimens formed after high-temperature annealing (4h 600 ℃) and two-steps annealing (2h 350 ℃ + 2h 600 ℃), respectively. As indicated in the T.T.T diagram of β Ti alloys, the high-temperature annealing is dominant by β → β + α transformation, while the two-steps annealing experience β → β + ω → β + ω + α reactions with the precursor ω phases formed in the step of low-temperature ageing treatment. There were three variants of α phase formed in high temperature annealed Ti5553 alloys (Fig.2.15a-b), and five variants in two-step annealed specimens (Fig.2.15c). The clustering of α variants in β Ti alloys was attributed to the low strain energy criteria [61,62]. According to the self-accommodation principle, the system would favour the reduced total

system energy during the phase transformations[63]. If the precursor ω phase exists, the ω-assisted nucleation of α will transform with the self-accommodating clusters. This is why the specimens processed by two-step annealing would obtain more variants of α clusters. Thus they possessed higher efficiency for the α nucleation.

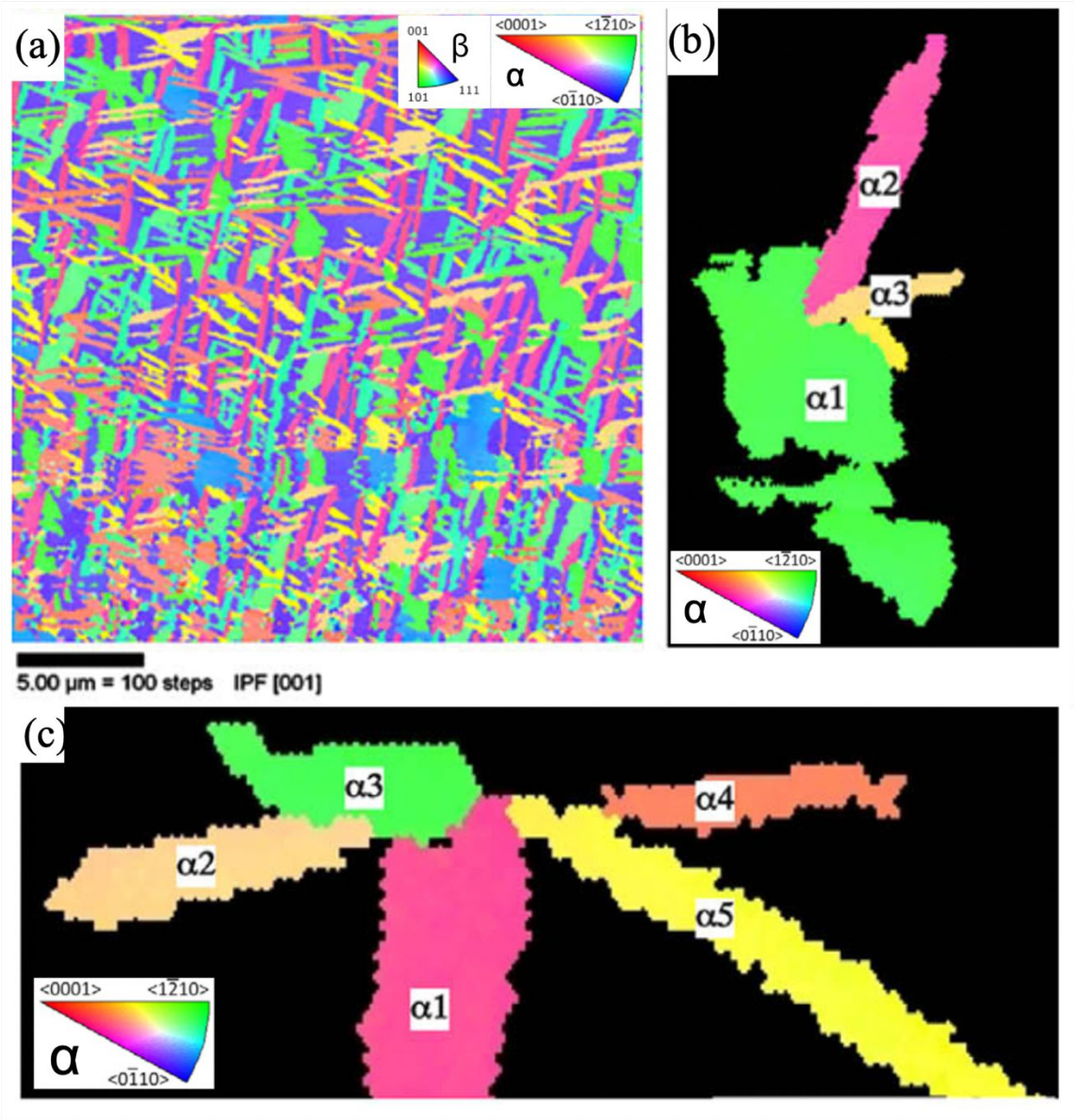


Fig. 2.15. (a) The inverse pole figure (IPF) maps of β+α phases in Ti-5553 alloy after solution heat treated and aged at 600 ℃. (b) The IPF map of α phases with only three variants. (c) The microstructure of the Ti5553 alloy is processed by double ageing (2h 350 ℃ + 2h 600 ℃): the IPF map of α phases with five variants (Modified from [61]).

After that, some works have investigated the mechanisms of ω-assisted α nucleation. Li et al. [64] have revealed the phase transformations in a new developed near β Ti-6Cr-5Mo-5V-4A1 alloy. As shown in Fig.2.16, the α phases were found to precipitate immediately after the formation of embryonic ω phases. During the transformation from embryonic ω to isothermal ω, the interphase of β/ω has accumulated high content of O element. As we discussed before, the O element is a vital α stabilizer element. The O rich region can also be the nucleation site for the α phases [65,66]. The rapid lattice reconstructions were also found in the ω /α interphases, which suggests the ω-assisted α transformation should be a mixed-mode of diffusion and displacive [64].

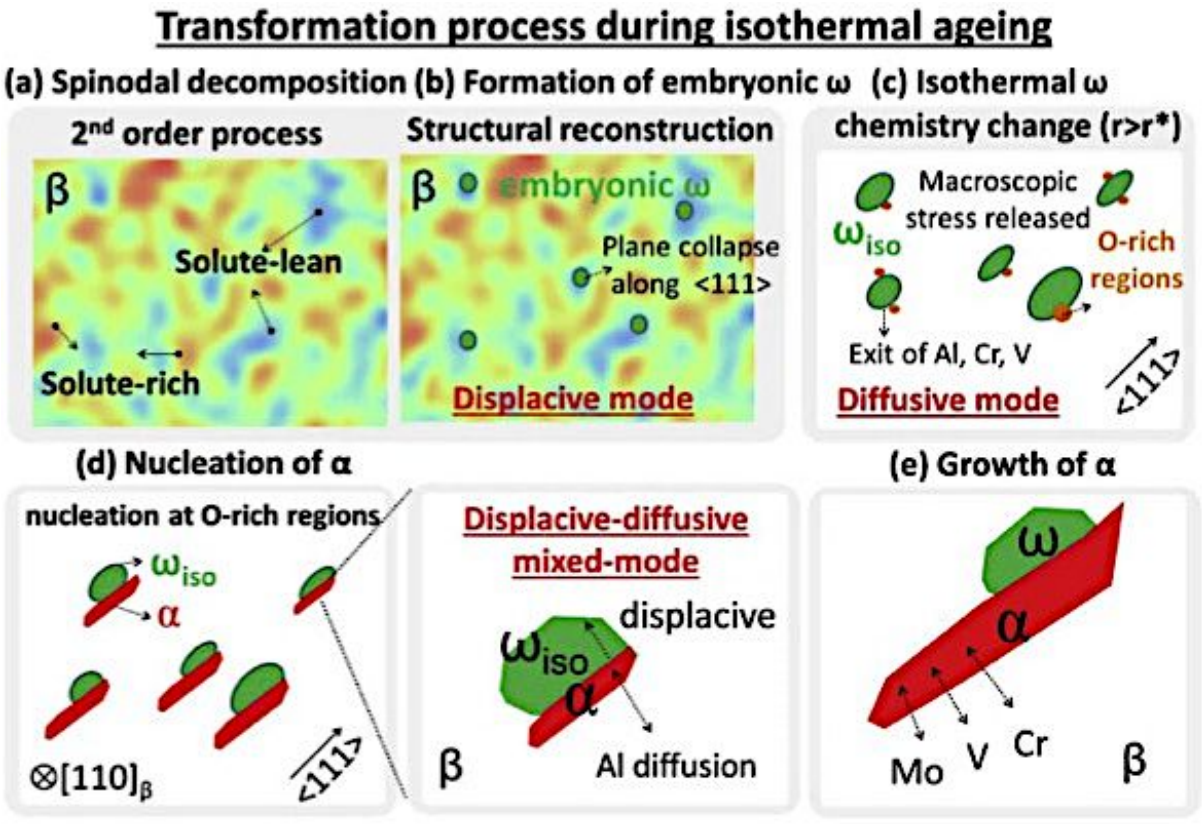


Fig. 2.16. (a-e) The schematic shows the pathway from ω transform to α phase during isothermal ageing treatments. (Modified from [64])

During the nucleation of ω-assisted α phases, the processing window can be adjustable by

modifying the morphology of ω phases. Various works have reported that the interface of β /ω, or near the ω, is the preferential nucleation site [64,65,67]. Moreover, the size, shape, and interfacial state of ω particles can significantly influence the nucleation of α [61,68]. Recently, Shi et al. [67] have found that the α precipitates prefer to nucleate at the selected plane of cuboidal ω phases, as shown in Fig.2.17. The intergranular α phases nucleated due to the combined effects of local enrichment of O element, elastic interaction, and catalytic potency of β/ω interphases.

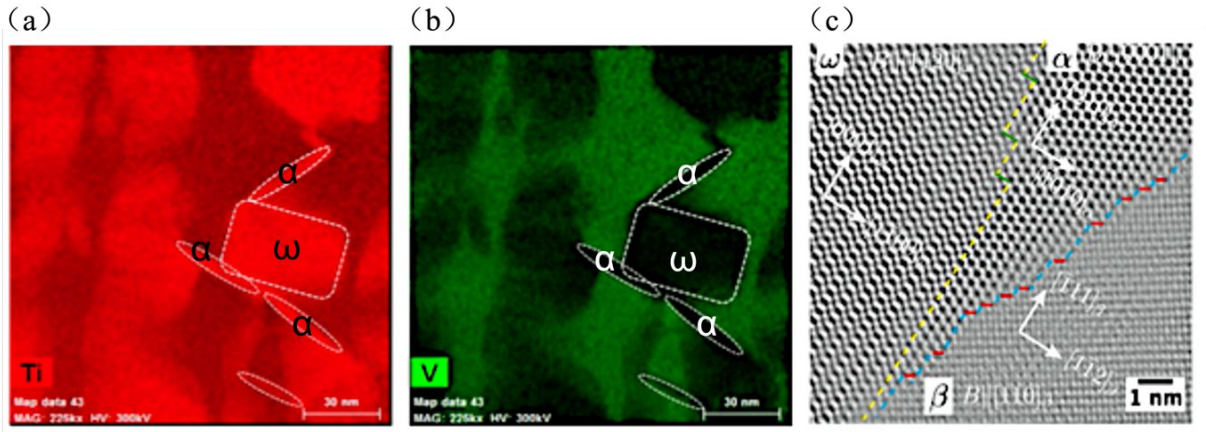


Fig. 2.17. X-ray energy dispersive spectrometry (XEDS) maps (a,b) and its high angle annular dark-field scanning transmission electron microscopy (HAADF-STEM) image (c) show the nucleation of α phases assisted by the isothermal ω phases. (Modified from [67])

(2) Nonequilibrium phases

Due to the instability of metastable β Ti alloys, various nonequilibrium phases can form during the fast cooling or ageing treatments [36]. Firstly, it is well-known that there are two kinds of ω phases, including isothermal and athermal ω phases [69,70]. The isothermal ω (ω_{iso}) is hexagonal symmetry, belongs to the space group of No.191, P6/mmm, which precipitates through ageing under a temperature typically lower than 450℃. The ω-assisted α transformation is also reported derived from the ω_{iso}. On the other hand, the athermal ω (ω_{ath}) is trigonal symmetry, belongs to the space group NO.164, P-3m1, which forms after quenching

from β region [71–73]. The β Ti alloys, which can precipitate ω_{ath}, typically possessed fewer β stabilizers, as shown in Fig.2.18. Moreover, some recent works [74,75] illustrated the third way to form the ω phase in metastable β Titanium which was induced by deformation or stress release. Yang et al. [76] proved the interfacial twin boundary (ITB) ω phase of Ti-24Nb-4Zr-8Sn alloy has vanished after loading, while the ITB-ω phase appeared again after the stress was released, mainly because of the reversion of {110}<110> α'' twins. Li et al.[77] found that the ω phase in Ti-29Nb-13Ta-4.6Zr alloy was induced by cold work deformation, which increased its elastic modulus. Based on tensile deformation of β Ti-9Cr-0.2O alloy, Liu et al.[78] revealed the reversal and re-orientation mechanism of ω phase, due to the shearing of particular $<111>_{\beta}$ partial dislocations and the unfavorable ω variants along the tensile direction, respectively.

More nonequilibrium phases of α' and α" can also form during quenching, depending on the concentrations of β stabilizers in the β Ti alloys [57]. For the Ti-Mo binary system, with an increase in Mo content, the martensite structure is obtained during fast cooling or from low-temperature ageing treatment, which changed from hexagonal (α') to orthorhombic (α") when 4 wt% was reached. The structure became the β phase when Mo was higher than 10 wt% [79,80]. The morphology of the martensite α phases is also changed from lamellar to acicular with the increase of Mo concentrations [39].

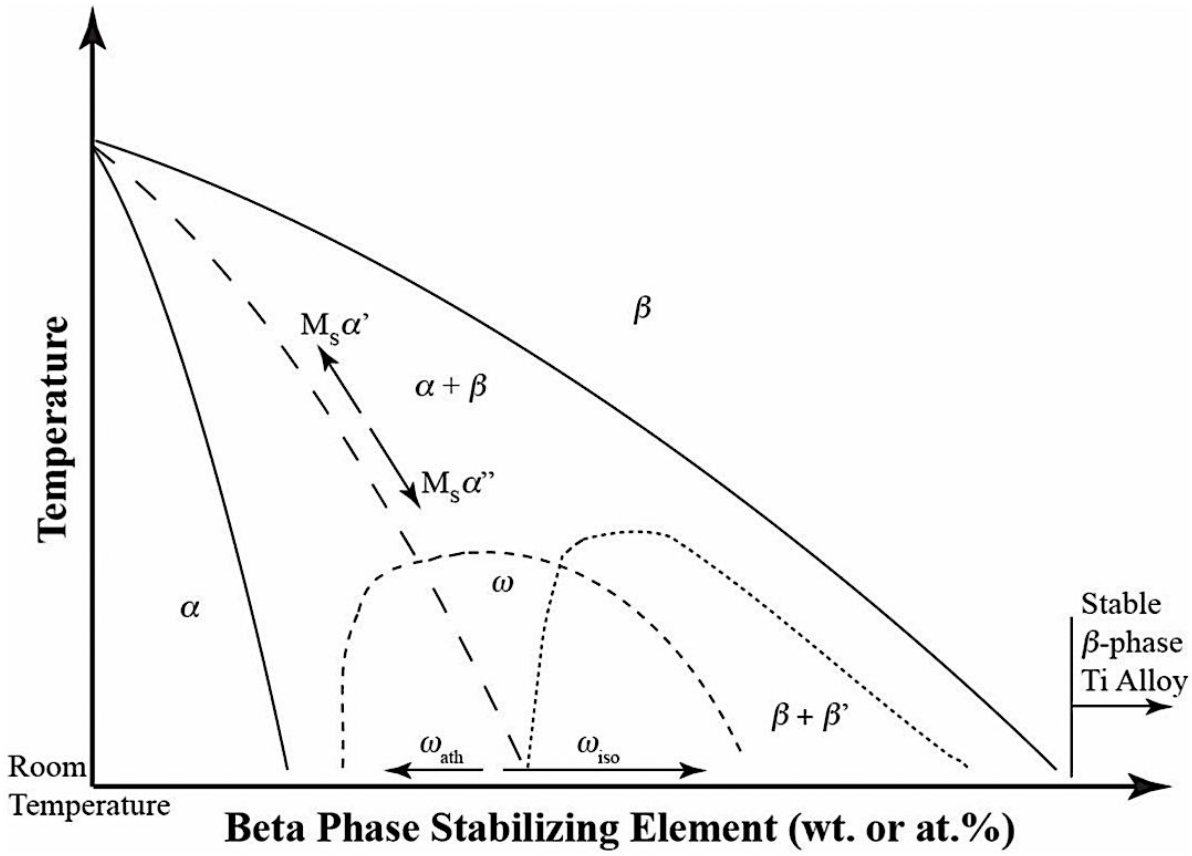


Fig. 2.18. The phase diagram shows the equilibrium and the non-equilibrium phases transformations in metastable β Ti alloys. (Modified from [36])

Three mechanisms are known to induce α" phase transformation in β stabilized Ti alloys: (i) the diffusion-less displacive transformation[81], (ii) diffusion-driven phase transformations [82] and (iii) spinodal decomposition [80]. The martensite α" phase formed by diffusion-less displacive mechanism does not have chemical differences with β matrix. If α" was formed by diffusion-driven, α" phase will be lean in alloying elements [82,83]. Recently, Qi et al. [83] have revealed the diffusional-displacive transformation of β → α" → α in a metastable β Ti alloy (Ti-15Nb-2.5Zr-4Sn) under various aging temperatures, as shown in Fig.2.19. The work enriches the understands of the martensitic phases' transformations in the metastable β Ti alloy.

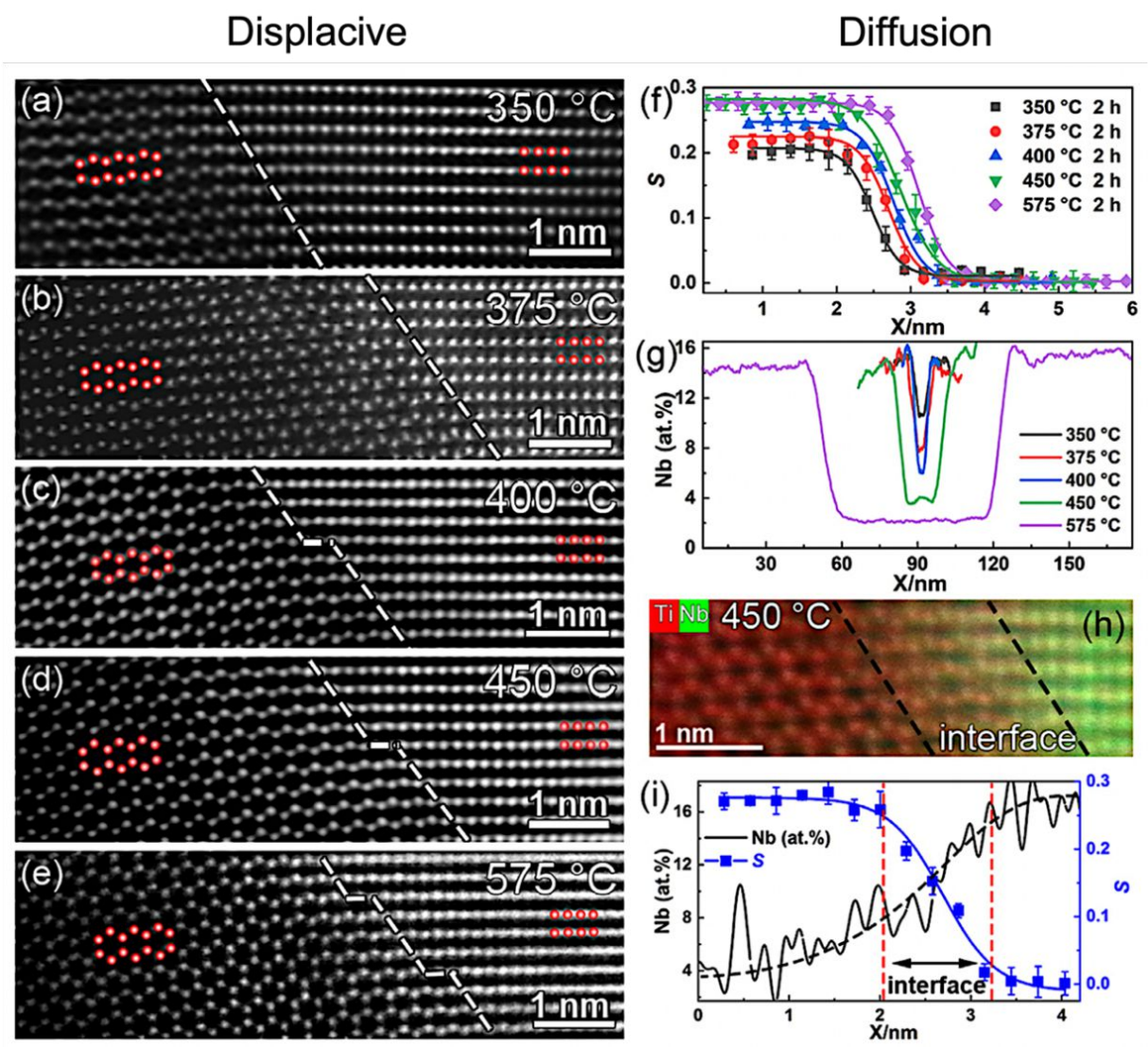


Fig. 2.19. (a-e) The HAADF-STEM images of the interfaces between the β/α" or β/α under different ageing temperatures. (f) S values under different conditions. (g) The Nb concentrations across the interface of phases. The EDS mapping of the phase boundaries (h) and its line profile (i). (Modified from [83]).

Moreover, some other works [79,82] suggested that α" phase formed during isothermal ageing treatments through the spinodal decomposition of β → α''_{rich} + α''_{lean}. As shown in Fig.2.20, a modulated structures of α" phases along the $[001]_{\alpha''}$ direction were revealed in Ti-6%Mo alloy after 798 k aged for 2400s [79]. The α" phases were composed of two variants of modulations. After that, the mechanisms of spinodal decompositions in the metastable β Ti

alloys were further investigated, involving α" or new B2 phases[79,84,85].

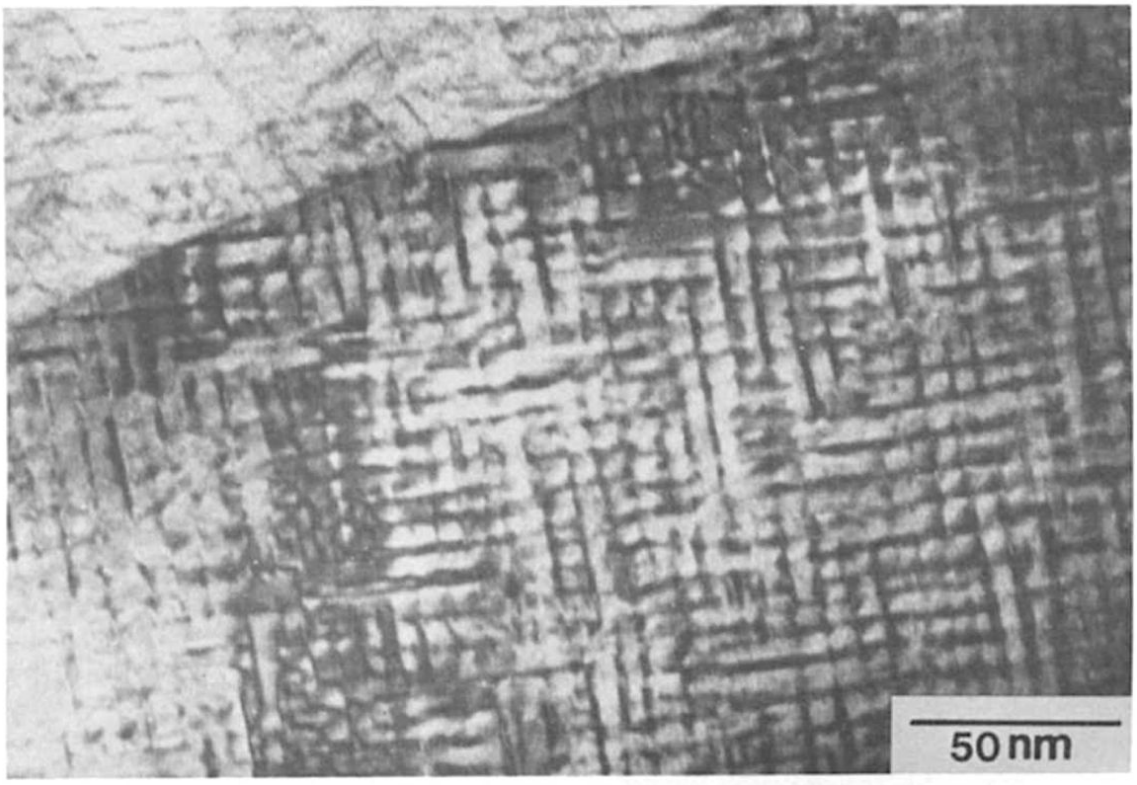


Fig. 2.20. The SEM image shows the martensite α" plate in the Ti-6%Mo alloy. (Modified from [79]).

With a high content of Mo elements (higher than the critical concentration) in some β Ti alloys, the β' phases can precipitate from the β matrix during low-temperature ageing treatments [41,86]. After that, the non-equilibrium phases will eventually decompose to equilibrium status of $\beta + \omega_{iso}$, $\beta + \alpha$, or $\beta + \alpha + \omega_{iso}$, depending on the stability of phases, the temperature and holding time of ageing treatments [41].

In recent works, the substitutional and interstitial solutes were proved to facilitate the instabilities of metastable β Ti alloys, thereby influencing the evolution of the microstructures [87–89]. Zheng et al. [90] had found that whether adding external solutes or in simple binary systems, only when the stability of ω phases was sufficiently reduced, the $\{110\}<1\bar{1}0>$ soft-phonon shuffle can be activated, resulting in the precipitation of O' phases (Fig.2.21a). As

shown in Fig.2.21b and c, it indicates the atomic column's small periodic displacements corresponding to the $\{110\}\langle 1\bar{1}0\rangle$ shuffle of O' phase.

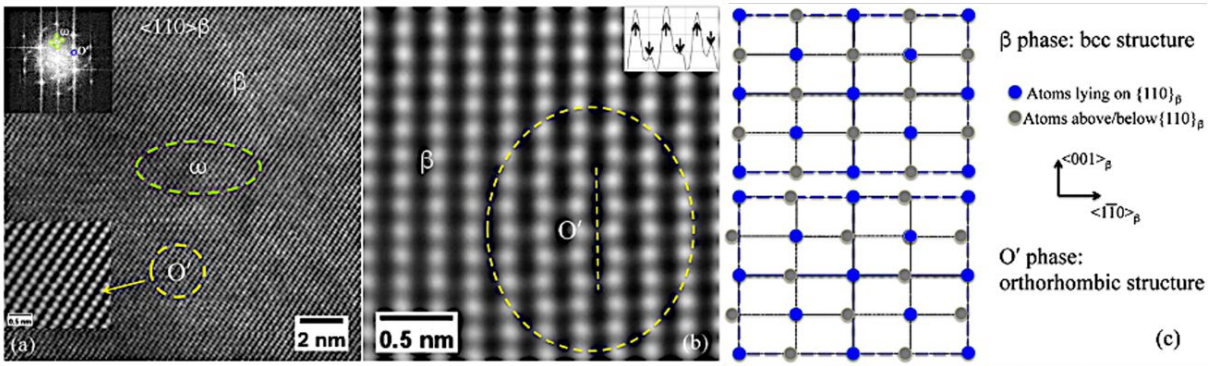


Fig. 2.21. (a) The HAADF-STEM images reveal the ω and O' phases in Ti-18Mo alloy. the lattice structures. (b) The high magnification HAADF-STEM image shows the lattice shuffle in O' phases. (c) The schematic showing the $\{110\}\langle 1\bar{1}0\rangle$ lattice shuffle from β to O' phases (Modified from [90]).

The various non-equilibrium phases in metastable β Ti alloys follow different lattice shearing modes in transformations [90–94]. During the β to α' martensite transformation, $\{11\bar{2}\}\langle 111\rangle$ and $\{110\}\langle 1\bar{1}0\rangle$ shears are induced, which transform the $\{110\}_\beta$ to the close-packed planes of α' phase (Fig.2.22a). The orthorhombic α" experiences less magnitude of the two shear modes, resulting in the orthorhombic symmetry, not the hexagonal. Moreover, the nano-domain induced instability of O' phase is transformed from β matrix by only the $\{110\}\langle 1\bar{1}0\rangle$ shuffle (Fig.2.22b). The last kind of elastic instability will explain the ω phase transformation, related to the 2/3 <111> phono shuffle (Fig.2.22c). During the shearing mode, two neighbour {111} lattice plane will collapse into one, which induces the BCC β transform to the hexagonal ω phase. The different martensitic phases transformations and corresponding shearing modes are also represented in the phase diagram of Fig.2.23. For the Ti-12Mo and Ti-12Mo-6Zr-2Fe alloy systems in this work, the β to α", ω, and O' phases' transformations could happen during the processing and post heat treatments.

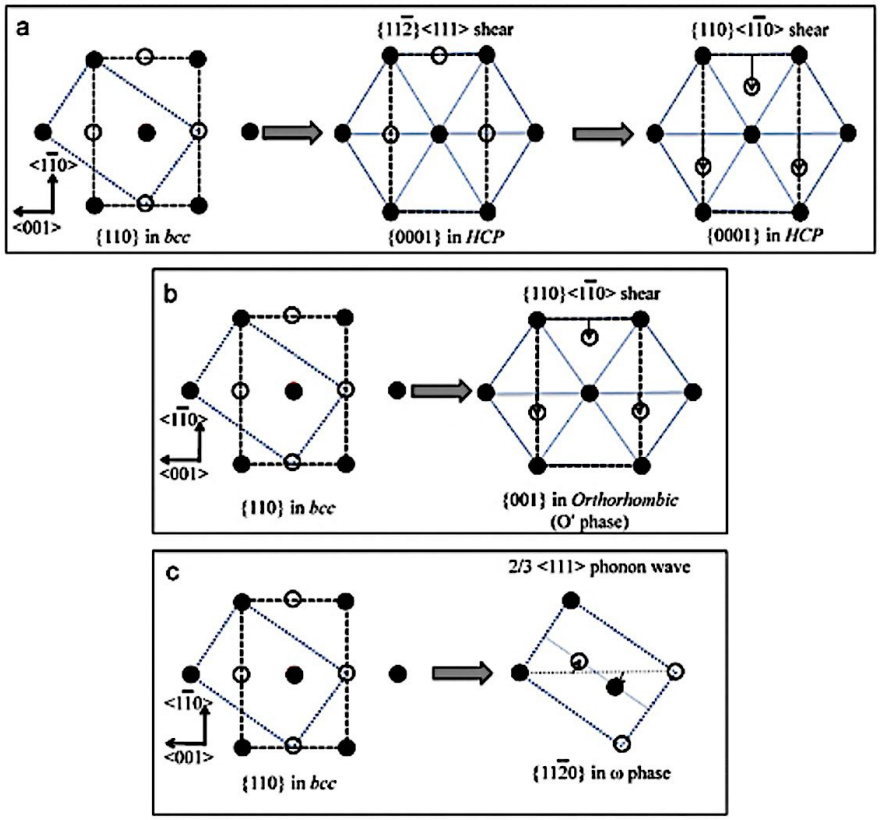


Fig. 2.22. The schematic shows the lattice transformations of the three different non-equilibrium phases in metastable β Ti alloys: (a) α'/α" phase; (b) O' phase; (c) ω phase. (Modified from [95]).

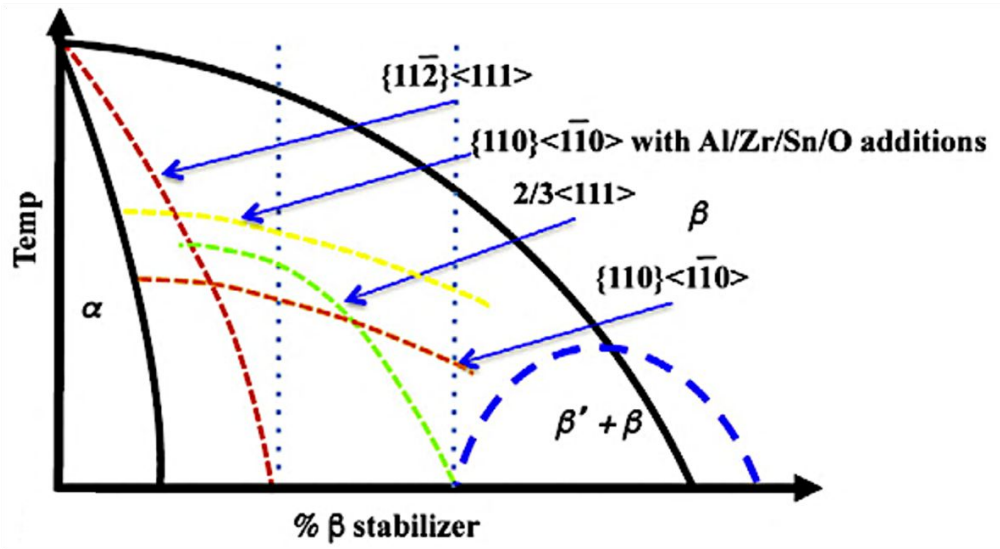


Fig. 2.23. The schematic figure shows the nonequilibrium phases of metastable β Ti alloys and their lattice transformations. (Modified from [90]).

2.2.4. Strengthening strategies

For strengthening β Ti alloys, the most effective strategies involve solid solution strengthening, grain refinement strengthening, and precipitation strengthening [38,55], which will be discussed below.

(1) Solid solution strengthening

Solid solution strengthening, so-called Solid-solution hardening (SSH), originates from dislocations' interaction with solute atoms, obstructing dislocation mobility [55]. The T_{CRSS} (critical resolved shear stress) is a term that refers to the level of stress required to move a dislocation through an array of random barriers [96]. After being developed by Gypen [97] and Caraballo [98], the SSH (σ_{ss}) can be expressed below for multicomponent systems:

$$\sigma_{ss} = \left(\sum_i B_i^{\frac{3}{2}} X_i \right)^{\frac{2}{3}} ; B_i = M\mu\lambda_i^{4/3} Z \tag{2.5}$$

Where B_i is the SSH coefficient, X_i is the concentration, i represents the solute element. M is the Taylor factor, which depends on the crystallographic orientations and slip systems of the alloy. μ is the shear moduli. Z represent the temperature-dependent coefficient. $\boldsymbol{\lambda}_i$ is the misfit parameter. The calculation of $\boldsymbol{\lambda}_i$ has considered the solute/solvent lattice misfit and shear modulus misfit between the Ti and other solutes.

As shown in Table 2.2, the SSH coefficients were calculated for the various solutes in β Ti alloys [99,100]. The essential strengthening effect is from the Pd due to its sizeable atomic size. Some eutectoid elements, such as Ni, Co, Cr, and Cu, have shown significant effects on SSH, while the isomorphous elements (Mo, Nb, and Ta) exhibit limited strengthening effects.

Table 2.2. The shear moduli (μ), Seitz radius(R), misfit parameter ($\boldsymbol{\lambda}_i$) and the coefficient of SSH (B_i) of the primary solutes in the β Ti alloys [99,100].

Element	μ (GPa)	R (Å)	λ_i	B_i (MPa · at.$^{-2/3}$)
Ti	45.6	1.615	-	-
Pd	48	1.935	12.65	3023
Sn	18.4	1.869	10.31	2303
In	4	1.85	9.99	2207
Ni	80	1.377	9.59	2090
Co	88.8	1.383	9.42	2041
Fe	81	1.411	8.26	1715
Cr	115	1.421	8.09	1665
Cu	46.8	1,413	8.03	1650
Mn	39	1.429	7.42	1485
Mg	17.3	1.77	6.62	1276
Zr	30	1.771	6.33	1201
V	46.7	1.489	5.01	879
Mo	125.5	1.55	3.64	575
W	160	1.559	3.64	574
Si	66.2	1.684	3.01	445
Al	26	1.583	2.15	285
Ag	30.3	1.597	1.53	181
Ta	69	1.626	1.42	164

(2) Grain refinement strengthening

The Hall-Petch (HP) relationship ($\sigma_y \propto k_0/\sqrt{\lambda}$, k_0 is the coefficient of HP, and λ represents the grain size) were typically used to evaluate the strengthening effects from refined grain size [101,102]. Therefore, the materials with smaller grains possess higher strength. Previously, the interdependence theory has successfully linked the formation of grains and nuclei selection to reveal grain refinements' mechanisms [103]. It is known that the solute and nuclei are the key impacts for the refinement's efficiency of grains. The nuclei offer a growth medium, whereas the solute supplies the constitutional cooling required to excite neighbouring nuclei [104,105]. Thus, the final grain size is proved to be controlled by three factors: (1) the critical undercooling required for nucleation; (2) the quantity of constitutional supercooling in front of the grain growth; and (3) the average distance between the possible nuclei particles. The alloy systems possess large constitutional supercooling zones and a small distance between

the nuclei cores, favouring refined grains after solidification.

The growth restriction factor Q determines the size of the constitutional supercooling zone [104], which was defined as:

$$Q = M_l C_0 (k - 1) \tag{2.6}$$

Where M_l is the slope of liquidus, C_0 represents the solute concentrations for the selected alloying systems, k means the partition coefficient. Table 2.3 illustrates the $M_l(k-1)$ values in Ti based binary systems, which shows the grain refinement efficiency of different solutes [106]. Various works have investigated adding the solute elements of Be (Fig.2.24), B, Si and Cu to refine the grain size in Ti alloys[104,106–108]. They were proved to refine the prime β grains due to higher growth restriction and more nucleation sites.

Table 2.3. The $M_l(k-1)$ values of varied elements in Ti matrix [106].

Element	M_l	k	M_l(k-1)
Hf	-0.7	→1	→0
Al	-2.1	→1	→0
V	-4.7	→1	→0
Sn	-0.8	→1	→0
Zr	-2.4	0.86	0.3
Pd	-6.6	0.84	1.1
Cr	-8.1	0.81	1.5
Pd	-10.5	0.77	2.4
Pt	-8.4	0.7	2.5
Bi	-5.5	0.54	2.5
Nd	-3.9	0.19	3.2
La	-5.7	0.43	3.3
Fe	-18	0.79	3.8
Er	-5	0.19	4.1
Tb	-4.4	0.04	4.2
Ce	-5.4	0.14	4.6
Gd	-6.2	0.13	5.4
Mn	-13.1	0.55	5.9
Ge	-16.4	0.62	6.2
Cu	-10.6	0.39	6.5
Sc	-11.2	0.4	6.7
Y	-8.8	0.09	7.93
Co	-23.7	0.63	8.8
O*	27.6	1.37	10.8

Ni*	-23.8	0.4	143
Si	-32.5	0.35	21.7
P	-29.1	0.11	25.9
S	-47	→0	47
B	-66	→0	66
Be	-92	0.21	72

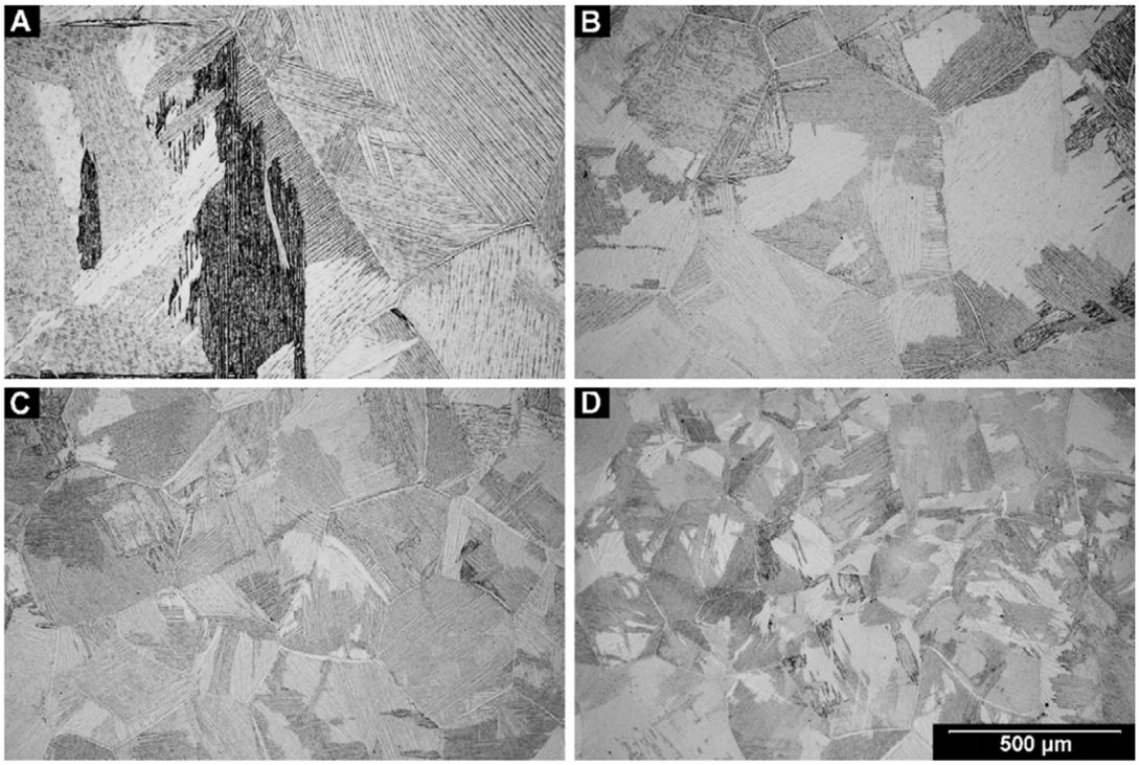


Fig. 2.24. The optical microscopy images of (A) pure Ti, (B) Ti-0.05Be, (C) Ti-0.1Be, and (D) Ti-0.2Be. (Modified from [106])

On the other hand, the deformation methods were also applied to refine the grains. The methods include conventional cold rolling, severe plastic deformations, and surface nanocrystallization treatments [109–112]. The cold rolling can significantly enhance the strength of β Ti alloys through engineering grain refinements and dislocation density. Generally, only the low rolling reduction rates were applied to β Ti alloys for controlling the amount of strain-induced martensite α'/α" [113]. For the severe plastic deformations (SPD) processing, equal-channel angular extrusion (ECAE) and high-pressure torsion (HPT) were the most used methods [111,114]. The SPD can introduce ultrafine grains, which enhance the strength without

significantly influencing the modulus. ECAE typically uses the shear strain to refine the grains effectively, while the HPT combines the vertical pressure and rotational shearing strain[114]. The resulting inhomogeneous microstructures, after HPT deformation, have recently attracted the researchers' interests.

The surface mechanical attrition treatment (SMAT) facilitates the vibration of spherical shots driven by the high-power, high-frequency ultrasound [112,115,116]. During the processing, the surface of the samples is peening shot numbers of times. As a result, the deformed regions after SMAT possess nanosized grains with a gradient microstructure across the side section of the specimens. The SMAT treatments are demonstrated for enhancing the fatigue properties and corrosion resistance of Ti alloys [112,115].

(3) Precipitation strengthening

In β Ti alloys, the ductility is mainly dependent on the β matrix, while some specific mechanical performance like strength is strongly influenced by the morphology, volume fraction and distribution of precipitations. Precipitation strengthening can be easily applied to metastable β Ti alloys because a variety of phases including ω_{ath} or ω_{iso} phases, HCP α/α', and orthorhombic α" can be introduced into the matrix during manufacturing and post-thermal-mechanical treatments [117,118]. Although ω precipitates typically harden β Ti alloys, it could lead to severe embrittlement in some work [119]. The recent investigation [120] on β Ti-Mo alloys applied atomic probe tomography (APT) technology to reveal the origin of embrittlement, which was attributed to the significantly increased shear modulus of ω phase, due to the Mo element was continuously rejected from the ω particles during the heat treatments. However, the influence of ω phases on the deformation mechanisms of β Ti alloys is still unclear.

Research works have focused on engineering α phases to strengthen β Ti alloy. One of the advanced, practical ways is to achieve the microstructure of hierarchical α phases. Arun et al.

[121] reported that microscale and nanoscale α phases contributed to the super high strength of a low-cost β TiAlVFe alloy, of which the tensile strength reached 1.7 GPa. The microstructures are composed of the hierarchical α phase, as shown in Fig.2.25. Recently, multiscale hierarchical α phases were obtained by annealing and ageing in a Ti-5Al-4Zr-8Mo-7V alloy, presenting a high yield strength (1460 MPa) [122]. The β Ti1023 alloys processed by forging and annealing also achieve the combination of high tensile strength and good ductility due to their hierarchical α phases [123].

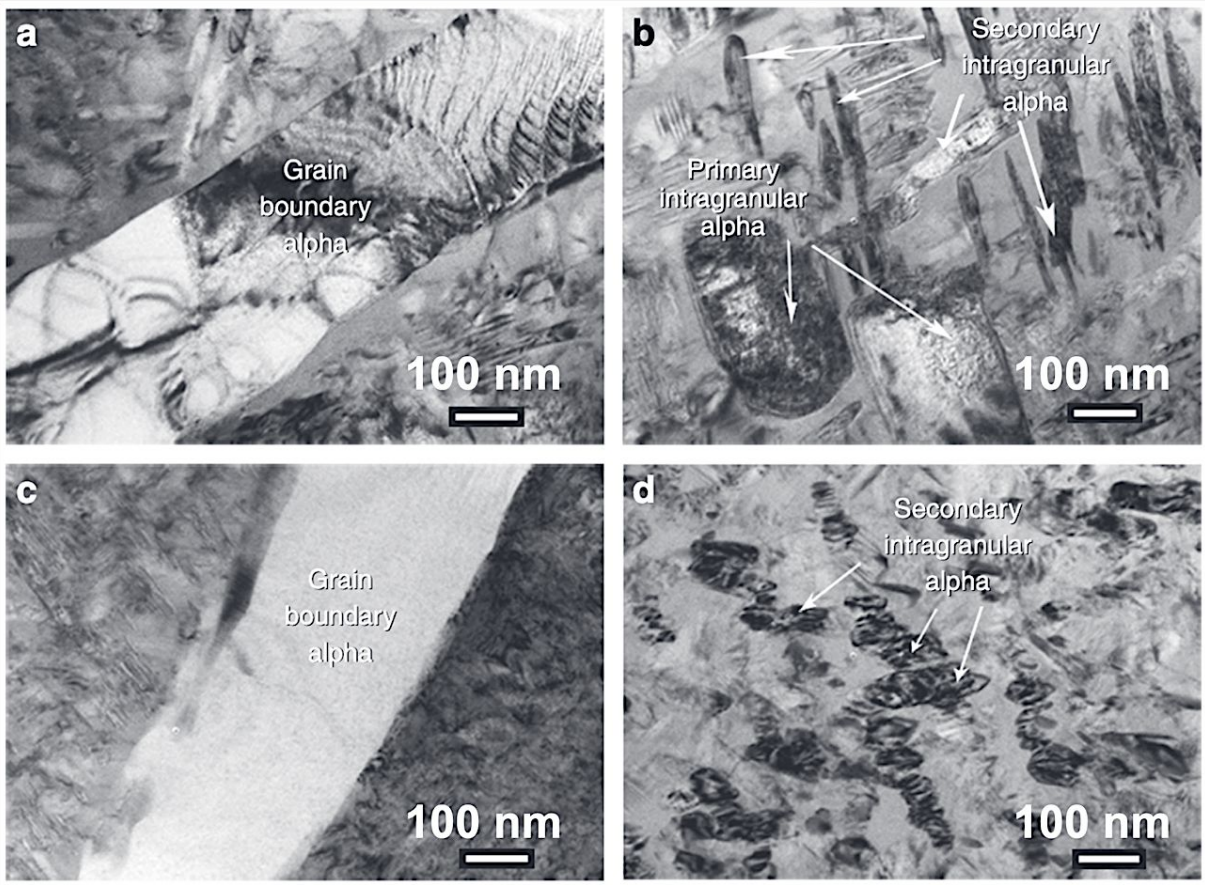


Fig. 2.25. The TEM bright field images show: (a, c) the coarse grain boundary α; (b, d) plate-like primary intragranular α, and nano-sized secondary intragranular α phases in β TiAlVFe alloy. (Modified from [121])

It is well-known that the ω_{iso} phases can mediate the nucleation of fine α phases. Relative theories were established recently on this process [67,124,125]. Various works have revealed

fine-scale α phases form in the β Ti alloys through intermediate ageing steps. Via this phenomenon, Mantri et al.[125] have controlled the size and fraction of ω phases in Beta-21S alloy through precursor ageing treatments at 350℃ and holding various hours (0-150 hours), as shown in Fig.2.26. After that, the different specimens have experienced the same high-temperature ageing step (600 ℃ for 1 hour) to precipitate the α phase. They found that the α phases were gradually refined with the increase of holding times at low temperatures (350℃). Finally, the α phases reached nano size, and the tensile strength significantly improved from 1.2 GPa to 1.8 GPa. Furthermore, some β Ti alloys can also be strengthened through introducing refined high-density orthorhombic α" phases, after a single long-time low-temperature ageing treatment step [126].

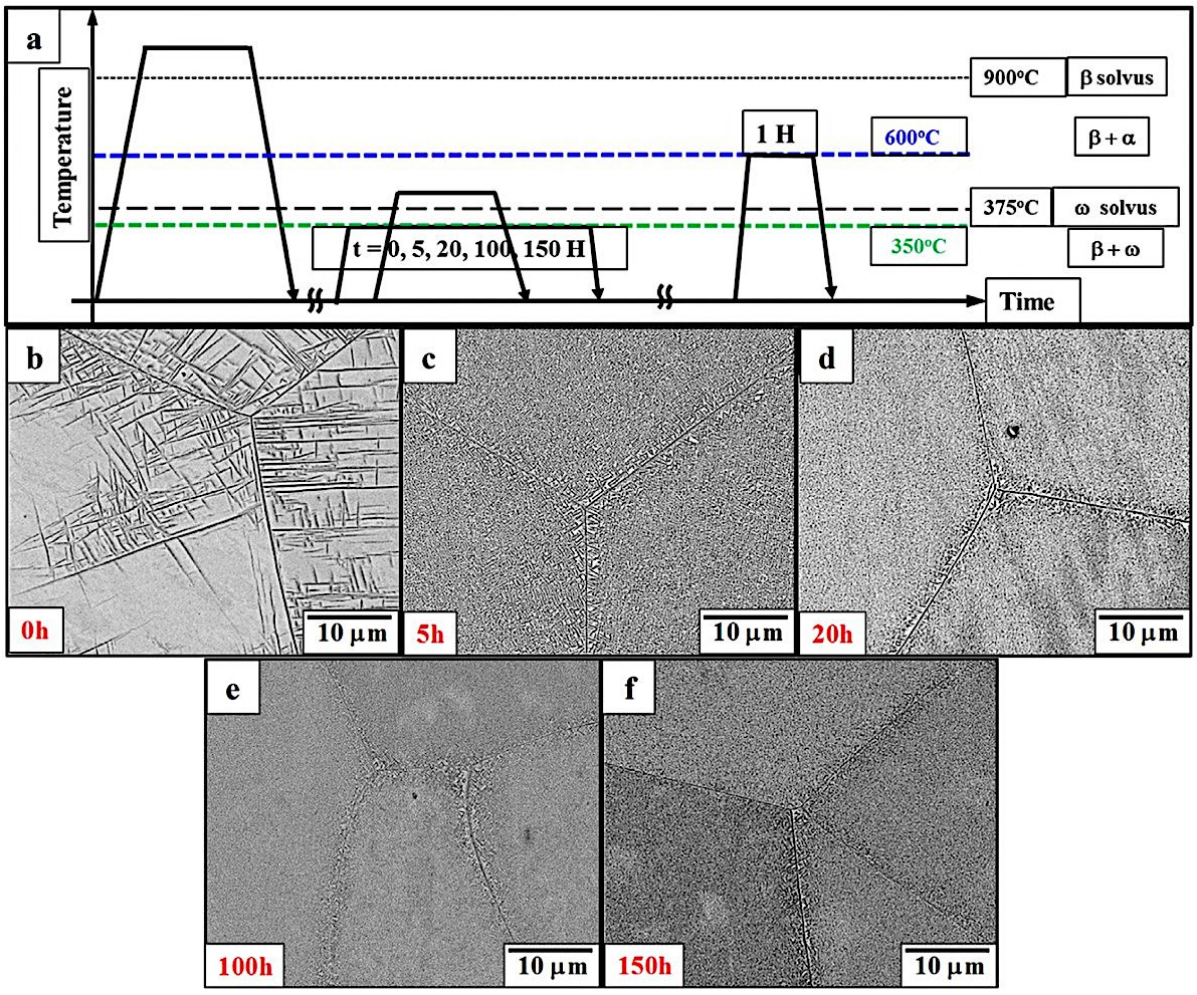


Fig. 2.26. (a) The schematic shows the details of heat treatment procedures. (b-f) The backscattered electron (BSE) images show the evolution of microstructures after different low-temperature holding times. (Modified from [125]).

2.2.5. Deformation modes

Within the last several years, the enhanced ductility has been reported in some β Ti alloys, of which the deformation mechanisms, especially the twinning induced plasticity (TWIP) and transformation induced plasticity (TRIP) effects, were widely studied [127,128]. According to Mo equivalent function (Mo_{eq}), the so-called stabled β titanium alloys (Mo_{eq} > 30) was dominated by the dislocation slip during the plastic deformation [129]. After reducing the β phase stability to the metastable state, additional deformation mechanisms including {332}<113> β twinning, {112}<111> β twinning, and stress-induced martensitic (SIM) α”/α’ transformation can be activated [130]. Moreover, the relationship between the deformation mechanisms and MoE (Mo_{eq}) is concluded in Fig.2.27. With the increase of the Mo_{eq}, the succession of deformation mechanisms of β Ti matrix is as follows: β to α’ → β to α” → β to ω + β twinning → β twinning → β twinning + β slip → β slip. Thereby the β phase stability is an essential factor governing the mechanical properties, especially the plastic deformation behaviour.

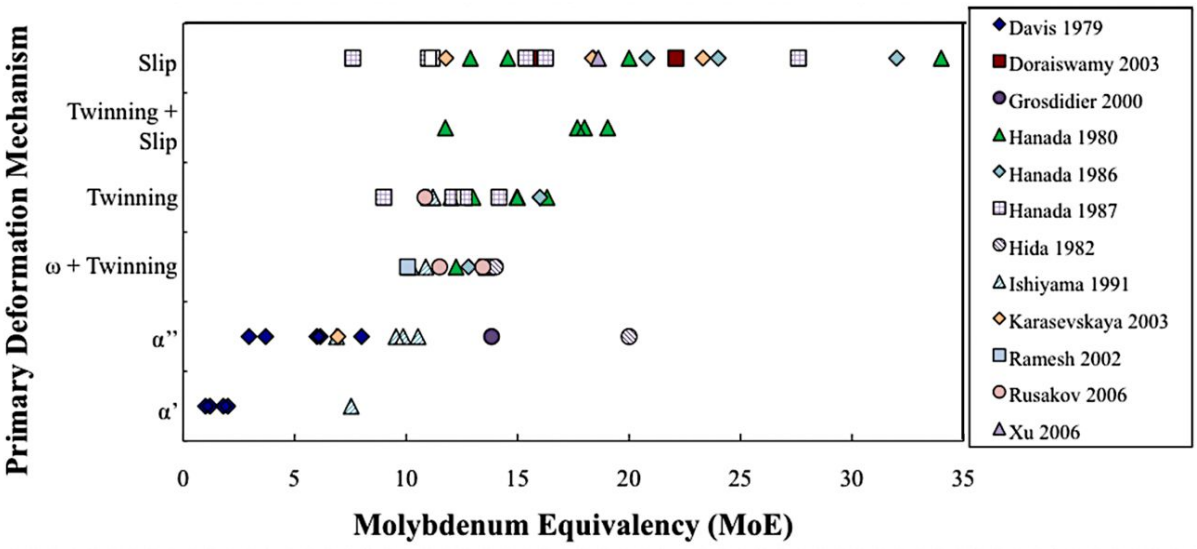


Fig. 2.27. The deformation modes in varied β Ti alloys are divided by Mo_{eq}. (Modified from [36,131])

However, it is not accurate to divide the deformation modes only using Mo_{eq} as some β Ti alloys simultaneously activate twinning and martensites during the plastic deformation [132,133]. For precisely evaluating the β phase stability and developing new Ti alloys, Kuroda [42] proposed an alloying design approach based on a molecular orbital method, which is called the $\overline{Bo} - \overline{Md}$ method. $\overline{Bo}$ is the average covalent bond strength between the Ti and another alloying element. $\overline{Md}$ is the mean d-orbital energy level, which is related to the radius and electronegativity of metallic elements. After that, the $\overline{Bo} - \overline{Md}$ map was initiated and expanded further[134], as shown in Fig.2.28. It is not only used to divide the different deformation modes but also discriminate the regions of the phase of α, β and α+β.

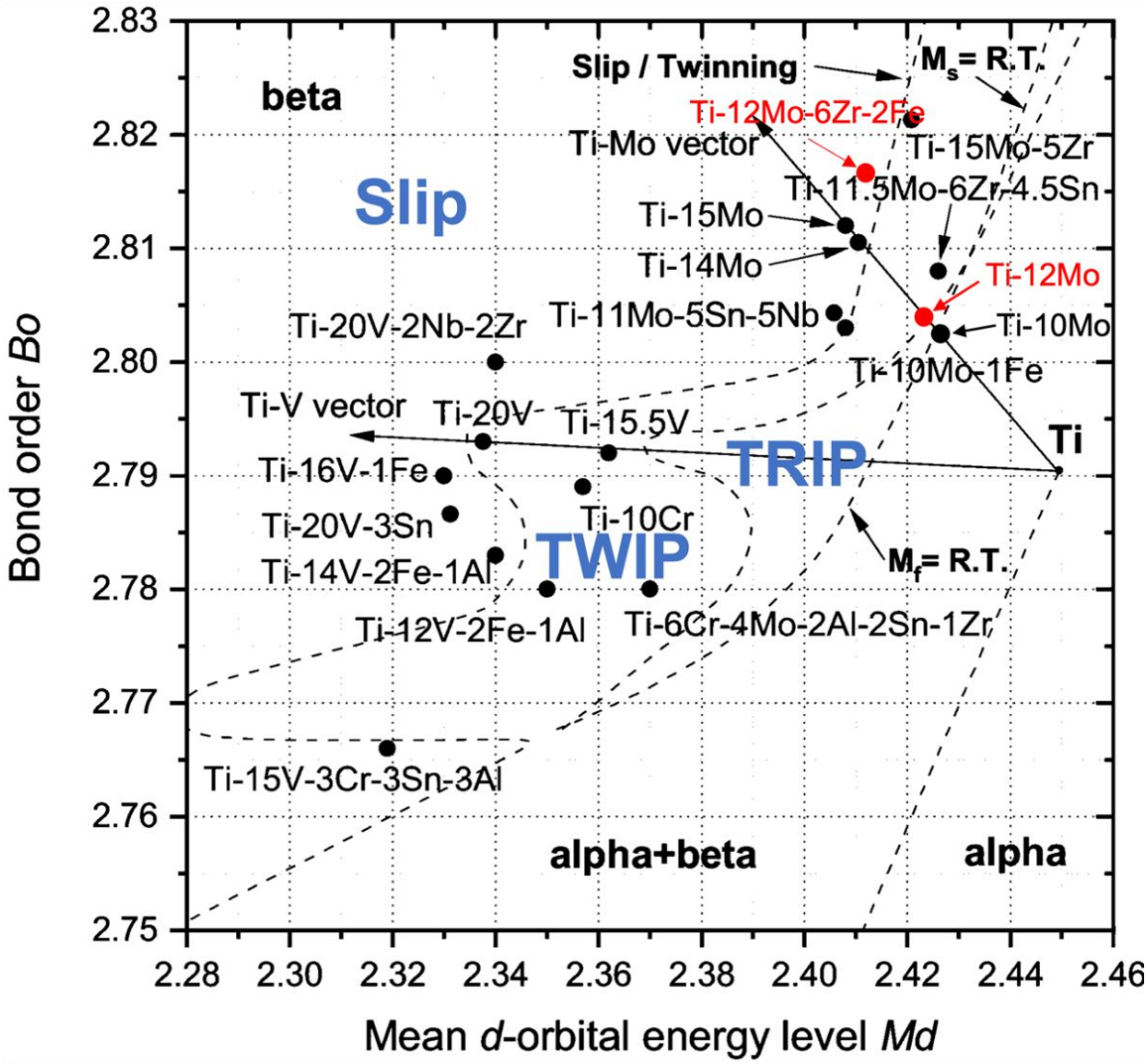


Fig. 2.28. The $\overline{Bo} - \overline{Md}$ map conclude the chemical stabilities and deformation modes of various β Ti alloys. (Modified from [42,96]).

In recent years, a variety of novel β titanium alloys with exceptional mechanical properties have been created based on the $\overline{Bo} - \overline{Md}$ map. Initially, it was used to develop low modulus β Ti alloys by applying low $\overline{Bo}$ and high $\overline{Md}$ values [135]. In this way, low modulus TiNbTaZr and TiNbSn alloys were created for biomedical applications [136–138]. After that, the method was used to develop β Ti-12Mo and Ti-9Mo-W alloys with super high ductility and high strain hardening capacity by triggering the deformation twinning and stress-induced

martensite phases [132,133]. However, these alloys exhibit a limited yield strength, which is less than 500 MPa. The low yield strength was attributed to the low critical stress (190 - 360 MPa) for tripping the martensite phase transformation, resulting in pseudo-elasticity. At the same time, the high strain hardening rate is normally observed in these alloys. A recent work [139] reported a Ti-15Nb-5Zr-4Sn-1Fe alloy possessed low yield strength with ultra-high strain hardening rate (~6.1 GPa) due to the martensitic transformation of β to α'. Furthermore, the research interest was turned to explore β Ti alloys that possessed high strength and excellent ductility. Based on the $\overline{Bo} - \overline{Md}$ method, Ren et al.[140], Sadeghpour et al.[141]. and Gao et al.[142] proposed Ti6Cr4Mo2Al2Sn1Zr, Ti3Al5Mo7V3Cr, and Ti7Mo3Cr β Ti alloys, respectively, exhibit high yield strength, high strain hardening rate, and good ductility. In these alloys, mechanical β twinning is the dominant deformation behaviour at the early stage, followed by the SIM α". After that, the metastable β Ti alloys, which only exhibit the TWIP effects during deformation, were developed. However, they usually show high yield strength but limited strain hardening rates [96]. Among these alloys, a new-developed Ti-4Mo-3Cr-1Fe illustrated high yield strength and extreme high strain hardening rate because of the deformation-induced nano-scale hierarchical twin structures[143]. Thus, the $\overline{Bo} - \overline{Md}$ method is an effective tool to develop high-performance β Ti alloys with high strength and good ductility.

2.2.6. Typical heat treatments

Post heat treatment of β Ti alloys is generally used to reduce inner stresses, homogenize the microstructures, enhance the capacity for machine tooling, or strengthen the component by precipitating secondary phases [36,39,57]. The procedure can improve the ductility, strength, fracture toughness, fatigue, and corrosion resistance of the β Ti alloys. Moreover, considering

the different applications of β Ti alloys in biomedical and aerospace industries, the requirements are varied. Then β Ti components need appropriate heat treatment processes for the specific applicational purpose and mechanical requirements [52,144].

Firstly, annealing to release the residual stress is needed for improving the fabricability and workability of β Ti alloys after or during the thermo-mechanical processing [52]. Some β Ti alloys are annealed under a temperature slightly higher than the β transus for less than 1 hour, as shown in process A of Fig.2.29 [38,41]. The annealing time should not be too long for controlling the grain size and precipitation of grain boundary α, which can be detrimental to the mechanical performance[145]. The annealing can also be performed under a temperature slightly less than β transus, followed by air cooling (B of Fig.2.29). The oil or water quench could lead to excessive residual stress and undesirable non-equivalent phases, especially for the metastable β Ti alloys [36].

Moreover, the ideal microstructure for the industrial application of β Ti alloys is generally achieved through solution heat treatments, quenching, and then post ageing, enabling the sequence of solutions, supersaturation of concentrations, and precipitating. There are two different solution heat treatments, which involve the super-transus and sub-transus heat treatments [58]. The super-transus heat treatments are performed over the β transus, which will lead to significant growth of grain size, thus obtaining high ductility and low strength. The sub-transus heat treatment can restrict grain size growth due to lower temperatures or pinning effects from some primary α phases formed during the process [57]. Therefore, the alloy should have higher strength while limited ductility. For the applications in biomedical implants, some β Ti alloys adapt the super-transus heat treatments without subsequent ageing to acquire the low elastic modulus. The ageing treatments to precipitate α phases should raise the elastic modulus due to the higher modulus of HCP α phase than BCC β phase [144]. For the applications in the

aerospace industry, the β Ti alloys can be solution treated at super-transus or sub-transus temperatures, which can also be applied with or without subsequent ageing treatments depend on the desired mechanical properties [52].

After that, the post ageing treatments include high-temperature ageing treatments (C in Fig.2.29), low-temperature ageing treatments (D in Fig.2.29), or duplex ageing treatments with two steps [146]. As discussed before, the varied ageing treatments after solution heat treatment will result in different sizes, shapes, and densities of α phases. Typically, more refined α phases will lead to higher strength and hardness, while the ductility could be less. The ω_{iso}, formed during low-temperature ageing treatment, could also embrittle the β Ti alloys[35].

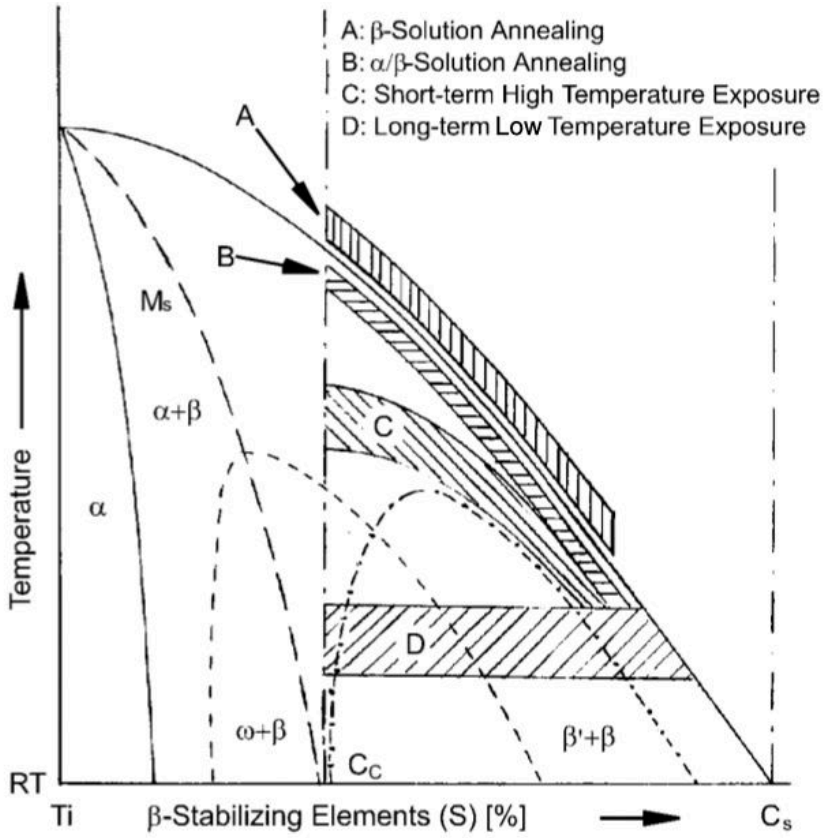


Fig. 2.29. The phase diagram shows the typical heat treatments of β Ti alloys. (Modified from [38])

2.3. Laser Powder Bed Fusion of β Ti Alloys

Although β Ti alloys possess high specific strength, low modulus, excellent corrosion, and fatigue resistance, making them the appropriate structural material for biomedical or aerospace applications, the difficulties in processing limited its widely applications [38]. Applying the LPBF to process β Ti alloys allows the integrated fabrication of the components with highly complex geometric, which paves a cost and time-saving method for producing the final parts [10]. It is known that the final microstructure of β Ti alloys, processed by LPBF, depends on the processing parameters and the thermal history [147]. Therefore, the microstructure is adjustable by modifying the LPBF processing conditions to fulfil the requirements from biomedical, aerospace, power generation and petrochemical industries [36,37]. Nevertheless, research findings so far are still limited in terms of additive manufacturing printability, microstructural evolutions, and mechanical properties of β Ti materials printed by LPBF.

2.3.1. LPBF using pre-alloyed powders

The LPBF processing of β Ti alloys has been developed for over ten years, while the candidate pre-alloyed (PA) β Ti powders is still limited[148,149]. For aerospace applications, researchers generally focus on the LPBF processing of conventional β Ti alloys, like Ti10V2Fe3Al (Ti1023) and Ti5Al5Mo5V3Cr (Ti5553) alloys [150,151]. On the other hand, there are more choices to build β Ti materials for biomedical applications, such as Ti-Nb and Ti-Zr systems [152,153]. Recently, it was extended to Ti-Mo systems[154]. However, the LPBF of β Ti alloys has not been extensively investigated, which can be attributed to the lack of pre-alloyed powders.

Beta Ti1023 alloy was developed for the aerospace applications, such as landing gear and airframes, due to its high strength, good fracture toughness and ductility [149]. The stress-

induced martensite during plastic deformation is significant for its high mechanical performance [155,156]. The investigations on LPBF processing of Ti1023 were reported by Qiu et al. [150,157,158] recently. They revealed the varied mechanical performances of the specimens processed by diverse energy density, which can be attributed to the different morphology of grains and α phases. Their abnormal strain hardening behaviour was caused by the β to α' phases transformations [150]. The modified content Ti-Al-8V-5Fe (Ti185) was also investigated [118], which illustrated high compressive strength because of the refined grains and nano-scale precipitates formed during the fast-cycling cooling of LPBF. Another low-cost β Ti5553 alloy for the aerospace industry was also successfully fabricated using LPBF, which exhibited high strength and ductility [159]. After the duplex post ageing treatments, the compressive strength was significantly improved from 1000 MPa to 1600 MPa [160]. Furthermore, Deng et al. [161] have studied the LPBF processing of modified Ti5553-1Zr alloy, which were subsequent heat-treated by varied schemes. The anisotropic mechanical performances are shown strongly adjustable by post-heat treatments.

The Nb, Mo, Zr and Sn elements have shown good biocompatibility and bio inertness as the implant materials in human bodies. They are also the strong β stabilizers for β Ti alloys. For exploring the LPBF printability of low modulus and biocompatible β Ti alloys, researchers have studied the Ti-Nb, Ti-Mo, and Ti-Zr systems in recent years [162–164]. The Ti24Nb4Zr8Sn (Ti2448) alloy is one of the most attractive candidates due to its low modulus (≧42 GPa), excellent biocompatibility, and superelasticity [165,166]. Zhang et al. [148] used the LPBF to produce the Ti2448 with PA powders and built the near fully dense specimens, of which the mechanical properties were also close to that of samples processed the conventional method without any post-treatment. The Ti2448 components fabricated by LPBF and electron beam melting were also compared [166]. The LPBF specimens showed higher strength and lower

modulus due to refined microstructures after fast cooling. After that, Yang et al. [167] found that the T2448 processed by LPBF obtained a high strength and good ductility, attributed to the bimodal grain structures. Considering the TRIP effects, Liu et al. [168] have compared the mechanical performances of a Ti25Nb3Zr3Mo2Sn alloy prepared by LPBF and hot-rolled. The samples fabricated by LPBF illustrated the improved tensile properties because of the texture, strong TRIP and "hard-wrap-soft" effects.

However, the main challenge for exploring more β Ti alloying systems is the high cost of producing high-quality PA powders with a suitable size range for LPBF due to the difficulties in preparing homogeneous ingots and low powder yield of atomization. These make the LPBF fabrications to be inflexible and costly.

2.3.2. LPBF using blended elemental powders (in-situ alloying)

To discover more β Ti alloying systems by LPBF, a growing number of works choose to use the blended elemental (BE) powders, so-called in-situ alloying based LPBF processing [5,30]. The method has already shown its advantages, including cost-effective, efficient, and flexible chemical concentrations benefiting from the highly concentrated and localized energy input of LPBF [8].

A primary concern of LPBF using BE powders is the chemical inhomogeneous [8,30]. Powder blending is the first critical stage for achieving the homogeneous microstructure in LPBF processed components. Other factors influence the chemical homogeneous including the partial melting, laser remelting, solidification segregations and Marangoni effect, which depend on the laser processing parameters, physical properties, chemical compositions of BE powders[169,170]. The methods of powder blending involve conventional, satelliting, and mechanical mixing. Generally, the conventional powder mixing method uses the tumbler mixer,

tubular shakers, and jar mills, as illustrated in Fig.2.30a [30,170,171]. The method needs the elemental powders to have narrow size distributions, suitable spherical shapes and flowabilities, to facilitate the blending homogeneity.

Moreover, the satellite blending method uses fine-sized powders to decorate the coarse powders, consuming the polyvinyl alcohol solution as the bonding agent [172]. Compared with conventional methods, the technique (Fig.2.30b) raised the homogeneity of powders blending and laser processing quality. Some other researchers applied mechanical milling to blend the elemental powders, which increased the initial chemical homogenization of powders[173–175]. However, the method can introduce impurity elements, increase the inner stress, and change the spherical shape. These features can influence the printability of the powders using LPBF.

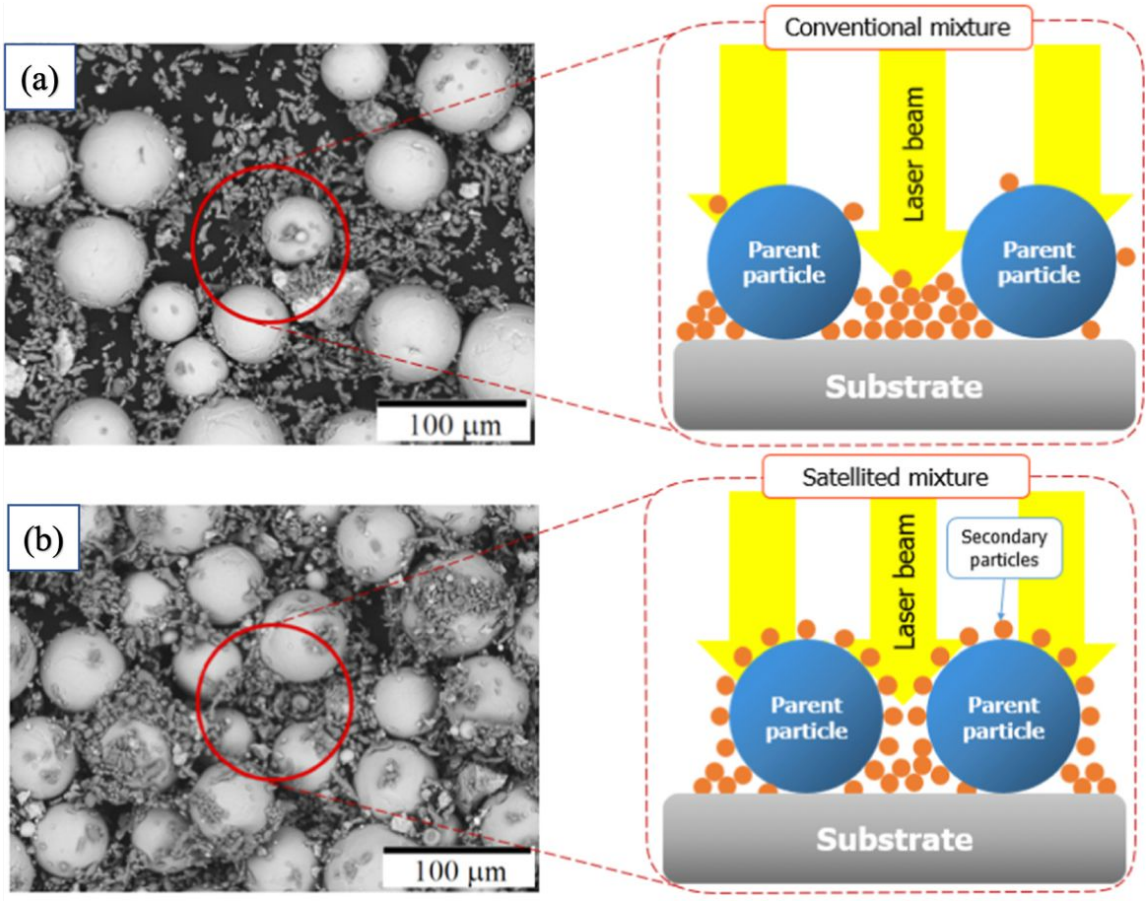


Fig. 2.30. The BE powders' BSE images (Ti, Al and V) and the laser beam's interaction schematics using conventional mixing (a) and satellited blending (b). (Modified from [30]).

To stabilize the β phases in Ti alloys, researchers choose to blend the β stabilizer elements into CP Ti or Ti6Al4V powders before the LPBF processing. Vrancken et al.[176] processed a novel β Titanium by LPBF through powder blending of Ti6Al4V and Mo element powders. The as-LPBF specimens contain mainly β matrix and some un-melted Mo particles, as shown Fig.2.31a, whereas they possess high strength and ductility. Other works performed the LPBF processing of Ti6Al4V+Cu[177] or Ti6Al4V+Fe[178], in which the phases compositions and grain structures were changed compared with that in as-LPBFed Ti6Al4V. More works investigated the microstructures and mechanical performance of the LPBFed specimens using mixed feedstock powders of β stabilizer elements with CP Ti powders. Sing et al. [179] and Fischer et al. [180] have adopted LPBF to fabricate Ti-50Ta and Ti-26Nb (Fig.2.31b) using mixed powders. However, they all faced inhomogeneous and un-melted refractory particles, which may become the nucleation sites for failure in service.

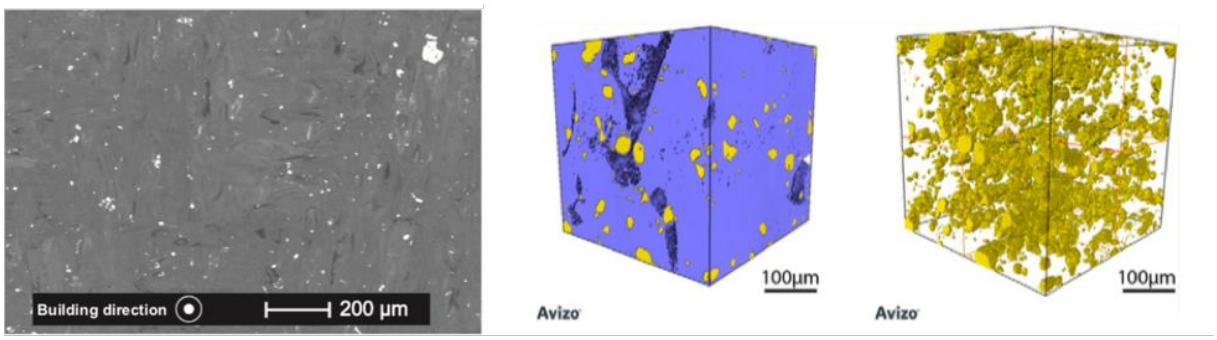


Fig. 2.31. (a) The BSE image shows the microstructure of in-situ alloyed Ti64-Mo. (b) The 3D XCT images of in-situ alloyed Ti-26Nb. (Modified from [179,180])

There are two methods to homogenize the powder layers during the in-situ alloying based LPBF. One uses the laser remelt, so-called rescanning, for each powder layer, as performed by Brodie et al. [170], which can be seen from Fig.2.32(a-c). The residual Ta particles were visually reduced after applying the remelt strategy. Others use exceptionally high energy input

(up to 950w) to eliminate the refractory Nb particles in Ti-34Nb alloy, as reported by Huang et al. [181]. Fig.2.33 shows the reduction of porosities and Nb particles with the increase of laser power.

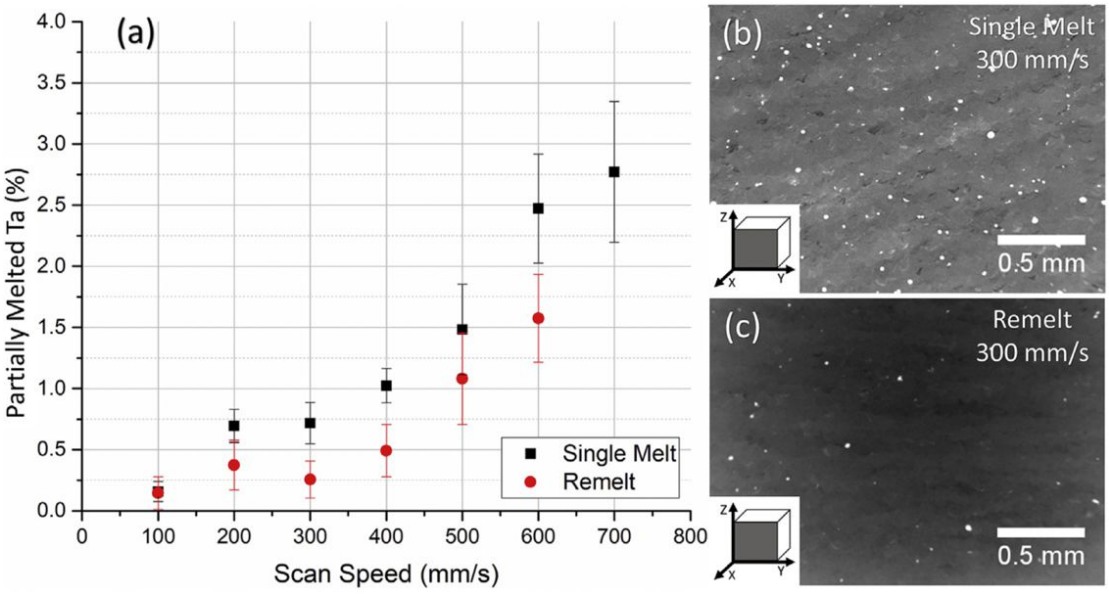


Fig. 2.32. (a) Area percentage of residual Ta particles in in-situ alloyed Ti-Ta using varied scanning speeds and melting strategies. (b) The BSE image shows the microstructure of the specimen fabricated using the single melt strategy. (c) The BSE image shows the microstructure of the specimen fabricated using remelt strategy. (Modified from [170])

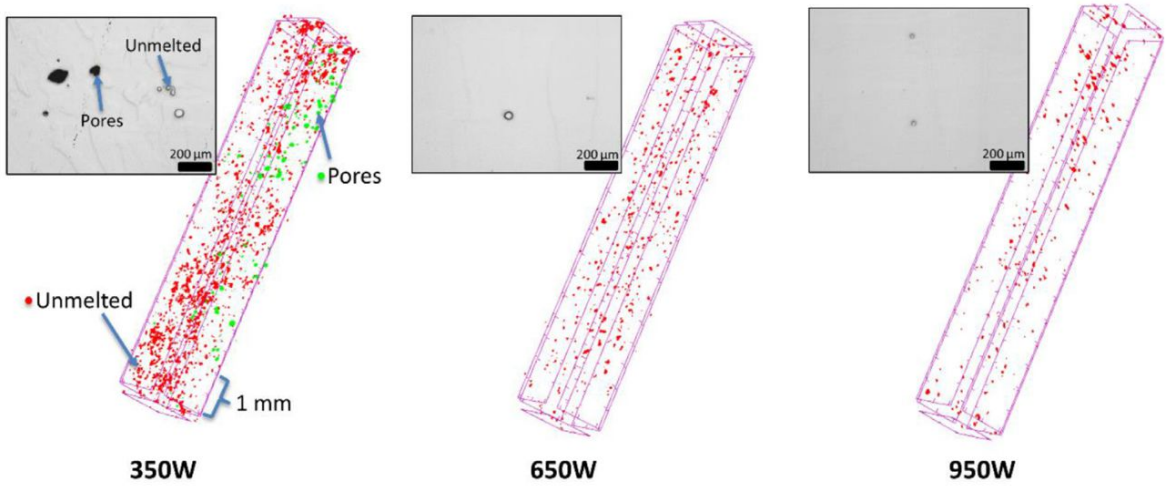


Fig. 2.33. The 3D XCT results show the evolution of porosity and residual Nb particles in the Ti34Nb samples with the increase of laser energy from 350w to 950w. (Modified from [181]).

According to the previous works, neither the remelt strategy nor extreme high laser power can entirely remove all residual refractory particles. Thus, the compositional inhomogeneity and segregations look inevitable to be avoided in the parts prepared by in-situ alloying based LPBF, although Marangoni forces and laser remelting can promote the diffusion of the blended elemental powders. The unmelted particles will influence the fatigue properties and processing repeatability from batch to batch when considering the industrial applications, which will need to be resolved in future works.

We then summarize the tensile behaviours of varied β Ti alloys prepared by LPBF using pre-alloyed (PA) or blended elemental powders (BE), as shown in Table 2.4. The mechanical properties of β Ti alloys fabricated by in-situ methods could be comparable to those prepared using pre-alloyed powders.

Table 2.4. The mechanical properties of LPBF processed β Ti alloys.

	β Ti alloys (wt%)	Hardness (HV)	Elastic Modulus (GPa)	Yield Strength (MPa)	Ultimate Tensile Strength (MPa)	Elongation (%)	Ref.
Using Pre-alloyed Powders	Ti24Nb4Zr8Sn	220 ± 6	53 ± 1	563 ± 38	665 ± 18	13.8 ± 4.1	[148]
	Ti25Nb3Zr3Mo2Sn	202	-	592 ± 21	716 ± 14	37 ± 5	[168]
	Ti35Nb7Zr5Ta	205 ± 10	81	309	631	15	[162]
	Ti13Nb13Zr	-	65	794 ± 15	996 ± 13	5	[182]
	Ti5Al5Mo5V3Cr	-	-	780	800	14	[159]
	Ti5Al5Mo5V3Cr	-	-	804 ± 5	819 ± 7	17	[161]
	1Zr	-	-	1180 ± 9	1234 ± 5	11	
	Ti3Al8V6Cr4Zr4	309 ± 10	68 ± 5	845 ± 1	863 ± 2	31 ± 3	[183]

	Mo						
	Ti10V2Fe3Al	-	-	934	939	10	[158]
	Ti-15Mo	-	-	728 ± 34	804	37 ± 6	[154]
		-	-	392 ± 4	650 ± 7	53 ± 3	
Using Blended Elemental Powders	Ti6Al4V+10Mo	338 ± 5	73 ± 1	858 ± 16	919 ± 10	20 ± 2	[176]
	Ti6Ta	241 ± 3	108 ± 4	595 ± 5	697 ± 2	17.5	[184]
	Ti12Ta	267 ± 10	99 ± 6	650 ± 7	783 ± 18	14.2	
	Ti18Ta	296 ± 10	96 ± 3	668 ± 20	808 ± 17	10	
	Ti25Ta	353 ± 11	89 ± 4	1029 ± 8	1186±14	6	
	Ti50Ta	285 ± 11	76 ± 4	883 ± 20	925 ± 9	12 ± 1	[179]
	Ti15TaxZr	-	92 ± 9	869 ± 19	890 ± 50	16 ± 1	[185]
		-	71 ± 4	925 ± 35	960 ± 32	19 ± 2	
		-	43 ± 3	769 ± 16	805 ± 19	15 ± 1	
		-	72 ± 5	663 ± 31	691 ± 19	25 ± 2	
	Ti25Nb	250 ± 4	86 ± 2	612 ± 11	731 ± 14	21 ± 1	[174]
	Ti26Nb	-	-	768	799	14.3	[186]
	Ti34Nb	-	67 ± 9	793 ± 19	793 ± 18	3 ± 1	[181]
		-	58 ± 10	742 ± 54	743 ± 54	5 ± 1	
	Ti35Nb	274 ± 7	84 ± 2	648 ± 13	803 ± 33	4 ± 1	[187]
		311 ± 16	86 ± 2	602 ± 14	713 ± 17	6 ± 2	
	Ti37Nb6Sn	-	66	775	892	27	[188]
		-	72	793	885	25	
	Ti7.5Mo	-	70.6	570	740	9	[189]
	Ti15Mo	435 ± 35	-	-	894 ± 24	3 ± 2	[177]

2.3.3. Microstructural evolutions of β Ti alloys

During the LPBF, various processing parameters, like laser energy, scanning speed, hatch spacing, and powder bed thickness, can influence the solidification of alloys, which determines the specimens' mechanical performance. The solidification microstructures are mainly dependent on the factors, which involve temperature gradient (G), solidification speed (R) and undercooling rate.

The undercooling rate relies on the alloying system applied in the LPBF processing. Typically, we use the G (K/mm) and R (mm/s) to construct a solidification map, as shown in Fig.2.34a. G/R ratios are related to the solidification structure's morphology, while the G・R (cooling rate) decides the microstructure's scale. The size of planar, cellular, columnar dendritic or equiaxed dendritic is refined with the increase of G・R. Thus, the solidification map can be applied to predict the solidification structure of β Ti alloys after LPBF processing. The columnar to equiaxed transformation (CET) was frequently reported in Ti alloys after the LPBF processing, which happens when nucleation of adequately equiaxed dendrites occurs in the constitutionally undercooled liquid neighbouring to the front of columnar dendritic[190]. The solidification microstructures experience fast heating and cooling during LPBF, forming more refined structures than the conventional methods. As shown in Fig.2.34b of the solidification map of Ti6Al4V, the boundaries between equiaxed, columnar, and mixed structures can be divided depending on the G and R.

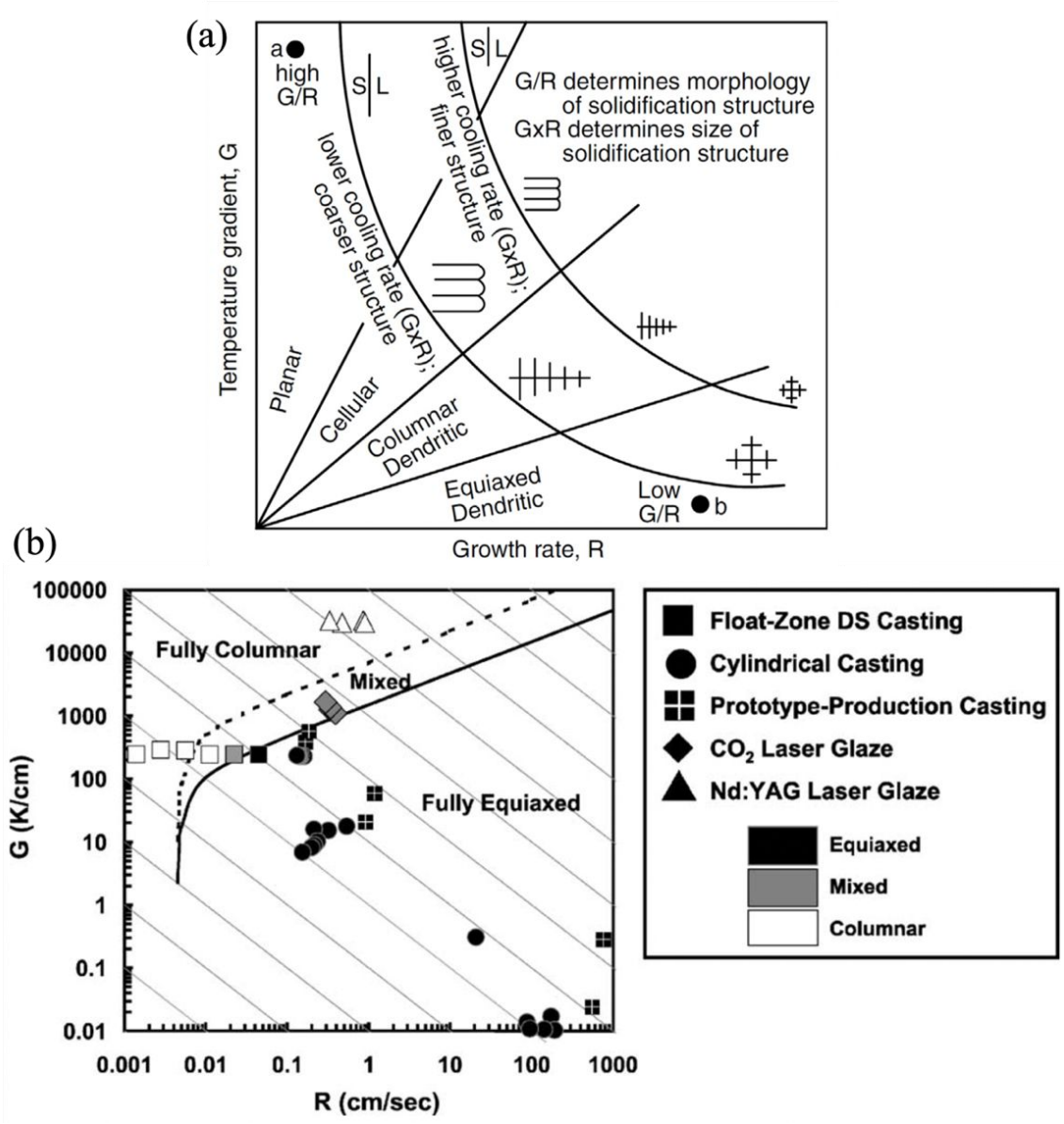


Fig. 2.34. (a) The influence of G and R on the morphology of solidification microstructure. (b) The solidification map of Ti6Al4V alloy. (Modified from [8,191])

The LPBF processing of Ti alloys also experiences the intrinsic fast cooling and super-high thermal gradient, which introduced the refined columnar grains with strong textures, thus, raising the mechanical anisotropy of the LPBF processed components. However, the features of LPBF processing suppress the region of constitutional super undercooling. Some research works have tried adding some solute elements with higher grain growth restriction factors to

expand the constitutional supercooling zone and refine the grains, as shown in Table.2.4. Zhang et al.[104] introduced Cu element to Ti powder base and successfully fabricated the β Ti-Cu alloys with super-refined equiaxed grains using the in-situ alloying based additive manufacturing. We can clearly distinguish the Ti6Al4V (Fig.2.35a) and Ti-8.5Cu (Fig.2.35b) alloys with columnar and equiaxed grains, respectively. As shown in Fig.2.35c, the addition of Cu has significantly enlarged the supercooling zone, which causes the essential grain refinements effects in the Ti-Cu systems after AM. In this way, some other works have investigated the Ti6Al4V-Cu and Ti-Ni systems processed by LPBF [192,193] and obtained refined equiaxed grain structures.

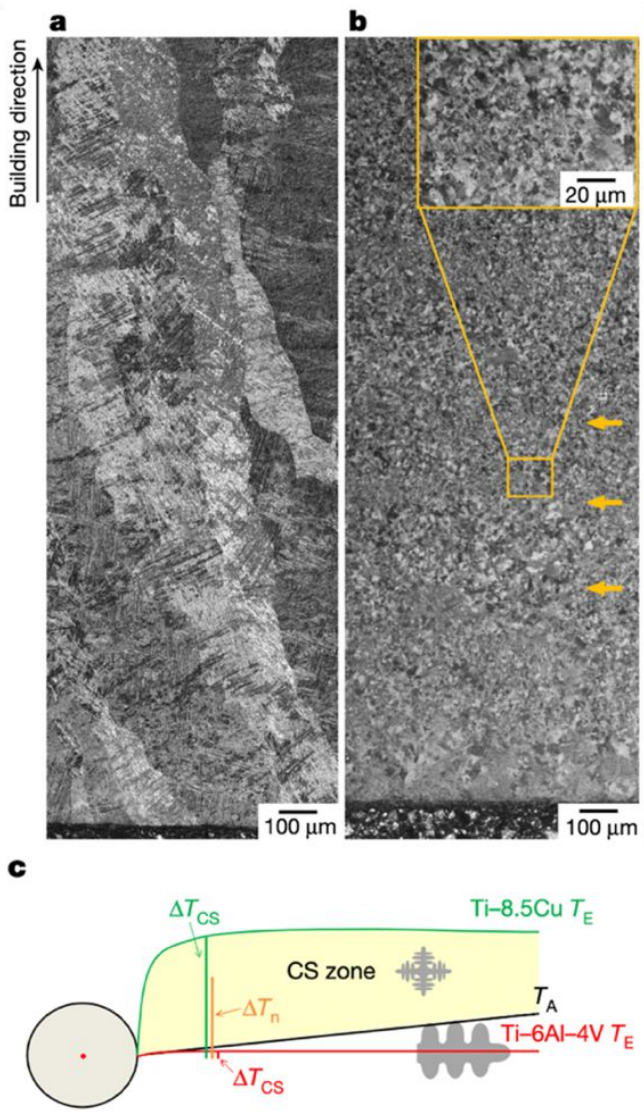


Fig. 2.35. The OM images show the grain structure of Ti6Al4V (a) and Ti-8.5Cu (b) alloys processed by LPBF, respectively. (c) The grain growth mechanisms of the above two alloys, where T_A and T_E are the profile of the melt temperature and equilibrium liquidus temperature, respectively. The value of ΔT_{CS} is equal to $T_E - T_A$, and ΔT_n is regarded as the magnitude of the length bar. (Modified from [104])

The precipitates of α, α', α", ω_{ath}, ω_{iso}, β', O' and O" phases can exhibit in β Ti alloys, depending on the β phases stability and thermal histories during the thermal-mechanical processing, as discussed in section 2.23. During the LPBF processing, each powder layer experienced multiple remelts and fast cooling, of which the rate ranges from 10^3-10^8 K/s [194,195]. According to the phase diagram (Fig. 2.18 and 2.23), various non-equilibrium phases can form accompanied by the equilibrium phases of β + α. Brodie et al. [170] found the Ti25Ta is mainly composed of α' phases in the equiaxed β grains after in-situ alloying based LPBF processing, while the α" phases are preferred after changing the scanning strategy from single melt to remelt, as presented in Fig.2.36. β + α' was previously revealed in the LPBF processed Ti5553 alloys[160,196] and Ti38644 [183], while Ti1023 was mainly composed of β + ω [150,158]. α" phase was also found dominantly existed in the various Ti-Nb based alloys prepared by LPBF[188,197].

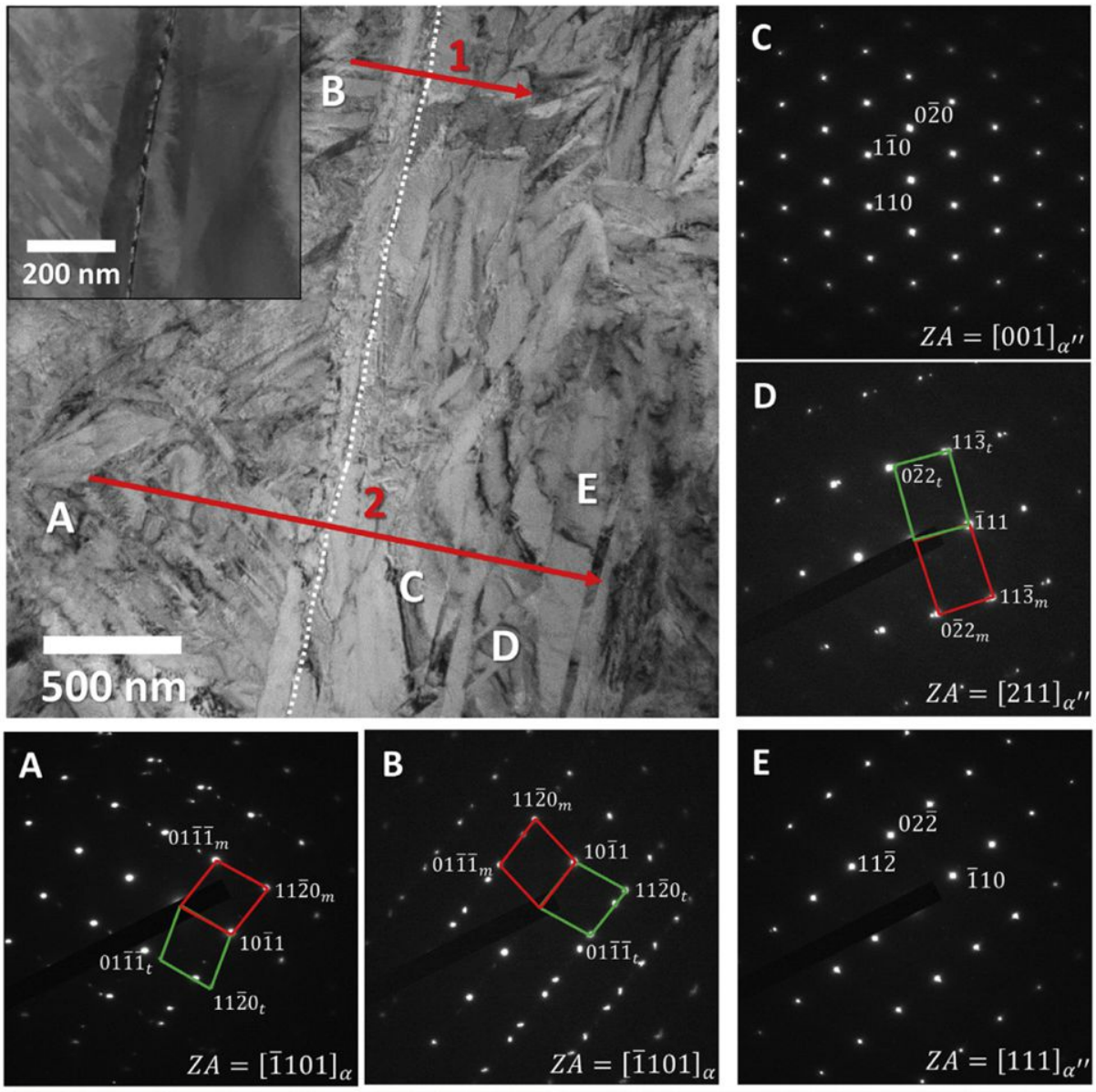


Fig. 2.36. Microstructures of Ti-25Ta alloys after laser remelt and the corresponding selected area diffraction (SAED) patterns from different regions (The SAED patterns of A, B, C, D, and E were acquired from the position A, B, C, D, and E, respectively). (Modified from [170])

2.3.4. Controlling elastic modulus of β Ti

Considering β Ti's application in biomaterials, except for the element toxicity, the stress shielding is another big challenge for hard-tissue implantations due to the modulus' mismatch. Basically, the chemical constitutions can strongly influence Young's modulus. Ozaki et al. [135]

have investigated Young's modulus of Ti-V and Ti-Nb binary systems, which were solution heat-treated and water quench. Young's modulus are varied with the increase of β stabilizers in Ti alloys. In Ti-V systems, the Ti-11V has obtained the lowest Young's modulus of 66 GPa (Fig.2.37a). In Ti-Nb systems, the Ti-42Nb possess the lowest Young's modulus of 62 GPa (Fig.2.37b).

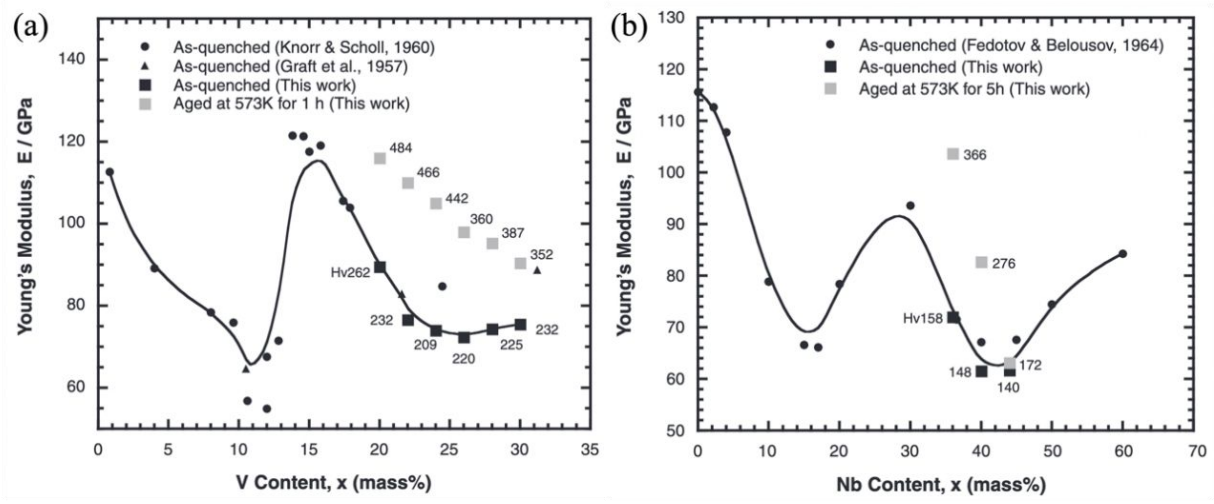


Fig. 2.37. The V and Nb contents' dependence of Young's modulus in Ti-V (a) and Ti-Nb (b) binary systems, respectively. (Modified from [135])

Currently, the elastic modulus of β Titanium is still higher than that of cortical bone (20-40GPa). Additive manufacturing technologies make it possible to further reduce the elastic modulus by controlling the grain orientation, phase constitutions and the design of complex porous structures.

(1) Texture Control

The elastic modulus of β Ti alloys is varied along the different crystallographic orientations. For example, the metastable β Ti-15Mo-5Zr-3Al alloy has the highest elastic modulus along the <111> orientation of 120GPa, while that along the <001> orientation is only 44.4GPa, which is much closer to the cortical bone's [198,199]. Therefore, the elastic modulus can be controlled by tailoring the textures of the components based on the specific requirements

of different implantations.

Previous research has proved that the grains' crystallographic orientations fabricated by LPBF can be tailored by changing processing parameters, scan strategies, chamber, or substrate preheating. Li et al. [200] found the crystallographic orientations of LPBF-processed Ti45Al2Cr5Nb was changed from strong <0001> to the integration of <0001>, <10$\bar{1}$1> and <11$\bar{2}$1> with the increasing of laser energy input. Ishimoto et al. [164] revealed the different crystallographic orientations between two as-fabricated Ti15Mo5Zr3Al samples processed using different scanning strategies (Fig.2.38). The apparent modulus' anisotropy can be obtained by the scan strategy X without scanning rotation. The lowest elastic modulus of 68.7GPa was obtained along the <001> orientation. Li et al. [201] also found that Ti45Al2Cr5Nb with the specific grain orientation can be obtained by applying the hot bed preheating during the LPBF.

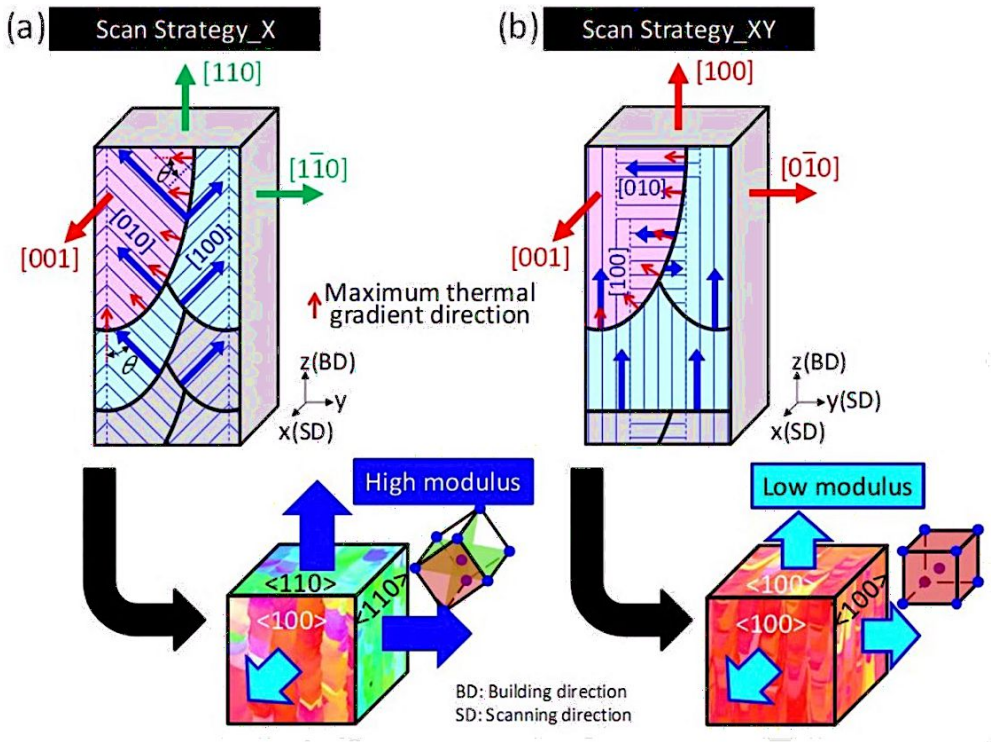


Fig. 2.38. The textures of as-SLMed Ti-15Mo-5Zr-3Al alloys are processed by different scan strategies: (a) scanning without rotation for each layer; (b) scanning with rotation for each layer. (Modified from [199]).

(2) Phases Control

The primary precipitates in metastable β Ti alloys are α, α', α'', and ω (isothermal and athermal) phases. Controlling the precipitates is typically performed by changing the β phase stabilizers or applying varied heat treatments [36]. The mechanical properties of these phases are in a sequence. The micro-hardness is $HV_{\omega} > HV_{\alpha'} > HV_{\alpha''} > HV_{\beta} > HV_{\alpha}$ and the elastic modulus is $E_{\omega} > E_{\alpha} > E_{\alpha'} > E_{\alpha''} > E_{\beta}$ [144,202]. The ω phase has 137.9 GPa modulus, as calculated using the Voigt-Reuss-Hill method, the highest elastic modulus from the phases present in metastable β-Ti alloys [203]. Although the existence of ω can strengthen β Ti alloys, it is brittle and has a high elastic modulus [144]. Hence, controlling the ω phase is critical for obtaining a low elastic modulus metastable β Ti alloy. Considering the complex thermal histories during the LPBF, more future works will be needed to understand the relationship between the processing parameters, phase constitutions and elastic modulus.

(3) Porous structure design

The natural bone is composed of the graded structure of outer cortical and inner trabecular bone with changeable stiffness and un-uniform porous structures, which allow the high strength, low modulus and inner bone tissue to regenerate [204]. Due to the increased flexibility of LPBF technology, it is possible to design the structures of complicated porous implants to fulfilling the need of the biomedical hard tissue. In order to use Ti alloys as the long-term bone replacement, the geometrical optimization of porous structures (Fig.2.39a) for LPBF processing has attracted researchers' interest [205]. Finally, the customized implantations combined with solid and porous structures (Fig.2.39b) can help avoid implant failure due to insufficient implant integration into the bone tissue environment by improving mechanical compatibility and osseointegration [206].

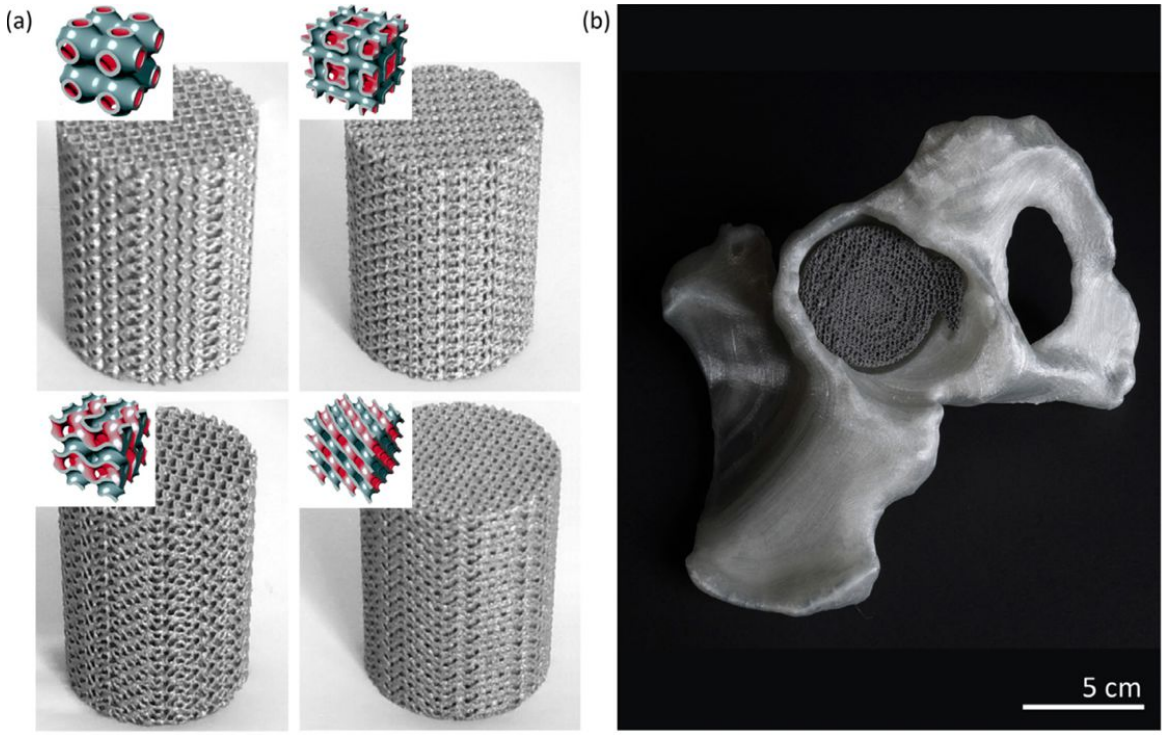


Fig. 2.39. (a) The LPBF processed porous Ti6Al4V alloys with varied triply periodic minimal surfaces design. (b) A Ti implant combined with solid and porous structures fabricated by LPBF. (Modified from [205–207])

2.3.5. Creating functional gradient structures by LPBF

Nature creates functional gradient structures to obtain a biological system with high strength and toughness to endure the complex natural environment [208]. These bioinspired gradient systems have proved their superiority to the conventional homogeneous structures [209]. Several methods have been developed to manufacture bioinspired gradient metallic structures, such as the surface mechanical attrition treatment [116], spark plasma sintering [210] and high-pressure torsion [211]. The gradient structures show an excellent combination of high strength and ductility. Recently, laser additive manufacturing has been used to process gradient structures. Different laser scanning parameters could introduce significantly different thermal histories during processing [212], which could be a potential method to produce bioinspired gradient structures by varying the processing parameters. Philipp *et al*. [213] have produced a

Damascus steel with a microstructure of alternating soft and hard layers by controlling the laser scanning pauses. This microstructure exhibits improved mechanical properties than ancient Damascus steel. Popovich *et al.*[214] used two lasers with 250 W and 950 W power to process the Inconel 718 specimens with functional gradient structures, including varied grains' morphologies and textures. Yang *et al*. [215] prepared three-dimensional functional gradient nickel (Ni)-Ti alloy by controlling the repetitive laser melting, which obtained the exceptional strain hardening capacity, as shown in Fig.2.40. However, the research works on creating the functional gradient β Ti alloys by LPBF is still scarce. The adjustable microstructure of grains, textures, and phases constitutions in β Ti alloys during LPBF processing provides great potential to create the advanced functional gradient β Ti alloys.

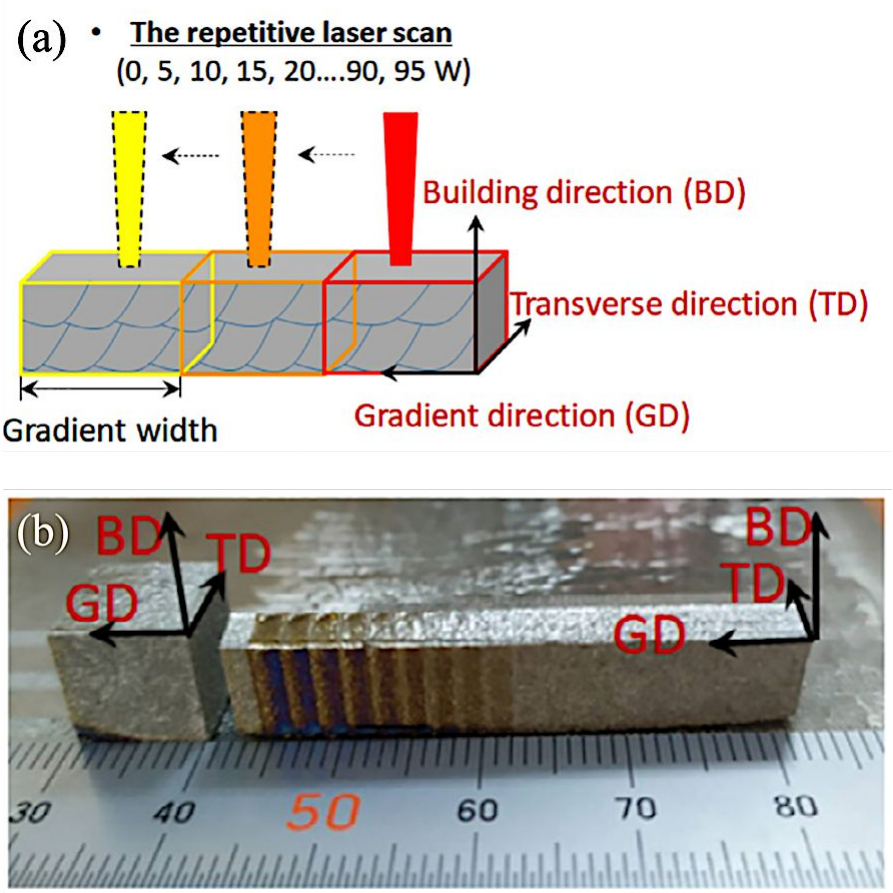


Fig. 2.40. (a) The schematic shows the repetitive laser scan process with varied laser energy. (b) The as-fabricated gradient NiTi specimens. (Modified from [215])

2.4. Summary of the Literature and Knowledge Gaps for Further Investigations.

The chapter has introduced the LPBF technology and summarized the physical aspects of laser and powder bed interaction. The possible defects and their eliminating methods were also presented for future parametrical studies in this work. Furthermore, we identified the difficulties and high costs of preparing β Ti components using the conventional melting or casting methods and raised the importance of developing LPBF technologies.

Additionally, the typical heat treatments, phase transformations, strengthening strategies, deformation mechanisms and new advancements of β Ti alloys were also introduced. However, the main findings were only derived from the β Ti alloys prepared by conventional methods. The solidification microstructures and phases in the β Ti alloys processed by LPBF were different and adjustable depending on varied laser scanning parameters and the complex thermal history. During the fabrication, the in-situ alloying based LPBF technology can even introduce more sophisticated physical reactions than LPBF using PA powders. The textures and phases are shown to be controllable during the LPBF processing of PA powders, while the microstructural evolutions of the specimens prepared by in-situ alloying based LPBF are still unclear. Moreover, whether the methods can be applied to build high-performance FGC materials is still scarcely reported.

Furthermore, the relative research findings and knowledge gaps will be addressed in this work can be concluded below:

- Previous works have verified the difficulties of eliminating all residual refractory particles in some β Ti alloys processed by in-situ alloying based LPBF. Whereas identifying the printability of Ti-Mo alloys that are chemically homogeneous and near fully dense is still needed. The underlying mechanisms for chemical homogenisations and densification are

also essential to other alloying systems processed using this method.

- The evolutions of the microstructures, especially the residual stress, grains structures and precipitations, of β Ti specimens are rare reported processed by in-situ alloying based LPBF using different laser energy input or scanning strategies.
- There are still limited studies on the precipitation strengthening mechanism of LPBFed β Ti alloys, which is known to induce the precipitation of various phases resulting from the complicated heating and cooling cycles.
- Low modulus β Ti components have been achieved after LPBF processing using PA powders through texture control or porous structure design. While most previous works have not dealt with the validation of β Ti's modulus control using in-situ alloying based LPBF. Moreover, it is unclear whether the low modulus of the printed alloy will maintain after heat treatments.
- Although the adjustable microstructures have been verified in β Ti alloys through controlling the laser processing parameters, the possibility to create β Ti materials with gradient composition and microstructure through in-situ alloying based LPBF has not been attempted.
- It can be perceived that the most efforts to improve the mechanical behaviour of β Ti alloys were paid to develop new chemical compositions, while rare research considers the influences of processing methods. Moreover, no previous study has systematically investigated the strengthening mechanisms and deformation sequence in β Ti alloys prepared by the in-situ alloying based LPBF.

2.5. References

[1] I. Gibson, D.W. Rosen, B. Stucker, Additive Manufacturing Technologies, (2010). https://doi.org/10.1007/978-1-4419-1120-9.

[2] J.O. Milewski, Additive Manufacturing of Metals, From Fundamental Technology to Rocket Nozzles, Medical Implants, and Custom Jewelry, 2017. https://doi.org/10.1007/978-3-319-58205-4.

[3] L. Yang, K. Hsu, B. Baughman, D. Godfrey, F. Medina, M. Menon, S. Wiener, Additive Manufacturing of Metals: The Technology, Materials, Design and Production, 2017. https://doi.org/10.1007/978-3-319-55128-9.

[4] T. Mukherjee, J.S. Zuback, A. De, T. DebRoy, Printability of alloys for additive manufacturing, Sci Rep-Uk. 6 (2016) 19717. https://doi.org/10.1038/srep19717.

[5] S.L. Sing, S. Huang, G.D. Goh, G.L. Goh, C.F. Tey, J.H.K. Tan, W.Y. Yeong, Emerging Metallic Systems for Additive Manufacturing: In-situ Alloying and Multi-metal Processing in Laser Powder Bed Fusion, Prog. Mater. Sci. (2021) 100795. https://doi.org/10.1016/j.pmatsci.2021.100795.

[6] A.M. Kiss, A.Y. Fong, N.P. Calta, V. Thampy, A.A. Martin, P.J. Depond, J. Wang, M.J. Matthews, R.T. Ott, C.J. Tassone, K.H. Stone, M.J. Kramer, A. van Buuren, M.F. Toney, J.N. Weker, Laser-Induced Keyhole Defect Dynamics during Metal Additive Manufacturing, Adv Eng Mater. 21 (2019) 1900455. https://doi.org/10.1002/adem.201900455.

[7] C.D. Boley, S.A. Khairallah, A.M. Rubenchik, Calculation of laser absorption by metal powders in additive manufacturing, Appl Optics. 54 (2015) 2477. https://doi.org/10.1364/ao.54.002477.

[8] T. DebRoy, H.L. Wei, J.S. Zuback, T. Mukherjee, J.W. Elmer, J.O. Milewski, A.M. Beese, A. Wilson-Heid, A. De, W. Zhang, Additive manufacturing of metallic components - Process, structure and properties, Prog. Mater. Sci. 92 (2018) 112–224. https://doi.org/10.1016/j.pmatsci.2017.10.001.

[9] G.G. Gladush, I. Smurov, Physics of Laser Materials Processing, Theory and Experiment, Springer, USA, 2011. https://doi.org/10.1007/978-3-642-19831-1.

[10] I. Gibson, D. Rosen, B. Stucker, M. Khorasani, Additive Manufacturing Technologies, Springer, Switzerland, 2021. https://doi.org/10.1007/978-3-030-56127-7.

[11] S.A. Khairallah, A.T. Anderson, A. Rubenchik, W.E. King, Laser powder-bed fusion additive manufacturing: Physics of complex melt flow and formation mechanisms of pores, spatter, and denudation zones, Acta Mater. 108 (2016) 36–45. https://doi.org/10.1016/j.actamat.2016.02.014.

[12] M.J. Matthews, G. Guss, S.A. Khairallah, A.M. Rubenchik, P.J. Depond, W.E. King, Denudation of metal powder layers in laser powder bed fusion processes, Acta Mater. 114 (2016) 33–42. https://doi.org/10.1016/j.actamat.2016.05.017.

[13] S.I. Anisimov, V.A. Khokhlov, Instabilities in Laser-matter Interaction, CRC, Boca Raton,FI, 1995.

[14] S.A. Khairallah, A. Anderson, A.M. Rubenchik, J. Florando, S. Wu, H. Lowdermilk, Simulation of the main physical processes in remote laser penetration with large laser spot size, Aip Adv. 5 (2015) 047120. https://doi.org/10.1063/1.4918284.

[15] T. Majumdar, N. Eisenstein, J.E. Frith, S.C. Cox, N. Birbilis, Additive Manufacturing of Titanium Alloys for Orthopedic Applications: A Materials Science Viewpoint, Adv Eng Mater. 65 (2018) 1800172–28. https://doi.org/10.1002/adem.201800172.

[16] C.L. Druzgalski, A. Ashby, G. Guss, W.E. King, T.T. Roehling, M.J. Matthews, Process optimization of complex geometries using feed forward control for laser powder bed fusion additive manufacturing, Addit Manuf. 34 (2020) 101169. https://doi.org/10.1016/j.addma.2020.101169.

[17] A.M. Khorasani, I. Gibson, U.S. Awan, A. Ghaderi, The Effect of SLM Process Parameters on Density, Hardness, Tensile Strength and Surface Quality of Ti-6Al-4V, Addit Manuf. 25 (2018) 176–186. https://doi.org/10.1016/j.addma.2018.09.002.

[18] L. Thijs, F. Verhaeghe, T. Craeghs, J.V. Humbeeck, J.-P. Kruth, A study of the microstructural evolution during selective laser melting of Ti–6Al–4V, Acta Mater. 58 (2010) 3303–3312. https://doi.org/10.1016/j.actamat.2010.02.004.

[19] N.T. Aboulkhair, N.M. Everitt, I. Ashcroft, C. Tuck, Reducing porosity in AlSi10Mg parts processed by selective laser melting, Addit Manuf. 1 (2014) 77–86. https://doi.org/10.1016/j.addma.2014.08.001.

[20] N.H. Paulson, B. Gould, S.J. Wolff, M. Stan, A. Greco, Correlations between thermal history and keyhole porosity in laser powder bed fusion, Addit Manuf. 34 (2020) 101213. https://doi.org/10.1016/j.addma.2020.101213.

[21] R. Cunningham, S.P. Narra, T. Ozturk, J. Beuth, A.D. Rollett, Evaluating the Effect of Processing Parameters on Porosity in Electron Beam Melted Ti-6Al-4V via Synchrotron X-ray Microtomography, Jom-Us. 68 (2016) 765–771. https://doi.org/10.1007/s11837-015-1802-0.

[22] L. Bian, N. Shamsaei, J.M. Usher, Laser-Based Additive Manufacturing of Metal Parts: Modeling, Optimization, and Control of Mechanical Properties, CRC, Boca Raton, 2018.

[23] M.C. Brennan, J.S. Keist, T.A. Palmer, Defects in Metal Additive Manufacturing Processes, J Mater Eng Perform. 30 (2021) 4808–4818. https://doi.org/10.1007/s11665-021-05919-6.

[24] R. Cunningham, C. Zhao, N. Parab, C. Kantzos, J. Pauza, K. Fezzaa, T. Sun, A.D. Rollett, Keyhole threshold and morphology in laser melting revealed by ultrahigh-speed x-ray imaging, Science. 363 (2019) 849–852. https://doi.org/10.1126/science.aav4687.

[25] C. Zhao, Q. Guo, X. Li, N. Parab, K. Fezzaa, W. Tan, L. Chen, T. Sun, Bulk-Explosion-Induced Metal Spattering During Laser Processing, Phys Rev X. 9 (2019) 21052. https://doi.org/10.1103/physrevx.9.021052.

[26] K. Hirano, R. Fabbro, M. Muller, Experimental determination of temperature threshold for melt surface deformation during laser interaction on iron at atmospheric pressure, J. Phys. D: Appl. Phys. 44 (2011) 435402. https://doi.org/10.1088/0022-3727/44/43/435402.

[27] J. Mazumder, H. Ki, P.S. Mohanty, Role of recoil pressure, multiple reflections, and free surface evolution during laser keyhole welding, Int Congr Appl Lasers Electro-Optics. (2002) 881291. https://doi.org/10.2351/1.5065773.

[28] C. Zhao, N.D. Parab, X. Li, K. Fezzaa, W. Tan, A.D. Rollett, T. Sun, Critical instability at moving keyhole tip generates porosity in laser melting, Science. 370 (2020) 1080–1086. https://doi.org/10.1126/science.abd1587.

[29] S. Kou, Weld Metal Solidification II: Microstructure within Grains, in: Second, John Wiley & Sons, 2003.

[30] M.H. Mosallanejad, B. Niroumand, A. Aversa, A. Saboori, In-Situ Alloying in Laser-Based Additive Manufacturing Processes: A Critical Review, J. Alloys Compd. 872 (2021) 159567. https://doi.org/10.1016/j.jallcom.2021.159567.

[31] P. Gao, W. Huang, H. Yang, G. Jing, Q. Liu, G. Wang, Z. Wang, X. Zeng, Cracking behavior and control of β-solidifying Ti-40Al-9V-0.5Y alloy produced by selective laser melting, J Mater Sci Technol. 39 (2020) 144–154. https://doi.org/10.1016/j.jmst.2019.08.026.

[32] Y.T. Tang, C. Panwisawas, J.N. Ghoussoub, Y. Gong, J. Clark, A. Németh, D.G. McCartney, R.C. Reed, Alloys-By-Design: Application to New Superalloys for Additive Manufacturing, Acta Mater. 202 (2020) 417–436. https://doi.org/10.1016/j.actamat.2020.09.023.

[33] C.J. Marvel, J.C. Sabol, T. Pasang, M. Watanabe, W.Z. Misiolek, Improving the Mechanical Properties of the Fusion Zone in Electron-Beam Welded Ti-5Al-5Mo-5V-3Cr Alloys, Metallurgical Mater Transactions. 48A (2017) 1921–1930. https://doi.org/10.1007/s11661-017-3968-2.

[34] J.H. Martin, B.D. Yahata, J.M. Hundley, J.A. Mayer, T.A. Schaedler, T.M. Pollock, 3D printing of high-strength aluminium alloys, Nature. 549 (2017) 365–369. https://doi.org/10.1038/nature23894.

[35] D. Banerjee, J.C. Williams, Perspectives on Titanium Science and Technology, Acta Mater. 61 (2013) 844–879. https://doi.org/10.1016/j.actamat.2012.10.043.

[36] R.P. Kolli, A. Devaraj, A Review of Metastable Beta Titanium Alloys, Metals-Basel. 8 (2018) 506. https://doi.org/10.3390/met8070506.

[37] G. Lütjering, J.C. Williams, Titanium, Springer, USA, 2007.

[38] C. Leyens, M. Peters, Titanium and Titanium Alloys, WILEY-VCH, Germany, 2019. https://doi.org/10.1002/3527602119.

[39] F.H. Froes, Titanium: Physical Metallurgy, Processing, and Applications, ASM International, USA, 2015.

[40] P.J. Bania, Beta titanium alloys and their role in the titanium industry, Jom-Us. 46 (1994) 16–19. https://doi.org/10.1007/bf03220742.

[41] J.D. Cotton, R.D. Briggs, R.R. Boyer, S. Tamirisakandala, P. Russo, N. Shchetnikov, J.C. Fanning, State of the Art in Beta Titanium Alloys for Airframe Applications, Jom-Us. 67 (2015) 1281–1303. https://doi.org/10.1007/s11837-015-1442-4.

[42] D. Kuroda, M. Niinomi, M. Morinaga, Y. Kato, T. Yashiro, Design and mechanical properties of new β type titanium alloys for implant materials, Mater. Sci. Eng., A. 243 (1998) 244–249. https://doi.org/10.1016/s0921-5093(97)00808-3.

[43] L. Zhang, L. Chen, A Review on Biomedical Titanium Alloys: Recent Progress and Prospect, Adv Eng Mater. 21 (2019) 1801215. https://doi.org/10.1002/adem.201801215.

[44] M. Niinomi, Recent titanium R&D for biomedical applications in japan, Jom-Us. 51 (1999) 32–34. https://doi.org/10.1007/s11837-999-0091-x.

[45] S.G. Steinemann, Metal implants and surface reactions, Inj. 27 (1996) S/C16-S/C22. https://doi.org/10.1016/0020-1383(96)89027-9.

[46] J.B. Park, R. Lakes, Metallic Implant Materials, Biomaterials. (2007) 99–137. https://doi.org/10.1007/978-0-387-37880-0_5.

[47] S. Kumar, T.S.N.S. Narayanan, Corrosion behaviour of Ti–15Mo alloy for dental implant applications, J Dent. 36 (2008) 500–507. https://doi.org/10.1016/j.jdent.2008.03.007.

[48] G. Welsch, R. Boyer, E.W. Collings, Materials Properties Handbook, ASM International, 1993.

[49] K.S. JEPSON, A.R.G. BROWN, J.A. GRAY, The Science, Technology and Application of Titanium, Sect Vi Phase Transformations Heat Treat Part Aphase Transformations Part Phase Transformations. (1970) 677–690. https://doi.org/10.1016/b978-0-08-006564-9.50074-9.

[50] W. Sprengel, T. Yamada, H. Nakajima, Interdiffusion in Binary β-Titanium Alloys, Defect Diffusion Forum. 143–147 (1997) 431–436. https://doi.org/10.4028/www.scientific.net/ddf.143-147.431.

[51] M. Qian, F. H.(Sam)Froes, Titanium Powder Metallurgy: Science, Technology and Applications, Elsevier, USA, 2015.

[52] V. Moiseyev, Titanium Alloys Russian Aircraft and Aerospace Applications, CRC, Boca Raton, 2006. https://doi.org/10.1201/9781420037678.ch6.

[53] F.H. Froes, H.B. Bomberger, The Beta Titanium Alloys, Jom-Us. 37 (1985) 28–37. https://doi.org/10.1007/bf03259693.

[54] J. Zhang, C.C. Tasan, M.J. Lai, A.-C. Dippel, D. Raabe, Complexion-mediated martensitic phase transformation in Titanium, Nat Commun. 8 (2017) 14210. https://doi.org/10.1038/ncomms14210.

[55] R.I. Jaffee, N.E. Promisel, I. of Metals, M.S. of AIME, A.S. for Metals, The science, technology, and application of titanium, Pergamon, 1970.

[56] R.I. Jaffee, The physical metallurgy of titanium alloys, Prog Met Phys. 7 (1958) 65–163. https://doi.org/10.1016/0502-8205(58)90004-2.

[57] R. Boyer, G. Welsch, E.W. Collings, Materials Properties Handbook: Titanium Alloys, ASM International, USA, 1994.

[58] S.Banerjee, P.Mukhopadhyay, Phase Transformations - Examples from Titanium and Zirconium Alloys, Elsevier, USA, 2007. https://doi.org/10.1016/s1470-1804(07)x8038-6.

[59] S. Balachandran, A. Kashiwar, A. Choudhury, D. Banerjee, R. Shi, Y. Wang, On variant distribution and coarsening behavior of the α phase in a metastable β titanium alloy, Acta Mater. 106 (2016) 374–387. https://doi.org/10.1016/j.actamat.2016.01.023.

[60] Y.W. Chai, H.Y. Kim, H. Hosoda, S. Miyazaki, Self-accommodation in Ti–Nb shape memory alloys, Acta Mater. 57 (2009) 4054–4064. https://doi.org/10.1016/j.actamat.2009.04.051.

[61] S. Nag, R. Banerjee, R. Srinivasan, J.Y. Hwang, M. Harper, H.L. Fraser, ω-Assisted nucleation and growth of α precipitates in the Ti–5Al–5Mo–5V–3Cr–0.5Fe β titanium alloy, Acta Mater. 57 (2009) 2136–2147. https://doi.org/10.1016/j.actamat.2009.01.007.

[62] S. Nag, Y. Zheng, R.E.A. Williams, A. Devaraj, A. Boyne, Y. Wang, P.C. Collins, G.B. Viswanathan, J.S. Tiley, B.C. Muddle, R. Banerjee, H.L. Fraser, Non-classical homogeneous precipitation mediated by compositional fluctuations in titanium alloys, Acta Mater. 60 (2012) 6247–6256. https://doi.org/10.1016/j.actamat.2012.07.033.

[63] S.M.C. van Bohemen, A. Kamp, R.H. Petrov, L.A.I. Kestens, J. Sietsma, Nucleation and variant selection of secondary α plates in a β Ti alloy, Acta Mater. 56 (2008) 5907–5914. https://doi.org/10.1016/j.actamat.2008.08.016.

[64] T. Li, D. Kent, G. Sha, L.T. Stephenson, A.V. Ceguerra, S.P. Ringer, M.S. Dargusch, J.M. Cairney, New insights into the phase transformations to isothermal ω and ω-assisted α in near β-Ti alloys, Acta Mater. 106 (2016) 353–366. https://doi.org/10.1016/j.actamat.2015.12.046.

[65] T. Li, D. Kent, G. Sha, H. Liu, S.G. Fries, A.V. Ceguerra, M.S. Dargusch, J.M. Cairney, Nucleation driving force for ω-assisted formation of α and associated ω morphology in β-Ti alloys, Scripta Mater. 155 (2018) 149–154. https://doi.org/10.1016/j.scriptamat.2018.06.039.

[66] T. Li, D. Kent, G. Sha, J.M. Cairney, M.S. Dargusch, The role of ω in the precipitation of α in near-β Ti alloys, Scripta Mater. 117 (2016) 92–95. https://doi.org/10.1016/j.scriptamat.2016.02.026.

[67] R. Shi, Y. Zheng, R. Banerjee, H.L. Fraser, Y. Wang, ω-Assisted α nucleation in a metastable β titanium alloy, Scripta Mater. 171 (2019) 1–5. https://doi.org/10.1016/j.scriptamat.2019.06.020.

[68] Y. Zheng, D. Choudhuri, T. Alam, R.E.A. Williams, R. Banerjee, H.L. Fraser, The role of cuboidal ω precipitates on α precipitation in a Ti-20V alloy, Scripta Mater. 123 (2016) 81–85. https://doi.org/10.1016/j.scriptamat.2016.06.004.

[69] T. Sakamoto, K. Nakai, M. Maeda, S. Kobayashi, Variation of Hardness with Microstructure Evolutions in Metastable β Titanium Alloy TIMETAL®LCB, Materials Science Forum. 561–565 (2007) 2067–2070. https://doi.org/10.4028/www.scientific.net/msf.561-565.2067.

[70] Y. Zheng, R.E.A. Williams, J.M. Sosa, T. Alam, Y. Wang, R. Banerjee, H.L. Fraser, The indirect influence of the ω phase on the degree of refinement of distributions of the α phase in metastable β-Titanium alloys, Acta Mater. 103 (2016) 165–173. https://doi.org/10.1016/j.actamat.2015.09.053.

[71] F. Langmayr, P. Fratzl, G. Vogl, W. Miekeley, Crossover from ω-phase to α-phase precipitation in bcc Ti-Mo, Phys Rev B. 49 (1994) 11759–11766. https://doi.org/10.1103/physrevb.49.11759.

[72] A. Devaraj, S. Nag, R. Srinivasan, R.E.A. Williams, S. Banerjee, R. Banerjee, H.L. Fraser, Experimental evidence of concurrent compositional and structural instabilities leading to ω precipitation in titanium–molybdenum alloys, Acta Mater. 60 (2012) 596–609. https://doi.org/10.1016/j.actamat.2011.10.008.

[73] F.H. Froes, C.F. Yolton, J.M. Capenos, M.G.H. Wells, J.C. Williams, The relationship between microstructure and age hardening response in the metastable beta titanium alloy Ti-11.5 Mo-6 Zr-4.5 Sn (beta III), Metallurgical Transactions. 11 (1980) 21–31. https://doi.org/10.1007/bf02700435.

[74] X. Ma, Z. Chen, D. Zhong, S.N. Luo, L. Xiao, W. Lu, S. Zhang, Effect of rotationally accelerated shot peening on the microstructure and mechanical behavior of a metastable β titanium alloy, J Mater Sci Technol. 75 (2021) 27–38. https://doi.org/10.1016/j.jmst.2020.10.034.

[75] W. Chen, K. Li, G. Yu, J. Ren, Y. Zha, J. Sun, Deformation twinning-induced single-variant ω-plates in metastable β-Ti alloys containing athermal ω-precipitates, J Mater Sci. 56 (2021) 7710–7726. https://doi.org/10.1007/s10853-020-05706-z.

[76] Y. Yang, P. Castany, E. Bertrand, M. Cornen, J.X. Lin, T. Gloriant, Stress release-induced interfacial twin boundary ω phase formation in a β type Ti-based single crystal

displaying stress-induced α" martensitic transformation, Acta Mater. 149 (2018) 97–107. https://doi.org/10.1016/j.actamat.2018.02.036.

[77] Q. Li, M. Niinomi, J. Hieda, M. Nakai, K. Cho, Deformation-induced ω phase in modified Ti–29Nb–13Ta–4.6Zr alloy by Cr addition, Acta Biomater. 9 (2013) 8027–8035. https://doi.org/10.1016/j.actbio.2013.04.032.

[78] H. Liu, M. Niinomi, M. Nakai, K. Cho, Athermal and deformation-induced ω-phase transformations in biomedical beta-type alloy Ti–9Cr–0.2O, Acta Mater. 106 (2016) 162–170. https://doi.org/10.1016/j.actamat.2016.01.008.

[79] R. Davis, H.M. Flower, D.R.F. West, The decomposition of Ti-Mo alloy martensites by nucleation and growth and spinodal mechanisms, Acta Metall. 27 (1979) 1041–1052. https://doi.org/10.1016/0001-6160(79)90192-5.

[80] R. Davis, H.M. Flower, D.R.F. West, Martensitic transformations in Ti-Mo alloys, J. Mater. Sci. 14 (1979) 712–722. https://doi.org/10.1007/bf00772735.

[81] Y. Danard, F. Sun, T. Gloriant, I.F.V. Thüngen, M. Piellard, F. Prima, The Influence of Twinning on the Strain–Hardenability in TRIP/TWIP Titanium Alloys: Role of Solute–Solution Strengthening, Frontiers Mater. 7 (2020) 240. https://doi.org/10.3389/fmats.2020.00240.

[82] M. Bönisch, A. Panigrahi, M. Stoica, M. Calin, E. Ahrens, M. Zehetbauer, W. Skrotzki, J. Eckert, Giant thermal expansion and α-precipitation pathways in Ti-alloys, Nat. Commun. 8 (2017) 1429. https://doi.org/10.1038/s41467-017-01578-1.

[83] L. Qi, S. He, C. Chen, B. Jiang, Y. Hao, H. Ye, R. Yang, K. Du, Diffusional-displacive transformation in a metastable β titanium alloy and its strengthening effect, Acta Mater. 195 (2020) 151–162. https://doi.org/10.1016/j.actamat.2020.05.058.

[84] J.M. Bennett, E.J. Pickering, J.S. Barnard, D. Rugg, H.J. Stone, N.G. Jones, Observation of a new B2 structured phase in Ti-15Mo (wt%), Mater Charact. 142 (2018) 523–530. https://doi.org/10.1016/j.matchar.2018.06.017.

[85] M. Bönisch, M. Stoica, M. Calin, Routes to control diffusive pathways and thermal expansion in Ti-alloys, Scientific Reports. 10 (2020) 3045. https://doi.org/10.1038/s41598-020-60038-x.

[86] R. Santhosh, M. Geetha, M.N. Rao, Recent Developments in Heat Treatment of Beta Titanium Alloys for Aerospace Applications, T Indian I Metals. 70 (2017) 1681–1688. https://doi.org/10.1007/s12666-016-0985-6.

[87] Q. Liang, D. Wang, Y. Zheng, S. Zhao, Y. Gao, Y. Hao, R. Yang, D. Banerjee, H.L. Fraser, Y. Wang, Shuffle-nanodomain regulated strain glass transition in Ti-24Nb-4Zr-8Sn alloy, Acta Mater. 186 (2020) 415–424. https://doi.org/10.1016/j.actamat.2019.12.056.

[88] Y. Chong, M. Poschmann, R. Zhang, S. Zhao, M.S. Hooshmand, E. Rothchild, D.L. Olmsted, J.W. Morris, D.C. Chrzan, M. Asta, A.M. Minor, Mechanistic basis of oxygen sensitivity in titanium, Sci Adv. 6 (2020) eabc4060. https://doi.org/10.1126/sciadv.abc4060.

[89] X. ji, S. Emura, T. Liu, K. Suzuta, X. Min, K. Tsuchiya, Effect of oxygen addition on microstructures and mechanical properties of Ti-7.5Mo alloy, J Alloy Compd. 737 (2018) 221–229. https://doi.org/10.1016/j.jallcom.2017.12.072.

[90] Y. Zheng, D. Banerjee, H.L. Fraser, A nano-scale instability in the β phase of dilute Ti–Mo alloys, Scripta Mater. 116 (2016) 131–134. https://doi.org/10.1016/j.scriptamat.2016.01.044.

[91] Y. Zheng, D. Wang, R. Banerjee, D. Banerjee, Y. Wang, H.L. Fraser, Exploration of Nano-scale Structural Instabilities in Metastable β Titanium Alloys Using Advanced Electron Microscopy, Matec Web Conf. 321 (2020) 12001. https://doi.org/10.1051/matecconf/202032112001.

[92] Y. Zheng, S. Antonov, H. Fraser, Exploration of Novel Ordering Mechanism in Titanium Alloys Using Atom Probe Tomography and Aberration-corrected Scanning Transmission Electron Microscopy, Microsc Microanal. 26 (2020) 2078–2079. https://doi.org/10.1017/s143192762002036x.

[93] Y. Zheng, D. Huber, H.L. Fraser, Investigation of a nano-scale, incommensurate, modulated domain in a Ti-Fe alloy, Scripta Mater. 154 (2018) 220–224. https://doi.org/10.1016/j.scriptamat.2018.06.010.

[94] Q. Liang, Y. Zheng, D. Wang, Y. Hao, R. Yang, Y. Wang, H.L. Fraser, Nano-scale structural non-uniformities in gum like Ti-24Nb-4Zr-8Sn metastable β-Ti alloy, Scripta Mater. 158 (2019) 95–99. https://doi.org/10.1016/j.scriptamat.2018.08.043.

[95] Y. Zheng, R.E.A. Williams, S. Nag, R. Banerjee, H.L. Fraser, D. Banerjee, The effect of alloy composition on instabilities in the β phase of titanium alloys, Scripta Mater. 116 (2016) 49–52. https://doi.org/10.1016/j.scriptamat.2016.01.024.

[96] G.-H. Zhao, X. Xu, D. Dye, P.E.J. Rivera-Díaz-del-Castillo, Microstructural evolution and strain-hardening in TWIP Ti alloys, Acta Mater. 183 (2019) 155–164. https://doi.org/10.1016/j.actamat.2019.11.009.

[97] L.A. Gypen, A. Deruyttere, Multi-component solid solution hardening, J Mater Sci. 12 (1977) 1034–1038. https://doi.org/10.1007/bf00540988.

[98] I. Toda-Caraballo, P.E.J. Rivera-Díaz-del-Castillo, Modelling solid solution hardening in high entropy alloys, Acta Mater. 85 (2015) 14–23. https://doi.org/10.1016/j.actamat.2014.11.014.

[99] G.H. Zhao, X.Z. Liang, B. Kim, P.E.J. Rivera-Díaz-del-Castillo, Modelling strengthening mechanisms in beta-type Ti alloys, Mater. Sci. Eng., A. 756 (2019) 156–160. https://doi.org/10.1016/j.msea.2019.04.027.

[100] V.A. Lubarda, On the effective lattice parameter of binary alloys, Mech Mater. 35 (2003) 53–68. https://doi.org/10.1016/s0167-6636(02)00196-5.

[101] T. Chookajorn, H.A. Murdoch, C.A. Schuh, Design of Stable Nanocrystalline Alloys, Science. 337 (2012) 951–954. https://doi.org/10.1126/science.1224737.

[102] C.A. Schuh, K. Lu, Stability of nanocrystalline metals: The role of grain-boundary chemistry and structure, Mrs Bull. 46 (2021) 225–235. https://doi.org/10.1557/s43577-021-00055-x.

[103] D.H. StJohn, M. Qian, M.A. Easton, P. Cao, The Interdependence Theory: The relationship between grain formation and nucleant selection, Acta Mater. 59 (2011) 4907–4921. https://doi.org/10.1016/j.actamat.2011.04.035.

[104] D. Zhang, D. Qiu, M.A. Gibson, Y. Zheng, H.L. Fraser, D.H. StJohn, M.A. Easton, Additive manufacturing of ultrafine-grained high-strength titanium alloys, Nature. 576 (2019) 91–95. https://doi.org/10.1038/s41586-019-1783-1.

[105] D. Zhang, A. Prasad, M.J. Bermingham, C.J. Todaro, M.J. Benoit, M.N. Patel, D. Qiu, D.H. StJohn, M. Qian, M.A. Easton, Grain Refinement of Alloys in Fusion-Based Additive Manufacturing Processes, Metallurgical Mater Transactions. (2020) 1–19. https://doi.org/10.1007/s11661-020-05880-4.

[106] M.J. Bermingham, S.D. McDonald, D.H. StJohn, M.S. Dargusch, Beryllium as a grain refiner in titanium alloys, J Alloy Compd. 481 (2009) L20–L23. https://doi.org/10.1016/j.jallcom.2009.03.016.

[107] M.J. Bermingham, S.D. McDonald, K. Nogita, D.H.St. John, M.S. Dargusch, Effects of boron on microstructure in cast titanium alloys, Scripta Mater. 59 (2008) 538–541. https://doi.org/10.1016/j.scriptamat.2008.05.002.

[108] H. Dong, X.Y. Li, T. Bell, Hardening response and tempering behaviour of electron beam surface melted Ti–8.5Si alloy, J Alloy Compd. 283 (1999) 231–240. https://doi.org/10.1016/s0925-8388(98)00903-7.

[109] C.B. Lan, Y. Wu, L.L. Guo, F. Chen, Effects of cold rolling on microstructure, texture evolution and mechanical properties of Ti-32.5Nb-6.8Zr-2.7Sn-0.30 alloy for biomedical applications, Mater Sci Eng. 690 (2017) 170–176. https://doi.org/10.1016/j.msea.2017.02.045.

[110] J. Song, L. WANG, X. ZHANG, X. SUN, H. Jiang, Z. FAN, C. XIE, M.H. Wu, Effects of second phases on mechanical properties and martensitic transformations of ECAPed TiNi and Ti–Mo based shape memory alloys, T Nonferr Metal Soc. 22 (2012) 1839–1848. https://doi.org/10.1016/s1003-6326(11)61395-2.

[111] K. Vaclavova, J. Strasky, P. Zhanal, J. Vesely, V. Polyakova, I. Semenova, M. Janeček, Ultra-fine grained microstructure of metastable beta Ti-15Mo alloy and its effects on the

phase transformations, Iop Conf Ser Mater Sci Eng. 194 (2017) 012021. https://doi.org/10.1088/1757-899x/194/1/012021.

[112] R. Huang, Y. Han, The effect of SMAT-induced grain refinement and dislocations on the corrosion behavior of Ti–25Nb–3Mo–3Zr–2Sn alloy, Materials Science and Engineering: C. 33 (2013) 2353–2359. https://doi.org/10.1016/j.msec.2013.01.068.

[113] Y.F. Xu, D.Q. Yi, H.Q. Liu, X.Y. Wu, B. Wang, F.L. Yang, Effects of cold deformation on microstructure, texture evolution and mechanical properties of Ti–Nb–Ta–Zr–Fe alloy for biomedical applications, Mater Sci Eng. 547 (2012) 64–71. https://doi.org/10.1016/j.msea.2012.03.081.

[114] A. Panigrahi, B. Sulkowski, T. Waitz, K. Ozaltin, W. Chrominski, A. Pukenas, J. Horky, M. Lewandowska, W. Skrotzki, M. Zehetbauer, Mechanical properties, structural and texture evolution of biocompatible Ti-45Nb alloy processed by severe plastic deformation, J Mech Behav Biomed. 62 (2016) 93–105. https://doi.org/10.1016/j.jmbbm.2016.04.042.

[115] X. Yan, S. Yin, C. Chen, R. Jenkins, R. Lupoi, R. Bolot, W. Ma, M. Kuang, H. Liao, J. Lu, M. Liu, Fatigue strength improvement of selective laser melted Ti6Al4V using ultrasonic surface mechanical attrition, Mater Res Lett. 7 (2019) 327–333. https://doi.org/10.1080/21663831.2019.1609110.

[116] X. Wu, P. Jiang, L. Chen, F. Yuan, Y.T. Zhu, Extraordinary strain hardening by gradient structure, P. Natl. Acad. Sci. USA. 111 (2014) 7197–7201. https://doi.org/10.1073/pnas.1324069111.

[117] S. Nag, R. Banerjee, J. Stechschulte, H.L. Fraser, Comparison of microstructural evolution in Ti-Mo-Zr-Fe and Ti-15Mo biocompatible alloys, J. Mater. Sci.: Mater. Med. 16 (2005) 679–685. https://doi.org/10.1007/s10856-005-2540-6.

[118] H. Azizi, H. Zurob, B. Bose, S.R. Ghiaasiaan, X. Wang, S. Coulson, V. Duz, A.B. Phillion, Additive manufacturing of a novel Ti-Al-V-Fe alloy using selective laser melting, Addit. Manuf. 21 (2018) 529–535. https://doi.org/10.1016/j.addma.2018.04.006.

[119] W. Chen, S. Cao, W. Kou, J. Zhang, Y. Wang, Y. Zha, Y. Pan, Q. Hu, Q. Sun, J. Sun, Origin of the ductile-to-brittle transition of metastable β-titanium alloys: Self-hardening of ω-precipitates, Acta Mater. 170 (2019) 187–204. https://doi.org/10.1016/j.actamat.2019.03.034.

[120] M.J. Lai, T. Li, F.K. Yan, J.S. Li, D. Raabe, Revisiting ω phase embrittlement in metastable β titanium alloys: Role of elemental partitioning, Scr. Mater. 193 (2021) 38–42. https://doi.org/10.1016/j.scriptamat.2020.10.031.

[121] A. Srivastava, S. Manandhar, V. Moxson, V.A. Duz, C. Lavender, A. Devaraj, V.V. Joshi, A low-cost hierarchical nanostructured beta-titanium alloy with high strength, Nat. Commun. 6 (2016) 1–8. https://doi.org/10.1038/ncomms11176.

[122] W. Zhu, J. Lei, C. Tan, Q. Sun, W. Chen, L. Xiao, J. Sun, A novel high-strength β-Ti alloy with hierarchical distribution of α-phase: The superior combination of strength and ductility, Mater. Design. 168 (2019) 107640. https://doi.org/10.1016/j.matdes.2019.107640.

[123] X. Bao, W. Chen, J. Zhang, Y. Yue, J. Sun, Achieving high strength-ductility synergy in a hierarchical structured metastable β-titanium alloy using through-transus forging, J Mater Res Technology. 11 (2021) 1622–1636. https://doi.org/10.1016/j.jmrt.2021.02.012.

[124] Y. Zheng, R.E.A. Williams, D. Wang, R. Shi, S. Nag, P. Kami, J.M. Sosa, R. Banerjee, Y. Wang, H.L. Fraser, Role of ω phase in the formation of extremely refined intragranular α precipitates in metastable β-titanium alloys, Acta Mater. 103 (2016) 850–858. https://doi.org/10.1016/j.actamat.2015.11.020.

[125] S.A. Mantri, D. Choudhuri, T. Alam, G.B. Viswanathan, J.M. Sosa, H.L. Fraser, R. Banerjee, Tuning the scale of α precipitates in β-titanium alloys for achieving high strength, Scripta Mater. 154 (2018) 139–144. https://doi.org/10.1016/j.scriptamat.2018.05.040.

[126] Y. Mantani, Y. Takemoto, M. Hida, A. Sakakibara, M. Tajima, Phase Transformation of α" Martensite Structure by Aging in Ti-8 mass%Mo Alloy, Mater. Trans. 45 (2004) 1629–1634. https://doi.org/10.2320/matertrans.45.1629.

[127] F. Sun, J.Y. Zhang, M. Marteleur, T. Gloriant, P. Vermaut, D. Laillé, P. Castany, C. Curfs, P.J. Jacques, F. Prima, Investigation of early stage deformation mechanisms in a metastable β titanium alloy showing combined twinning-induced plasticity and transformation-induced plasticity effects, Acta Materialia. 61 (2013) 6406–6417. https://doi.org/https://doi.org/10.1016/j.actamat.2013.07.019.

[128] Y. Yang, P. Castany, Y.L. Hao, T. Gloriant, Plastic deformation via hierarchical nano-sized martensitic twinning in the metastable β Ti-24Nb-4Zr-8Sn alloy, Acta Mater. 194 (2020). https://doi.org/10.1016/j.actamat.2020.04.021.

[129] M. Li, X. Min, K. Yao, F. Ye, Novel insight into the formation of α″-martensite and ω-phase with cluster structure in metastable Ti-Mo alloys, Acta Mater. 164 (2019) 322–333. https://doi.org/10.1016/j.actamat.2018.10.048.

[130] B. Qian, J. Zhang, Y. Fu, F. Sun, Y. Wu, J. Cheng, P. Vermaut, F. Prima, In-situ microstructural investigations of the TRIP-to-TWIP evolution in Ti-Mo-Zr alloys as a function of Zr concentration, J Mater Sci Technol. 65 (2020) 228–237. https://doi.org/10.1016/j.jmst.2020.04.078.

[131] R.P. Kolli, W.J. Joost, S. Ankem, Phase Stability and Stress-Induced Transformations in Beta Titanium Alloys, Jom-Us. 67 (2015) 1273–1280. https://doi.org/10.1007/s11837-015-1411-y.

[132] F. Sun, T. Gloriant, P. Vermaut, P. Jacques, F. Prima, Beta Titanium Alloys with Very High Ductility Induced by Complex Deformation Mechanisms: a New Material Perspective for Coronary Stent Applications, Solid State Phenomen. 172–174 (2011) 129–134. https://doi.org/10.4028/www.scientific.net/ssp.172-174.129.

[133] M. Marteleur, F. Sun, T. Gloriant, P. Vermaut, P.J. Jacques, F. Prima, On the design of new β-metastable titanium alloys with improved work hardening rate thanks to simultaneous TRIP and TWIP effects, Scripta Materialia. 66 (2012) 749–752. https://doi.org/https://doi.org/10.1016/j.scriptamat.2012.01.049.

[134] L. Lilensten, Y. Danard, R. Poulain, R. Guillou, J.M. Joubert, L. Perrière, P. Vermaut, D. Thiaudière, F. Prima, From single phase to dual-phase TRIP-TWIP alloys: design approach and properties, Materialia. 12 (2020) 100700. https://doi.org/10.1016/j.mtla.2020.100700.

[135] T. Ozaki, H. Matsumoto, S. Watanabe, S. Hanada, Beta Ti Alloys with Low Young's Modulus, Mater Trans. 45 (2004) 2776–2779. https://doi.org/10.2320/matertrans.45.2776.

[136] M. Niinomi, T. Akahori, S. Katsura, K. Yamauchi, M. Ogawa, Mechanical characteristics and microstructure of drawn wire of Ti–29Nb–13Ta–4.6Zr for biomedical applications, Mater Sci Eng C. 27 (2007) 154–161. https://doi.org/10.1016/j.msec.2006.04.008.

[137] P. Laheurte, F. Prima, A. Eberhardt, T. Gloriant, M. Wary, E. Patoor, Mechanical properties of low modulus β titanium alloys designed from the electronic approach, J Mech Behav Biomed. 3 (2010) 565–573. https://doi.org/10.1016/j.jmbbm.2010.07.001.

[138] T.-K. Jung, S. Semboshi, N. Masahashi, S. Hanada, Mechanical properties and microstructures of β Ti–25Nb–11Sn ternary alloy for biomedical applications, Mater Sci Eng C. 33 (2013) 1629–1635. https://doi.org/10.1016/j.msec.2012.12.072.

[139] Y. Fu, W. Xiao, D. Kent, M.S. Dargusch, J. Wang, X. Zhao, C. Ma, Ultrahigh strain hardening in a transformation-induced plasticity and twinning-induced plasticity titanium alloy, Scripta Mater. 187 (2020) 285–290. https://doi.org/10.1016/j.scriptamat.2020.06.029.

[140] L. Ren, W. Xiao, C. Ma, R. Zheng, L. Zhou, Development of a high strength and high ductility near β-Ti alloy with twinning induced plasticity effect, Scripta Mater. 156 (2018) 47–50. https://doi.org/https://doi.org/10.1016/j.scriptamat.2018.07.012.

[141] S. Sadeghpour, S.M. Abbasi, M. Morakabati, A. Kisko, L.P. Karjalainen, D.A. Porter, A new multi-element beta titanium alloy with a high yield strength exhibiting transformation and twinning induced plasticity effects, Scripta Materialia. 145 (2018) 104–108. https://doi.org/https://doi.org/10.1016/j.scriptamat.2017.10.017.

[142] J. Gao, Y. Huang, D. Guan, A.J. Knowles, L. Ma, D. Dye, W.M. Rainforth, Deformation mechanisms in a metastable beta titanium twinning induced plasticity alloy with high yield strength and high strain hardening rate, Acta Mater. 152 (2018) 301–314. https://doi.org/10.1016/j.actamat.2018.04.035.

[143] L. Ren, W. Xiao, D. Kent, M. Wan, C. Ma, L. Zhou, Simultaneously enhanced strength and ductility in a metastable β-Ti alloy by stress-induced hierarchical twin structure, Scripta Materialia. 184 (2020) 6–11. https://doi.org/10.1016/j.scriptamat.2020.03.039.

[144] S. Bahl, S. Suwas, K. Chatterjee, Comprehensive review on alloy design, processing, and performance of β Titanium alloys as biomedical materials, Int Mater Rev. 66 (2020) 1–26. https://doi.org/10.1080/09506608.2020.1735829.

[145] C. Sauer, G. Luetjering, Thermo-mechanical processing of high strength β-titanium alloys and effects on microstructure and properties, J Mater Process Tech. 117 (2001) 311–317. https://doi.org/10.1016/s0924-0136(01)00788-9.

[146] N. Yumak, K. Aslantaş, A review on heat treatment efficiency in metastable β titanium alloys: the role of treatment process and parameters, J Mater Res Technology. 9 (2020) 15360–15380. https://doi.org/10.1016/j.jmrt.2020.10.088.

[147] G. Liu, X. Zhang, X. Chen, Y. He, L. Cheng, M. Huo, J. Yin, F. Hao, S. Chen, P. Wang, S. Yi, L. Wan, Z. Mao, Z. Chen, X. Wang, Z. Cao, J. Lu, Additive manufacturing of structural materials, Mater Sci Eng R Reports. (2021) 100596. https://doi.org/10.1016/j.mser.2020.100596.

[148] L.C. Zhang, D. Klemm, J. Eckert, Y.L. Hao, T.B. Sercombe, Manufacture by selective laser melting and mechanical behavior of a biomedical Ti–24Nb–4Zr–8Sn alloy, Scr. Mater. 65 (2011) 21–24. https://doi.org/10.1016/j.scriptamat.2011.03.024.

[149] J.C. Colombo-Pulgarín, C.A. Biffi, M. Vedani, D. Celentano, A. Sánchez-Egea, A.D. Boccardo, J.-P. Ponthot, Beta Titanium Alloys Processed By Laser Powder Bed Fusion: A Review, J Mater Eng Perform. (2021) 1–24. https://doi.org/10.1007/s11665-021-05800-6.

[150] C. Qiu, Q. Liu, R. Ding, Significant enhancement in yield strength for a metastable beta titanium alloy by selective laser melting, Mater Sci Eng. 816 (2021) 141291. https://doi.org/10.1016/j.msea.2021.141291.

[151] C. Zopp, S. Blümer, F. Schubert, L. Kroll, Processing of a metastable titanium alloy (Ti-5553) by selective laser melting, Ain Shams Eng J. 8 (2017) 475–479. https://doi.org/10.1016/j.asej.2016.11.004.

[152] P. Qin, L.Y. Chen, C.H. Zhao, Y.J. Liu, C.D. Cao, H. Sun, L.C. Zhang, Corrosion behavior and mechanism of selective laser melted Ti35Nb alloy produced using pre-alloyed and mixed powder in Hank's solution, Corros Sci. 189 (2021) 109609. https://doi.org/10.1016/j.corsci.2021.109609.

[153] P. Qi, B. Li, T. Wang, L. Zhou, Z. Nie, Evolution of microstructural homogeneity in novel Ti-6Zr-5Fe alloy fabricated by selective laser melting, Mater Charact. (2020) 110729. https://doi.org/10.1016/j.matchar.2020.110729.

[154] H. Xu, Z. Li, A. Dong, H. Xing, D. Du, L. He, H.P. Peng, G. Zhu, D. Wang, B. Sun, Selective laser melting of biomedical Ti15Mo alloy: a proper combination of strength and ductility under the effects of multiple mechanisms, J Alloy Compd. (2021) 159686. https://doi.org/10.1016/j.jallcom.2021.159686.

[155] L. Qi, X. Qiao, L. Huang, X. Huang, X. Zhao, Effect of structural stability on the stress induced martensitic transformation in Ti-10V-2Fe-3Al alloy, Mater Sci Eng. 756 (2019) 381–388. https://doi.org/10.1016/j.msea.2019.04.058.

[156] L. Qi, X. Qiao, L. Huang, X. Huang, W. Xiao, X. Zhao, Effect of cold rolling deformation on the microstructure and properties of Ti-10V-2Fe-3Al alloy, Mater Charact. 155 (2019) 109789. https://doi.org/10.1016/j.matchar.2019.109789.

[157] C. Qiu, Q. Liu, Multi-scale microstructural development and mechanical properties of a selectively laser melted beta titanium alloy, Addit Manuf. 30 (2019) 100893. https://doi.org/10.1016/j.addma.2019.100893.

[158] Q. Liu, C. Qiu, Variant selection of α precipitation in a beta titanium alloy during selective laser melting and its influence on mechanical properties, Mater Sci Eng. 784 (2020) 139336. https://doi.org/10.1016/j.msea.2020.139336.

[159] H. Schwab, F. Palm, U. Kühn, J. Eckert, Microstructure and mechanical properties of the near-beta titanium alloy Ti-5553 processed by selective laser melting, Mater Design. 105 (2016) 75–80. https://doi.org/10.1016/j.matdes.2016.04.103.

[160] H. Schwab, M. Bönisch, L. Giebeler, T. Gustmann, J. Eckert, U. Kühn, Processing of Ti-5553 with improved mechanical properties via an in-situ heat treatment combining selective laser melting and substrate plate heating, Mater Design. 130 (2017) 83–89. https://doi.org/10.1016/j.matdes.2017.05.010.

[161] H. Deng, W. Qiu, S. Cao, L. Chen, Z. Hu, Y. Wei, Z. Xia, L. Zhou, X. Cui, J. Tang, Heat-treatment induced microstructural evolution and enhanced mechanical property of selective laser melted near β Ti-5Al-5Mo-5 V-3Cr-1Zr alloy, J Alloy Compd. 858 (2021) 158351. https://doi.org/10.1016/j.jallcom.2020.158351.

[162] R. Ummethala, P.S. Karamched, S. Rathinavelu, N. Singh, A. Aggarwal, K. Sun, E. Ivanov, L. Kollo, I. Okulov, J. Eckert, K.G. Prashanth, Selective laser melting of high-strength, low-modulus Ti–35Nb–7Zr–5Ta alloy, Materialia. 14 (2020) 100941. https://doi.org/10.1016/j.mtla.2020.100941.

[163] A. Kreitcberg, V. Brailovski, S. Prokoshkin, New biocompatible near-beta Ti-Zr-Nb alloy processed by laser powder bed fusion: Process optimization, J Mater Process Tech. 252 (2018) 821–829. https://doi.org/10.1016/j.jmatprotec.2017.10.052.

[164] T. Ishimoto, K. Hagihara, K. Hisamoto, S.-H. Sun, T. Nakano, Crystallographic texture control of beta-type Ti-15Mo-5Zr-3Al alloy by selective laser melting for the development of novel implants with a biocompatible low Young's modulus, Scr. Mater. 132 (2017) 34–38. https://doi.org/10.1016/j.scriptamat.2016.12.038.

[165] Y.J. Liu, X.P. Li, L.C. Zhang, T.B. Sercombe, Processing and properties of topologically optimised biomedical Ti–24Nb–4Zr–8Sn scaffolds manufactured by selective laser melting, Mater Sci Eng. 642 (2015) 268–278. https://doi.org/10.1016/j.msea.2015.06.088.

[166] Y.J. Liu, S.J. Li, H.L. Wang, W.T. Hou, Y.L. Hao, R. Yang, T.B. Sercombe, L.C. Zhang, Microstructure, defects and mechanical behavior of beta-type titanium porous structures manufactured by electron beam melting and selective laser melting, Acta Mater. 113 (2016) 56–67. https://doi.org/10.1016/j.actamat.2016.04.029.

[167] C.L. Yang, Z.J. Zhang, S.J. Li, Y.J. Liu, T.B. Sercombe, W.T. Hou, P. Zhang, Y.K. Zhu, Y.L. Hao, Z.F. Zhang, R. Yang, Simultaneous improvement in strength and plasticity of Ti-24Nb-4Zr-8Sn manufactured by selective laser melting, Mater Design. 157 (2018) 52–59. https://doi.org/10.1016/j.matdes.2018.07.036.

[168] Y.J. Liu, Y.S. Zhang, L.C. Zhang, Transformation-induced plasticity and high strength in beta titanium alloy manufactured by selective laser melting, Materialia. 6 (2019) 100299. https://doi.org/10.1016/j.mtla.2019.100299.

[169] S.N. Tedman-Jones, S.D. McDonald, M.J. Bermingham, D.H. StJohn, M.S. Dargusch, A new approach to nuclei identification and grain refinement in titanium alloys, J Alloy Compd. 794 (2019) 268–284. https://doi.org/10.1016/j.jallcom.2019.04.224.

[170] E.G. Brodie, A.E. Medvedev, J.E. Frith, M.S. Dargusch, H.L. Fraser, A. Molotnikov, Remelt processing and microstructure of selective laser melted Ti25Ta, J. Alloys Compd. 820 (2020) 153082. https://doi.org/10.1016/j.jallcom.2019.153082.

[171] J.C. Wang, Y.J. Liu, P. Qin, S.X. Liang, T.B. Sercombe, L.C. Zhang, Selective laser melting of Ti–35Nb composite from elemental powder mixture: Microstructure, mechanical behavior and corrosion behavior, Mater Sci Eng. 760 (2019) 214–224. https://doi.org/10.1016/j.msea.2019.06.001.

[172] M. Simonelli, N.T. Aboulkhair, P. Cohen, J.W. Murray, A.T. Clare, C. Tuck, R.J.M. Hague, A comparison of Ti-6Al-4V in-situ alloying in Selective Laser Melting using simply-mixed and satellited powder blend feedstocks, Mater. Charact. 143 (2018) 118–126. https://doi.org/10.1016/j.matchar.2018.05.039.

[173] W. Zhai, Z. Zhu, W. Zhou, S.M.L. Nai, J. Wei, Selective laser melting of dispersed TiC particles strengthened 316L stainless steel, Compos Part B Eng. 199 (2020) 108291. https://doi.org/10.1016/j.compositesb.2020.108291.

[174] D. Zhao, C. Han, J. Li, J. Liu, Q. Wei, In situ fabrication of a titanium-niobium alloy with tailored microstructures, enhanced mechanical properties and biocompatibility by using selective laser melting, Mater Sci Eng C. 111 (2020) 110784. https://doi.org/10.1016/j.msec.2020.110784.

[175] Z. Zhou, Y. Liu, X. Liu, Q. Zhan, K. Wang, Microstructure evolution and mechanical properties of in-situ Ti6Al4V–TiB composites manufactured by selective laser melting, Compos Part B Eng. 207 (2021) 108567. https://doi.org/10.1016/j.compositesb.2020.108567.

[176] B. Vrancken, L. Thijs, J.P. Kruth, J.V. Humbeeck, Microstructure and mechanical properties of a novel β titanium metallic composite by selective laser melting, Acta Mater. 68 (2014) 150–158. https://doi.org/10.1016/j.actamat.2014.01.018.

[177] I. Yadroitsev, P. Krakhmalev, I. Yadroitsava, Titanium Alloys Manufactured by In Situ Alloying During Laser Powder Bed Fusion, J. Occup. Med. 69 (2017) 2725–2730. https://doi.org/10.1007/s11837-017-2600-7.

[178] F. Huber, T. Papke, C. Scheitler, L. Hanrieder, M. Merklein, M. Schmidt, In Situ Formation of a Metastable β-Ti Alloy by Laser Powder Bed Fusion (L-PBF) of Vanadium and Iron Modified Ti-6Al-4V, Metals-Basel. 8 (2018) 1067. https://doi.org/10.3390/met8121067.

[179] S.L. Sing, W.Y. Yeong, F.E. Wiria, Selective laser melting of titanium alloy with 50 wt% tantalum: Microstructure and mechanical properties, J. Alloys Compd. 660 (2016) 461–470. https://doi.org/10.1016/j.jallcom.2015.11.141.

[180] M. Fischer, D. Joguet, G. Robin, L. Peltier, P. Laheurte, In situ elaboration of a binary Ti-26Nb alloy by selective laser melting of elemental titanium and niobium mixed powders, Mater. Sci. Eng., C. 62 (2016) 852–859. https://doi.org/10.1016/j.msec.2016.02.033.

[181] S. Huang, R.L. Narayan, J.H.K. Tan, S.L. Sing, W.Y. Yeong, Resolving the porosity-unmelted inclusion dilemma during in-situ alloying of Ti34Nb via Laser Powder Bed Fusion, Acta Mater. 204 (2020) 116522. https://doi.org/10.1016/j.actamat.2020.116522.

[182] L. Zhou, T. Yuan, R. Li, J. Tang, M. Wang, F. Mei, Anisotropic mechanical behavior of biomedical Ti-13Nb-13Zr alloy manufactured by selective laser melting, J Alloy Compd. 762 (2018) 289–300. https://doi.org/10.1016/j.jallcom.2018.05.179.

[183] C. Madikizela, L.A. Cornish, L.H. Chown, H. Möller, Microstructure and mechanical properties of selective laser melted Ti-3Al-8V-6Cr-4Zr-4Mo compared to Ti-6Al-4V, Mater Sci Eng. 747 (2019) 225–231. https://doi.org/10.1016/j.msea.2018.12.100.

[184] D. Zhao, C. Han, Y. Li, J. Li, K. Zhou, Q. Wei, J. Liu, Y. Shi, Improvement on mechanical properties and corrosion resistance of titanium-tantalum alloys in-situ fabricated via selective laser melting, J Alloy Compd. 804 (2019) 288–298. https://doi.org/10.1016/j.jallcom.2019.06.307.

[185] L. Yan, Y. Yuan, L. Ouyang, H. Li, A. Mirzasadeghi, L. Li, Improved mechanical properties of the new Ti-15Ta-xZr alloys fabricated by selective laser melting for biomedical application, J Alloy Compd. 688, Part A (2016) 156–162. https://doi.org/10.1016/j.jallcom.2016.07.002.

[186] G. Yablokova, S. Dadbakhsh, M. Speirs, A. Khangholi, J.-P. Kruth, J. Luyten, J. Schrooten, J.V. Humbeeck, TMS 2015 144th Annual Meeting & Exhibition, Supplemental Proceedings, (2015) 507–514. https://doi.org/10.1007/978-3-319-48127-2_64.

[187] J. Wang, Y. Liu, C.D. Rabadia, S.-X. Liang, T.B. Sercombe, L.-C. Zhang, Microstructural homogeneity and mechanical behavior of a selective laser melted Ti-35Nb alloy produced from an elemental powder mixture, J Mater Sci Technol. 61 (2021) 221–233. https://doi.org/10.1016/j.jmst.2020.05.052.

[188] W. Chen, C. Chen, X. Zi, X. Cheng, X. Zhang, Y.C. Lin, K. Zhou, Controlling the microstructure and mechanical properties of a metastable beta titanium alloy by selective laser melting, Mater. Sci. Eng., A. 726 (2018) 240–250. https://doi.org/10.1016/j.msea.2018.04.087.

[189] N. Kang, Y. Li, X. Lin, E. Feng, W. Huang, Microstructure and tensile properties of Ti-Mo alloys manufactured via using laser powder bed fusion, J. Alloys Compd. 771 (2019) 877–884. https://doi.org/10.1016/j.jallcom.2018.09.008.

[190] M. Gäumann, C. Bezençon, P. Canalis, W. Kurz, Single-crystal laser deposition of superalloys: processing–microstructure maps, Acta Mater. 49 (2001) 1051–1062. https://doi.org/10.1016/s1359-6454(00)00367-0.

[191] P.A. Kobryn, S.L. Semiatin, Microstructure and texture evolution during solidification processing of Ti–6Al–4V, J Mater Process Tech. 135 (2003) 330–339. https://doi.org/10.1016/s0924-0136(02)00865-8.

[192] W. Zong, S. Zhang, C. Zhang, L. Ren, Q. Wang, Design and characterization of selective laser-melted Ti6Al4V–5Cu alloy for dental implants, Mater Corros. 71 (2020) 1697–1710. https://doi.org/10.1002/maco.202011650.

[193] Z. Xiong, X. Pang, S. Liu, Z. Li, R.D.K. Misra, Hierarchical refinement of nickel-microalloyed titanium during additive manufacturing, Scripta Mater. 195 (2021) 113727. https://doi.org/10.1016/j.scriptamat.2021.113727.

[194] M. Markl, C. Körner, Multiscale Modeling of Powder Bed--Based Additive Manufacturing, Annu Rev Mater Res. 46 (2015) 1–31. https://doi.org/10.1146/annurev-matsci-070115-032158.

[195] D. Gu, Laser Additive Manufacturing of High-Performance Materials, Springer, Berlin, Heidelberg, 2015. https://doi.org/10.1007/978-3-662-46089-4.

[196] H.D. Carlton, K.D. Klein, J.W. Elmer, Evolution of Microstructure and mechanical properties of selective laser melted Ti-5Al-5V-5Mo-3Cr after heat treatments, Sci Technol Weld Joi. 24 (2019) 1–9. https://doi.org/10.1080/13621718.2019.1594589.

[197] C.D. Rabadia, Y.J. Liu, G.H. Cao, Y.H. Li, C.W. Zhang, T.B. Sercombe, H. Sun, L.C. Zhang, High-strength β stabilized Ti-Nb-Fe-Cr alloys with large plasticity, Mater Sci Eng. 732 (2018) 368–377. https://doi.org/10.1016/j.msea.2018.07.031.

[198] S.H. Lee, M. Todai, M. Tane, K. Hagihara, H. Nakajima, T. Nakano, Biocompatible low Young's modulus achieved by strong crystallographic elastic anisotropy in Ti-15Mo-5Zr-3Al alloy single crystal, J. Mech. Behav. Biomed. Mater. 14 (2012) 48–54. https://doi.org/10.1016/j.jmbbm.2012.05.005.

[199] T. Nakano, T. Ishimoto, A. Matsugaki, K. Hagihara, Y. Koizumi, R. Ozasa, Control of crystallographic orientation by metal additive manufacturing process of β-type Ti alloys based

on the bone tissue anisotropy, Matec Web Conf. 321 (2020) 05002. https://doi.org/10.1051/matecconf/202032105002.

[200] W. Li, J. Liu, S. Wen, Q. Wei, C. Yan, Y. Shi, Crystal orientation, crystallographic texture and phase evolution in the Ti–45Al–2Cr–5Nb alloy processed by selective laser melting, Mater Charact. 113 (2016) 125–133. https://doi.org/10.1016/j.matchar.2016.01.012.

[201] W. Li, J. Liu, Y. Zhou, S. Wen, Q. Wei, C. Yan, Y. Shi, Effect of substrate preheating on the texture, phase and nanohardness of a Ti–45Al–2Cr–5Nb alloy processed by selective laser melting, Scripta Mater. 118 (2016) 13–18. https://doi.org/10.1016/j.scriptamat.2016.02.022.

[202] C.M. Lee, C.P. Ju, J.H.C. Lin, Structure-property relationship of cast Ti-Nb alloys., Journal of Oral Rehabilitation. 29 (2002) 314–322.

[203] X. Zhao, M. Niinomi, M. Nakai, J. Hieda, Beta type Ti–Mo alloys with changeable Young's modulus for spinal fixation applications, Acta Biomater. 8 (2012) 1990–1997. https://doi.org/10.1016/j.actbio.2012.02.004.

[204] A.A. Zadpoor, Bone tissue regeneration: the role of scaffold geometry, Biomater Sci-Uk. 3 (2015) 231–245. https://doi.org/10.1039/c4bm00291a.

[205] F.S.L. Bobbert, A.A. Zadpoor, Effects of bone substitute architecture and surface properties on cell response, angiogenesis, and structure of new bone, J Mater Chem B. 5 (2017) 6175–6192. https://doi.org/10.1039/c7tb00741h.

[206] A.A. Zadpoor, Design for Additive Bio-Manufacturing: From Patient-Specific Medical Devices to Rationally Designed Meta-Biomaterials, Int J Mol Sci. 18 (2017) 1607. https://doi.org/10.3390/ijms18081607.

[207] N.E. Putra, M.J. Mirzaali, I. Apachitei, J. Zhou, A.A. Zadpoor, Multi-material additive manufacturing technologies for Ti-, Mg-, and Fe-based biomaterials for bone substitution., Acta Biomater. 109 (2020) 1–20. https://doi.org/10.1016/j.actbio.2020.03.037.

[208] H. Gao, B. Ji, I.L. Jäger, E. Arzt, P. Fratzl, Materials become insensitive to flaws at nanoscale: Lessons from nature, P. Natl. Acad. Sci. USA. 100 (2003) 5597–5600. https://doi.org/10.1073/pnas.0631609100.

[209] S. Suresh, Graded Materials for Resistance to Contact Deformation and Damage, Science. 292 (2001) 2447–2451. https://doi.org/10.1126/science.1059716.

[210] S. Xu, M. Du, J. Li, K. Yan, B. Cai, Q. He, Q. Fang, O. Magdysyuk, B. Liu, Y. Yang, Y. Liu, Bio-mimic Ti–Ta composite with hierarchical "Brick-and-Mortar" microstructure, Materialia. 8 (2019) 100463. https://doi.org/10.1016/j.mtla.2019.100463.

[211] X. Ma, F. Li, Z. Sun, J. Hou, X. Fang, Y. Zhu, C.C. Koch, Achieving Gradient Martensite Structure and Enhanced Mechanical Properties in a Metastable β Titanium Alloy, Metall. Mater. Trans. A. 50 (2019) 2126–2138. https://doi.org/10.1007/s11661-019-05157-5.

[212] P. Krakhmalev, I. Yadroitsava, G. Fredriksson, I. Yadroitsev, In situ heat treatment in selective laser melted martensitic AISI 420 stainless steels, Mater. Design. 87 (2015) 380–385. https://doi.org/10.1016/j.matdes.2015.08.045.

[213] P. Kürnsteiner, M.B. Wilms, A. Weisheit, B. Gault, E.A. Jägle, D. Raabe, High-strength Damascus steel by additive manufacturing, Nature. 582 (2020) 515–519. https://doi.org/10.1038/s41586-020-2409-3.

[214] V.A. Popovich, E.V. Borisov, A.A. Popovich, V.Sh. Sufiiarov, D.V. Masaylo, L. Alzina, Functionally graded Inconel 718 processed by additive manufacturing: Crystallographic texture, anisotropy of microstructure and mechanical properties, Mater Design. 114 (2017) 441–449. https://doi.org/10.1016/j.matdes.2016.10.075.

[215] Y. Yang, J.B. Zhan, J.B. Sui, C.Q. Li, K. Yang, P. Castany, T. Gloriant, Functionally graded NiTi alloy with exceptional strain-hardening effect fabricated by SLM method, Scr. Mater. 188 (2020) 130–134. https://doi.org/10.1016/j.scriptamat.2020.07.019.

Chapter 3: Materials and Experimental Methods

3.1. Feedstock Powders

Gas atomised Ti powder (Purity>99.9%, TLS Technik GmbH, Germany) was used as the base powder for Ti-12Mo and Ti-12Mo-6Zr-2Fe (TMZF) powder blends. The original alloying elemental powders of Ti and Mo (Purity>99.9%, TLS Technik GmbH, Germany) were spherical in a size range of 20-63 μm. The Zr and Fe spherical powders (Purity>99.9%, TLS Technik GmbH, Germany) had particle size ranges of 15-45 μm and 45-63 μm, respectively. The mixed Ti-12Mo and TMZF powders were blended for 24 h, under the protection of argon atmosphere, using a tumbler mixer to ensure uniform blending. If no agglomeration of the Mo powders in the blended powders was observed, suggesting a uniform blending.

The flowability of the pure Ti powder and Ti-12Mo mixed powders was tested using the RST-XS Schulze Ring Shear Tester (Germany), in accordance with the standard of ASTM-D6773 [1], to ensure appropriate spreading during LPBF. In addition, the Hausner ratio was measured, which means the ratio between the tap and apparent density of powders. There was good flowability if the Hausner ratio was <1.25.

3.2. LPBF Processing and Post-treatments

All specimens and components were fabricated using a Concept Laser M2 Cusing® LPBF system, which was equipped with a 400 W Nd:YAG continuous laser source and a laser spot diameter of ~70 μm. The Ti6Al4V plate, with a dimension of 90 mm × 90 mm, was used as the substrate for the fabrication. The builds were carried out using a 20 μm powder layer thickness under a controlled argon atmosphere, where the oxygen content was ~1000 ppm.

This work firstly used the simple scanning strategy to optimise the processing parameters based on the Ti-12Mo system. The analysis of variance (ANOVA), one of the designs of experiment (DOE) methodologies, was applied to optimise the LPBF processing parameters for acquiring the samples without defects and un-melted refractory elements. As shown in Table 3.1, all parameters of laser power, scanning speed, and hatch spacing were separated into five levels within the designed space. Thereby the five-level central composite response surface model was used to arrange the distribution of experiment points.

Table 3.1. LPBF processing parameters in five levels using the simple scanning strategy.

Parameters	Units	Levels				
Laser power	W	200	250	300	350	400
Scanning speed	mm/s	1000	1500	2000	2500	3000
Hatch spacing	μm	30	45	60	75	90

However, only several Ti-12Mo samples can be successfully built by LPBF using the above parameters. Then the optimum processing parameters for the specimens that possess near fully dense and largely homogeneous microstructures can be extracted.

To manufacture large components, the simple scanning strategy results in high thermal residual stress, which would increase cracking potential [2], due to the considerable scan track length and slower cooling rate [3]. To reduce the inner residual stress, it is necessary to use more advanced scanning strategies, such as chessboard scanning with a smaller scan track length [4]. Therefore, we then introduce the chessboard (island) scanning strategy to process the specimens. The island spacing (IS; the overlap of neighbouring islands) and the laser beam delay (LBD; laser dwelling time) were further optimised to obtain samples without defects in the chessboard scanned samples. After that, the optimum processing parameters were also verified in processing high-quality TMZF samples.

3.3. Microstructure Characterisation

The techniques of microstructural characterisation and mechanical properties tests in this work are summarised in Fig.3.1, and the details are described below.

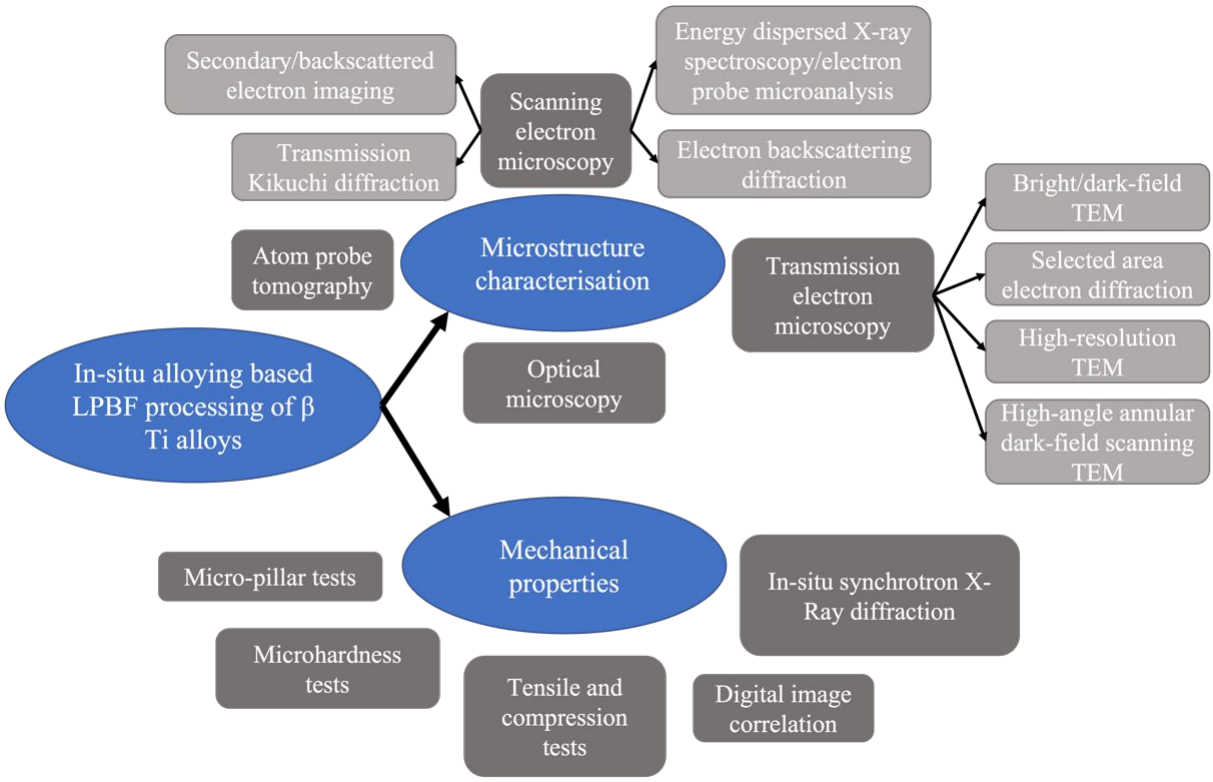


Fig. 3.1. The microstructure characterisations and mechanical properties tests have been employed to the β Ti alloys prepared by in-situ alloying based LPBF.

The as-fabricated specimens were sectioned for microstructural characterisation and mechanical testing using electrical discharge machining. For scanning electron microscopy (SEM) and optical microscopy (OM) observations, the specimens were sequentially grounded with 220 and 1200 grit SiC papers and polished by MD-Chem with OPS-H2O2 (7:3) solution (Struers, Denmark). The surface stress generated in the sample preparation process was eliminated through electrochemical polishing (6% perchloric acid + 94% methanol solution at a direct voltage of 30 V at the temperature of 243 k) for the higher quality microstructural

characterisations. To observe melt pool microstructure and secondary phases of the samples, they were etched using Kroll's reagent (2% HF + 6% HNO_3 + 92% distilled water).

The Zeiss axioskop 2 microscope was used for OM observation. The detailed microstructure of the alloys and fracture morphology was studied using scanning electron microscopy (SEM, TESCAN MIRA 3, Czech Republic) operated in secondary electron (SE) and backscattered electron (BSE) modes. The elemental distribution was analysed using energy dispersive X-Ray spectroscopy (EDS) performed using X-Max^N Silicon Drift Detector (Oxford Instruments, Oxford, UK), equipped in SEM, and electron probe microanalysis (EPMA) characterised by a JXA-8530 analyser (JEOL, Tokyo, Japan). The grain structure, crystallographic orientation, precipitations, and deformation microstructures were characterised using electron backscattering diffraction (EBSD) with a step size range from 0.05 to 1.5 μm and analysed using Aztec-crystal software. The transmission Kikuchi diffraction (TKD) maps were acquired using the step size of 8 nm. The EBSD and TKD tests use the beam voltage of 15 kv and 30 kv, respectively. The general TKD settings use the on-axis or off-axis detectors, respectively [5,6], as shown in Fig.3.2a. In this work, we utilised the off-axis detector to perform the TKD characterisations. As shown in Fig.3.2b, the thin foil is set close to the electron beam column, of which the working distance is between 5-7 mm. The sample is slightly higher than the top of the detector's screen. The extreme resolution can be 3 nm, depending on the electron beam size and the quality of the thin foil.

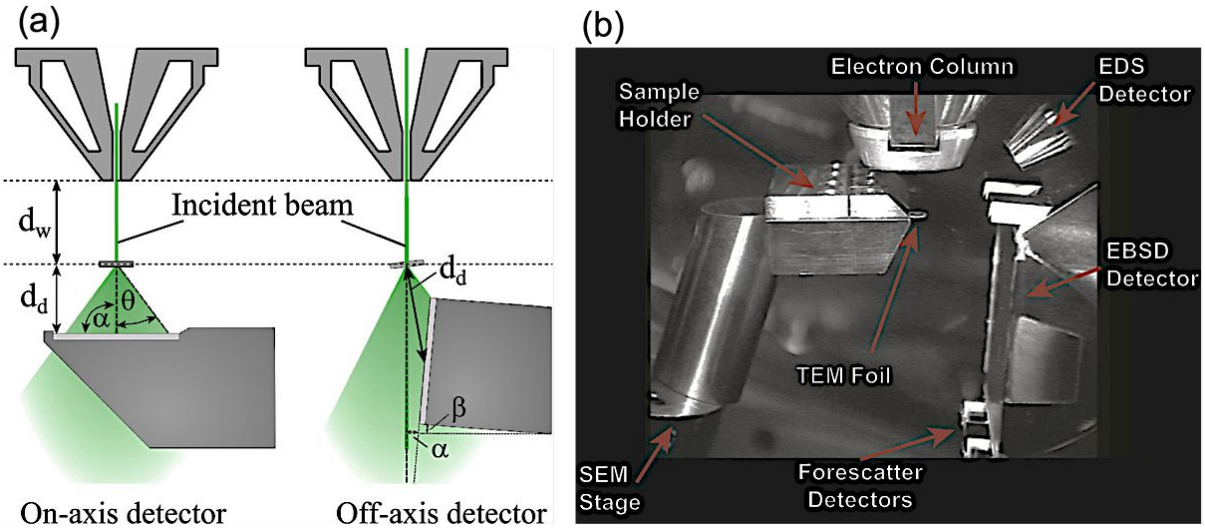


Fig. 3.2. (a) The schematic shows the interaction of incident beam and specimen during the TKD characterisations, where the structure of on-axis and off-axis detectors are also illustrated. (b) The photograph of the chamber of the off-axis TKD test. (Modified from [5,6])

In addition, the microstructure was investigated using a transmission electron microscope (TEM; Tecnai F30, FEI, US) operated at 300 kV. The high-angle annular dark-field scanning TEM (HAADF-STEM) imaging and EDS mapping were performed on an FEI Talos F200x TEM at 200 kV, equipped with four in-column SDD Super-X detectors. The simulations of selected area electron diffraction (SAED) patterns and the stereo-projection analysis of martensite and twinning were performed in a commercial software of SingleCrystal 4.14. Some thin foils were prepared using conventional grinding, polishing and ion milling (PIPS™, Gatan, Inc., Pleasanton, CA) for TEM or TKD characterisations. The other TEM specimens were lifted out from the selected region of the samples, which were performed using the focused ion beam (FIB; Dual Beam Heilos™ Nanolab 600i, FEI).

Lift-outs and annular milling in an FEI Scios FIB/SEM were utilised to create needle-shaped specimens for atom probe tomography (APT) testing. Characterisations of APT were carried out in a local electrode atom probe (CAMEACA LEAP 5000 XR). At 70 K in voltage

mode, the specimens were examined at a pulse repetition rate of 200 kHz, a pulse fraction of 20%, and an evaporation detection rate of 0.2 per cent atom per pulse. The 3D reconstructions and data analysis were carried out using Imago Visualization and Analysis Software (IVAS) version 3.8.

X-ray diffraction (XRD) patterns were recorded using a Rigaku Smartlab-9kW diffractometer (Rigaku, Tokyo, Japan) in the 2θ range of 20˚-100˚ with Cu Kα radiation (λ = 1.54056 Å, 45 kV, 200 mA). The volume fraction of phases, lattice parameters, and microstrain were analysed using the Rietveld method performed by MAUD software [7] on the acquired XRD patterns to isolate the broadening effects caused by the crystallite size, microstrain and instrument. The instrument broadening parameters were calibrated using the annealed standard silicon powder.

The specimens' densities were measured using the Archimedes principle using a Practum 224 balance (Sartorius, Germany). NIH ImageJ software was used to calculate the porosity percentage, relative density (100% - void percentage), and the percentage of unmelted Mo. The oxygen and nitrogen content of the Ti-12Mo and TMZF samples were measured using the ON736 elemental analyser (LECO, US). The differential scanning calorimetry (DSC) curves were tested by the NETZSCH DSC 404 C machine under the protection of the Argon atmosphere.

3.4. In-situ Synchrotron X-Ray Diffraction

The tensile specimens for in-situ X-ray diffraction tests have a gauge of 4 × 1 mm (length × width), of which the total length is 42 mm. The surfaces of tensile specimens were sequentially grounded with 220 and 1200 grit SiC papers before the tests. In situ synchrotron XRD data were recorded on a beamline I15 (Diamond, UK) using a 2D area flat panel detector

Perkin Elmer. The wavelength calibration (λ= 0.22723 Å) and 2D powder diffraction data reduction were performed with DAWN software using LaB6 as a calibration standard [8–10].

In situ XRD measurements were performed at various loads using Deben CT5000 rig. The beam size of 1.1 × 1.1 mm was used during measurements. At each loading stage, the sample was rotated in steps of 10° over 180° rotation around the load direction. The resulting images were summed for every load. The full azimuthal integration (i.e. azimuthal integration over 360°) was performed for Rietveld refinement of the relative amount of phases as a function of load. Additional azimuthal integrations of 15° (from - 7.5° till 7.5°) were performed for three directions: along the tensile (load) direction, Poisson direction, and for the diagonal direction at 45° between these two directions. Integration over 15° provides a good statistic for data analysis. Additional integration over 10° (from - 5° till 5°) instead of 15° showed that there is no difference in peak position or peak intensities between these two datasets.

3.5. Mechanical Properties

Ex-situ tensile tests were performed for both as-fabricated and post heat-treated samples. All tensile specimens were fabricated according to the ASTM E8 [11] with the tensile direction perpendicular to the building direction. The tensile tests were performed at room temperature, with a 1 $mm \cdot min^{-1}$ crosshead rate for at least three independent tensile tests per group, using a Zwick/Roell universal testing machine (Zwick 1445, Zwick-Roell, Ulm, Germany) equipped with an extensometer with a gauge length of 25 mm.

Vickers microhardness tests were tested using a Struers DuraScan machine equipped with an automated indenter under a load of 100 g for 15 s per point. The groups of single crystal micropillars (2 μm diameters) were prepared using FIB (Dual Beam Heilos^{TM} Nanolab 600i, FEI) operated at an ion beam voltage of 30 kV, along the <001> orientation of the β matrix.

The uniaxial compression tests were performed using a Hysitron Ti-950 nanoindenter equipped with a 10 μm flat diamond tip at a constant strain rate of 5×10^{-4}/s. Macro-compression tests (with a sample size of 3 mm × 3 mm × 7 mm) were conducted using an MTS CMT 5000 machine with a 0.2 mm/min crosshead rate following the ASTM E9-09 standard [12]. Digital image correlation (DIC) technology with a camera (Canon, Japan) recording was performed during compression tests. The obtained images were analysed using GOM correlate software (Zeiss, Germany). The sample surfaces were mechanically polished and sparkle-sprayed before the tests. Each test was repeated at least three times to verify the reproducibility of the results.

3.6. References

[1] A.B. Spierings, M. Voegtlin, T. Bauer, K. Wegener, Powder flowability characterisation methodology for powder-bed-based metal additive manufacturing, Prog Addit Manuf. 1 (2016) 9–20. https://doi.org/10.1007/s40964-015-0001-4.

[2] I. Gibson, D.W. Rosen, B. Stucker, Additive Manufacturing Technologies, (2010). https://doi.org/10.1007/978-1-4419-1120-9.

[3] H. Ali, H. Ghadbeigi, K. Mumtaz, Effect of scanning strategies on residual stress and mechanical properties of Selective Laser Melted Ti6Al4V, Mater. Sci. Eng., A. 712 (2018) 175–187. https://doi.org/10.1016/j.msea.2017.11.103.

[4] L.N. Carter, C. Martin, P.J. Withers, M.M. Attallah, The influence of the laser scan strategy on grain structure and cracking behaviour in SLM powder-bed fabricated nickel superalloy, J. Alloys Compd. 615 (2014) 338–347. https://doi.org/10.1016/j.jallcom.2014.06.172.

[5] P.W. Trimby, Y. Cao, Z. Chen, S. Han, K.J. Hemker, J. Lian, X. Liao, P. Rottmann, S. Samudrala, J. Sun, J.T. Wang, J. Wheeler, J.M. Cairney, Characterizing deformed ultrafine-grained and nanocrystalline materials using transmission Kikuchi diffraction in a scanning electron microscope, Acta Mater. 62 (2014) 69–80. https://doi.org/10.1016/j.actamat.2013.09.026.

[6] F. Niessen, A. Burrows, A.B. da S. Fanta, A systematic comparison of on-axis and off-axis transmission Kikuchi diffraction, Ultramicroscopy. 186 (2018) 158–170. https://doi.org/10.1016/j.ultramic.2017.12.017.

[7] L. Lutterotti, S. Matthies, H.R. Wenk, A.S. Schultz, J.W. Richardson, Combined texture and structure analysis of deformed limestone from time-of-flight neutron diffraction spectra, J. Appl. Phys. 81 (1997) 594–600. https://doi.org/10.1063/1.364220.

[8] M. Basham, J. Filik, M.T. Wharmby, P.C.Y. Chang, B.E. Kassaby, M. Gerring, J. Aishima, K. Levik, B.C.A. Pulford, I. Sikharulidze, D. Sneddon, M. Webber, S.S. Dhesi, F. Maccherozzi, O. Svensson, S. Brockhauser, G. Náray, A.W. Ashton, Data Analysis WorkbeNch (DAWN), J Synchrotron Radiat. 22 (2015) 853–858. https://doi.org/10.1107/s1600577515002283.

[9] J. Filik, A.W. Ashton, P.C.Y. Chang, P.A. Chater, S.J. Day, M. Drakopoulos, M.W. Gerring, M.L. Hart, O.V. Magdysyuk, S. Michalik, A. Smith, C.C. Tang, N.J. Terrill, M.T. Wharmby, H. Wilhelm, Processing two-dimensional X-ray diffraction and small-angle scattering data in DAWN 2, J Appl Crystallogr. 50 (2017) 959–966. https://doi.org/10.1107/s1600576717004708.

[10] M.L. Hart, M. Drakopoulos, C. Reinhard, T. Connolley, Complete elliptical ring geometry provides energy and instrument calibration for synchrotron-based two-dimensional X-ray diffraction, J Appl Crystallogr. 46 (2013) 1249–1260. https://doi.org/10.1107/s0021889813022437.

[11] ASTM E8/E8M-16a, Standard Test Methods for Tension Testing of Metallic Materials, ASTM International, West Conshohocken, PA, 2016. https://www.astm.org.

[12] ASTM E9-09, Standard Test Methods of Compression Testing of Metallic Materials at Room Temperature, ASTM International, West Conshohocken,PA, 2009. https://www.astm.org.

Chapter 4: In-situ Alloying Based LPBF Fabrication of β Ti-12Mo Alloy and Its Functionally Graded Composites

β-titanium (Ti) alloys combined with high strength and good ductility have attracted extensive research interest for use in many advanced industrial applications. In this study, LPBF parameters were first optimised to fabricate highly dense metastable β Ti-12Mo alloy with a largely homogeneous structure from low-cost elemental powders. When the laser area energy density (AED) increased to 4 J/mm^2 under the simple scan mode, the refractory Mo powder melted and dissolved into the Ti matrix due to the increased melting pool temperature and increased cycles of remelting. However, keyhole-induced defects emerged at the island boundaries when the same high AED was used in the chessboard scanning mode. The laser beam delay (LBD) and island spacing (IS) settings were optimised to eliminate keyhole defects. Additionally, it is found that using low and high AED (e.g. 1.6 and 4 J/mm^2), the builds show significantly different microstructure and mechanical properties. In view of this, a Ti-Mo functional gradient composite (FGC) was fabricated via alternating AEDs of 1.6 and 4 J/mm^2 layer-wise. A gradient distribution of α" phase with varied sizes and quantities across the designed layer boundaries was produced. The Ti-Mo FGCs possessed a high compressive yield strength of 1173 (± 15) MPa and improved strain hardening capacity. The developed approach demonstrated the potential for the fabrication of FGCs using an in situ alloying based LPBF.

The chapter is originated from the following publication:

R. Duan, S. Li, B. Cai, Z. Tao, W. Zhu, F. Ren, M.M. Attallah, In situ alloying based laser powder bed fusion processing of β Ti–Mo alloy to fabricate functionally graded composites, Compos Part B Eng. 222 (2021) 109059.

4.1. Introduction

Metastable β-Titanium (Ti) alloys have a wide range of potential structural and biomedical applications due to their high specific strength, low modulus, and excellent fatigue and corrosion resistance [1]. Ti-Mo alloys are among the most promising metastable β-Ti alloys, which exhibit high ultimate strength and exceptional ductility [1,2]. However, Ti-Mo based alloys are difficult to be fabricated using conventional methods, such as vacuum arc melting and powder metallurgy. Due to the high melting point of Mo and the low interdiffusion rate between Mo and Ti [3], vacuum arc melting of Ti-Mo alloys usually requires several remelting cycles, followed by long-term homogenisation heat treatment [4,5]. For the powder metallurgy route, preparing pre-alloyed powders through atomisation is expensive and time-consuming [6]. In addition, machining β-Ti alloys are not easy because of their low thermal conductivity, which reduces the heat diffusion between the tool and workpiece and decreases the tool life [7,8]. Therefore, it is of interest to find an alternative low-cost approach to fabricate β Ti-Mo alloys in a near-net-shape form.

Recently, laser powder bed fusion (LPBF), a disruptive additive manufacturing (AM) technology, has demonstrated significant potential for the fabrication of β-Ti alloys [9]. Several β-Ti alloys have been successfully fabricated using LPBF [9,10], such as Ti-24Nb-4Zr-8Sn (weight per cent, and hereafter) [9], and Ti-15Mo-5Zr-3Al [10]. However, most previous studies used pre-alloyed powders, which require long processing cycles, including preparing homogeneous ingots and atomisation processes, which is expensive due to the low powder yield in the optimum size range (approximately 15–60 μm) for LPBF [6]. In situ alloying of the blended powders is, therefore, attractive for the AM fabrication of β-Ti alloys, which has been demonstrated in Ti alloys [11–13], steels[14], Ni-based superalloys[15],NiTi alloys[16], and Zn alloys[17]. Using in situ alloying methods, instead of pre-alloyed powders, to process Ti

alloys is cost-effective and offers great opportunities to produce non-conventional alloys [18–21]. However, unmelted refractory elemental particles and inhomogeneous element distribution have been observed in the β-Ti alloys fabricated using in situ alloying methods [12] due to the high melting points and low interdiffusion rates of the refractory alloying elements in Ti-based alloys [3]. For instance, Mo has a melting point of 2,623°C, approximately 1,000°C higher than Ti (1,668°C). The laser reflectance of Mo is also higher than Ti [22]. These factors mean that it is hard to melt the Mo particles completely. Although the elements are entirely soluble [12], according to the Ti-Mo phase diagram, previous studies have shown an extremely low interdiffusion coefficient between Ti and Mo in the range from 10^{-14} to 10^{-11} m^2/s depending on the homogenisation temperatures [3]. Therefore, it is challenging to produce Ti-Mo alloys without unmelted Mo particles that are free from chemical heterogeneity using in situ alloying based LPBF. In this study, the optimisation and processing conditions (mainly the input laser power density) for LPBF of a Ti-Mo binary alloy are presented, which would allow the dissolution and homogenisation of Mo in the Ti matrix.

Keyhole-induced defects form during LPBF, which lead to low fatigue strength and premature failure [23]. Therefore, the reduction of keyhole defects is essential for the structural integrity of the printed components. When the energy input increases, the melt pool transfers from a shallow and semicircular shape to a narrow and deep shape, forming the keyhole [23]. Although the keyhole might facilitate the absorption of laser and energy efficiency relatively, it could be trapped in the components due to the defects caused by the laser's multiple reflections inside the keyhole [24]. Recently, the high-speed synchrotron X-ray radiographic observations [23] revealed that keyholes formation followed the sequence of vaporisation, suppression of the liquid surface, instability, and then pore formation. The suppression of the liquid surface was caused by the recoil pressure [25], which formed as a result of vaporisation

[26]. The acoustic waves generated by the keyhole instability are also a key driving force for its formation [27]. In this work, when the optimised laser processing parameters to melt and homogenise Mo in the Ti-Mo alloy were identified, keyhole defects were introduced. Then, the laser scanning parameters were optimised further, which largely eliminated the keyhole defects.

Nature creates functional gradient structure to obtain a biological system with high strength and toughness to endure the complex natural environment [21,28]. These bioinspired gradient systems have proved their superiority to the conventional homogeneous structure [29]. Several methods have been developed to manufacture bioinspired gradient metallic structures, such as the surface mechanical attrition treatment [30] and high-pressure torsion [31]. The gradient structure shows an excellent combination of high strength and ductility. Recently, laser additive manufacturing has been used to process gradient structures. Different laser scanning parameters could introduce significantly different thermal history during processing [32], which means that it could be a potential method to produce the bioinspired gradient structure by varying the processing parameters. Philipp *et al*. [33] have produced a Damascus steel with a microstructure of alternating soft and hard layers by controlling the laser scanning pauses, which illustrated improved mechanical properties than ancient Damascus steel. This work explored the feasibility of using an in situ alloying based LPBF to produce FGCs.

In this study, a processing route for the fabrication of Ti-Mo alloys and Ti-Mo FGC using an in situ alloying based LPBF is presented. The contribution of this study is two-fold: (1) LPBF in situ alloying is demonstrated to be a promising manufacturing route for new alloy fabrication when pre-alloyed powders are challenging to produce; and (2) in situ alloying LPBF could be used to create components with gradient composition and microstructure, which has the potential to fabricate high-performance FGCs.

4.2. Experimental

4.2.1. Powders

Gas atomised pure Ti (Purity>99.9%) and Mo (Purity>99.9%) powders (TLS Technik GmbH, Germany) were used as the base powders for Ti-12Mo powder blends. Both Ti and Mo powders were spherical. The Ti powder had a size in the range of 20-63 μm, and a d50 of 42.9 μm (Fig. 4.1a), while the Mo powder was sieved using 50 μm sieves and had a particle size in the range of 5-45 μm and a d50 of 20.7 μm (Fig. 4.1a). The mixed powders were blended for 24 h using a tumbler mixer (Fig. 4.1b), under the protection of an Argon atmosphere. As shown in the backscattered electron (BSE) micrograph (Fig. 4.1c), no agglomeration of the Mo powders in the blended powders was observed, suggesting a uniform blending.

The flowability of the pure Ti powder and Ti-12Mo mixed powders were tested using the RST-XS Schulze Ring Shear Tester (Germany), in accordance with the standard of ASTM-D6773 [34], to ensure appropriate spreading during LPBF (Table 4.1). The flow function coefficient (F.F.C), which indicates the powder flowability, was >10 in the blended powders, indicating free-flowing powders. In addition, the Hausner ratio was measured, and there was good flowability because the Hausner ratio was <1.25. This shows that the flowability of blended powders of Ti and Mo is as good as that of pure Ti powders.

Table 4.1. Characteristics of pure Ti and Ti-12Mo blended powders.

	Apparent density (g/cm^3)	Tap density (g/cm^3)	F.F.C.	Hausner ratio
Ti	2.2 ± 0.01	2.6 ± 0.01	19.0 ± 1.0	1.2 ± 0.01
Ti-12Mo	2.5 ± 0.03	3.0 ± 0.02	22.5 ± 0.4	1.2 ± 0.01

4.2.2. LPBF process

All specimens and components were fabricated using a Concept Laser M2 Cusing® LPBF system, which was equipped with a 400 W Nd:YAG continuous laser source and a laser spot diameter of ~70 μm. The LPBF in situ alloying processing is shown in Fig. 4.1d. The Ti6Al4V plate, with a dimension of 90 mm × 90 mm, was used as the substrate for the fabrication. The builds were carried out using a 20 μm powder layer thickness under a controlled argon atmosphere, where the oxygen content was ~1000 ppm. The oxygen and nitrogen content of the fabricated Ti-12Mo samples were measured using the ON736 elemental analyser (LECO, US), which was 0.236 (± 0.010) wt% and 0.091 (± 0.008) wt%, respectively. Simple scan and chessboard (island) scan strategies (Fig. 4.1e) were used with varied input energy, scanning speed, and hatch spacing, as shown in Table 4.2. The island spacing (IS; the overlap of neighbouring islands) and the laser beam delay (LBD; laser dwelling time) were optimised to obtain samples without defects (Fig. 4.1f). To represent an equivalent heat input in LPBF, when different processing parameters were applied, the laser area energy density (AED) was calculated [35], which is given by:

$$AED(J/mm^2) = \frac{Laser\ Power(W)}{Scan\ speed(mm/s) \cdot Hatch\ spacing(mm)} \quad (4.1)$$

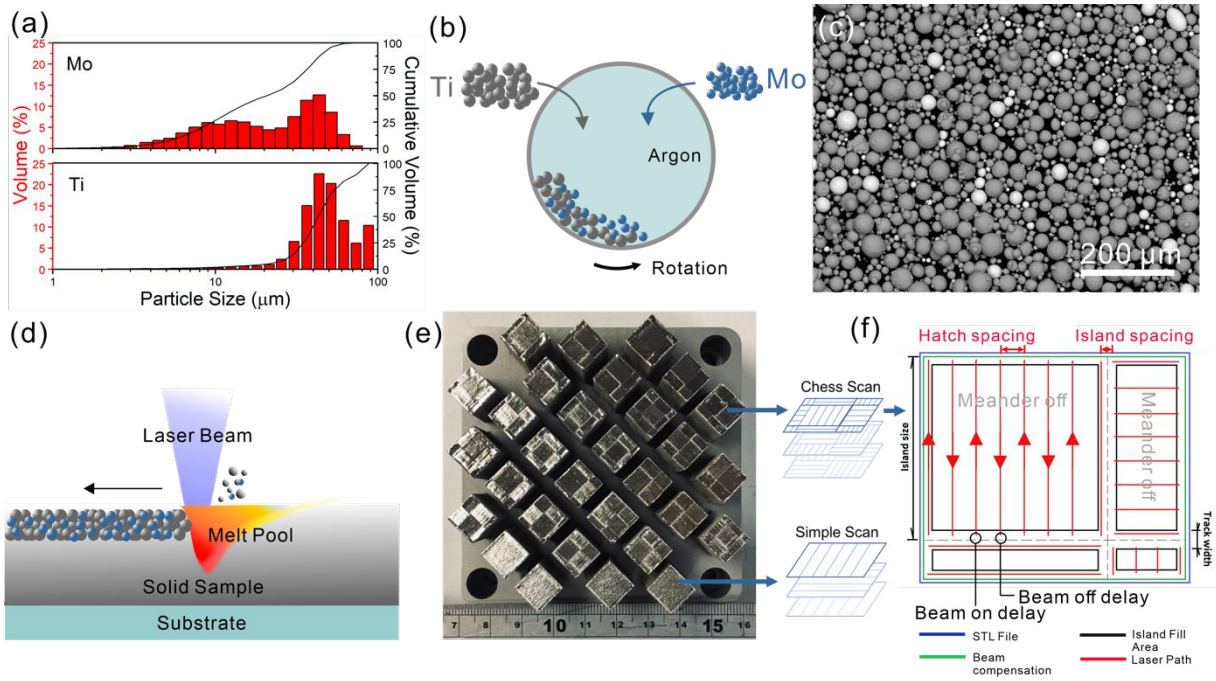


Fig. 4.1. (a) The particle size distributions of Ti and Mo elemental powders; (b) the schematic of the powder blending process; (c) BSE micrograph of Ti12Mo blended powder; (d) the schematic of LPBF in situ alloying processing; (e) as-fabricated samples with different scanning parameters; and (f) schematic illustration of the scanning strategies depicting the island spacing, and beam delay settings.

Table 4.2. Scanning parameters of the Ti-12Mo alloy using LPBF.

No.	Laser power (w)	Scan speed (mm/s)	Hatch spacing (mm)	Linear energy density (J/mm)	Area energy density (J/mm^2)
1	250	2500	0.075	0.10	1.3
2	200	2000	0.06	0.10	1.7
3	250	1500	0.075	0.17	2.2
4	300	1000	0.075	0.30	4
5	200	1000	0.045	0.20	4.4
6	300	1000	0.06	0.30	5

4.2.3. Microstructural characterisation

The fabricated specimens were sectioned for microstructural characterisation and mechanical testing using electrical discharge machining. For scanning electron microscopy (SEM) and optical microscopy (OM) observations, the specimens were sequentially ground with 220- and 1200-grit papers, polished using MD-Chem with OPS-H_2O_2 solution (Struers, Denmark), and etched using Kroll's reagent (2% HF + 6% HNO_3 + 92% distilled water) for 30 s. Zeiss Axioskop 2 microscopes were used for OM observation. The microstructure of the polished samples was studied using SEM (TESCAN MIRA 3, Czech Republic) operated in secondary electron and BSE imaging modes (without etching). The elemental distribution was analysed using energy dispersed X-ray spectroscopy (EDS) performed using X-Max^N Silicon Drift EDS Detector (Oxford Instruments, Oxford, UK), equipped in SEM, and electron probe microanalysis (EPMA) characterised by a JXA-8530 analyser (JEOL, Tokyo, Japan). The crystallographic orientation and local misorientations were characterised using electron backscattering diffraction (EBSD) with a step size of 0.5 μm and analysed using Channel 5 software. In addition, the microstructure was investigated using a transmission electron microscope (TEM; Tecnai F30, FEI, US) operated at 300 kV. The high-angle annular dark-field scanning TEM (HAADF-STEM) imaging and EDS mapping were performed on an FEI Talos TEM at 200 kV. The TEM samples were prepared using Ga focus ion beam (FIB; Dual Beam Heilos^{TM} Nanolab 600i, FEI) milling. X-ray diffraction (XRD) patterns were recorded using a Rigaku Smartlab-9kW diffractometer (Rigaku, Tokyo, Japan) in the 2θ range of 20˚-100˚ with Cu-Kα radiation (λ = 1.54056 Å, 45 kV, 200 mA). The specimens' densities were measured by a Practum 224 balance (Sartorius, Germany) using the Archimedes principle. NIH ImageJ software was used to calculate the porosity percentage, relative density (100% - void percentage), and the percentage of unmelted Mo.

4.2.4. Mechanical testing

Vickers microhardness tests were performed using a Struers DuraScan machine equipped with an automated indenter under a load of 100 g for 15 s per point. The groups of single crystal micropillars (2 μm diameters) were prepared using FIB (Dual Beam Heilos^{TM} Nanolab 600i, FEI) operated at an Ga ion beam voltage of 30 kV, along the <001> orientation of the β matrix. The uniaxial compression tests were performed using a Hysitron Ti-950 nanoindenter equipped with a 10 μm flat diamond tip, at a constant strain rate of 5×10^{-4}/s. Macro-compression tests (with the sample size of 3 mm × 3 mm × 7 mm) were conducted using an MTS CMT 5000 machine with a crosshead rate of 0.2 mm/min, following the ASTM E9-09 standard [36]. Digital image correlation (DIC) technology with a camera (Canon, Japan) recording was performed during compression tests. The obtained images were analysed using GOM correlate software (Zeiss, Germany). The tests were repeated three times to verify the reproducibility of the results.

4.3. Results and Discussion

First, the melting and homogenisation of refractory Mo particles during LPBF processing of a Ti-12Mo alloy as a function of laser energy input were investigated using a simple scanning strategy. When the optimal laser energy input was identified, the chessboard scan strategy was used to print the Ti-12Mo alloy; however, keyhole defects formed. The keyhole defects were largely eliminated by controlling LBD and IS settings. In addition, we produced a layered Ti-Mo FGC, of which the macro- and micro-mechanical properties, and the microstructures were characterised in detail.

4.3.1. Melting and homogenisation

To obtain Ti-Mo alloys with no unmelted Mo particles and ensure that Mo was homogeneously distributed, the LPBF parameters were optimised using a simple scan strategy, varying laser energy, scan speed and hatch spacing, as specified in Table 4.2. The corresponding AED was calculated according to Eq. 4.1. Fig. 4.2a shows the BSE micrographs for the residual unmelted Mo powder within the builds with the increase of AED. The percentage of unmelted Mo was measured from the BSE images, which is plotted as a function of AED, as shown in Fig. 4.2b. The percentage of unmelted Mo decreased with an increase in AED from 1.3 to 4 J/mm^2. Then, the unmelted Mo particles reached an extremely low level ($\leq$ 0.15 %) when the AED was > 4 J/mm^2. This meant that the Mo particles were almost completely melted into the Ti matrix using LPBF with a high AED of 4 J/mm^2. The diffraction peaks of Mo was detected in the XRD patterns of the Ti-12Mo builds (Fig. 4.2c) at a laser AED of 1.7 J/mm^2, but such peaks disappeared at 4 J/mm^2, which indicate the melting and dissolution of Mo at 4 J/mm^2. The BSE image of Fig. 4.2d also shows no residual Mo particles.

The elemental distributions and chemical homogeneity of the Ti–12Mo alloy, prepared at 4 J/mm^2, were confirmed by EDS (Fig. 4.2e-f) and EPMA (Fig. 4.2h-i). The elemental maps were all taken from the middle of the sample. EDS elemental maps (Fig. 4.2e-f) show that Ti and Mo were distributed uniformly in the Ti-12Mo alloy, which accounted for 88.2 ($\pm$ 0.1) wt% and 11.8 ($\pm$ 0.1) wt%, respectively. The BSE image (Fig. 4.2g) revealed the grain boundaries and melt pool boundaries of the Ti-12Mo alloy at a higher magnification. The corresponding EPMA elemental maps (Fig. 4.2h and i) show that a small amount of Mo is segregated along the melt pool boundaries, which are indicated by black arrows. The lowest and highest Mo concentrations were 7.84 wt% and 15.42 wt%, respectively.

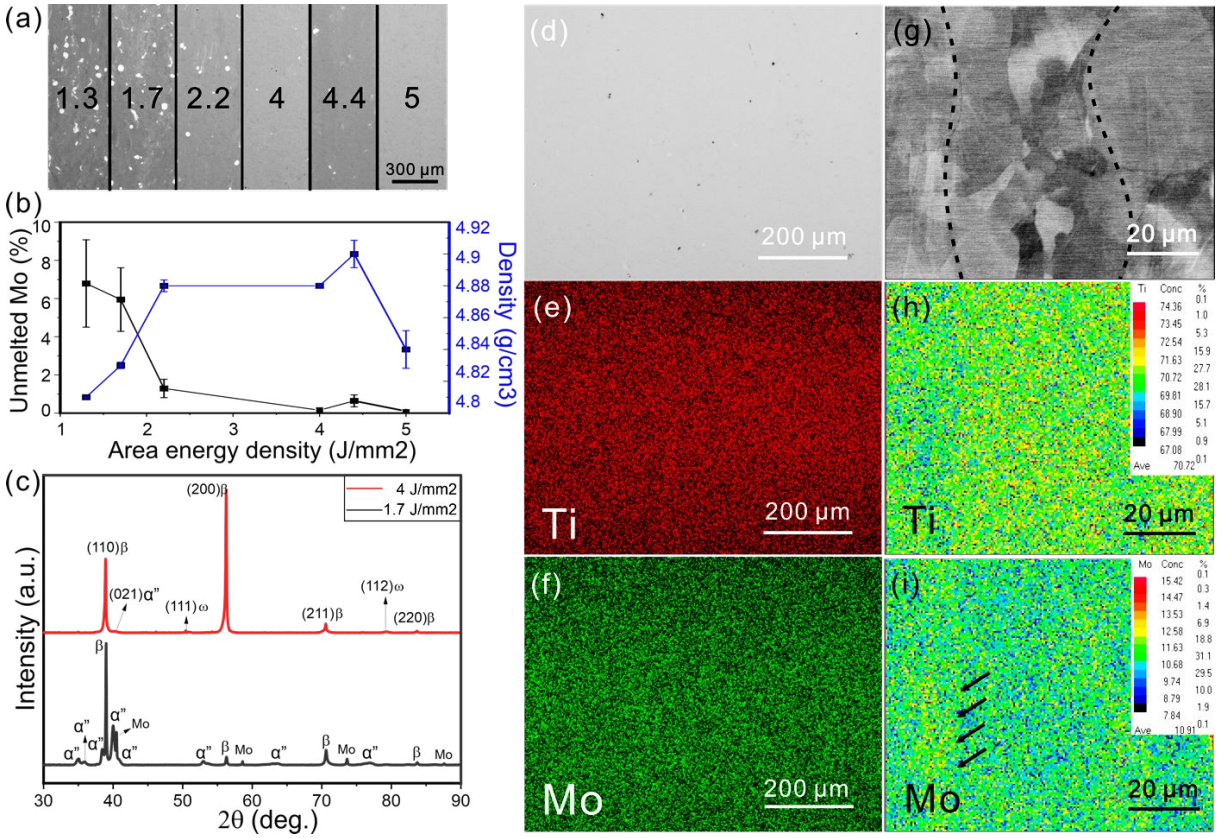


Fig. 4.2. (a) BSE images of as-fabricated Ti-12Mo specimens (values on the images are the AED); (b) effect of AED on the percentage of un-melted Mo and density; (c) XRD patterns of as-fabricated Ti-12Mo cube specimens; (d) BSE micrograph of Ti-12Mo sample; (e) and (f) are EDS elemental maps of Ti and Mo, respectively; (g) high magnification BSE micrograph (black dotted lines indicated the melt pool boundaries); (h) and (i) are the EPMA maps of Ti and Mo, respectively (Black arrows indicated the chemical segregations).

The melt pool's microstructure was further examined for the builds with AEDs of 1.7, 2.2 and 4 J/mm^2. At a low AED of 1.7 J/mm^2, fish scale-like melt pools were observed with many unmelted Mo particles (Fig. 4.3a). Mo particles or Mo-riched regions were much brighter than the Ti matrix in the BSE image. Most of the coarse Mo particles were round, which indicated that those particles were hardly melted. There was some indication of Mo particles' melting, for example, irregular Mo particles and crescent-shaped Mo enriched areas. The crescent-shaped Mo enriched areas (pointed by the red arrows) were less bright than the round-shaped Mo

particles. The shapes and contrast suggested that these were the regions where Mo particles had been melted and mixed with Ti; however, they were not homogenised. The residual Mo particles ' quantity was significantly lower at a higher AED of 2.2 J/mm^2 (Fig. 4.3b). Many irregulars or crescent-shaped Mo enriched areas (red arrows) and some partially melted Mo particles in a semicircular shape. At the AED of 4 J/mm^2 (Fig. 4.3c), no apparent residual Mo particles were observed. There was no prominent crescent-shaped Mo enriched area either.

Fig. 4.3d shows the sample's melt pool depth processed by an AED of 1.7 J/mm^2, which was 99.1 (± 5.6) μm. When the AED increased to 2.2 J/mm^2, the melt pool depth increased to be 181.6 (± 10.1) μm (Fig. 4.3e). The melt pool depth fabricated with an AED of 4 J/mm^2 was 379.0 (± 10.2) μm (Fig. 4.3f). The melt pool depth, which was the laser penetration depth, depended on the energy input and beam size, as well as the laser beam absorption, thermal conductivity and thermal diffusivity of the powder [37]. In this study, the melt pool depth depended on the AED value because the materials' physical properties and the laser beam size were the same for the three samples. The results showed a positive linear correlation between the AED and melt pool depth, as shown in Fig. 4.4, in good agreement with previous findings [38].

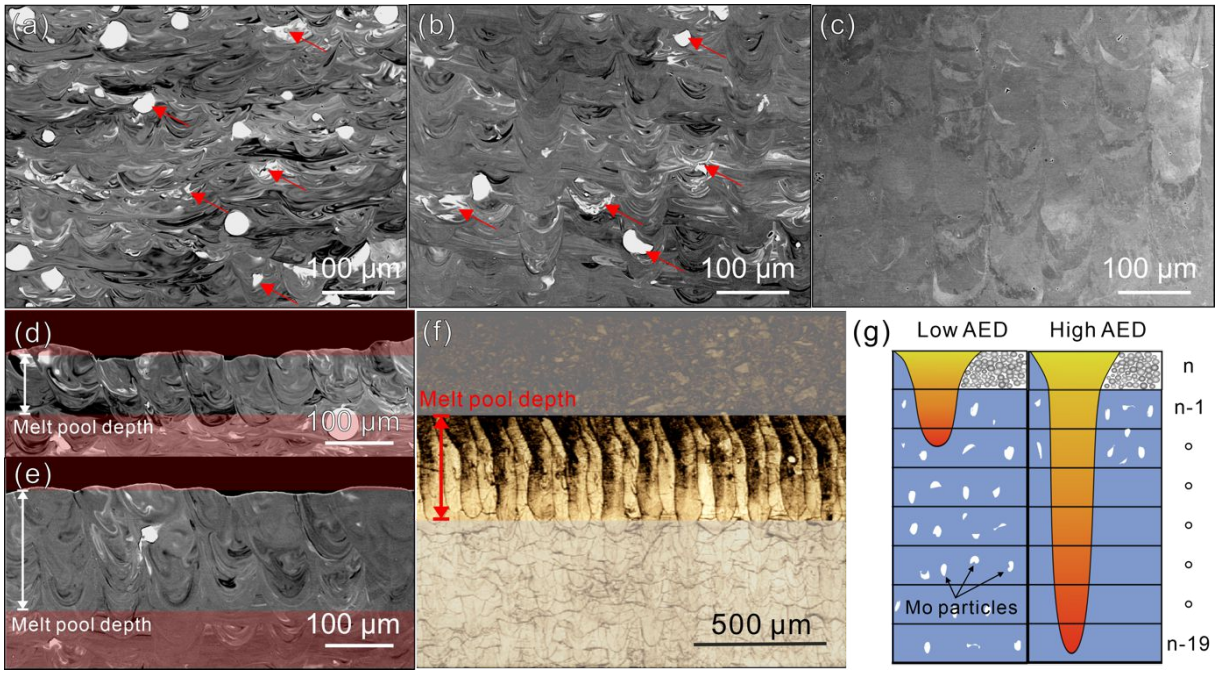


Fig. 4.3. (a)–(c) are side-view BSE micrographs of the as-fabricated Ti-12Mo sample under different processing conditions: (a) low AED (1.7 J/mm^2), (b) middle AED (2.2 J/mm^2), and (c) high AED (4 J/mm^2); (d) and (e) are the side-view BSE images of the top layer of the samples fabricated using the AED of 1.7 and 2.2 J/mm^2, respectively; (f) the side-view optical micrograph of the top layer of the sample fabricated using AED of 4 J/mm^2; (g) the schematic illustration shows the remelting process of Mo particles during LPBF.

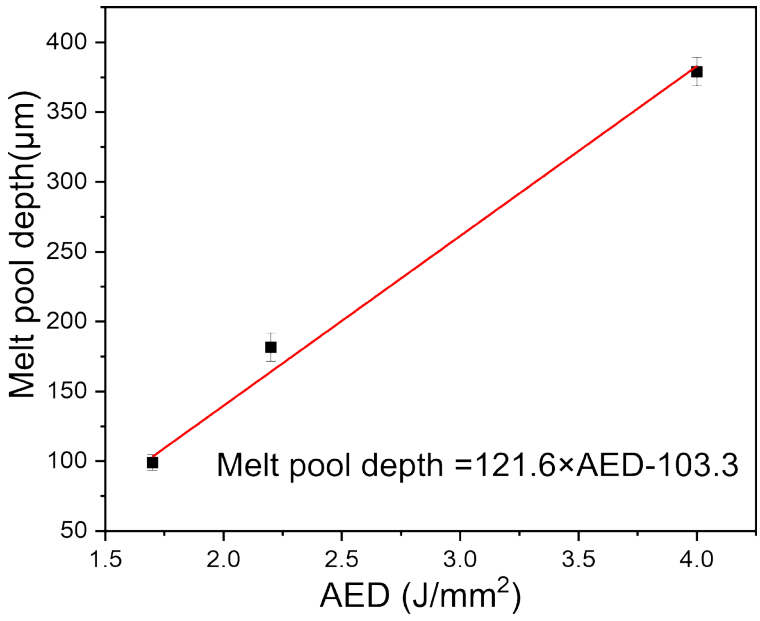


Fig. 4.4. The linear correlation between the melt pool depth (μm) and AED (J/mm^2).

To manufacture a Ti-Mo alloy from Ti and Mo powders using LPBF, the first challenge that must be overcome is to melt the Mo particles. Mo has a very high melting temperature of 2,623°C. To melt the Mo particles in the blends, the melt pool temperature needed to reach over the melting point of Mo. However, due to the lack of direct temperature monitoring of the melt pool in this study, the melt pool temperature could only be inferred from the melt pool characterisation. At a higher AED (e.g., 4 J/mm^2), the Mo particles were fully melted (no residual Mo, Fig. 4.3d). Some residual Mo particles were observed at a lower AED (e.g., 1.7 and 2.2 J/mm^2). However, some crescent-shaped Mo enriched areas (Fig. 4.3a and 4.3b, marked by red arrows) indicated melting of Mo, which suggests that the temperature in the melt pools was higher than the melting point of Mo particles during processing. The unmelted Mo particles were relatively large (> 23.3 ± 6.4 μm diameter) when AED is low (Fig. 4.3a and 4.3b), indicating that the coarse Mo particles require higher AED to melt entirely.

The second challenge for the in-situ alloying LPBF processing of Ti-Mo alloys is to homogenise Mo into the Ti matrix. There are two methods to homogenise the powder layers during the in-situ alloying based LPBF. One uses laser rescanning for each powder layer, as Brodie et al. [39] performed. The other uses extremely high energy input (up to 950w), as Huang et al. [40] reported. In this work, we have investigated microstructural evolutions on Ti-Mo binary system with the energy input from low AED to high AED. The homogeneous microstructure was achieved via multiple remelts. During LPBF, each layer experiences multiple remelts from the laser beam, while the number of remelts depends on the melt pool depth. A constant powder layer thickness of 20 μm was used. The melt pool depths that used an AED of 1.7, 2.2 and 4 J/mm^2 were 99, 182 and 379 μm, respectively. The remelt cycles can be estimated by dividing the melt pool depth by the layer thickness (20 μm). Therefore, the remelt cycles of the three samples were estimated to be 5, 9 and 19, respectively. A higher AED

of the laser significantly increased the number of remelts.

In a conventional arc melting process to cast Ti-Mo alloys, at least five remelts are applied to ensure homogenization[41]. Fig. 4.3g schematically shows how multiple remelts can help the homogenisation of Mo. At a low AED of 1.7 J/mm^2, the melt pool was remelted five times. A large amount of Mo did not thoroughly mix into the Ti matrix, as shown in Fig. 4.3a and g. At a higher AED of 4 J/mm^2, the melt pool remelted approximately 19 times, allowing Mo to dissolve into the Ti matrix fully (Fig. 4.3c and g). Therefore, the homogenisation of Mo into the Ti matrix at a higher AED was attributed to the increased penetration depth, which enabled each layer to experience increased remelt cycles.

In summary, using a suitable high AED parameter, the laser beam could melt the refractory Mo particles into Ti and Mo powder blends and homogenise the composition. This would ensure the chemical homogenisation and mechanical repeatability in the Ti-12Mo component produced by the cost-effective LPBF in situ alloying.

4.3.2. Keyhole-induced defects

When simple scanning was applied at an AED of 4 J/mm^2, no pores were found visually inside the specimens (Fig. 4.3c), and the relative density reached 99.99 (± 0.01) %. However, upon further increasing the AED to 5 J/mm^2, the relative density showed a slight decrease to 99.45 (± 0.03) %, due to the formation of keyhole pores, as demonstrated in Fig. 4.5.

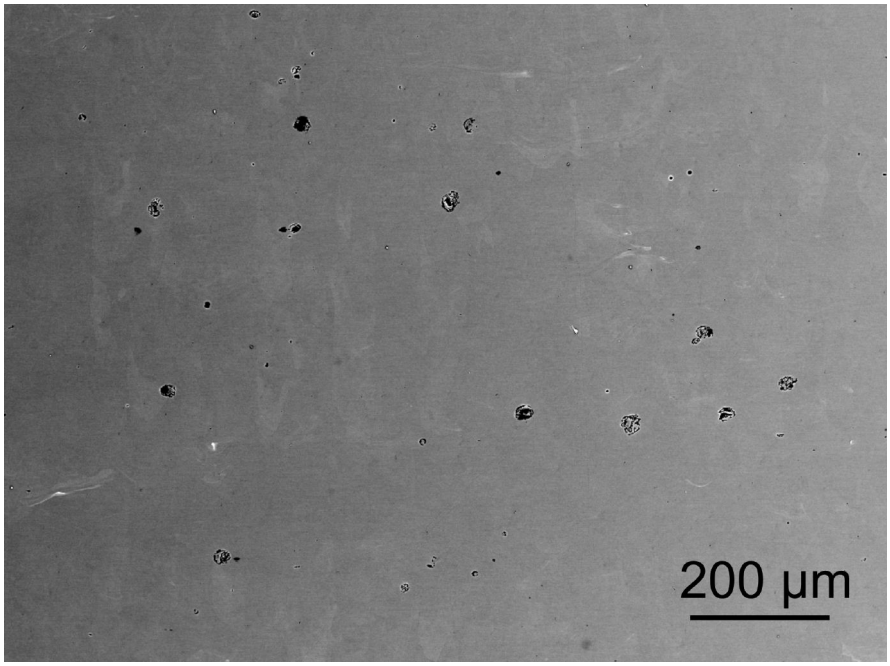


Fig. 4.5. The BSE image of the Ti-12Mo sample was fabricated using the AED of 5 J/mm^2.

The optimisation of LPBF processing parameters via a simple scan strategy showed that, at an AED of 4 J/mm^2, Mo particles could be melted, and the composition was homogeneous. However, to manufacture large components, the simple scanning strategy results in high thermal residual stress, which would increase cracking potential [42], due to the considerable scan track length and slower cooling rate [43]. To reduce the inner residual stress, it is necessary to use more advanced scanning strategies, such as chessboard scanning with a smaller scan track length [44]. However, keyhole defects emerged when chessboard scanning was conducted at the AED of 4 J/mm^2, as shown in Fig. 4.6a. Some regions contain high-density keyholes, where the width is the same as the island's (5 mm). The spacing between the keyholes is mainly consistent. Thus, the regions may be located right on the edge of two neighbour islands because the scanning traces are perpendicular between the adjoint islands. Fig. 4.6b shows the melt pool morphology on the top layer of the chessboard scanned Ti-12Mo alloy, which did not experience successive remelts. The keyhole defects were located at the bottom of the melt pool.

Fig. 4.6c shows the melt pools and pores in the middle layer of the chessboard scanned Ti-12Mo alloy. Some pores were observed at the bottom of the melt pools, while some elongated pores crossed a few layers.

Keyhole defects are related to the laser energy input. If the laser energy is too high, large keyhole defects could form [23]. The formation mechanism for keyhole defects is shown in Fig. 4.6d. During the interaction between the laser beam and powder bed, holes were generated at the bottom of the melt pool (Fig. 4.6b) after a single melt, where the highest energy was concentrated at the bottom of the melt pool [45]. This induced a temperature gradient from the bottom to the top of the melt pool. The laser beam penetrated deep into the material if sufficiently high energy was applied. In this case, the metal vaporised from the bottom of the melt pool, which could cause intense recoil pressure that would push the liquid metal away from the solid part [46]. Following solidification, pores were trapped at the bottom of the melt pool (Fig. 4.6c). If the laser energy was high enough to cause deep multiple remelts, beam penetration could repeatedly open the pore defects, which elongated the keyholes, as schematically shown in Fig. 4.6d.

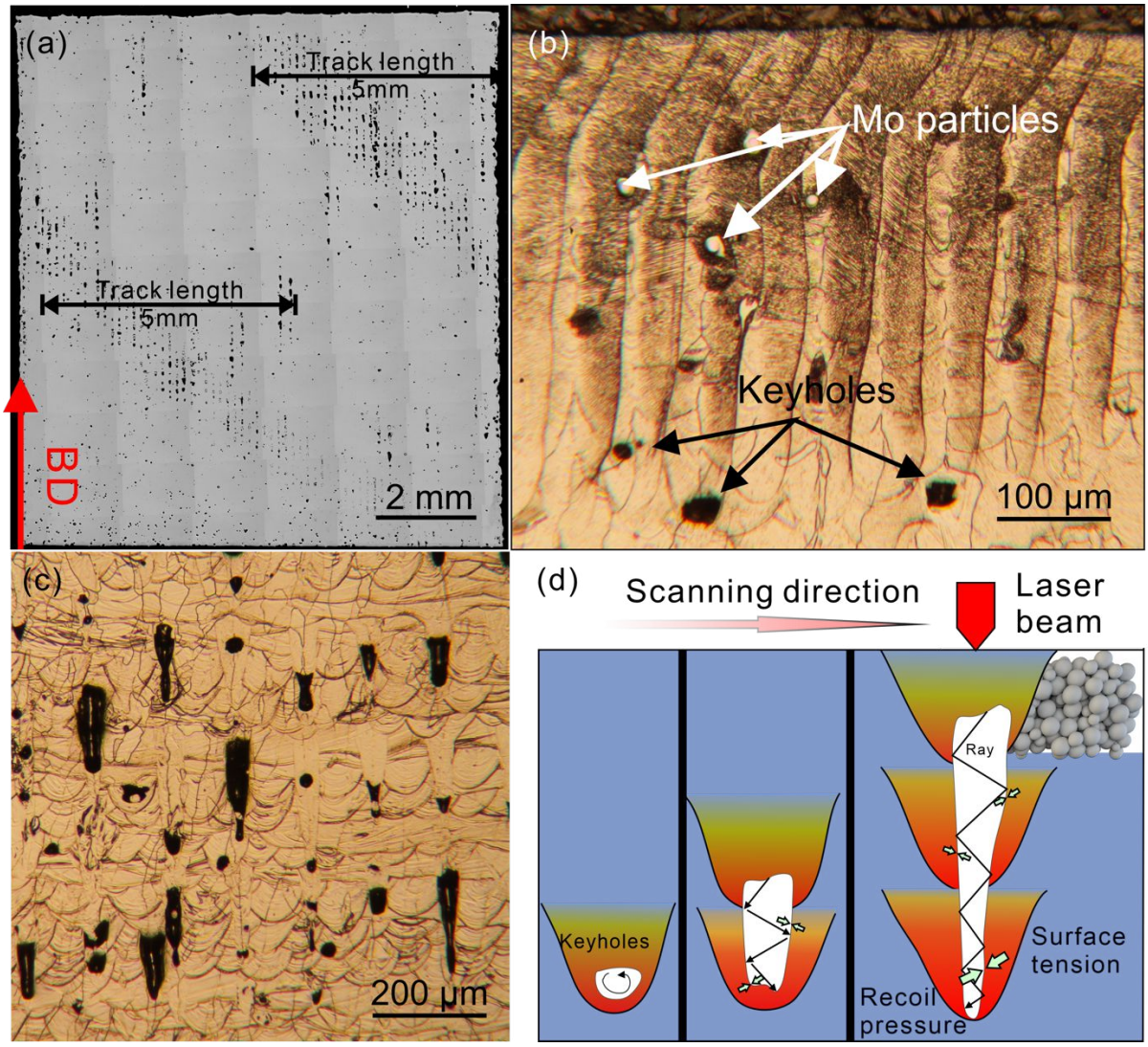


Fig. 4.6. (a) Optical micrograph of the full side section of the chessboard-scanned Ti-12Mo sample fabricated using AED of 4 J/mm^2, and high LBD settings; (b) and (c) are side-view optical micrographs of the keyholes of the chessboard-scanned Ti-12Mo alloy: (b) top layer; and (c) middle layer; and (d) the schematic illustration of the formation of keyholes defects.

Using the same AED of 4 J/mm^2, the keyhole-induced defects were observed in the samples processed by the chessboard scanning strategy (Fig. 4.6a), and also in the edge of the samples prepared using simple scanning strategy with high LBD (Fig. 4.7a).

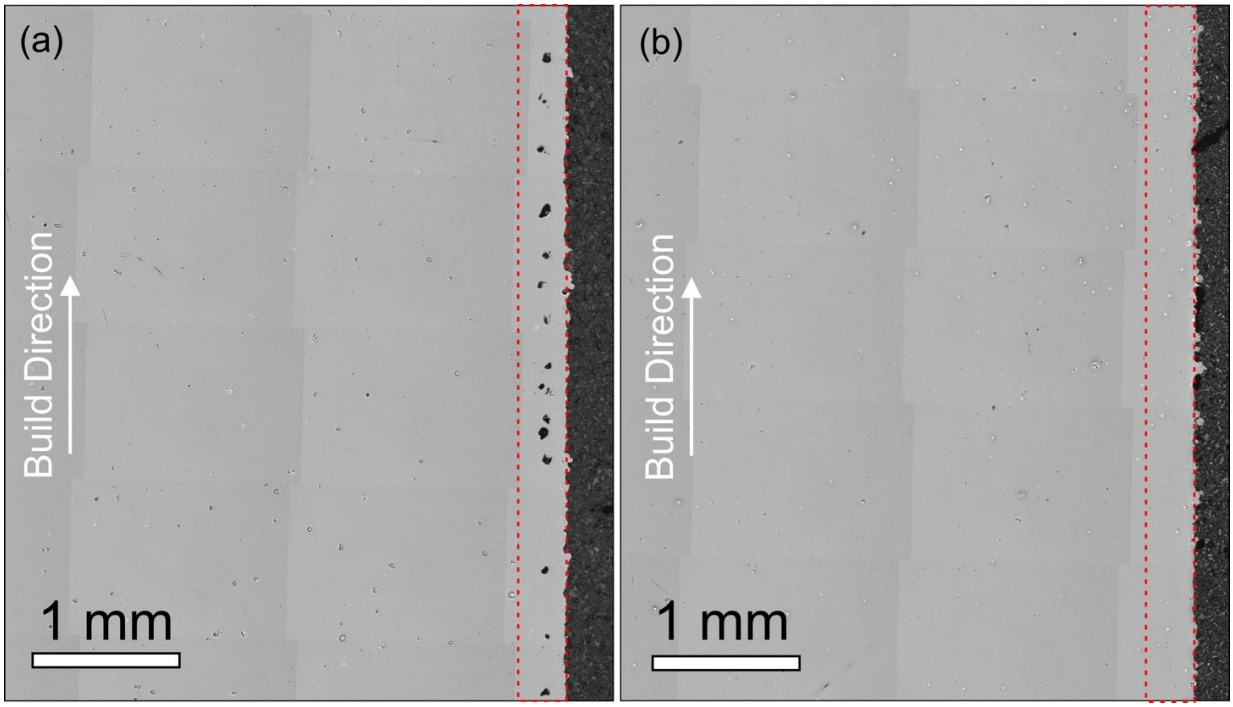


Fig. 4.7. The OM microstructures of the specimens were fabricated using the simple scanning strategy with high (a) and low (b) LBD settings, respectively, of which the other scanning parameters are the same.

In this study, low and high LBD values were set to 0.1 and 0.3 ms, respectively. The microstructure of the samples processed using the same parameters of chessboard scanning strategy, with varied LBD settings, have been compared (Fig. 4.8a and 4.8b). The melt pool shapes can be clearly observed. The deep melt pool can be seen from the start and endpoint of scanning trace in the high LBD sample (Fig. 4.8a). Some keyholes were also formed at the edge of the islands. These findings indicate that the laser dwelled at the scan trace's start and endpoint before changing the laser vector (Fig. 4.8c). Due to the island shift (X + 1 mm and Y + 1 mm) and rotation (90º) for each layer, the keyholes were also found in some layers. These keyholes should be formed right on the edge of the neighbour island. The distance of the keyholes along the build direction is about 200 μm, which is ten times the powders' layer thickness. This is because the island would move to the original position with the same scanning direction after ten shifts because of the island shift and rotation. The chessboard scan profile is also shown in

Fig. 4.8d, where the red lines indicate scan traces. According to Fig. 4.8c, a higher dwelling time at the start (t1 to t2) and end (t5 to t6) of the scan path resulted in a higher laser energy input than that of the middle of the scan trace (which is the same as the simple scan used the same overall AED of 4 J/mm^2). Hence, the AED should be higher than 4 J/mm^2 during dwelling, accelerating and slowing down of laser beam. As we stated before, pores defects also formed when AED was increased to 5 J/mm^2 for the simple scan. Therefore, keyhole defects formed at the start and end of the scan paths.

Due to the high AED applied in this work, the formation of keyholes is sensitive to the LBD setting. Although the time to achieve final velocity is short, a bit more delaying (0.2 ms) of dwelling time can induce higher heat concentrations. To eliminate keyhole defects formed during the chessboard scanning, the optimisation of LBD and IS settings were possible solutions. As shown in Fig. 4.8e, the IS could be described as the compensation of adjacent islands to obtain the adequate overlap between the neighbouring islands (marked by green circles in Fig. 4.8d). Comparing the relative density of the chessboard scanned samples with high and low LBD settings, a low LBD could produce samples of high relative density (≥ 99.7%), regardless of the IS (Fig. 4.8f). The LBD setting influenced the melt pool's penetration depth [46], whereby lower LBD led to shallower melt pools at the ends of the scan trace (Fig. 4.8b and 4.8c) that had a lower potential to generate keyhole-induced defects. However, at a higher LBD, IS settings had a strong influence on the relative density. At low IS values, the relative density was low, which indicated the formation of keyhole defects. When the IS was 0.105 mm, the relative density of the print was 99.1 %. The relative density increased to 99.98% with the decrease of IS from 0.15 to – 0.45 mm, which indicated that keyhole defects were eliminated. With suitable IS settings (0.06 mm), the vapour in the keyhole had time to escape from the melt pool before solidification, and the melt pool was not deep enough to create new

pores at the start and end of the scan trace, which allowed the keyholes to close during subsequent remelting. However, the samples cracked when the absolute value of IS settings was too high (≥ 0.45 mm), as shown in Fig. 4.9, which indicated that the high LBD and IS might increase the local inner stresses.

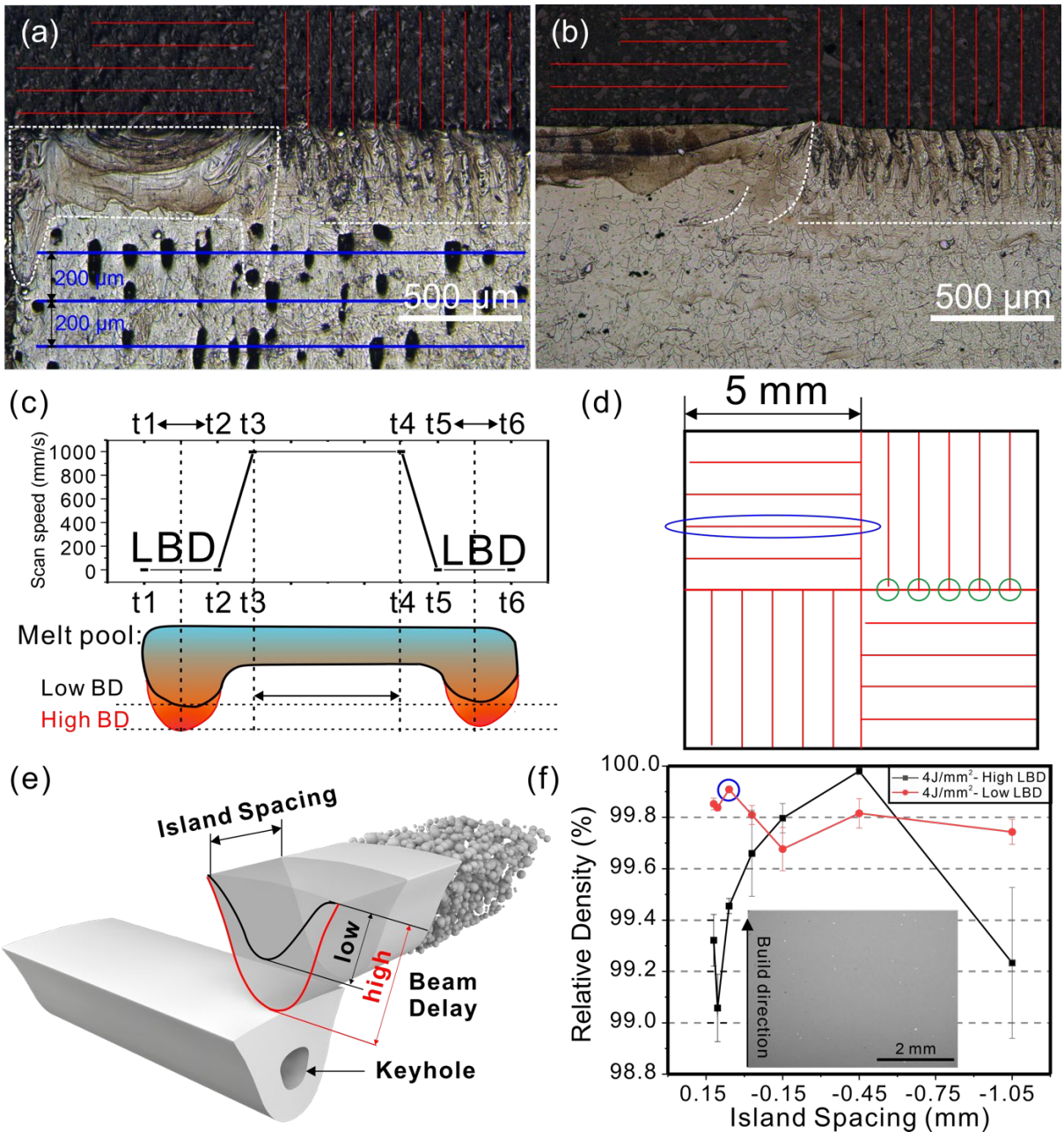


Fig. 4.8. The OM images of the specimens were processed using chessboard scanning strategy with high LBD (a) and low LBD (b), respectively (Red lines indicate the scanning directions of the top layer, the white lines present some melt pool boundaries, and the blue lines indicate

the spacing between the keyholes along the build direction). (c) Schematic illustration of the scanning speed variations during the single scanning trace and the corresponding melt pool shape; (d) scanning traces (red lines) of chessboard-scanned samples (the blue circle marks the single scanning trace, while the green circles indicate the overlap points between the neighbouring island); (e) schematic illustration of the definition of IS parameters and LBD settings; (f) the relationship between the samples' relative density fabricated using 4 J/mm^2 with different IS and LBD settings (inset is the BSE micrograph of the Ti-12Mo alloy fabricated using low LBD and 0.06 IS settings).

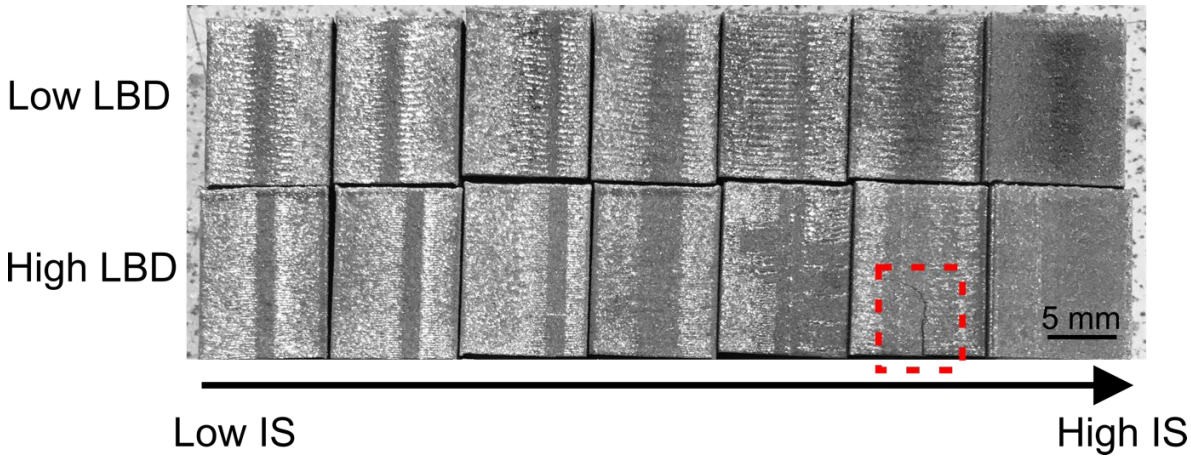


Fig. 4.9. The side-view optical images of the samples for the optimisation of LBD and IS.

In summary, keyhole defects can be formed when laser AED is too high (e.g., > 4.4 J/mm^2). During chessboard scanning, the laser beam is dwelling before accelerating, and after slowing down, its velocity is lower at the two ends of the scanning trace; therefore, the AED was higher. When an AED of 4 J/mm^2 was used for the chessboard scan, the AED at the start and end of the scan trace was much higher than that in the middle, then the keyhole defects formed at the boundaries of the chessboard islands. Thus, reducing the LBD settings helped to eliminate the keyholes. Additionally, a relatively high IS could consolidate the keyholes via remelting and refilling, particularly for high LBD settings. Therefore, the LPBF processing parameters of 4 J/mm^2 AED with a low LBD of 0.1 ms and the IS value of 0.06 mm can fabricate dense Ti-12Mo components with high relative density (> 99.9 %).

4.3.3. Microstructure of the Ti-12Mo alloy

The microstructures of Ti-Mo samples were compared with varied AEDs. The samples processed by low AED (1.6 J/mm^2) and high AED (4 J/mm^2) were named low energy (LE) and high energy (HE) specimens, respectively. The processing parameters are given in Table 4.3. For the LE sample, the XRD pattern in Fig. 4.10a revealed the body-centred cubic (BCC) β and orthorhombic α" phase inside the LE sample, as well as the peaks of Mo. Fig. 4.10b shows the coarse residual Mo particles inside the LE sample, which were partially melted. As shown in Fig. 4.10c, high-density fine α" plates were seen in the LE samples. For the HE specimen, XRD shown in Fig. 4.10d mainly illustrates the β phase and some ω phase, whereas the α" phase was limited. A few small Mo particles were found in the HE samples, as shown in Fig. 4.10e. Under higher magnification (Fig. 4.10f), no α" phase was observed in the BSE image. Comparing HE and LE samples, it was concluded that the amount of residual Mo particles and the phase constitutes were different between the two sets of specimens.

Table 4.3. Scanning parameters of the Ti-Mo FGC using LPBF.

Ti-Mo	Laser power (w)	Scan speed (mm/s)	Hatch spacing (mm)	Island size (mm×mm)	Area energy density (J/mm^2)
LE	120	1000	0.075	5×5	1.6
HE	300	1000	0.075	5×5	4

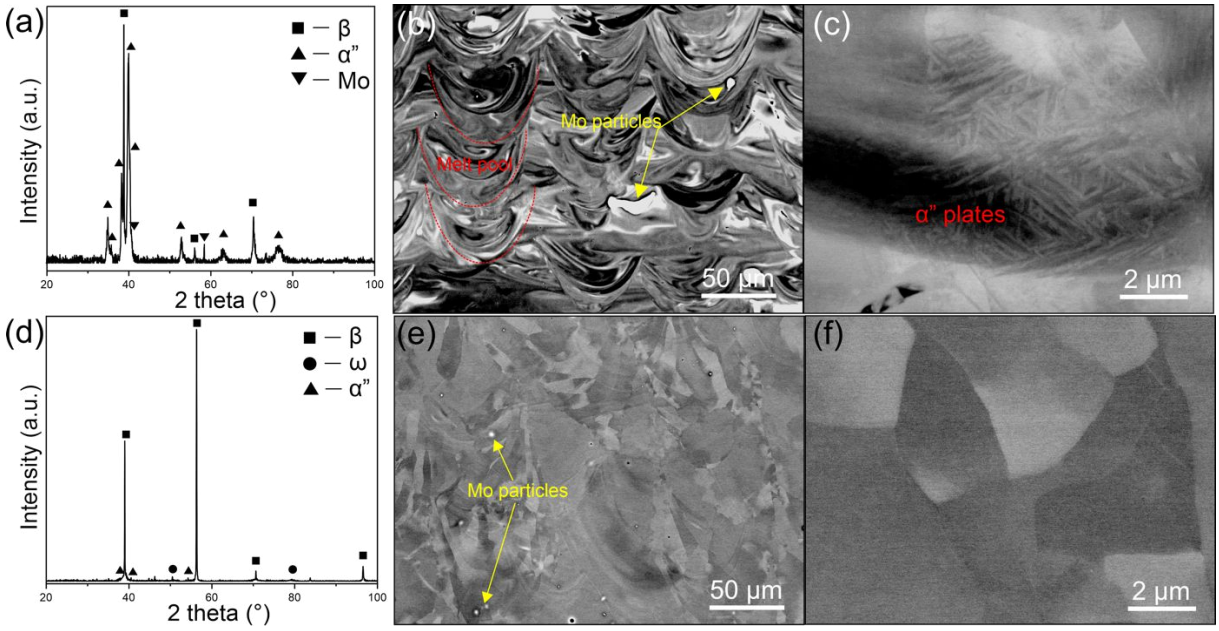


Fig. 4.10. (a)–(c) are the XRD pattern, low magnification and high magnification BSE images of Ti-12Mo alloy fabricated using a low AED of 1.6 J/mm^2, respectively; (d)–(f) are the XRD pattern, low magnification and high magnification BSE images of Ti-12Mo alloy fabricated using a high AED of 4 J/mm^2, respectively.

4.3.4. Fabrication of the Ti-Mo FGC

As shown, different Mo and phase contents can be obtained using different AEDs. Following this, a Ti-Mo FGC was designed with a layered composite structure that alternated the energy inputs, as shown in Fig. 4.11a. The matrix was produced by high energy input at 4 J/mm^2, designated as HE input layers. Two layers were printed using LE, designed with a thickness of 0.5 mm each, in the middle of the HE matrix. The detailed LPBF processing parameters of LE and HE layers were the same as that of the LE and HE samples, respectively (Table 4.3). As shown in Fig. 4.11b, the Ti-Mo FGC is near fully dense, with only a few minor defects. The unmelted Mo particles were found in the LE layer, and only a few unmelted Mo particles were observed in the HE matrix. Fig. 4.11c and 4.11d show the inhomogeneous distributions of Ti and Mo solute elements along the build direction (BD). In the HE layers, Ti

and Mo appeared to be homogeneously distributed. In the LE layers, Mo is still alloying into Ti, although the fraction was lower than that of the HE layers because some Mo particles were unmelted.

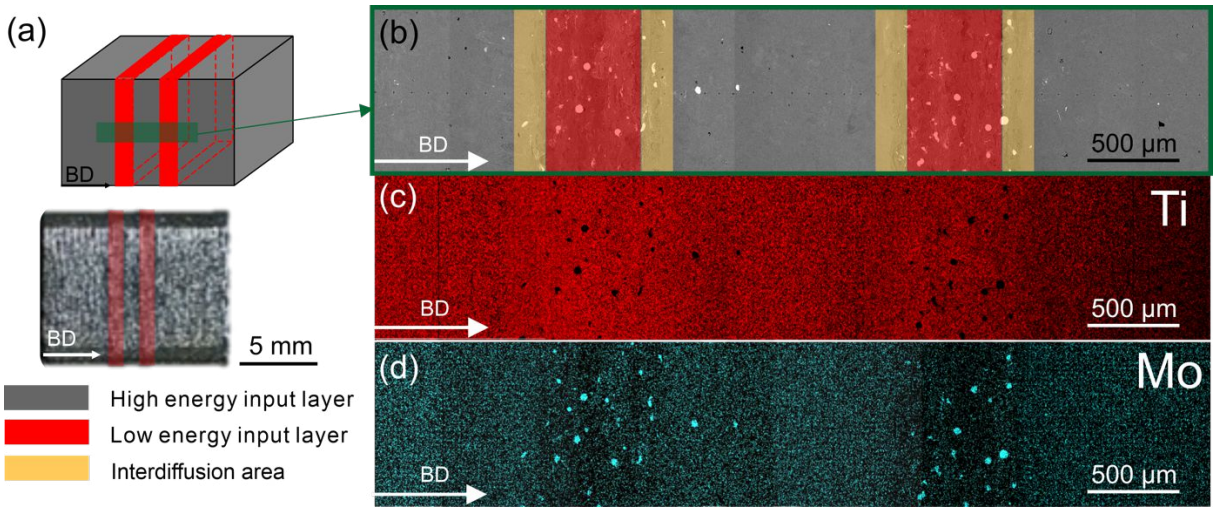


Fig. 4.11. (a) Schematic of the Ti-12Mo FGC with two designed low energy input layers; (b) the merged BSE micrograph of the FGC and the corresponding EDS elemental maps of Ti (c) and Mo (d).

4.3.5. Microstructure of the Ti-Mo FGC

To reveal the microstructure of the Ti-Mo FGC, EBSD was performed in the interdiffusion area between the HE and LE layers, as indicated by the transparent yellow square shown in Fig. 4.11b. The inverse pole figure (IPF) map (Fig. 4.12a) shows the grain structure of the β phase, which became coarser from the LE to HE area. In addition, the local misorientation decreased from the LE to HE areas steadily, as illustrated in the kernel average misorientation (KAM) map (Fig. 4.12b), which represents the density of geometrically necessary dislocations (GNDs) [47]. The higher KAM values mean a higher density of GNDs stored. Then, it shows higher stress concentrations when closer to the LE layers. As shown in Fig. 4.12c, the main phase across the boundary was the β phase. However, α" phase was heterogeneously distributed along

the build direction across the interface. Almost no α" phase was found in the HE layers at this resolution, and the amount of α" phase increased from the HE to LE side. The α" phase changed across the interface, and its size and distributions showed gradient distributions (Fig. 4.12g-i). The fine and dense α" particles in the LE areas (Fig. 4.12i) became coarser and sparser when they approached the HE area (Fig. 4.12h). Then, there was no apparent α" phase in the HE area (Fig. 4.12g).

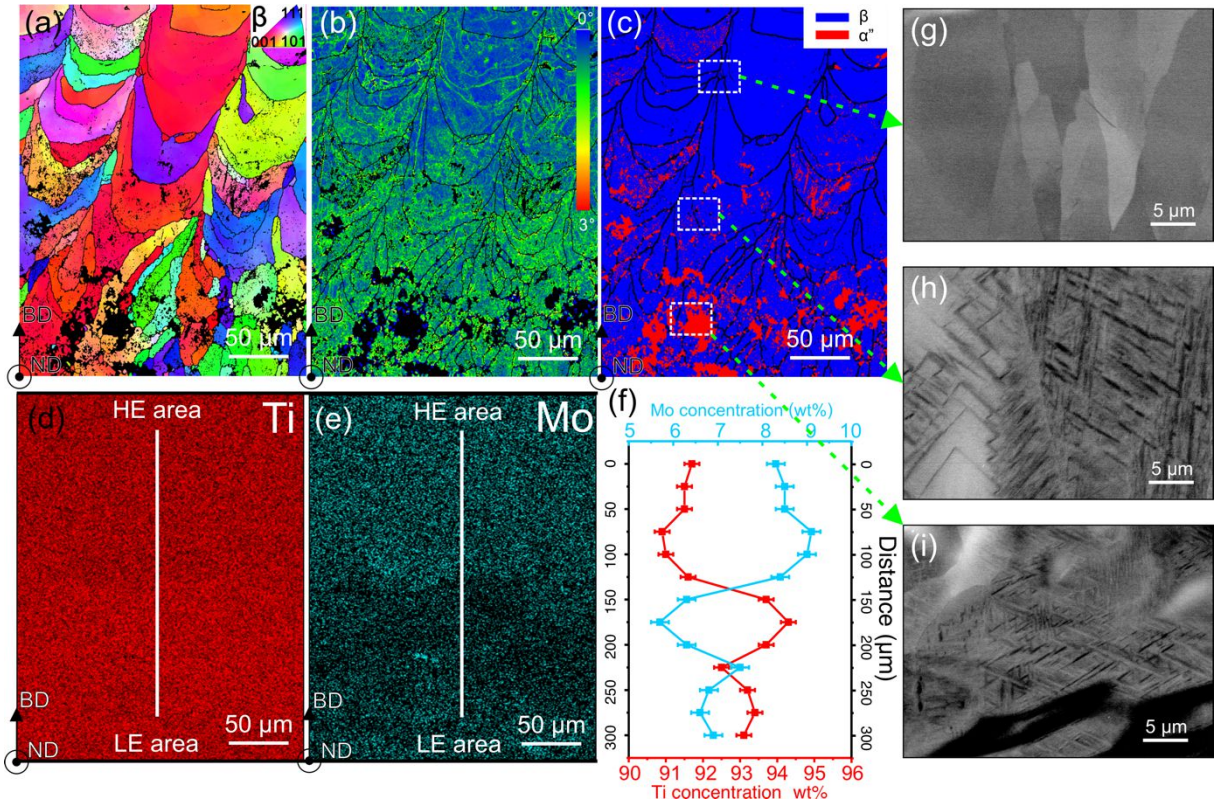


Fig. 4.12. The microstructure of the interdiffusion area: (a) an EBSD IPF map of β phase; (b) KAM map of the β Ti matrix; (c) the phase distributions map of α" and β; (d) and (e) are the EDS elemental maps of Ti and Mo, respectively; (f) EDS line profiles of Ti and Mo elements' concentration along the solid white lines in (d) and (e); (g)–(i) are the BSE micrographs of the regions selected in (c), respectively.

The elemental distribution mapping and points scanning results (Fig. 4.12d–f) revealed the detailed distributions of Mo, the β stabiliser. Mo concentration was higher in the area closer to the HE layers and gradually decreased in the region close to the LE layer. This variation of

Mo contents substantially influenced the phase constituents in Ti-Mo binary alloys [48]. In addition, the microstructure of the interdiffusion area from HE to LE on the other side is shown in Fig. 4.13, where the melt pool depth changed from deep to shallow. During the LPBF processing, each layer was remelted several times. The melt pool depth of the LE layers was 100 ± 11 μm, according to Fig. 4.14. Therefore, there were five remelts for the LE areas, in contrast to 19 for the HE layers. The remelting times play a vital role in dissolving Mo into the Ti matrix (Fig. 4.3a-c). Therefore, the Mo content was lower in the LE layer, which experienced fewer remelts.

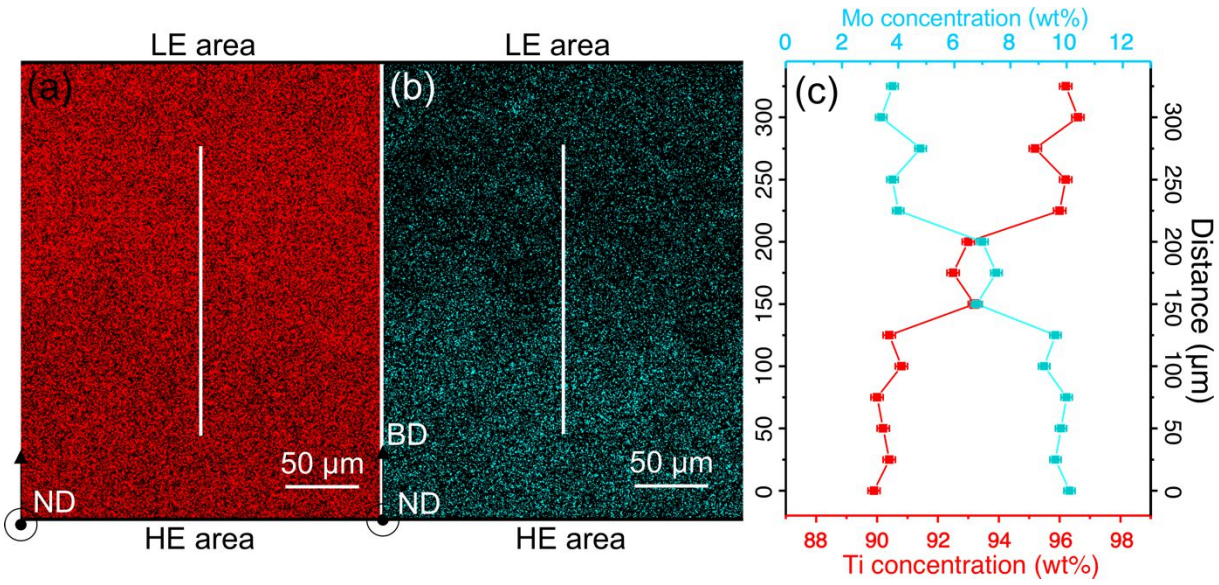


Fig. 4.13. Elemental distribution across the interdiffusion region. (a) and (b) are the EDS elemental maps of Ti and Mo, respectively; (c) is EDS line profiles along the solid white line in (a) and (b).

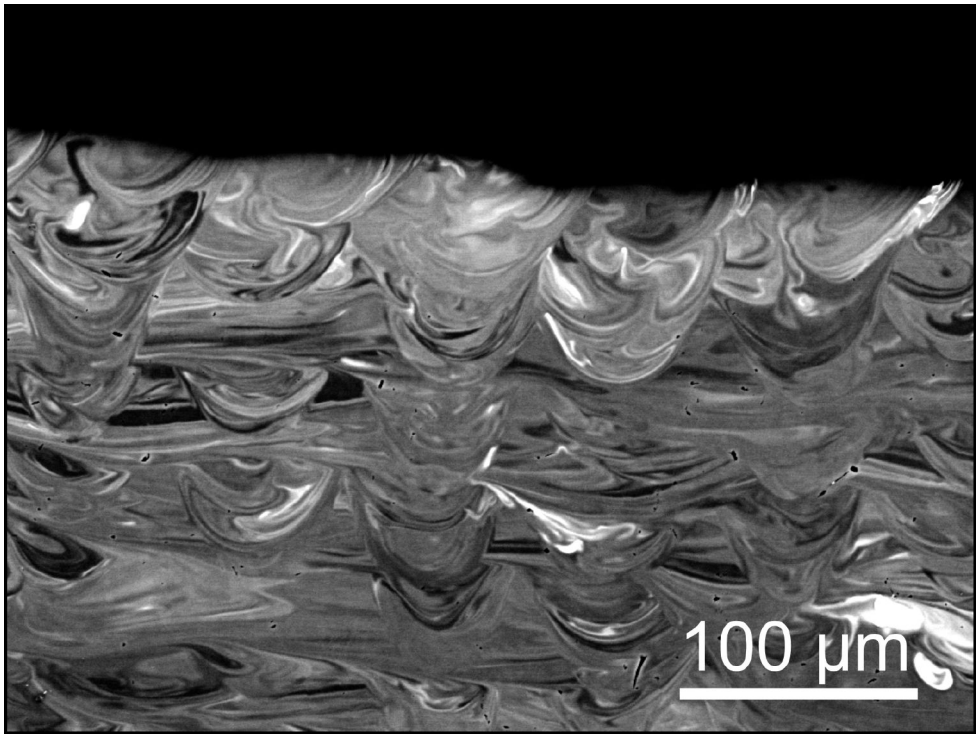


Fig. 4.14. The side-view BSE image of the top layer of the LE sample shows the melt pools' depth.

In addition, the detailed microstructures in the HE and LE areas were characterised by TEM. The FIB lamellar was lifted out across a grain boundary inside the HE area (Fig. 4.15a). It is found that the nano-sized α" phases were located along the grain boundaries (Fig. 4.15b). The bright-field TEM micrograph (Fig. 4.15c) illustrates the high-density black ellipses. The selected area electron diffraction (SAED) pattern along the $[\bar{1}13]_{\beta}$ zone axis shows diffraction spots of ω phases, which were of high intensity without diffuse streaks. This indicated the high-density ω phases in the HE area. The dark-field TEM images (Fig. 4.15d and 4.15e) revealed the morphology of the ω phases with two different orientations, ω1 and ω2, which were collected from the SAED pattern (Fig. 4.15c). Although the $[\bar{1}13]_{\beta}$ zone axis was not perpendicular to the displacement vector of the B and C planes of the β phase; it was appropriate to differentiate the ω phases region, particularly for the dark-field TEM images.

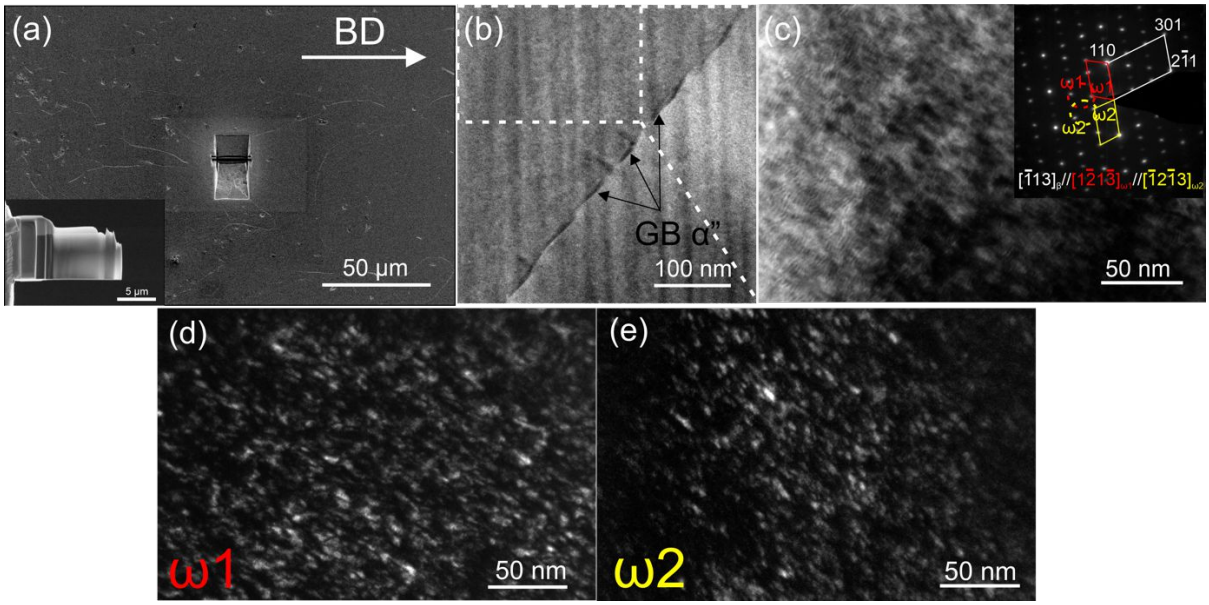


Fig. 4.15. The microstructure of the matrix of the Ti-12Mo alloy fabricated using a high AED of 4 J/mm^2 (HE layer in FGC). (a) SEM micrograph shows the selected site for FIB milling with the inset showing the morphology of FIB lamella; (b) the HAADF-STEM image; (c) the bright-field TEM image (magnified from selected region in (b)) and corresponding SAED pattern; (d) and (e) are the dark-field TEM images show ω1 and ω2 phases, respectively.

Another FIB lamella was lifted out from the LE area of the Ti-Mo FGC (marked in Fig. 4.16a). Fig. 4.16b shows the bright-field TEM micrograph of a region in the FIB lamellar, observed along the $[111]_\beta$ zone axis. High-density plate-like α" phases were observed. The burgers orientation relationship (BOR) between the β and α" follows $[111]_\beta//[\bar{1}10]_{\alpha"}$ (Fig. 4.16c). The same BOR was reported in a previous study [49]. A bright-field TEM image (Fig. 4.16d) obtained from another region shows another BOR of $[111]_\beta//[101]_{\alpha"}$ (Fig. 4.16e). This BOR has also been reported previously [50]. The lattice parameters of orthorhombic α" phases were calculated based on the SAED patterns, with *a*, *b* and *c* of 3.07, 5.18 and 4.69 Å, respectively, which were close to those (*a* = 2.99, *b* = 5.05 and *c* = 4.67 Å) in the Inorganic Crystal Structure Database (No. 253845) [51]. The microstructure was composed of plate-like α" phases and thin β films between the α" plates (Fig. 4.16f-h). The α" phase was enriched with

Ti, and the β phase had small quantities of Ti and was rich in Mo.

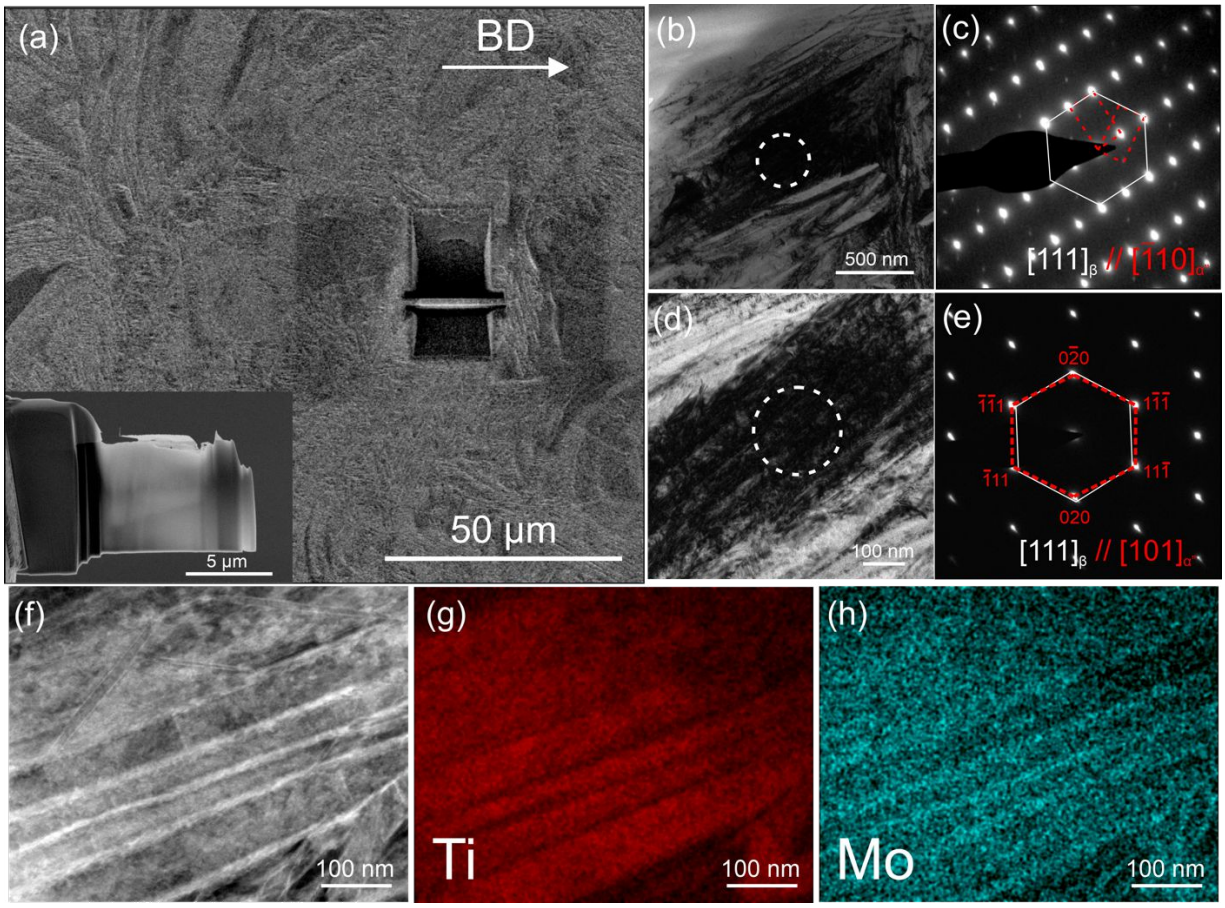


Fig. 4.16. The microstructure of the matrix of the Ti-12Mo alloy was fabricated using a low AED of 1.6 J/mm^2 (LE layer in FGC). (a) SEM micrograph shows the selected site for FIB milling with the inset showing the morphology of FIB lamella; (b) and (c) are the bright-field TEM image and corresponding SAED pattern, respectively; (d) and (e) are the bright-field TEM image, and corresponding SAED pattern from another region; (f)–(h) are the HAADF-STEM image and corresponding EDS elemental maps of Ti (g) and Mo (h), respectively.

In the Ti-Mo binary alloy system, the secondary phases' constitution in the quenched (over β transus) sample depends on the Mo content [49]. With an increase in Mo content, the martensite structure is obtained during fast cooling or from low-temperature ageing treatment, which changed from hexagonal (α') to orthorhombic (α") when 4 wt% was reached [52]. The structure became the β phase when Mo was close to or >10 wt%. During laser remelting, with

fast heating and a cooling rate (≤ 10^7 °C/s), the approximately fully β phase matrix could be fully retained at about 9 wt% Mo content (Fig. 4.12g). The coarse and sparse α" phases formed in the middle area when Mo content was approximately 6 wt%. The much finer α" phases formed in the area with a relative concentration, around 7 wt% Mo. Therefore, the Mo concentrations increased from approximately 6 wt% to 9 wt% across the interdiffusion region (Fig.4.12d-f), which played an essential role in determining the fraction and morphology of the α" phase in the FGC. In addition, the diffusion between the HE and LE layers could influence the precipitation of the α" phases, due to the deep melt pool depth, which penetrated from the HE to LE layers (Fig. 4.12d-f).

4.3.6. Macro and micro mechanical behaviours.

Fig. 4.17 shows the Vickers microhardness evolutions along the build direction, which cross the HE and LE layers, as shown in Fig. 4.11b. The results show that the microhardness was much higher in the HE layers than in the LE layers. The average microhardness in the LE was 410 (± 23) HV. For the HE layers, the microhardness results varied from the region between the LE layers and the region outside the middle area, where the average microhardness was 461 (± 13) HV and 508 (± 18) HV, respectively. The microhardness variation in the two HE regions might be due to the different thermal histories experienced during fabrication.

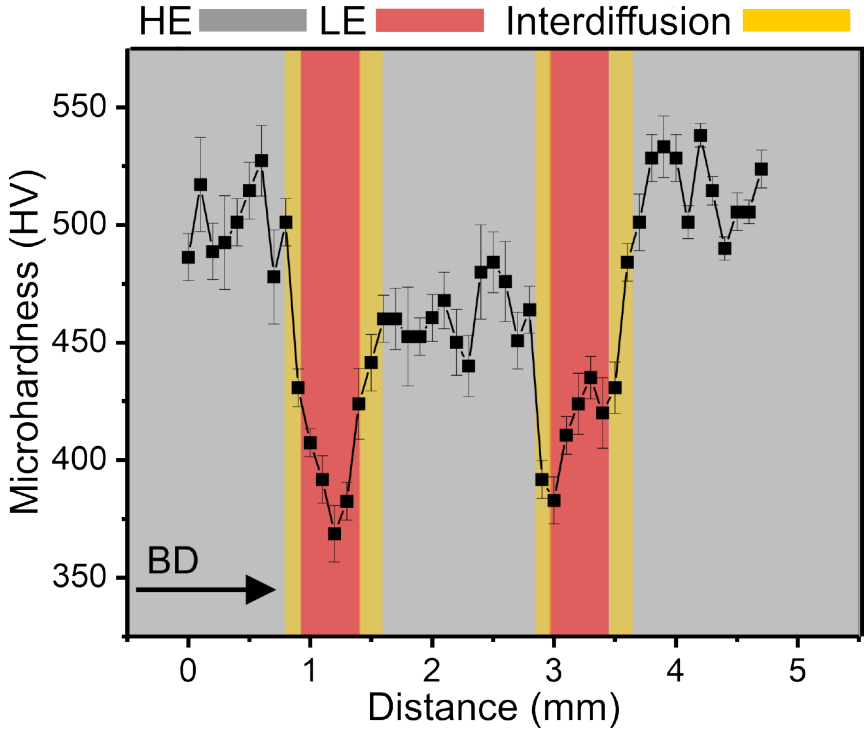


Fig. 4.17. The microhardness profile across the Ti-Mo FGCs along the build direction (The interval between adjacent hardness tests is 0.1 mm).

Fig. 4.18a shows the macro compressive stress-strain curves of the Ti-Mo FGC, LE and HE samples. The strains were measured by digital image correlation. The evolution and distribution of local strain can be seen in Fig. 4.19. The dynamic evolution of the strain distributions of the samples during compression are in the supplementary videos. In addition, the development of strain hardening rates is shown in Fig. 4.18b. The Ti-Mo FGC illustrated the best compression mechanical behaviours compared with the LE or HE samples. The LE samples show the lowest yield strength of 843 (± 22) MPa, and they possessed the highest work hardening rate during deformation. The HE samples illustrated a higher yield strength of 1168 (± 24) MPa, although there was no apparent work hardening capacity, particularly in the early plastic deformation stage. Following the introduction of two LE layers, the Ti-Mo FGC presented a slightly higher yield strength of 1173 (± 15) MPa, and significantly improved strain hardening rate, demonstrating better compression behaviour.

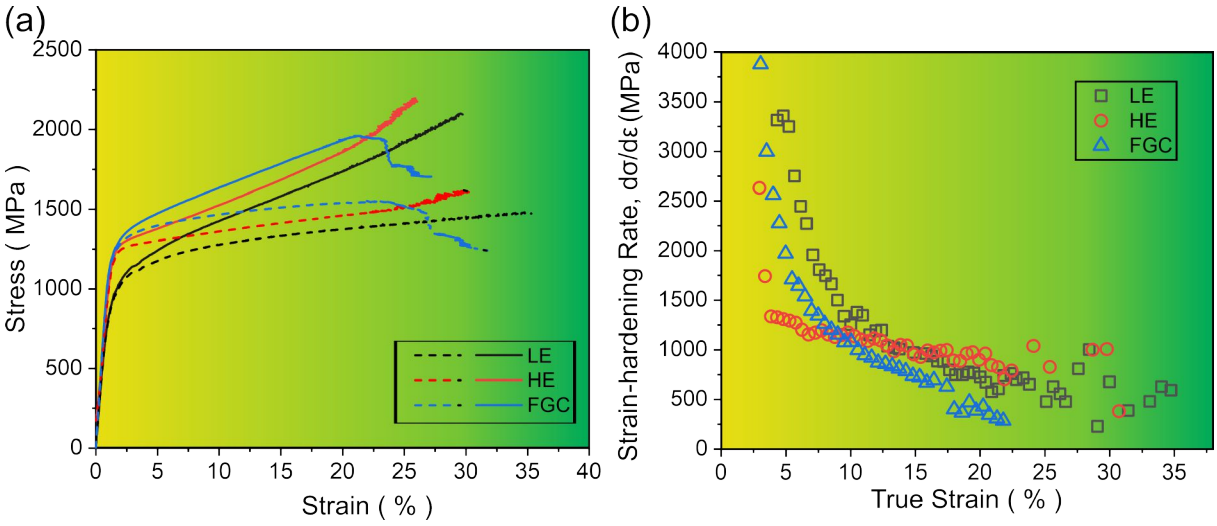


Fig. 4.18. (a) The engineering (solid lines) and true (dotted lines) stress-strain curves of the LE, HE and FGC samples; (b) the strain-hardening rates of LE, HE and FGC samples.

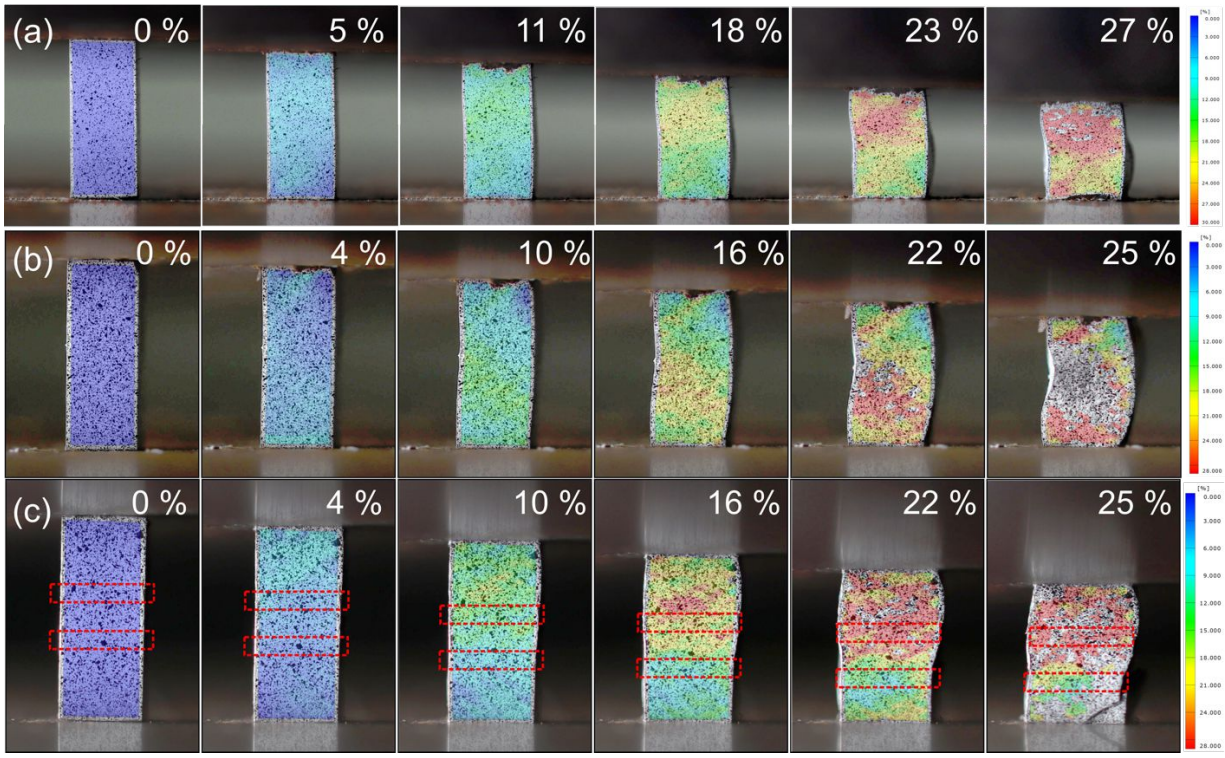


Fig. 4.19. The superimposed images of the samples' surfaces and the strain field during compression test: (a) LE sample; (b) HE sample; and (c) FGC sample.

To study the mechanical performance of the matrix, avoiding the impacts from grain boundaries, crystallographic orientations, and residual Mo particles, single crystal micropillars

were milled from the β grains with <001> orientation in the LE and HE layers. The single crystal micropillars in LE and HE layers were composed of β matrix + α" precipitates and β matrix + ω precipitates respectively, according to Fig. 4.15 and Fig. 4.16. Micropillar compression tests were carried out at room temperature. The typical stress-strain curves are shown in Fig. 4.20a. The curve is smooth and continuous for the micropillars from the LE layer, and no strain bursts were observed. The yield strength was 1483 (± 24) MPa. Strain hardening behaviour was observed. The stress-strain curve obtained from the micropillars taken from the HE layers showed significant strain bursts during deformation, different from that of the LE layer. The yield strength was 1301 (± 16) MPa. Fig. 4.20b-d shows the morphology of LE micropillars before and after the compression tests. The tortuous slip traces were observed from the surface of the deformed micropillars (Fig. 4.20d) instead of a normal slip band. Fig. 4.20e-g show the morphology of HE micropillars before and after the compression test. The parallel slip bands were observed on the HE layers micropillars' surface (Fig. 4.20g), which meant that the same slip system with fine slip steps was activated during compression.

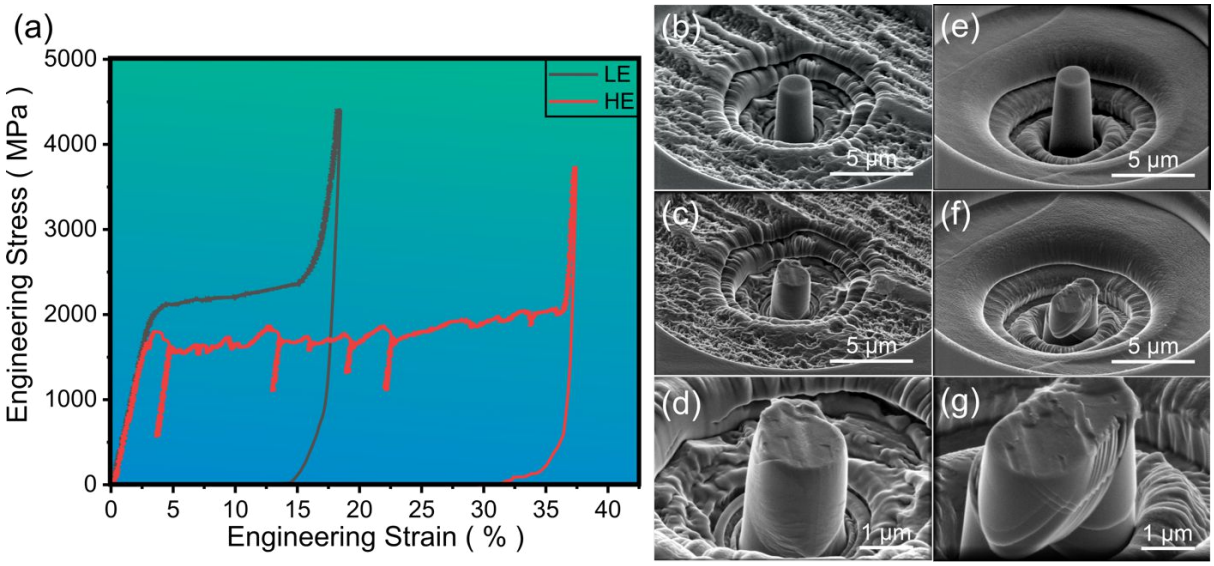


Fig. 4.20. Compressive behaviours of the micropillars in LE and HE layers of FGC. (a) The engineering stress-strain curves; (b, c, d) the SEM image of the micropillar of LE: (a) as-milled, (c and d) after compression; (e, f, g) the SEM image of the micropillar of HE:(e) as-milled, (f

and g) after compression.

4.3.7. Post-deformation characterisation

Fig. 4.21 illustrated the microstructures of the deformed HE layers of the FGC sample. Some slip traces are observed inside the FIB lamellar marked by the dotted lines, as shown in Fig. 4.21a. There are only β and ω phases revealed in the FIB lamella, and slip traces are along the $\{11\bar{2}\}<111>$ slip system, according to the SAED pattern (Fig. 4.21b and c). Inside the slip traces, the dislocations are visible. As illustrated in Fig. 4.21d, the slip traces were ω free channels, suggesting the ω → β phase transformation during the compression tests [53]. The BOR between the hexagonal ω and BCC β phases is following $[11\bar{2}0]_\omega$ //$[\bar{1}10]_\beta$ and $(0001)_\omega$//$(111)_\beta$ [54]. Then $\{\bar{1}100\}_\omega$, the prismatic slip plane of ω phase is parallel to the $\{11\bar{2}\}_\beta$, which corresponds with the activated slip plane [55]. Due to the coherence phase boundaries between the β and ω phases, it is much easier for the coherent slip planes to transfer from $\{11\bar{2}\}_\beta$ to $\{\bar{1}100\}_\omega$ planes [56]. Therefore, the dislocations move and shear the ω phases during the deformation, forming the ω phases free channels in the slip traces. These channels reduce the resistance for dislocations to move, making the plastic flow localised and then boosting dislocations' movement along the traces. Therefore, the strain bursts happened as observed in the micropillar compression test of the HE sample. This phenomenon can be account for the low strain hardening capacity. Although the ω phase is well-known to significantly strengthen the β Ti alloys due to its high shear modulus [57], the micro compression tests show limited strength. Obviously, there was no obstruction from the grain boundaries during the deformation of the single-crystal micropillars with β + ω phases. Thus, the significant strain burst can frequently occur during the deformation, limiting micropillars' strength.

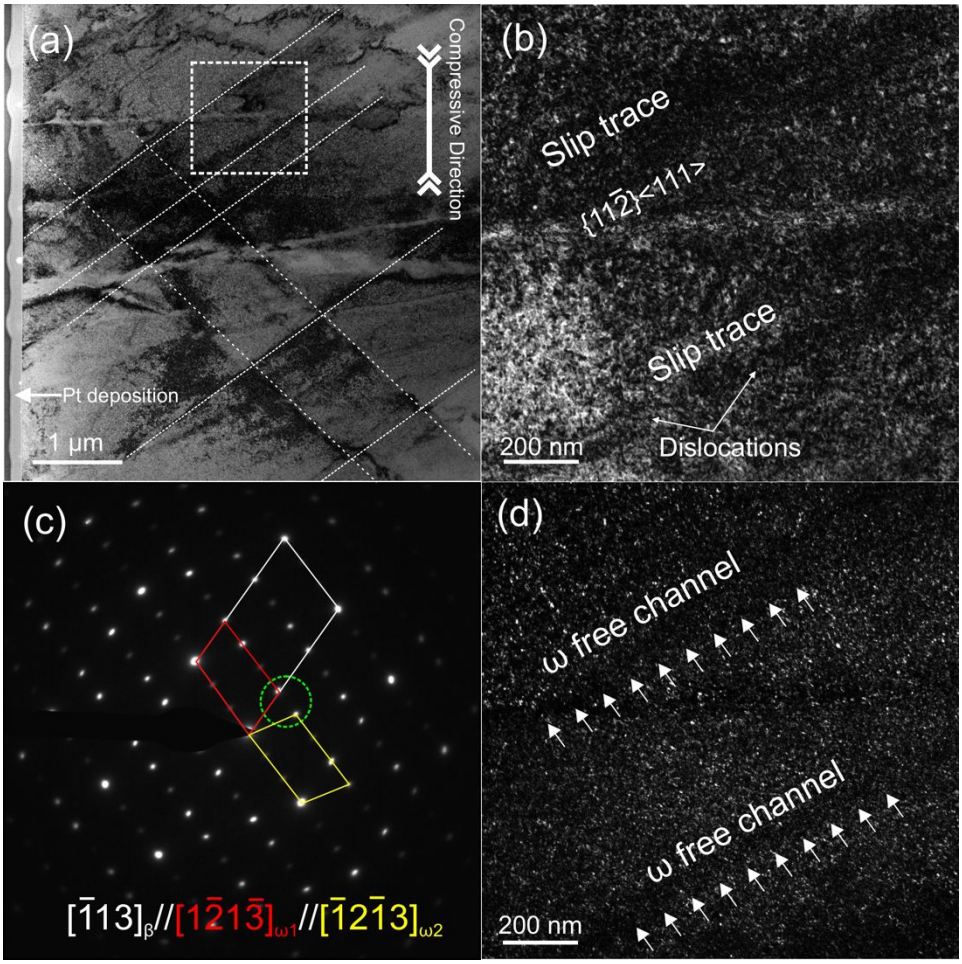


Fig. 4.21. (a) The BF TEM image shows the microstructure of the FIB thin film, lifted out from the HE area in FGC specimens, which aligned with the compressive direction. (b) The BF TEM image, magnified from (a), and the corresponding SAED pattern (c). (d) The DF TEM image shows the distribution of ω phases.

In LE layers, the microstructure is composed of β, multiple α" variants and some crescent Mo particles. These Mo particles may be surrounded by the transitional phases' composition of α', α" or α depending on the localised Mo concentrations [12]. Fig. 4.22 shows the microstructure of the deformed LE layers (without Mo particles), which were composed of β and α" phases before the compression. As shown in Fig. 4.22b, the SAED pattern illustrates that the α" variant is aligned with the $[111]_{\alpha''}$ zone axis. The high-density dislocations can be observed in Fig. 4.22c, which were found in all α" grains. Therefore, the multi variants of α"

and the interfaces between α" and the matrix can impede the continuous movement of dislocations during deformation. And the deformable α" phases show great storage capability of high-density dislocations. The orthorhombic α" is an intermediate phase between the BCC β and HCP α, of which the transformation of β → α" should require much smaller principal strains than that of β → α [52]. After compression, the β matrix phase (Fig. 4.16f-h) was not observed, suggesting the martensite phase transformation of β → α" might occur. Therefore, due to the trapping of dislocations by α" phases and the possible martensite phase transformation during deformation, the high strength and strain hardening rate are obtained for micropillars in the LE layers.

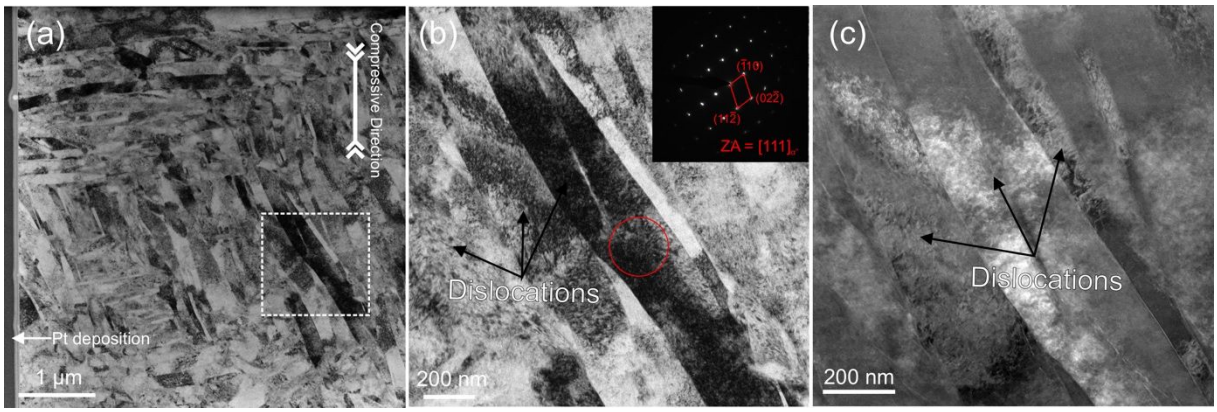


Fig. 4.22. (a) The BF TEM image shows the microstructure of the FIB thin film, lifted out from the LE area in FGC specimens, which aligned with the compressive direction. (b) The BF TEM image, magnified from (a), with the SAED pattern inserted. (c) The HAADF STEM image shows high-density dislocations.

The α" phases rich layers (LE) can act as the role of the barriers and sinks to the dislocations (Fig. 4.22c), which is similar to the α phase [55,58]. After introducing the two LE layers with rich α" to the HE samples, the dislocations' accumulation and interaction are enhanced, providing an obvious strain hardening rate up-turn in the FGC materials. With both β + ω and β + α" structures in FGC materials, high strength and high strain hardening rate were obtained. Such mechanical performance is inherent to FGC material and does not exist in

homogeneous materials (HE or LE).

The LE samples show high strength in single-crystal micropillars while low strength in macro compressive tests. One reason is the size effect of the β + α" structure [58,59]. Thereby, the LE samples can follow the "smaller is stronger". Another one is the effects of the unmelted Mo particles in LE samples, which might be detrimental to the strength of LE macro samples. Future work is needed to reveal the strengthening effects of undissolved Mo particles in such a complicated microstructure.

4.4. Outlook and Challenges

FGCs have several potential applications in structural and functional applications, and the increase in AM will significantly accelerate the development of metallic FGCs. However, their fabrication methods and control mechanisms require further investigations [21]. Several studies have shown that fabricating using different alloy gradients could lead to severe defects [21], due to various thermophysical properties. The rules for the material selection of FGCs have not been systematically investigated. In addition, the optimisation of parameters for laser processing is critical to forming highly dense FGCs by AM. The blends contained particles with different thermophysical properties, and the influence of the size, distribution, and content of the residual particles on the mechanical properties of solid samples remains undetermined. In this study, the size and content of refractory particles in the matrix were successfully controlled by tailoring the scanning parameters of the LPBF to obtain highly dense Ti-Mo FGCs. Different laser scanning parameters and strategies could significantly influence the solute concentrations and the thermal history of the processing, which could result in a gradient distribution of the precipitated phase composition, as shown in this study. More in-depth studies are required to achieve precise control of the microstructure of FGCs. Finally, the inhomogeneity, as well as

the reproducibility of the components, from batch to batch, constitutes a major challenge due to the random nature of the powder quality and the particle size distributions. Therefore, further work is required to ensure quality control before the industrial applications of FGCs prepared by AM.

4.5. Conclusions

By exploring the relationship between the scanning parameters and the corresponding microstructure, the promising approach of in situ based LPBF alloying has been demonstrated to produce a near fully dense Ti-12Mo alloy and its FGC, which has a combination of high strength and excellent strain hardening behaviour. The key findings were summarised as follows:

(1) Mo particles melted and dissolved into the Ti matrix using high laser energy input (4 J/mm^2), attributed to repeated remelt. Keyhole-induced defects formed due to excessively high HE input could be eliminated by optimising the LBD and IS settings of LPBF processing. By applying the optimised parameters of 4 J/mm^2 AED, with low LBD and IS values of 0.1 ms and 0.06 mm, the highly-dense (> 99.9%) Ti-12Mo alloy could be fabricated.

(2) During LPBF in situ alloying of Ti-12Mo, the input energy density significantly influenced the specimen's microstructure, including the grain structures, the inner stress, and the phases constitutions. At an AED of 1.6 J/mm^2, the microstructure contained refined grains, high residual stress and β + α" phases. At an AED of 4 J/mm^2, the microstructure consisted of the larger grains and reduced residual stress, where the phases constitutions were mainly β and ω phases, with a small amount of α" phase along the grain boundaries. The grain, composed of β and α" phases, showed high

strength and large strain hardening capacity. In contrast, the grain with β and ω phases showed substantial strain bursts without apparent strain hardening.

(3) The highly dense Ti-Mo FGCs were successfully prepared by controlling the energy input for the LPBF processing of the powder blends. The Ti-Mo FGCs illustrated a high yield strength of 1173 (± 15) MPa, with substantially improved strain hardening capacity at the early plastic deformation stage. This finding opens a new opportunity to design and engineer biomimetic FGCs using LPBF in situ alloying from powder blends.

4.6. References

[1] C. Leyens, M. Peters, Titanium and titanium alloys: fundamentals and applications, Wiley-VCH, New York, 2003.

[2] F. Sun, J.Y. Zhang, M. Marteleur, T. Gloriant, P. Vermaut, D. Laillé, P. Castany, C. Curfs, P.J. Jacques, F. Prima, Investigation of early stage deformation mechanisms in a metastable β titanium alloy showing combined twinning-induced plasticity and transformation-induced plasticity effects, Acta Mater. 61 (2013) 6406–6417. https://doi.org/10.1016/j.actamat.2013.07.019.

[3] L. Zhu, Q. Zhang, Z. Chen, C. Wei, G.-M. Cai, L. Jiang, Z. Jin, J.-C. Zhao, Measurement of interdiffusion and impurity diffusion coefficients in the bcc phase of the Ti–X (X = Cr, Hf, Mo, Nb, V, Zr) binary systems using diffusion multiples, J. Mater. Sci. 52 (2016) 3255–3268. https://doi.org/10.1007/s10853-016-0614-0.

[4] W.F. Ho, C.P. Ju, J.H.C. Lin, Structure and properties of cast binary Ti–Mo alloys, Biomaterials. 20 (1999) 2115–2122. https://doi.org/10.1016/s0142-9612(99)00114-3.

[5] S.L. Sing, W.Y. Yeong, F.E. Wiria, Selective laser melting of titanium alloy with 50 wt% tantalum: Microstructure and mechanical properties, J. Alloys Compd. 660 (2016) 461–470. https://doi.org/10.1016/j.jallcom.2015.11.141.

[6] T. DebRoy, H.L. Wei, J.S. Zuback, T. Mukherjee, J.W. Elmer, J.O. Milewski, A.M. Beese, A. Wilson-Heid, A. De, W. Zhang, Additive manufacturing of metallic components - Process, structure and properties, Prog. Mater. Sci. 92 (2018) 112–224. https://doi.org/10.1016/j.pmatsci.2017.10.001.

[7] J. Niu, G. Dai, Y. Guo, Z. Sun, Z. Dan, Y. Dong, H. Chang, I.V. Alexandrov, L. Zhou, Microstructure and mechanical properties of B modified Ti–Fe alloy manufactured by casting,

forging and laser melting deposition, Compos Part B Eng. 216 (2021) 108854. https://doi.org/10.1016/j.compositesb.2021.108854.

[8] S. Veeck, D. Lee, R. Boyer, R. Briggs, The castability of Ti-5553 alloy: Its microstructure and properties, Journal of Advanced Materials. 37 (2005) 40–45.

[9] L.C. Zhang, D. Klemm, J. Eckert, Y.L. Hao, T.B. Sercombe, Manufacture by selective laser melting and mechanical behavior of a biomedical Ti–24Nb–4Zr–8Sn alloy, Scr. Mater. 65 (2011) 21–24. https://doi.org/10.1016/j.scriptamat.2011.03.024.

[10] T. Ishimoto, K. Hagihara, K. Hisamoto, S.-H. Sun, T. Nakano, Crystallographic texture control of beta-type Ti-15Mo-5Zr-3Al alloy by selective laser melting for the development of novel implants with a biocompatible low Young's modulus, Scr. Mater. 132 (2017) 34–38. https://doi.org/10.1016/j.scriptamat.2016.12.038.

[11] Z. Zhou, Y. Liu, X. Liu, Q. Zhan, K. Wang, Microstructure evolution and mechanical properties of in-situ Ti6Al4V–TiB composites manufactured by selective laser melting, Compos Part B Eng. 207 (2021) 108567. https://doi.org/10.1016/j.compositesb.2020.108567.

[12] B. Vrancken, L. Thijs, J.P. Kruth, J.V. Humbeeck, Microstructure and mechanical properties of a novel β titanium metallic composite by selective laser melting, Acta Mater. 68 (2014) 150–158. https://doi.org/10.1016/j.actamat.2014.01.018.

[13] M. Fang, Y. Han, Z. Shi, G. Huang, J. Song, W. Lu, Embedding boron into Ti powder for direct laser deposited titanium matrix composite: Microstructure evolution and the role of nano-TiB network structure, Compos Part B Eng. 211 (2021) 108683. https://doi.org/10.1016/j.compositesb.2021.108683.

[14] W. Zhai, Z. Zhu, W. Zhou, S.M.L. Nai, J. Wei, Selective laser melting of dispersed TiC particles strengthened 316L stainless steel, Compos Part B Eng. 199 (2020) 108291. https://doi.org/10.1016/j.compositesb.2020.108291.

[15] Q. Han, Y. Gu, J. Huang, L. Wang, K.W.Q. Low, Q. Feng, Y. Yin, R. Setchi, Selective laser melting of Hastelloy X nanocomposite: Effects of TiC reinforcement on crack elimination and strength improvement, Compos Part B Eng. 202 (2020) 108442. https://doi.org/10.1016/j.compositesb.2020.108442.

[16] S. Liu, S. Han, L. Zhang, L.-Y. Chen, L. Wang, L. Zhang, Y. Tang, J. Liu, H. Tang, L.-C. Zhang, Strengthening mechanism and micropillar analysis of high-strength NiTi–Nb eutectic-type alloy prepared by laser powder bed fusion, Compos Part B Eng. 200 (2020) 108358. https://doi.org/10.1016/j.compositesb.2020.108358.

[17] Y. Yang, M. Yang, C. He, F. Qi, D. Wang, S. Peng, C. Shuai, Rare earth improves strength and creep resistance of additively manufactured Zn implants, Compos Part B Eng. 216 (2021) 108882. https://doi.org/10.1016/j.compositesb.2021.108882.

[18] M.H. Mosallanejad, B. Niroumand, A. Aversa, A. Saboori, In-Situ Alloying in Laser-Based Additive Manufacturing Processes: A Critical Review, J. Alloys Compd. 872 (2021) 159567. https://doi.org/10.1016/j.jallcom.2021.159567.

[19] S.L. Sing, S. Huang, G.D. Goh, G.L. Goh, C.F. Tey, J.H.K. Tan, W.Y. Yeong, Emerging Metallic Systems for Additive Manufacturing: In-situ Alloying and Multi-metal Processing in Laser Powder Bed Fusion, Prog. Mater. Sci. (2021) 100795. https://doi.org/10.1016/j.pmatsci.2021.100795.

[20] X. Meng, J. Min, Z. Sun, W. Zhang, H. Chang, Y. Han, Columnar to equiaxed grain transition of laser deposited Ti6Al4V using nano-sized B4C particles, Compos Part B Eng. 212 (2021) 108667. https://doi.org/10.1016/j.compositesb.2021.108667.

[21] J. Zhang, B. Song, L. Yang, R. Liu, L. Zhang, Y. Shi, Microstructure evolution and mechanical properties of TiB/Ti6Al4V gradient-material lattice structure fabricated by laser powder bed fusion, Compos Part B Eng. 202 (2020) 108417. https://doi.org/10.1016/j.compositesb.2020.108417.

[22] E. Palik, Handbook of Optical Constants of Solids, 1997. https://doi.org/10.1016/b978-012544415-6/50000-5.

[23] R. Cunningham, C. Zhao, N. Parab, C. Kantzos, J. Pauza, K. Fezzaa, T. Sun, A.D. Rollett, Keyhole threshold and morphology in laser melting revealed by ultrahigh-speed x-ray imaging, Science. 363 (2019) 849–852. https://doi.org/10.1126/science.aav4687.

[24] C. Zhao, Q. Guo, X. Li, N. Parab, K. Fezzaa, W. Tan, L. Chen, T. Sun, Bulk-Explosion-Induced Metal Spattering During Laser Processing, Phys Rev X. 9 (2019) 21052. https://doi.org/10.1103/physrevx.9.021052.

[25] K. Hirano, R. Fabbro, M. Muller, Experimental determination of temperature threshold for melt surface deformation during laser interaction on iron at atmospheric pressure, J. Phys. D: Appl. Phys. 44 (2011) 435402. https://doi.org/10.1088/0022-3727/44/43/435402.

[26] J. Mazumder, H. Ki, P.S. Mohanty, Role of recoil pressure, multiple reflections, and free surface evolution during laser keyhole welding, Int Congr Appl Lasers Electro-Optics. (2002) 881291. https://doi.org/10.2351/1.5065773.

[27] C. Zhao, N.D. Parab, X. Li, K. Fezzaa, W. Tan, A.D. Rollett, T. Sun, Critical instability at moving keyhole tip generates porosity in laser melting, Science. 370 (2020) 1080–1086. https://doi.org/10.1126/science.abd1587.

[28] W. Zhai, P. Wang, F.L. Ng, W. Zhou, S.M.L. Nai, J. Wei, Hybrid manufacturing of γ-TiAl and Ti–6Al–4V bimetal component with enhanced strength using electron beam melting, Compos Part B Eng. 207 (2021) 108587. https://doi.org/10.1016/j.compositesb.2020.108587.

[29] M. Naebe, K. Shirvanimoghaddam, Functionally graded materials: A review of fabrication and properties, Appl. Mater. Today. 5 (2016) 223–245. https://doi.org/10.1016/j.apmt.2016.10.001.

[30] X. Wu, P. Jiang, L. Chen, F. Yuan, Y.T. Zhu, Extraordinary strain hardening by gradient structure, P. Natl. Acad. Sci. USA. 111 (2014) 7197–7201. https://doi.org/10.1073/pnas.1324069111.

[31] X. Ma, F. Li, Z. Sun, J. Hou, X. Fang, Y. Zhu, C.C. Koch, Achieving Gradient Martensite Structure and Enhanced Mechanical Properties in a Metastable β Titanium Alloy, Metall. Mater. Trans. A. 50 (2019) 2126–2138. https://doi.org/10.1007/s11661-019-05157-5.

[32] P. Krakhmalev, I. Yadroitsava, G. Fredriksson, I. Yadroitsev, In situ heat treatment in selective laser melted martensitic AISI 420 stainless steels, Mater. Design. 87 (2015) 380–385. https://doi.org/10.1016/j.matdes.2015.08.045.

[33] P. Kürnsteiner, M.B. Wilms, A. Weisheit, B. Gault, E.A. Jägle, D. Raabe, High-strength Damascus steel by additive manufacturing, Nature. 582 (2020) 515–519. https://doi.org/10.1038/s41586-020-2409-3.

[34] A.B. Spierings, M. Voegtlin, T. Bauer, K. Wegener, Powder flowability characterisation methodology for powder-bed-based metal additive manufacturing, Prog Addit Manuf. 1 (2016) 9–20. https://doi.org/10.1007/s40964-015-0001-4.

[35] L.N. Carter, K. Essa, M.M. Attallah, Optimisation of selective laser melting for a high temperature Ni-superalloy, Rapid Prototyp. J. 21 (2015) 423–432. https://doi.org/10.1108/rpj-06-2013-0063.

[36] ASTM E9-09, Standard Test Methods of Compression Testing of Metallic Materials at Room Temperature, ASTM International, West Conshohocken,PA, 2009. https://www.astm.org.

[37] A.M. Rubenchik, W.E. King, S.S. Wu, Scaling laws for the additive manufacturing, J. Mater. Process. Technol. 257 (2018) 234–243. https://doi.org/10.1016/j.jmatprotec.2018.02.034.

[38] J. Trapp, A.M. Rubenchik, G. Guss, M.J. Matthews, In situ absorptivity measurements of metallic powders during laser powder-bed fusion additive manufacturing, Appl. Mater. Today. 9 (2017) 341–349. https://doi.org/10.1016/j.apmt.2017.08.006.

[39] E.G. Brodie, A.E. Medvedev, J.E. Frith, M.S. Dargusch, H.L. Fraser, A. Molotnikov, Remelt processing and microstructure of selective laser melted Ti25Ta, J. Alloys Compd. 820 (2020) 153082. https://doi.org/10.1016/j.jallcom.2019.153082.

[40] S. Huang, R.L. Narayan, J.H.K. Tan, S.L. Sing, W.Y. Yeong, Resolving the porosity-unmelted inclusion dilemma during in-situ alloying of Ti34Nb via Laser Powder Bed Fusion, Acta Mater. 204 (2020) 116522. https://doi.org/10.1016/j.actamat.2020.116522.

[41] J.Y. Zhang, G.F. Chen, Y.Y. Fu, Y. Fan, Z. Chen, J. Xu, H. Chang, Z.H. Zhang, J. Zhou, Z. Sun, B.L. Shen, F. Sun, Strengthening strain-transformable β Ti-alloy via multi-phase nanostructuration, J Alloy Compd. 799 (2019) 389–397. https://doi.org/10.1016/j.jallcom.2019.05.352.

[42] I. Gibson, D. Rosen, B. Stucker, M. Khorasani, Additive Manufacturing Technologies, Springer, Switzerland, 2021. https://doi.org/10.1007/978-3-030-56127-7.

[43] H. Ali, H. Ghadbeigi, K. Mumtaz, Effect of scanning strategies on residual stress and mechanical properties of Selective Laser Melted Ti6Al4V, Mater. Sci. Eng., A. 712 (2018) 175–187. https://doi.org/10.1016/j.msea.2017.11.103.

[44] L.N. Carter, C. Martin, P.J. Withers, M.M. Attallah, The influence of the laser scan strategy on grain structure and cracking behaviour in SLM powder-bed fabricated nickel superalloy, J. Alloys Compd. 615 (2014) 338–347. https://doi.org/10.1016/j.jallcom.2014.06.172.

[45] Y.J. Liu, S.J. Li, H.L. Wang, W.T. Hou, Y.L. Hao, R. Yang, T.B. Sercombe, L.C. Zhang, Microstructure, defects and mechanical behavior of beta-type titanium porous structures manufactured by electron beam melting and selective laser melting, Acta Mater. 113 (2016) 56–67. https://doi.org/10.1016/j.actamat.2016.04.029.

[46] V. Semak, A. Matsunawa, The role of recoil pressure in energy balance during laser materials processing, J. Phys. D: Appl. Phys. 30 (1997) 2541–2552. https://doi.org/10.1088/0022-3727/30/18/008.

[47] S.S.S. Kumar, B. Pavithra, V. Singh, P. Ghosal, T. Raghu, Tensile anisotropy associated microstructural and microtextural evolution in a metastable beta titanium alloy, Mater. Sci. Eng., A. 747 (2019) 1–16. https://doi.org/10.1016/j.msea.2019.01.053.

[48] P. Sochacka, A. Miklaszewski, M. Jurczyk, The Influence of Mo Content on Phase Transformation in Ti-Mo Alloys, Arch. Metall. Mater. 62 (2017) 2051–2056. https://doi.org/10.1515/amm-2017-0304.

[49] C.H. Wang, C.D. Yang, M. Liu, X. Li, P.F. Hu, A.M. Russell, G.H. Cao, Martensitic microstructures and mechanical properties of as-quenched metastable β-type Ti–Mo alloys, J. Mater. Sci. 51 (2016) 6886–6896. https://doi.org/10.1007/s10853-016-9976-6.

[50] L. Wang, C. Fu, Y. Wu, R. Li, X. Hui, Y. Wang, Superelastic effect in Ti-rich high entropy alloys via stress-induced martensitic transformation, Scr. Mater. 162 (2019) 112–117. https://doi.org/10.1016/j.scriptamat.2018.10.035.

[51] M. Sabeena, S. Murugesan, P. Anees, E. Mohandas, M. Vijayalakshmi, Crystal structure and bonding characteristics of transformation products of bcc β in Ti-Mo alloys, J. Alloys Compd. 705 (2017) 769–781. https://doi.org/10.1016/j.jallcom.2016.12.155.

[52] R. Davis, H.M. Flower, D.R.F. West, Martensitic transformations in Ti-Mo alloys, J. Mater. Sci. 14 (1979) 712–722. https://doi.org/10.1007/bf00772735.

[53] W. Chen, J. Zhang, S. Cao, Y. Pan, M. Huang, Q. Hu, Q. Sun, L. Xiao, J. Sun, Strong deformation anisotropies of ω-precipitates and strengthening mechanisms in Ti-10V-2Fe-3Al alloy micropillars: Precipitates shearing vs precipitates disordering, Acta Mater. 117 (2016) 68–80. https://doi.org/10.1016/j.actamat.2016.06.065.

[54] P. Zháňal, P. Harcuba, J. Šmilauerová, J. Stráský, M. Janeček, B. Smola, M. Hájek, Phase Transformations in Ti-15Mo Investigated by in situ Electrical Resistance, Acta Phys Pol A. 128 (2015) 779–783. https://doi.org/10.12693/aphyspola.128.779.

[55] W. Kou, Q. Sun, L. Xiao, J. Sun, Superior plasticity stability and excellent strength in Ti-55531 alloy micropillars via harmony slip in nanoscale α/β phases, Sci Rep-Uk. 9 (2019) 5075. https://doi.org/10.1038/s41598-019-41574-7.

[56] Y. Ohmori, T. Ogo, K. Nakai, S. Kobayashi, Effects of ω-phase precipitation on β→α, α″ transformations in a metastable β titanium alloy, Mater. Sci. Eng., A. 312 (2001) 182–188. https://doi.org/10.1016/s0921-5093(00)01891-8.

[57] M.J. Lai, T. Li, F.K. Yan, J.S. Li, D. Raabe, Revisiting ω phase embrittlement in metastable β titanium alloys: Role of elemental partitioning, Scr. Mater. 193 (2021) 38–42. https://doi.org/10.1016/j.scriptamat.2020.10.031.

[58] Y. Pan, Q. Sun, L. Xiao, X. Ding, J. Sun, Plastic deformation behavior and microscopic mechanism of metastable Ti-10V-2Fe-3Al alloy single crystal pillars orientated to <011>β in submicron scales Part I: Double size effects and martensitic transformation prediction, Mater. Sci. Eng., A. 743 (2019) 798–803. https://doi.org/10.1016/j.msea.2018.11.140.

[59] W. Kou, Q. Sun, L. Xiao, J. Sun, Coupling effect of second phase and phase interface on deformation behaviours in microscale Ti-55531 pillars, J. Alloys Compd. 820 (2020) 153421. https://doi.org/10.1016/j.jallcom.2019.153421.

Chapter 5: In-Situ Alloying Based LPBF Fabrication of A High Strength and Low Modulus β Ti-12Mo-6Zr-2Fe Alloy

Biocompatible β Ti-alloys with high strength and low modulus are attractive materials for biomedical implants. This study successfully fabricated a metastable β Ti-12Mo-6Zr-2Fe (TMZF) alloy with a highly dense structure by laser powder bed fusion (LPBF) from low-cost elemental powders. The different scanning strategies (simple and chessboard scan) and post-heat treatment can regulate the texture and secondary phases. The formation of strong {100}<001> texture leads to the low Young's modulus of TMZF alloys, while nano-sized α" phases induce significantly strengthening effect. The as-fabricated TMZF alloy via simple scanning strategy shows considerably high strength due to the high-density α", ω phases and sessile dislocations, but it is brittle owing to the presence of ω-phase. The TMZF alloy, manufactured using chessboard scanning strategy, possessed a high yield strength of 1026 MPa, low Young's modulus of 85.7 GPa and good ductility of 12.7 %. This results from its unique hierarchical microstructure containing α" phases, heterogeneous grains and the formation of {100}<001> texture. After solution heat treatment, the specimens exhibit stronger {100}<001> texture, hence a lower modulus of 70.9 GPa. The high yield strength of 943 MPa was maintained due to the formation of plate-like α" precipitates. The TMZF alloy fabricated by in situ alloying based LPBF demonstrates comparable strength to that of Ti-6Al-4V alloy but much lower Young's modulus, suggesting that it could be a desirable candidate for some implant applications.

The chapter is originated from the following publication:

R. Duan, S. Li, B. Cai, W. Zhu, F. Ren, M.M. Attallah, A high strength and low modulus

metastable β Ti-12Mo-6Zr-2Fe alloy fabricated by laser powder bed fusion in-situ alloying, Addit Manuf. 37 (2021) 101708.

5.1. Introduction

Titanium (Ti) alloys have been widely used in biomedical implants due to their high specific strength and outstanding corrosion resistance [1,2]. However, the widely used dual-phase (α + β)Ti alloys contain alloying elements (e.g. V and Al in Ti-6Al-4V alloy) that are associated with long term harmful effects, linked to cytotoxicity and Alzheimer's disease [3,4]. Furthermore, the elastic modulus mismatch between cortical bone (10-30 GPa) and the implants made from α + β Ti alloys (~110 GPa) would result in stress shielding and thus induce implant loosening and bone resorption [5]. Body-centred-cubic (BCC) β Ti alloys not only contain non-toxic and nonallergenic elements, such as Mo, Nb, Sn, Ta, Zr and Fe [6,7], but also can be optimised to obtain low elastic modulus (as low as 42 GPa), close to that of the cortical bone [8,9]. Hence, increasing interests have been drawn in developing β-Ti alloys for biomedical implants.

Ti-12Mo-6Zr-2Fe (weight per cent and hereafter) alloy, known as TMZF alloy, has been used as a femoral stem in total hip replacement since the early 2000s due to its outstanding biomechanical compatibility and corrosion resistance [10]. However, fabrication of TMZF alloy through conventional methods, such as casting, wrought and forging, is costly and time-consuming[11,12], while the subsequent machining for the complex-structured biomedical implant is also a challenge [13]. Recently, laser powder bed fusion (LPBF) has demonstrated high potential for the fabrication of β Ti alloys [14–17], especially for the components with complex geometry [18]. However, preparing appropriate pre-alloyed TMZF powders for LPBF is very expensive due to its extremely low powder yielding [19]. Therefore, LPBF is an efficient

and cost-effective method for alloy fabrication directly using pure elemental powders, so-called in-situ alloying based LPBF [20–22], and would thus be an attractive alternative. However, it is common to observe unmelted elemental particles of refractory elements and inhomogeneous element distribution in the as-fabricated condition [14,16,23,24], due to the high melting points and low interdiffusion rates of such refractory alloying elements. Moreover, stochastic defects like keyhole and gas porosity can also form during in-situ alloying based LPBF [25]. One purpose of the present study is to demonstrate the feasibility of fabricating TMZF alloy via in-situ alloying based LPBF from pure elemental powders.

Mechanical properties of the alloys used for biomedical implants require not only high strength and ductility but also low elastic modulus to reduce stress shielding [26]. According to ASTM standard [27], the yield strength and elongation of TMZF alloy are 897 MPa and 12 %, respectively. As reported in the literature, the elastic modulus of solution treated TMZF alloy ranges from 79 GPa to 85 GPa, which is still higher than that of cortical bone [28]. Hence, it would be ideal if TMZF alloys fabricated by LPBF could achieve a combination of lower modulus, higher strength, and reasonable ductility. To obtain the β Ti alloys with lower elastic modulus, in addition to composition optimisation [29], texture control is a promising approach, as the elastic modulus depends on the crystallographic orientation [30]. For β Ti alloys, the <001> orientation of BCC single crystal shows the lowest elastic modulus compared with the other crystallographic orientations [31]. Takuya et al. [32] have successfully produced Ti–15Mo–5Zr–3Al alloy with preferred orientation of <001> along the building direction (BD) using LPBF, achieving a low modulus of 68.7 GPa, and demonstrated that it is possible to obtain low modulus via specific LPBF scanning strategy. The issue here is that the additively manufactured components might require a heat treatment process, such as solution treatment, to optimise further the properties, during which recrystallisation might occur. It is unclear

whether the low modulus of the printed alloy will maintain after heat treatment.

Regarding the strengthening mechanism of β Ti alloys, various approaches, including grain refinement [33], precipitation strengthening [34], and introducing TWIP/TRIP (twinning induced plasticity/transformation induced plasticity) effects [35] have been used. Among them, precipitation strengthening can be easily applied to metastable β Ti alloys, because a variety of phases including ω-athermal or ω-isothermal phases, hexagonal close-packed (HCP) α, and orthorhombic α" can be introduced into the matrix during manufacturing and post heat treatment [36,37]. Although ω precipitates typically harden β Ti alloys, it could lead to embrittlement [38]. Therefore, engineering α phases to strengthen β Ti alloy is the primary research interest. Arun et al. [34] reported that microscale and nanoscale α phases contributed to the super high strength of a low-cost β TiAlVFe alloy. Recently, multiscale hierarchical α phases were also obtained by annealing and ageing in a Ti-5Al-4Zr-8Mo-7V alloy [39]. Similarly, the orthorhombic α", which can be formed during isothermal ageing treatment, can also strengthen the near β Ti alloys [40]. However, there are still limited studies on the precipitation strengthening mechanism of LPBFed metastable β Ti alloys, which induce the precipitation of secondary phases resulting from the complicated heating and cooling cycles.

This work successfully fabricated highly dense metastable β TMZF alloy via in-situ LPBF from pure elemental powders of Ti, Mo, Zr and Fe. An excellent combination of high strength, low Young's modulus, and good ductility was achieved via chessboard scanning strategy and post-heat-treatment. The formed hierarchical microstructure, including texture, heterogeneous grain structure, and nanoscale secondary phases, was characterised in detail. This work not only provides significant insights into the LPBF fabrication of biocompatible β Ti alloy via in-situ alloying of elemental powders, but also advance the mechanistic understanding of the relationship between processing strategies, microstructural characteristics and tensile properties

of additively manufactured Ti alloy.

5.2. Experimental

5.2.1. Powders

Gas atomised Ti powder (TLS Technik GmbH, Germany) was used as the base powder for Ti-12Mo-6Zr-2Fe powder blends. The pure Ti powder was spherical, in a size range of 20-63 μm with a d_{50} of 42.9 μm. The alloying elemental powders of Mo, Zr and Fe (TLS Technik GmbH, Germany) were also spherical. The Mo powder was sieved by a 50 μm sieve and had a particle size range of 5-45 μm with a d_{50} of 20.7 μm, which is much finer than the base Ti powder. This ensures that the weight of Ti and Mo powders are in a close range. The Zr and Fe powders had particle size ranges of 15-45 μm and 45-63 μm, respectively. The mixed powders were blended for 24 h, under the protection of argon atmosphere, using a tumbler mixer to ensure the uniform blending (Fig. 5.1a), as confirmed by the backscattered electron (BSE) micrograph (Fig. 5.1b) and energy-dispersive X-ray spectroscopy (EDS) elemental maps (Fig. 5.1c).

5.2.2. LPBF processing and heat treatment

All the specimens and components were fabricated using a Concept Laser M2 Cusing® LPBF system, equipped with a 400 W Nd:YAG continuous laser source and a laser spot diameter of ~ 70 μm. The builds were carried out under a controlled argon atmosphere and ensured the oxygen content was down to < 1000 ppm. The schematic of the in situ LPBF processing can be found in Fig. 5.1d. The optimised processing parameters are listed in Table 5.1. Near fully dense (≧99.8%) TMZF alloys were obtained using these parameters. Fig. 5.1f

shows the optical micrograph of the as-fabricated TMZF alloy, where few pores can be observed, neither residual un-melted Mo particles. Simple scan and chessboard (island) scan strategies were applied to fabricate the tensile samples of the alloy (Fig. 5.1e). The as-fabricated samples have dimensions of 12 mm in width and 65 mm in length, either using simple or chessboard scanning strategy. When using simple scanning strategy, the scanning direction is 45° to the tensile direction (TD), which rotate 90° for each layer. For the chessboard scanning strategy, the scanning direction is parallel or perpendicular to the TD with the island size of 5 mm × 5 mm. The as-fabricated chessboard-scanned alloy was then sealed in argon-filled quartz tubes and subjected to solution treatment at 1273 K (over the β transus temperature) for 1 h, followed by water quenching. The oxygen and nitrogen content of the fabricated TMZF samples were measured using the ON736 elemental analyser (LECO, US), which was 0.177 (± 0.004) wt% and 0.075 (± 0.003) wt%, respectively. After solution heat treatment, the oxygen and nitrogen content was slightly increased to 0.194 (± 0.005) wt% and 0.101 (± 0.003) wt%, respectively. The as-fabricated simple-scanned, chessboard-scanned, and solution heat-treated chessboard-scanned TMZF alloys were defined as AF-SS, AF-CS, and ST-CS TMZF hereafter, respectively.

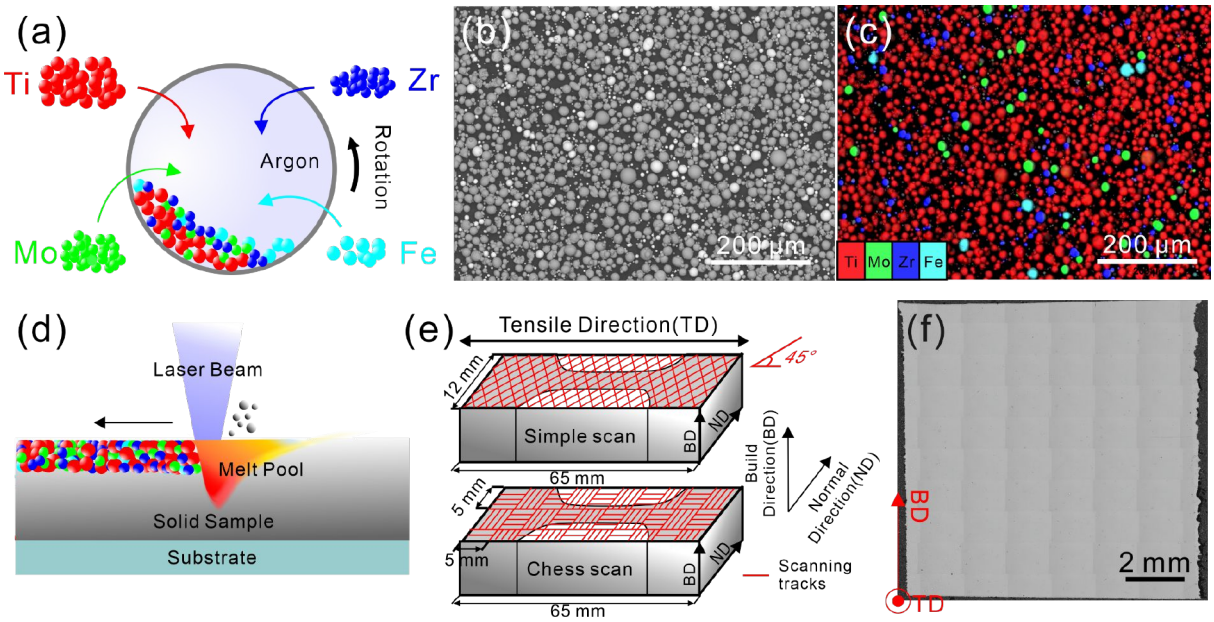


Fig. 5.1. (a) The schematic of the powders blending processing. (b) and (c) are the BSE image and the corresponding EDS elemental map of Ti-12Mo-6Zr-2Fe blended powder. (d) Schematic of the LPBF processing of the blended powders. (e) Schematic of scanning strategies for the fabrication of tensile bars, where the TD, build direction (BD), and their normal direction (ND) were indicated by the black arrows. (f) Optical micrograph of the side section of as-fabricated TMZF alloy.

Table 5.1. Optimised in-situ alloying based LPBF processing parameters for the fabrication of TMZF alloy.

Parameters	Value
Laser power (W)	300
Scanning speed (mm/s)	1000
Hatch spacing (mm)	0.075
Layer thickness (mm)	0.02
Area energy density (J/mm^2)	4
Laser beam delay (ms)	0.1
Island spacing (mm)	0.06

5.2.3. Microstructural characterisation

The as-fabricated specimens were sectioned for microstructural characterisation and mechanical testing using electrical discharge machining. For scanning electron microscopy (SEM) and optical microscopy (OM) observations, the specimens were sequentially grounded with 220 and 1200 grit SiC papers and polished by MD-Chem with OPS-H2O2 (7:3) solution (Struers, Denmark). They were etched using the Kroll's reagent to observe melt pool

microstructure and secondary phases of the samples. The Zeiss axioskop 2 microscope was used for OM observation. The alloys' microstructure and fracture morphology were studied using SEM (TESCAN MIRA 3, Czech Republic) operated in secondary electron (SE) and BSE modes. The elemental distribution was analysed by X-Max^N Silicon Drift EDS Detector (Oxford Instruments, Oxford, UK), equipped in SEM, and electron probe microanalysis (EPMA) performed by a JXA-8530 analyser (JEOL, Tokyo, Japan). The grain size and crystallographic orientation were characterised using electron backscattering diffraction (EBSD) with a step size of 1.5 μm (a much smaller step size of 0.05 μm was used to discriminate the bi-model grains and nano-sized α" phase) and analysed using Channel 5 software. The microstructure of the alloys was also investigated using a transmission electron microscope (TEM; Tecnai F30, FEI, USA) operated at 300 kV. The high-angle annular dark-field scanning TEM (HAADF-STEM) was performed on the FEI Talos TEM at 200 kV. The TEM samples were prepared using conventional grinding, polishing and ion milling (PIPS™, Gatan, Inc., Pleasanton, CA).

X-ray diffraction (XRD) patterns were recorded using a Rigaku Smartlab-9kW diffractometer (Rigaku, Tokyo, Japan) in the 2θ range of 20˚–100˚ with Cu Kα radiation (λ = 1.54056 Å, 45 kV, 200 mA). In order to isolate the broadening effects caused by the crystallite size, microstrain and instrument. The volume fraction of phases, lattice parameters, and microstrain were analysed using the Rietveld method performed by MAUD software [41] on the acquired XRD patterns. The instrument broadening parameters were calibrated using the annealed standard silicon powder. The differential scanning calorimetry (DSC) curves were tested by the NETZSCH DSC 404 C machine at the heating rate of 10 k/min, of which the chamber was under the protection of Argon atmosphere.

5.2.4. Mechanical tests

Tensile tests were performed for both as-fabricated and solution heat-treated samples. Vickers micro-hardness tests were performed using Struers DuraScan machine equipped with an automated indenter under a load of 100 g for 15 s. All tensile specimens were fabricated according to the ASTM E8 [42] with the tensile direction (TD) perpendicular to BD (Fig. 5.1e). The tensile tests were performed at room temperature, with a 1 $mm \cdot min^{-1}$ crosshead rate for at least three independent tensile tests per group, using a Zwick/Roell universal testing machine (Zwick 1445, Zwick-Roell, Ulm, Germany) equipped with an extensometer with a gauge length of 25 mm.

5.3. Results

The results were organised in the following order. We first present the mechanical properties of the AF-SS, AF-CS, and ST-CS TMZF alloys. After that, the influence of laser processing and heat treatment on the microstructure-mechanical properties relationship of the TMZF alloys were illustrated, of which the microstructure was characterised in detail including the chemical homogeneity, melt pool, grain structure, texture, and various secondary phases.

5.3.1. Mechanical properties

Fig. 5.2a shows the engineering and true tensile stress-strain curves of the AF-SS, AF-CS, and ST-CS TMZF alloys. Their yield strength (σ_y), ultimate tensile strength (σ_{UTS}), Young's modulus (E), and fracture strain (ε_f) are included in Table 5.2. The AF-SS TMZF alloy shows an extremely high tensile strength of 1291 (± 25) MPa, but fails prematurely before yielding and has a high E of 107.1 (± 3.3) GPa. The AF-CS TMZF alloy exhibits a high σ_y of 1026 (± 5) MPa, good ductility with ε_f of 12.7 (± 1.0) %, and significantly reduced E (85.7 (± 0.3) GPa).

After solution heat treatment, despite a slight decrease in σ_y (943 (± 8) MPa) and ε_f (12.0 (± 0.3) %), the ST-CS TMZF alloy shows the lowest *E* of 70.9 (± 0.1) GPa. The true stress-strain curves show slight strain hardening behaviour after tensile yielding. The low strain hardening capacity is a common characteristic of the β Ti alloys without TWIP/TRIP effects, which has also been reported in the TMZF alloys prepared using conventional methods [27,43].

Fig. 5.2b compared the yield strength and Young's modulus of the LPBF in-situ alloyed TMZF with other biomedical Ti alloys, including TiMo, TiMn, TiCr, TiNb, TiZr and TiTa systems, Ti6Al4V and commercially pure (CP) Ti [14,15,17,23,24,43–50]. The mechanical properties of some biomedical Ti alloys fabricated using additive manufacturing were also included in Fig. 5.2b. As is shown, the present TMZF alloy fabricated by LPBF demonstrates a good combination of high strength and simultaneously low Young's modulus. These combined mechanical properties are superior to those of Ti-6Al-4V alloys, TMZF alloy (fabricated using the conventional method) and comparable with, if not better than, a series of other β Ti alloys.

The fractography (Fig. 5.2c) of AF-SS TMZF shows the layered and flat cleavage surface, suggesting an intergranular brittle fracture. In contrast, the fractography of AF-CS TMZF shows broad and deep dimples (Fig. 5.2d), with some small cracks surrounding the open pores, suggesting an intragranular ductile fracture. Similar fractography was also observed in the ST-CS TMZF (Fig. 5.2e).

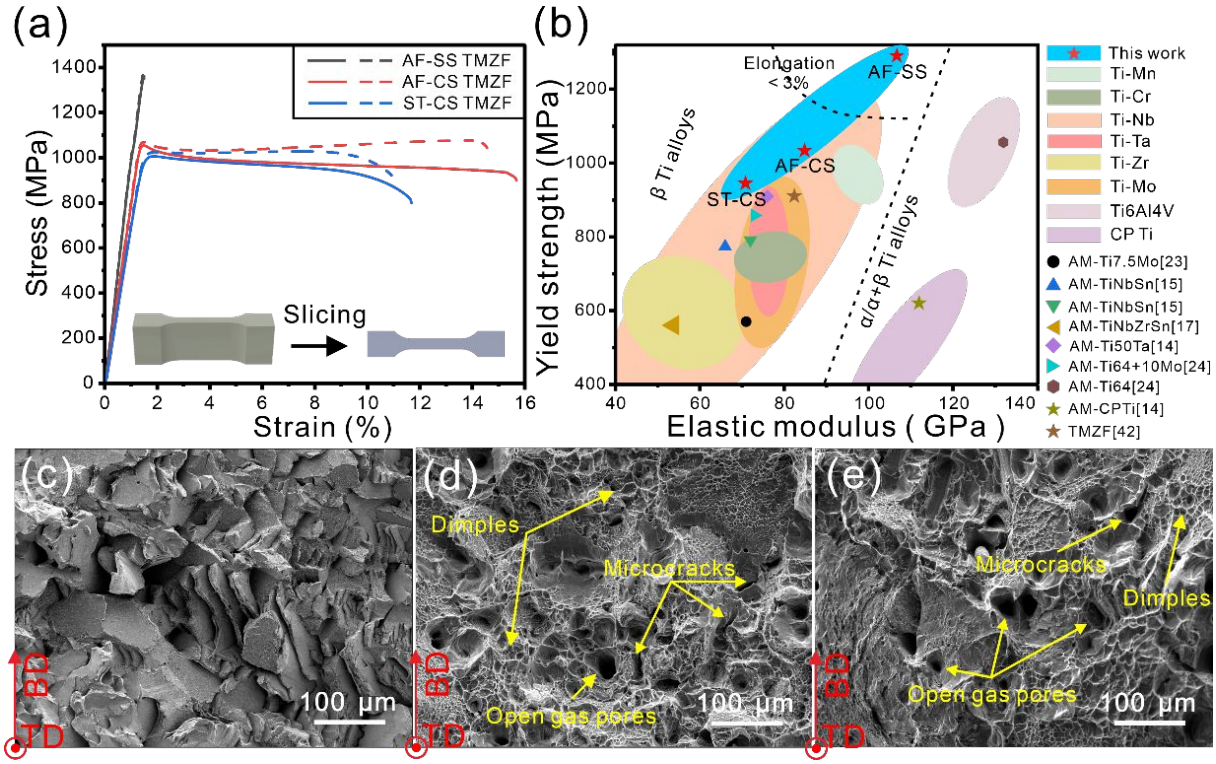


Fig. 5.2. (a) The engineering (solid lines) and true (dotted lines) stress-strain curves of AF-SS, AF-CS, and ST-CS TMZF alloys. (b) A comparison of the present TMZF alloys with other biomedical Ti alloys in yield strength and the ratio of yield strength to the Young's modulus. (c)-(e) are the fracture morphology of AF-SS, AF-CS, and ST-CS TMZF alloys, respectively.

Table 5.2. The mechanical properties of the AF-SS, AF-CS, and ST-CS TMZF alloys.

TMZF	σ_y (MPa)	σ_{UTS} (MPa)	E (GPa)	ε_f (%)	Vickers Hardness (HV)
AF-SS	-	1291 ± 25	107.1 ± 3.3	1.3 ± 0.1	488 ± 4
AF-CS	1026 ± 5	1026 ± 5	85.7 ± 0.3	12.7 ± 1.0	343 ± 5
ST-CS	943 ± 8	988 ± 14	70.9 ± 0.1	12.0 ± 0.3	326 ± 4

5.3.2. Chemical homogeneity

As shown in Fig. 5.3(a-d), the chemical homogeneity was evaluated. Twenty EDS mappings were carried out in an area of 4×5 mm on the side section of TMZF alloy, which was

then reconstructed to the contour map of elemental distributions. The Ti element distribution ranges from 78.70 to 81.30 wt% with an average of 80.27 ± 0.75 wt%. The Mo element was distributed in the range of 11.20 to 13.00 wt% with an average of 11.98 ± 0.55 wt%. The Zr element was distributed in the range of 5.30 to 5.80 wt% with an average of 5.63 ± 0.16 wt%. The Fe element was distributed in the range of 2.00 to 2.20 wt% with an average of 2.08 ± 0.06 wt%. Therefore, the average weight percentage of Ti, Mo, Zr, and Fe elements in TMZF alloy is close to that of the nominal composition of Ti-12Mo-6Zr-2Fe alloy. Some inhomogeneous distributions were observed, especially the Mo element (Fig. 5.3b). The absolute values of the local concentrations deviated from the average values of only 1.57, 1.02, 0.33 and 0.12 wt%, for Ti, Mo, Zr and Fe, respectively.

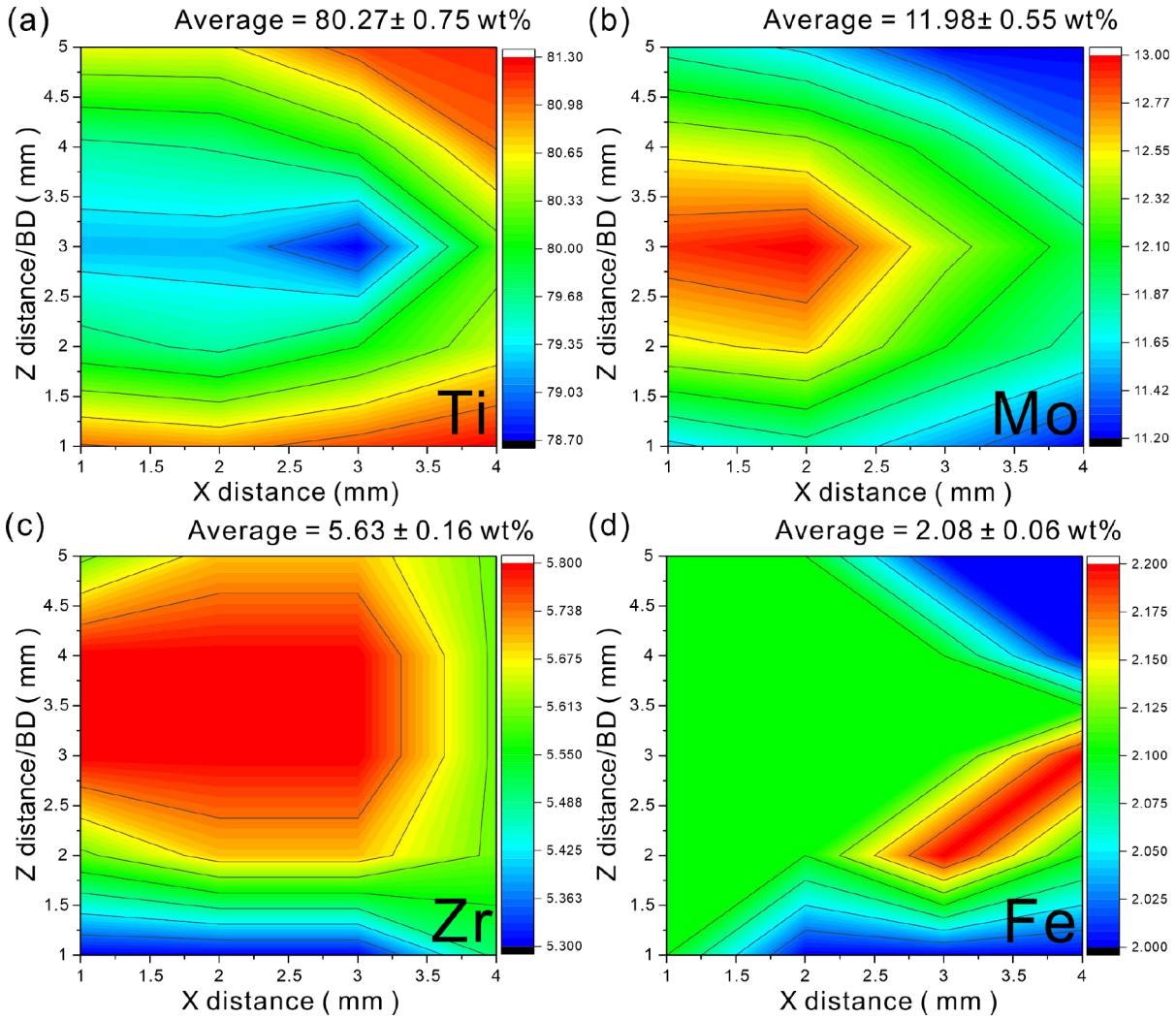


Fig. 5.3. The contour mapping shows the distributions of (a) Ti, (b) Mo, (c) Zr and (d) Fe elements in the side section of the AF-CS TMZF sample plane, parallel with the build direction.

The elemental distributions and chemical homogeneity of the AF-CS TMZF alloy under higher magnification were also illustrated in Fig. 5.4, performed by EDS and EPMA. All these elemental maps were taken from the middle part of the sample. No apparent residual Mo particles were present in the TMZF specimen, as evidenced by the uniform contrast in the BSE image of a large sample area (Fig. 5.4a). EDS elemental maps (Fig. 5.4b-e) show that the constituent Ti, Mo, Zr and Fe elements are distributed uniformly in TMZF alloy.

A higher magnification BSE image (Fig. 5.4f) reveals the grain boundaries and melt pool boundaries of AF-CS TMZF alloy. The corresponding EPMA elemental maps (Fig. 5.4g-j) show that a small amount of Mo element segregated along the molten pool boundaries (Fig. 5.4h). The lowest and highest Mo concentrations are 6.73 wt% and 13.15 wt%, respectively. Zr and Fe elements (Fig. 5.4i-j) are found to be depleted along the molten pool boundaries, whereas Ti element is slightly enriched. Although the elements in TMZF alloy are found generally homogeneous distributed in EDS elemental maps of a limited region, inhomogeneity is revealed whether in the area across the sample or the grain scale region characterised by EPMA mapping especially along the melt pool boundaries due to solidification segregations [51].

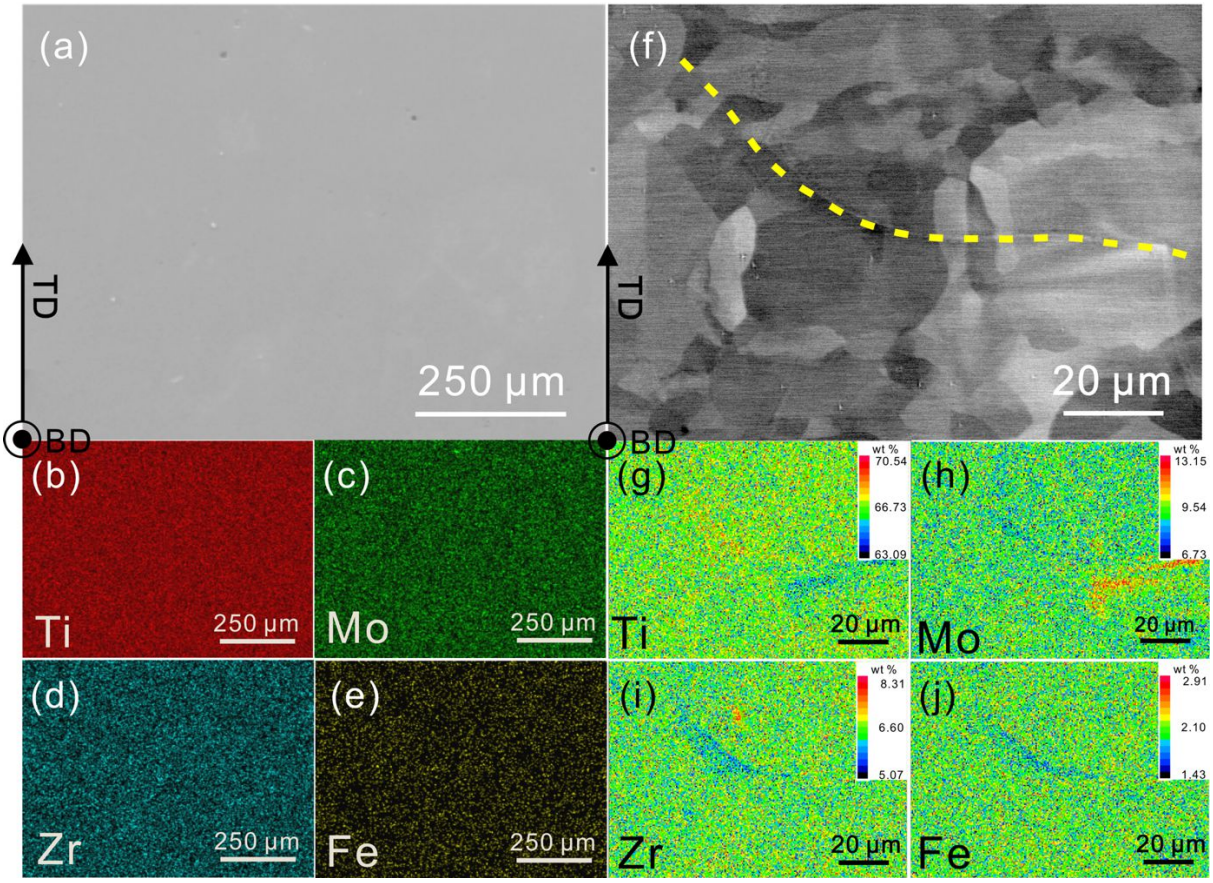


Fig. 5.4. BSE images and elemental distributions of the cross-section of AF-CS TMZF alloy. (a) A low magnification BSE image; (b)–(e) EDS elemental maps of Ti, Mo, Zr, and Fe, respectively; (f) a higher magnification BSE image (Yellow dotted lines indicated the melt pool boundaries); (g)–(j) EMPA elemental maps of Ti, Mo, Zr, and Fe, respectively.

5.3.3. Melt pool microstructure

Fig. 5.5 shows the morphology and grain structure of the melt pool of the AF-CS TMZF. The top layer, which did not experience repeated remelting, shows elongated grains that extend across a few build layers, where the cellular sub-grains (marked by the white dotted lines) started from the upper region of the melt pool and solidified from the melt pool boundaries to the middle, perpendicular to BD (Fig. 5.5a). After that, a few grain boundaries formed across the middle region of melt pools (as marked by the solid white lines in Figs. 5.5a-b). The middle layer, which experienced several remelting cycles, only shows narrow cellular structures along

the melt pool boundaries, with several refined grains in the middle of the melt pool (Fig. 5.5b-c).

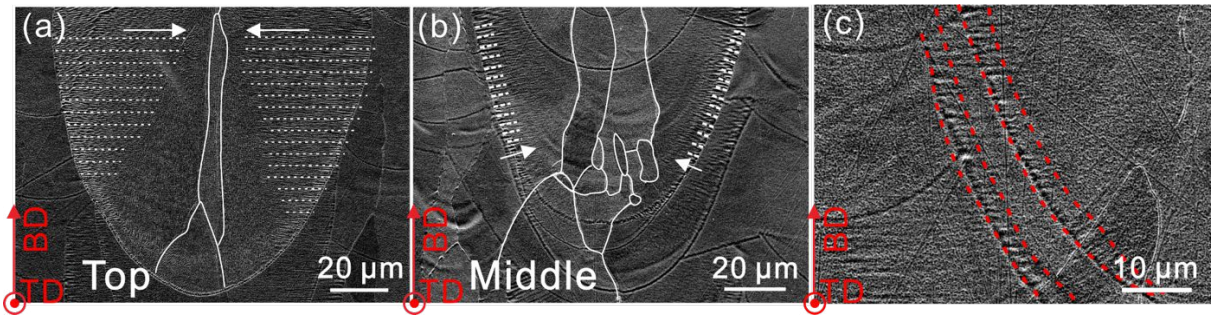


Fig. 5.5. SEM micrographs of the melt pool morphology of the AF-CS TMZF alloy, including the top layer (a), the middle layer after several heat cycles (b), and the thin region along the melt pool boundaries (c). The white dotted lines, white arrows, white solid lines and red dotted lines marked the cellular sub-grains, cellular solidification direction, grains boundaries, and the thin region of cellular structure, respectively.

5.3.4. Grain structure

The grain structure of the middle layer of the builds was characterised by EBSD. The AF-SS TMZF alloy mainly consists of long columnar grains that grew preferentially along BD (Fig. 5.6a), the size of which is comparable to that of specific layered structure observed in the fracture morphology of AF-SS TMZF (Fig. 5.2c). Grains of AF-CS TMZF alloy are composed of columnar and refined equiaxed grains, which can be clearly observed in the magnified micrograph (Fig. 5.6c-d), consistent with the melt pool microstructure presented in Fig. 5.5b. The ST-CS TMZF shows equiaxed grains with substantial recrystallisation and growth (Fig. 5.6e). The grain size, calculated as an equivalent circle diameter using the grain area, of which the distributions are presented in Fig. 5.6 (b, d and f). The average grain sizes of AF-SS, AF-CS and ST-CS TMZF alloys are 33.0 μm, 25.4 μm, and 83.7 μm, respectively. Note that non-equilibrium cellular structure within the melt pool of the top layer (Fig. 5.5a) was not observed in the middle layers of the melt pool, possibly due to the experienced multiple remelting cycles.

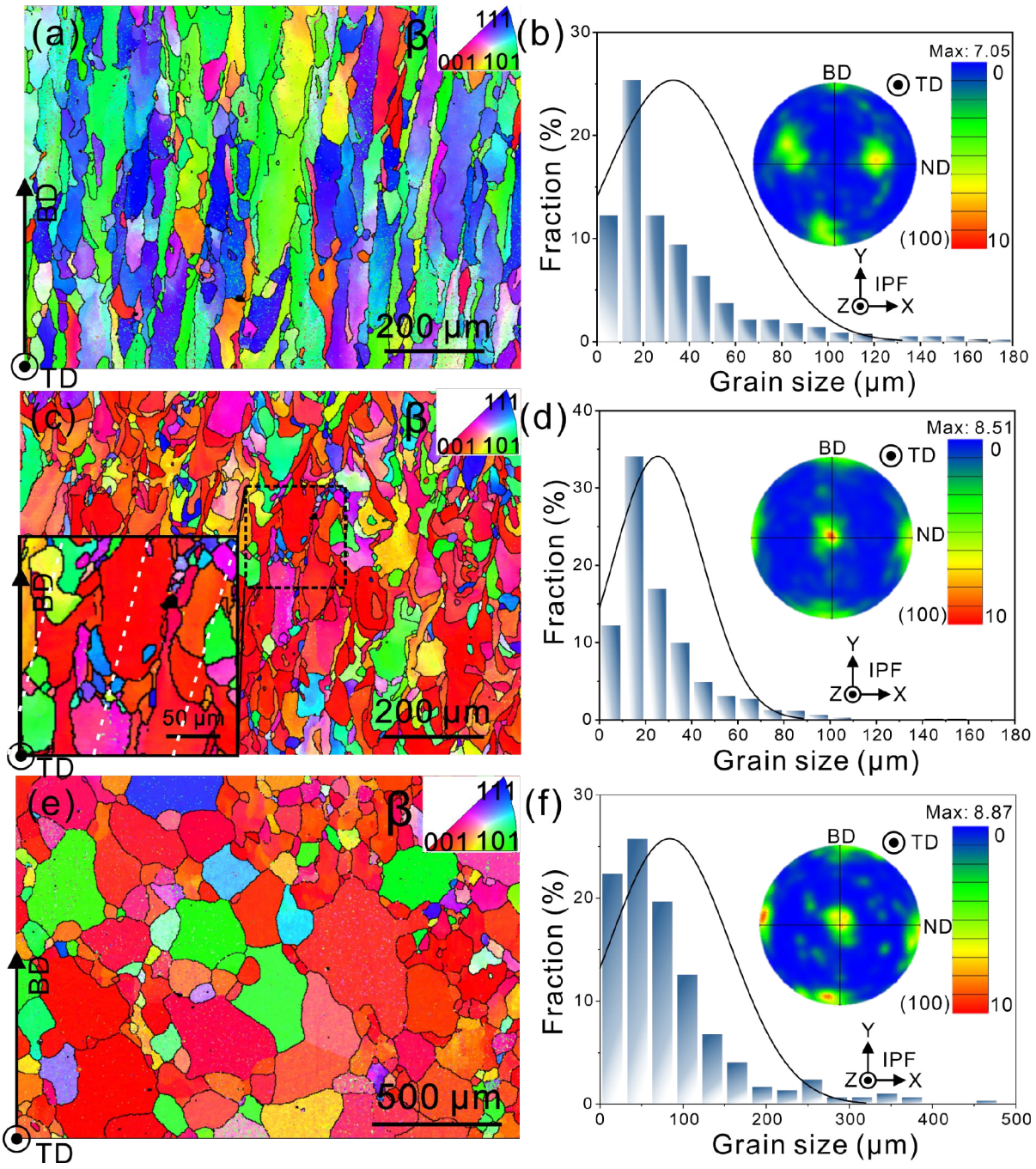


Fig. 5.6. EBSD inverse pole figure (IPF) maps (left column) and the grain size distributions (right column) of β phase in the middle layer of AF-SS (a, b), AF-CS (c, d) (the white dotted lines indicated the melt pool boundaries), and ST-CS (e, f) TMZF alloys (IPF Z-axis along the TD). The insets in (b, d, and f) are (100) pole figures.

To clearly reveal the heterogeneous grain structure formed inside the AF-CS TMZF alloy, a high magnification EBSD IPF map, obtained using a much smaller step size of 0.05 μm, was

performed within one single melt pool perpendicular to BD (Fig. 5.7). Many fine grains were located in the central region of the melt pool (Fig. 5.7a-b), with an average grain size of 8.18 μm. Some of those grains are elongated. The small grains inside the AF-CS TMZF alloy mainly consist of high angle grain boundaries (HAGBs) (Fig. 5.7b).

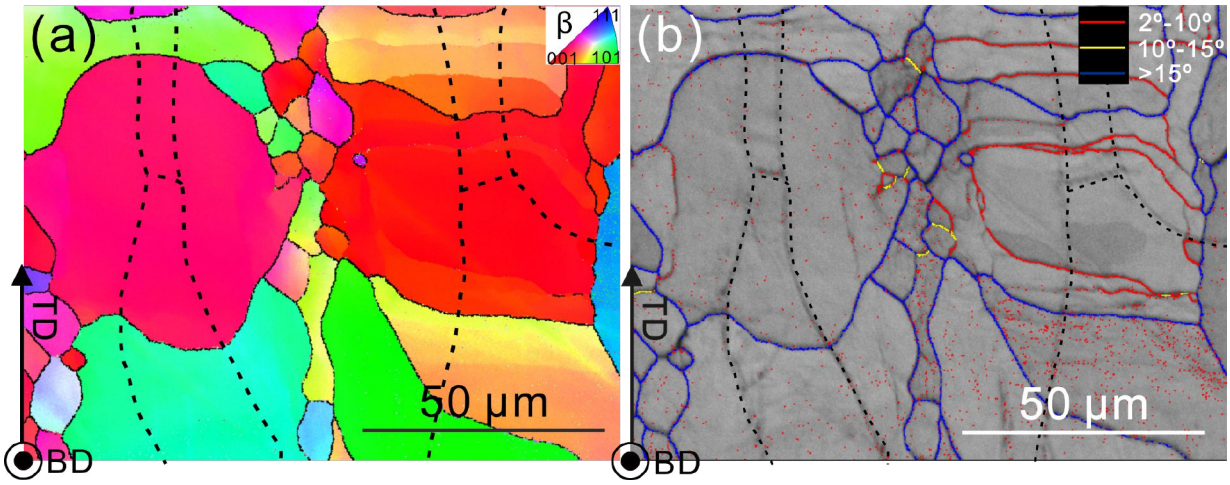


Fig. 5.7. Melt pool microstructure of the cross-section (perpendicular to BD) of AF-CS TMZF alloy: (a) an EBSD IPF map; (b) the EBSD band contrast map with superimposed LAGBs and HAGBs.

Moreover, the texture was substantially different between the three groups of TMZF alloys. The IPF maps (Fig. 5.6 (a, c, and e)) and its pole figures (insets of Fig. 5.6 (b, d, and f)) clearly show the texture evolution. The AF-SS TMZF shows strong preferential orientations of <011> along TD, while the AF-CS and ST-CS TMZF alloys clearly show strong {100}<001> texture.

Figs. 5.8a-c illustrate the XRD patterns with the sample surfaces perpendicular to TD (parallel with BD), of AF-SS, AF-CS and ST-CS TMZF alloys. The Rietveld method [52] was used to analyse the XRD patterns. The calculated lattice parameters, phase constitutions and microstrain of the TMZF samples are listed in Table 5.3. Fig. 5.8d shows the peak intensity ratios of $(200)_\beta$ to $(110)_\beta$, which can be used to assess the difference in texture between three groups of TMZF alloys. The higher the ratio, the stronger <001> preferential orientation. It is

found that ST-CS TMZF shows the strongest <001> alignments among the three groups of samples, followed by AF-CS and AF-SS TMZF alloys, respectively. These results agree well with the IPF maps (Fig. 5.6 (a, c, and e)) and (100) pole figures measured via EBSD (Fig. 5.6 (b, d, and f)).

5.3.5. Phase identification

In order to identify and quantify the different phases in the fabricated samples, a variety of characterisation techniques, including XRD Rietveld refinement analysis, high-resolution EBSD and TEM, were used. Several different phases can be present in β Ti alloys, including α, α", ω and O' phases. According to our XRD analysis, mainly β matrix and α" phase were identified, while no peaks of ω or O' phases were observed. If they formed, this might be due to the limited size and volume fraction of the ω and O' phases. The peaks of the α phase overlap with most of those of the α" phase; hence we could not exclude the possibility that a small amount of α could be present. Table 5.3 summarises the phase constitutes of the TMZF samples from XRD analysis. AF-SS TMZF alloy is composed of β matrix and α" phase, accounting for 67.07 ± 0.30 %, and 32.93 ± 0.39 % in volume fraction, respectively (Fig. 5.8a). The AF-CS TMZF contains mainly β matrix (97.51 ± 0.35 %) with a small fraction of α" phase (2.49 (± 0.08) %) (Fig. 5.8b). The ST-CS TMZF contains 96.05 (± 0.53) % β phase and 3.95 (± 0.38) % α” phase (Fig. 5.8c).

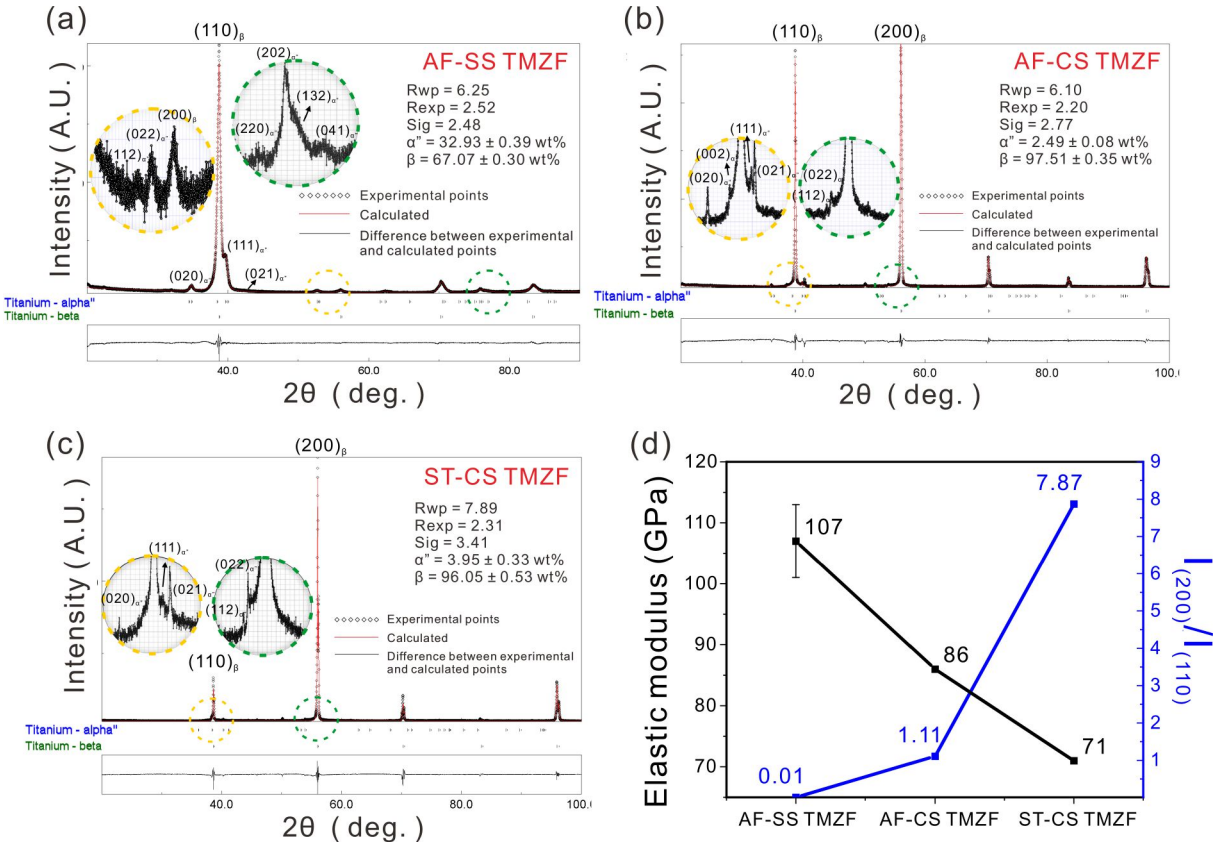


Fig. 5.8. Rietveld refinement analysis of the XRD patterns obtained from the planes perpendicular to TD, and parallel with BD, of (a) AF-SS, (b) AF-CS, and (c) ST-CS TMZF alloys (The different positions were magnified to label the peaks of α" phase, which were indicated by yellow or green dotted circles, respectively). (d) The Young's modulus and the peak intensity ratios of $(200)_\beta$ to $(110)_\beta$ of the three groups of samples in different processing conditions.

Table 5.3 The microstrain, dislocation density, β phase lattice parameters and phase constitutions of the three groups of TMZF alloys calculated by the Rietveld method.

TMZF	Microstrain ε_{micro} ($\times 10^{-4}$)	Dislocation density (m^{-2})	Volume fraction β (%)	$a = b =$ c (Å)	Volume fraction α" (%)
AF-SS	5.55 ± 0.08	2.68×10^{15}	67.07 ± 0.30	3.22	32.93 ± 0.39
AF-CS	0.88 ± 0.01	5.42×10^{13}	97.51 ± 0.35	3.27	2.49 ± 0.08
ST-CS	0.44 ± 0.02	1.12×10^{13}	96.05 ± 0.53	3.30	3.95 ± 0.38

Fig. 5.9 illustrates the morphology and distribution of secondary phases of AF-SS TMZF alloy using both EBSD and TEM. EBSD IPF map (Fig. 5.9a) shows a high density of α" phase, which is unevenly distributed. The SEM micrograph (Fig. 5.9b) shows that three α" precipitates formed a triangle. The HAADF-STEM image (Fig. 5.9c) further reveals the distribution of α" phase, with three variants, inside the matrix grains. These α" precipitates are needle-shaped with a thickness of 78 (± 12) nm and a length of 406 (± 62) nm. Interestingly, EDS elemental maps of a representative area containing α" phase triangle show a pronounced composition difference between α" (lean in solute elements) and the β phase matrix. In comparison with the β phase matrix, the precipitated α" is rich in Ti but deficient in Mo and Fe, while has almost no difference in Zr (Figs. 5.9d-g). Quantitative EDS analysis of the contents of each constituent elements in α" and β phase is presented in Table 5.4.

These α" precipitates are in three different variants, which rotate 60° with the $(\bar{1}10)$ common plane observed along the $[1\bar{1}1]_\beta$ zone axis, as shown in Figs. 5.9h-5.9i. For the phase transformation during LPBF, the total system (β + α") would favour the low strain energy, so-called self-accommodation, through clustering of certain selected variants [53]. The variants selection effects mainly were reported on the HCP α phase [54]. Similar orthorhombic α" variants, usually seen as the HCP structure deformed in its basal plane, were only reported in some near β Ti alloys, which required a low-temperature isothermal ageing treatment for an extended period [55]. Nevertheless, the observation of three variants of α"/α"-OR (orientation relationship) of $[\bar{1}10]/60^o$ with the neighbouring α" in metastable β TMZF alloys in this study provides novel insights into its formation mechanism, indicating that α" could be acted as the transformation stage for HCP α phases. Moreover, high-density sessile dislocation loops (Fig. 5.9j) were noticed around these α" variants. These dislocation loops might be there to accommodate the interfacial strain between the α" and the matrix.

SAED pattern of the area without α" phase along the $[0\bar{1}1]_{\beta}$ zone axis (Fig. 5.9k) also shows the presence of ω phase. The dark-field TEM image (Fig. 5.9l) further shows the nanoscale size of ω phase. The invisibility of ω phase in the XRD pattern should be attributed to its small size and low volume fraction. In conclusion, the AF-SS TMZF contains a high density of α" variants and nanoscale ω phase.

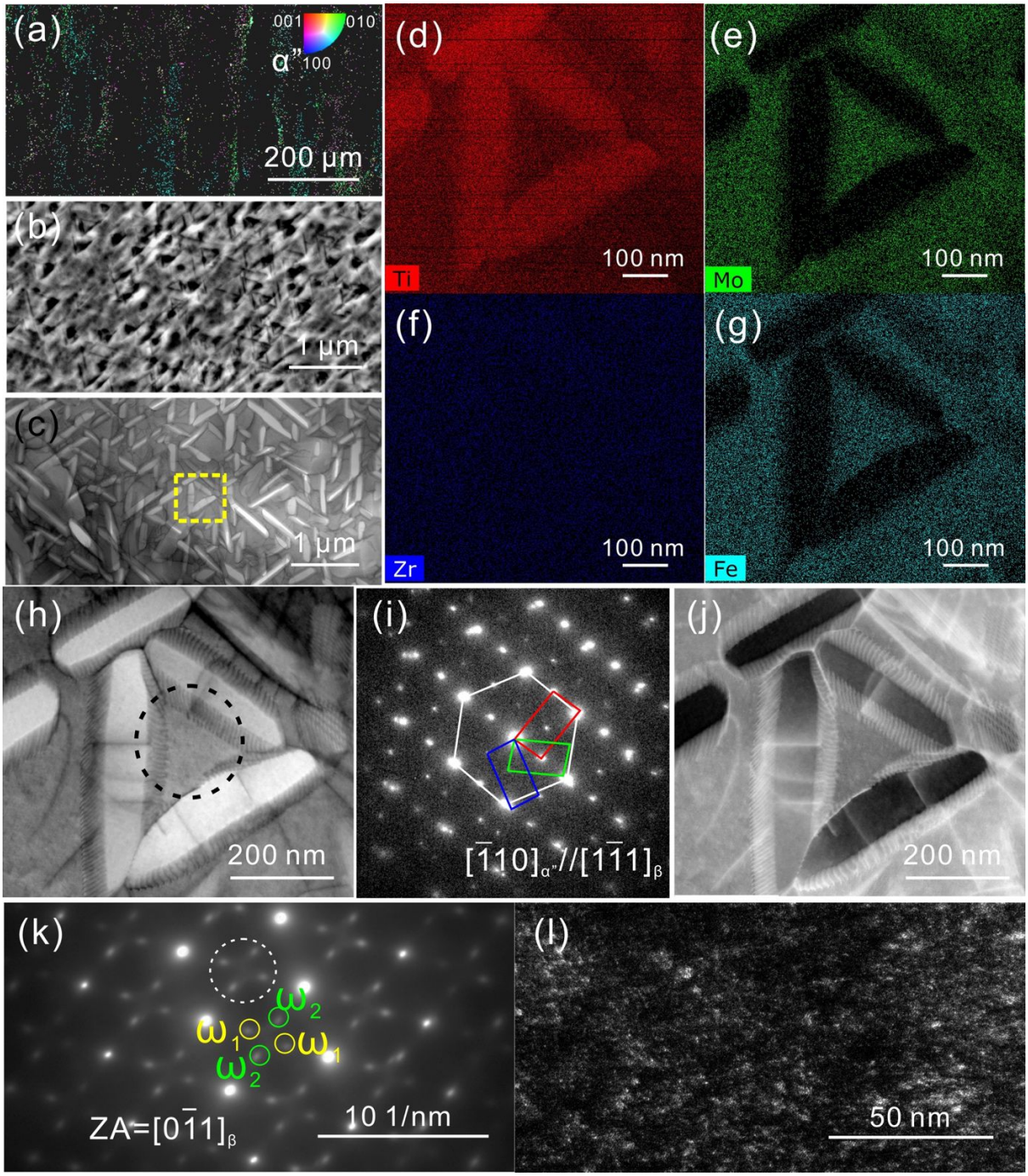


Fig. 5.9. The microstructure of the AF-SS TMZF alloy. (a) EBSD IPF map of the α" phase in the plane perpendicular to TD; (b) SEM image; (c) HAADF-STEM image of the α" phase; (d)-(g) EDS elemental maps of Ti, Mo, Zr, and Fe collected from the yellow dotted square in (c), respectively; (h) bright-field TEM image of a selected area containing α" phase; (i) the SAED pattern along the $[\bar{1}11]_{\beta}$ zone axis collected from the black dotted circle in (h) shows the orientation relationship of $[\bar{1}10]_{\alpha''}//[1\bar{1}1]_{\beta}$; (j) a HAADF-STEM image shows the β matrix and α" phases; (k) SAED pattern along the $[0\bar{1}1]_{\beta}$ zone axis collected from the area without α" phase; and (l) dark-field TEM image selected from the ω reflections as indicated by the white circle in (k).

Fig. 5.10 shows the secondary phases of the AF-CS TMZF alloy. The EBSD IPF map (Fig. 5.10a) reveals the morphology of grains along the melt pool boundaries (marked by the black dotted lines), where the grain boundaries were decorated by a chain of α" phase (Fig. 5.10b). The tiny difference (< 2°) in kernel average misorientation (KAM) (Fig. 5.10c) indicates low residual strain in β matrix. The localised distribution of α" precipitate was further confirmed by TEM (Fig. 5.10d), with a thickness of 132 (± 9) nm and a length of 504 (± 73) nm, where clusters of α" were observed. The SAED pattern obtained from an area free from the α" phase along the $[\bar{1}13]_{\beta}$ zone axis (inset of Fig. 5.10d) shows the presence of mainly β phase, while no ω phase was observed. Inside some β matrix grains, the α" phases were also observed, with a thickness of 144 (± 6) nm and length of 599 (± 84) nm (Figs. 5.10e-f). The SAED pattern (Fig. 5.10g) demonstrates that the burgers relationship between α" and β matrix is $[1\bar{3}1]_{\alpha"} // [1\bar{1}2]_{\beta}$. Similar to the composition of α" phase present in AF-SS TMZF alloy, the composition of α" phase in AF-CS TMZF also shows the substantial difference from that of the β matrix (Figs. 5.10h-l). The quantified results were also included in Table 5.4.

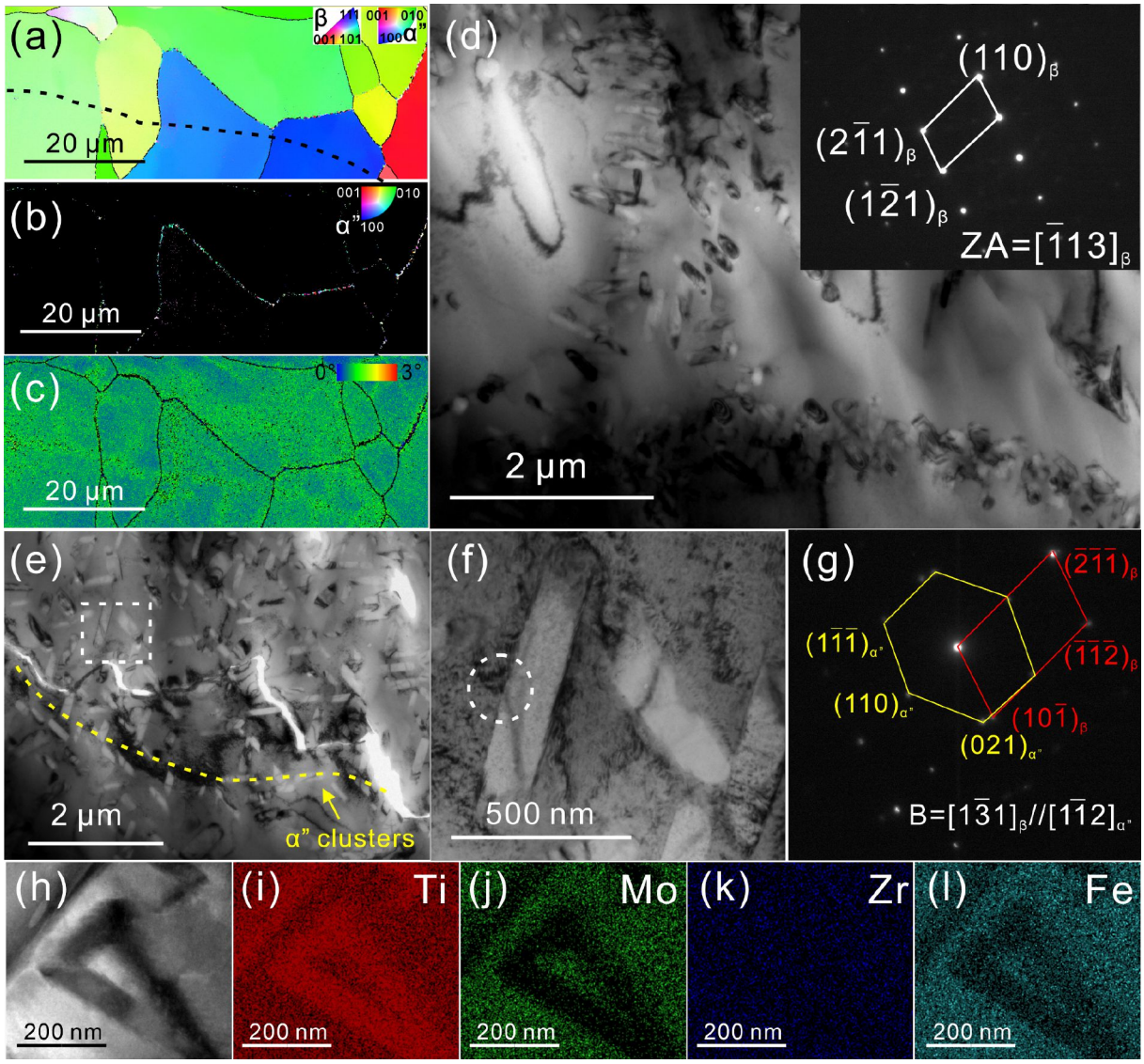


Fig. 5.10. The microstructure of the AF-CS TMZF alloy. (a) EBSD IPF map of β and α" phase; (b) EBSD IPF map only showing the α" phase; (c) KAM map of the β Ti matrix; (d) bright-field TEM image shows the grain boundaries clustering α" phases with the inserted SAED pattern along the $[\bar{1}13]_\beta$ zone axis collected from the area without α" phases; (e) bright-field TEM image shows the α" variants inside some grains; (f) bright-field TEM image magnified from the selected area (white dotted square) of (e); (g) SAED pattern along the $[1\bar{3}1]_\beta$ zone axis collected from the white dotted circle in (f); (h) a HAADF-STEM image shows the β matrix and α" phases in the AF-CS TMZF alloy; and (i)-(l) EDS elemental maps of Ti, Mo, Zr, and Fe, respectively.

Fig. 5.11 presents the secondary phases of the ST-CS TMZF alloy. The α" phase is

unevenly distributed in the β matrix grains (Fig. 5.11a). Some of the matrix grains contain a high density of α" phase (e.g. grains ① and ③ in Fig. 5.11b), while the others are nearly free of α" phase (e.g. grain ② in Fig. 5.11b). Moreover, the residual stress was higher in α" phase rich-matrix grains (grains ① and ③) than those free from α" phase (e.g. grain ②) (Fig. 5.11c). After solution heat treatment, the overall residual stress was reduced. Moreover, the α" precipitates inside the matrix grains get much coarser than those found in the AF-CS TMZF alloy, with the thickness of 372 (± 67) nm and length of 1014 (± 158) nm and in plate-like shape (Fig. 5.11d). A higher magnification TEM image (Fig. 5.11e) shows that dislocation tangles are formed in some α" phase, suggesting the high internal stress within α". The SAED pattern, along the $[\bar{1}10]_{\beta}$ zone axis, does not show the presence of ω phase (Fig. 5.11f). The absence of ω in the ST-CS TMZF might be attributed to the suppression effects of Zr and Fe on the formation of ω phase during fast cooling from the β phase region [56,57]. The HAADF-STEM image (Fig. 5.11g) and its corresponding EDS elemental maps (Figs. 5.11h-k) also reveal that the matrix in ST-CS TMZF are in the supersaturated state with a high content of β-stabilising elements (Mo and Fe), whereas the α" phase is deficient in Mo and Fe, similar to that in AF-SS and AF-CS TMZF samples. Quantitative composition data of α" phase and β-matrix are also included in Table 5.4.

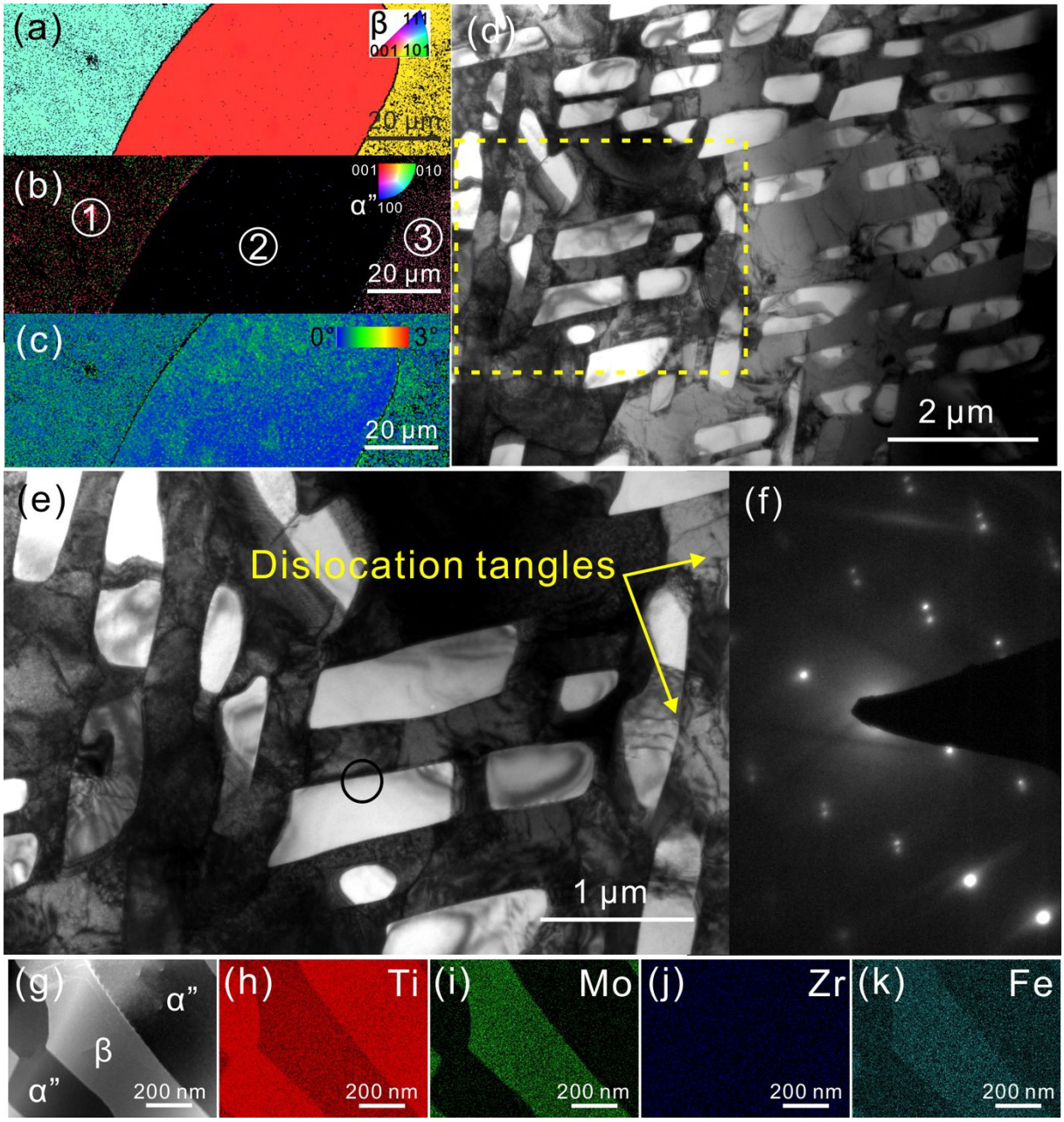


Fig. 5.11. The microstructure of the ST-CS TMZF. (a) the EBSD IPF map of β phase; (b) the EBSD IPF map only showing the α" phase; (c) the KAM map of the β Ti matrix; (d) a low magnification bright-field TEM image; (e) a higher magnification bright-field TEM image which clearly illustrates the dislocation tangles inside the α" phase; (f) SAED pattern along the $[011]_{\beta}$ zone axis collected from the interface of β and α" phases as indicated by the black circle in (e); (g) a HAADF-STEM image shows the β matrix and α" phases; and (h)-(k) EDS elemental maps of Ti, Mo, Zr, and Fe, respectively.

Table 5.4. Quantitative EDS analysis of the contents of Ti, Mo, Zr, and Fe in the α" and β

phases of the fabricated TMZF alloys.

TMZF - phases	The weight percentage of the constituent elements			
	Ti (wt%)	Mo (wt%)	Zr (wt%)	Fe (wt%)
AF-SS - β	74.7 ± 0.1	19.0 ± 0.8	3.8 ± 0.9	2.5 ± 0.3
AF-CS - β	76.0 ± 0.1	15.1 ± 1.4	6.4 ± 1.6	2.5 ± 1.0
ST-CS - β	74.7 ± 0.1	19.8 ± 0.2	4.4 ± 0.6	1.1 ± 0.4
AF-SS - α”	93.3 ± 0.1	1.3 ± 0.7	5.3 ± 1.2	0.2 ± 0.1
AF-CS - α”	92.2 ± 0.1	1.6 ± 0.8	6.0 ± 1.9	0.3 ± 0.1
ST-CS - α”	92.3 ± 0.1	1.4 ± 0.2	6.2 ± 0.4	0.2 ± 0.2

5.3.6. Heat treatment response

As shown in Fig. 5.12, the DSC curves illustrate the phase transformations' temperatures of AF-CS Ti12Mo and AF-CS TMZF. It displays the phase transformations of β to $\omega_{iso,}$ and β/ω_{iso} to α in the AF-CS Ti12Mo alloy is around 399℃ and 571℃, respectively. After adding Zr and Fe elements, the precipitating temperatures of these phases can be reduced to 361℃ and 529℃. Due to some inhomogeneous chemical concentrations and phases distributions, the decomposition of α” to β + α could happen in Mo lean (α” rich) region, when the β to ω_{iso} transforming in Mo rich region. The in-situ characterisations will be needed in future works to verify the decomposition of α” phase. Furthermore, the soluble temperatures of ω_{iso} and α phases in Ti12Mo specimens are 550℃ and 743℃, respectively. In TMZF samples, the temperatures were slightly reduced to 506℃ and 688℃ correspondingly.

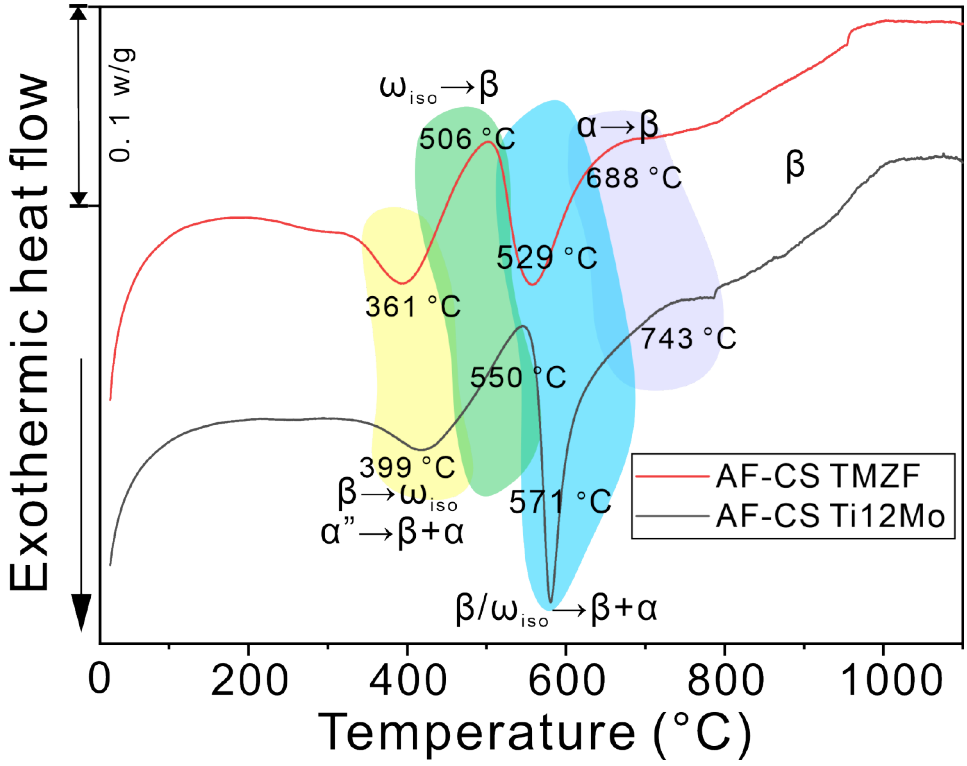


Fig. 5.12. DSC results of AF-CS Ti12Mo and TMZF.

5.4. Discussion

5.4.1. Chemical homogenisation

As represented in Fig. 5.13a, the melt pool depth and width (straight area) of the TMZF alloy fabricated using chessboard scanning strategy was measured to be 379 ± 15 µm and 91 ± 4 µm, respectively. The melt pool depth, as the laser penetration depth, depends on the energy input and beam size, as well as the laser beam absorption, thermal conductivity and thermal diffusivity of the powder [58]. The high melt pool depth is due to the laser scanning parameters used in this study according to a scaling law developed by Fabbro [59]:

$$d \propto \frac{AP}{\sigma u} \tag{5.1}$$

Where d is the melt pool depth, A is the laser absorptivity, P is laser power, σ is beam size,

and u is scanning speed.

Since melt pool depth d is 379 ± 15 μm while the layer thickness is only 20 μm, during LPBF, each layer experienced multiple remelts (about 19) from the laser beam. A schematic of laser remelts is illustrated in Fig. 5.13b. When performing the LPBF fabrication of TMZF alloy, the refractory particles, especially the Mo (Melting point: 2623 °C), were gradually dissolved into the alloy during repeated melting. To make sure each elemental particle is hit and remelted by the laser beams, the hatch spacing and beam shift were set to the appropriate value. The hatch spacing is 75 μm, while the beam shift is assigned to 22.5 μm (1/4 melt pool width), which means the laser beam would shift a constant distance for every two layers. And the scanning direction would rotate 90° for each powder layer. The hatch spacing, beam shift, scanning rotation, and deep melt pool depth would ensure every elemental powder to be remelted a number of times from different directions. The remelting process and the parameters should be the main reason for the refractory particles to be near fully dissolved (< 0.15 %), and become fairly evenly distributed in this study.

There have been several studies using LPBF to fabricate β Ti-Mo alloys from powder blends, such as Ti6Al4V+10Mo [24], Ti+15Mo [21], Ti+6.5Mo+3.5Mo_2C [60], and Ti+7.5Mo [23]. However, it is common to observe residual Mo particles inside the fabricated samples. It is known that in order to make Mo particles fully dissolved, there should be enough high energy input [60], but such high energy density (laser powers of 300 w and scanning speed of 1.2-1.6 m/s) would cause keyhole defects, due to deep penetration depth [21]. Hence, it is hard to balance the fraction of unmelted particles and porosities for β Ti-Mo alloys processed using LPBF in-situ alloying. We will discuss the optimisation routes to eliminate keyhole defects caused by the high energy density when processing powder mixtures of refractory elements using LPBF technology in future work.

However, as shown from Fig. 5.3 and 5.4, the composition is not entirely homogeneous. This could be due to several factors. Firstly, although care has been taken to ensure good homogenisation of elemental powders during mixing, it is inevitable that alloying powders' spatial distribution is sparse due to their low percentage, which could be inherited into the built material, causing inhomogeneity due to the relatively small size of the melt pool. This may also cause concerns for the repeatability of producing the mixed powders. Secondly, the low interdiffusion rate between Ti and Mo [23,61] means that the complete homogenisation of TMZF alloys takes time, but laser melting and cooling are very fast. Thirdly, solidification segregation of TMZF alloys can cause uneven distribution of alloying elements locally at a scale of grains and melt pools. Therefore, it remains a challenge to ensure chemical homogeneity across different scales.

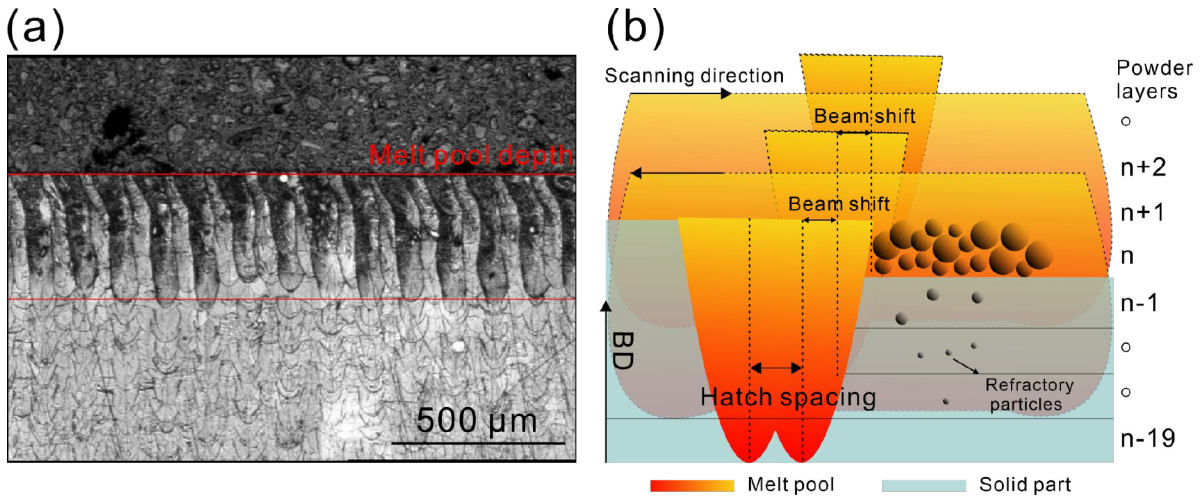


Fig. 5.13. (a) The optical microscopy image of the side section of the TMZF alloy manufactured by the chessboard scanning strategy shows the melt pool morphologies of the top layer. (b) The schematic represents the homogenisation mechanism during the laser remelts.

5.4.2. Second phases

As shown in STEM-EDS images of α" phase and Table 5.4, there is a compositional difference between α" and the β matrix. α" phase is lean in the solute element of Mo and Fe.

Three mechanisms are known to induce α" phase transformation in β stabilised Ti alloys: (i) the diffusionless displacive transformation, (ii) diffusion-driven phase transformations [62] and (iii) spinodal decomposition [63]. The martensite α" phase formed by diffusionless displacive mechanism does not have chemical differences with β matrix. On the other hand, if α" was formed by diffusion-driven, α" phase will be lean in alloying elements [62,64]. Some work [65] suggested that α" phase could form during water quench from β region through spinodal decomposition, which can also explain the α" phase formed in ST-CS TMZF samples. Our results, therefore, suggest that α" could be formed via either diffusion-driven phase transformation or spinodal decomposition, but not diffusionless displacive mechanism.

There are variations in constitutions, volume fraction, distribution, and size of secondary phases between AF-SS, AF-CS and ST-CS TMZF. Regarding the difference between AF-SS and AF-CS, the two experienced different thermal histories as a result of different laser processing parameters. Recently, studies [66,67] showed that the temperature oscillation depends on the scan track length, which is 17 mm for simple scanned specimens and 5 mm for the chessboard scanned specimens in this work. With the smaller scan track length and random sequence of the scanning for each island, the AF-CS samples are likely to have experienced higher peak temperatures, higher oscillation frequency, and faster cooling rate compared with the AF-SS samples. Therefore, the presence of varied phase constitutions and fractions between the AF-SS and AF-CS TMZF alloys could be due to the different thermal cycles they experienced. The solution treated TMZF has an additional thermal processing step. Hence it has the microstructure significantly different from the as-fabricated ones.

We also observed spatially uneven distribution of precipitations in our materials. For the AF-SS-TMZF, as shown from the EBSD map in Fig. 5.9a, there seem to be regions with a high density of α", and regions with much fewer. Similarly, for the AF-CS TMZF, inhomogeneous

distribution of α" can be found from the TEM images (Fig. 5.10d). Also, α" seems to decorate along the grain boundaries according to the EBSD results. This uneven distribution can also be observed from the ST-CS-TMZF alloy. As shown in Fig. 5.11b, grains 1 and 3 contain dense large second phase particles while grain 2 in between contains none. The uneven distribution of precipitates could be attributed to the local variation of composition distribution as the formation of α" phase is sensitive to the chemical composition of β Ti alloys [68]. Nevertheless, the mechanical properties of the AF-CS and ST-CS TMZF alloys are still satisfactory, with a good balance of strength and ductility. This indicates that entirely chemical homogeneity and subsequently homogeneous distribution of precipitates are not necessary for achieving good mechanical properties. Indeed, inhomogeneity and gradient structures have attracted research interests as new approaches to produce high-performance structural materials[69,70]. Therefore, our study suggests that in situ alloying based LPBF could be used to produce compositionally and microstructurally gradient components. Further evaluation of the mechanical properties of the printed samples, especially the fracture and fatigue properties, from different batches and across scales are needed to verify the consistency of properties upon scale up and from batch to batch.

5.4.3. Elastic modulus

It is well known that the elastic modulus of the metallic material is strongly influenced by the elemental composition and texture [32]. The elemental composition of the TMZF alloys is generally homogeneous, which is also close to the nominal composition (Fig. 5.4). Then the TMZF samples fabricated using the same processing parameters should be in similar composition, which would not cause a significant difference in elastic modulus. On the other hand, the lowest modulus was obtained along the $<001>_{\beta}$ orientation for β-Ti alloys compared

to other crystallographic textures [30,31]. As the results concluded from the EBSD (Fig. 5.6) and XRD Rietveld analysis (Fig. 5.8d), the three groups of TMZF alloys fabricated using different scanning strategies and heat treatment show pronounced texture variation. By switching the scanning strategy from the simple to chessboard scan, the texture changes from <011> preferential orientations to strong {100}<001> texture. As a result, the Young's modulus shows an apparent decrease from 107.1 GPa to 85.7 GPa. After solution heat treatment of the AF-CS sample, the {100}<001> texture shows a significant increase in intensity (Fig. 5.8d), leading to a further decrease of the elastic module to only 70.9 GPa. The grain rotation during recrystallisation should be the main driving force for the texture evolution during the solution heat treatment. Optimisation of the laser scanning strategy and subsequent heat treatment procedures could lead to strong {100}<001> texture in β Ti alloys, hence achieving low modulus. This texture engineering approach could potentially be used in β Ti alloys to reduce the Young's modulus, such as Ti-Nb alloys which already has an Young's modulus of ~ 45 GPa without texture optimisation [29], hence, enabling the fabrication of β Ti alloys with modulus as low as that of the human cortical bone.

The phase constituents may also affect the elastic modulus. The ω phase has 137.9 GPa as calculated using the Voigt-Reuss-Hill method, the highest elastic modulus from the phases present in metastable β-Ti alloys [10]. The high Young's modulus of AF-SS TMZF alloy might also come from the contribution of precipitated ω phase, together with its strong <011> preferential orientations along the TD. The AF-CS and ST-CS TMZF alloys are free from the ω phase and have a similar volume fraction of the α" phase. Therefore, their difference in Young's modulus should mainly result from the difference in texture.

5.4.4. Strengthening mechanisms

In order to quantitatively elucidate the strengthening mechanism of the TMZF alloys, dislocation slip system driven modelling will be used. The yield stress, which is comprised of the intrinsic strengthening (σ_i), dislocation strengthening (σ_{DS}), and precipitation strengthening (σ_{PS})， can be calculated using Eq. 5.2 [71] :

$$\sigma = \sigma_i + \sigma_{DS} + \sigma_{PS} \tag{5.2}$$

(a) Intrinsic strengthening

σ_i (Eq. 5.3) is the intrinsic strength, which is composed of the critical resolved shear stress(CRSS) of pure Ti ($\sigma_0 = M\tau_{CRSS}$ = 180 MPa [71,72]), grain boundary strengthening ($\sigma_{HP} = K_{H-P}d^{-1/2}$), and solid solution strengthening ($\sigma_{SS} = \left(\sum_i B_i^{3/2}X_i\right)^{2/3}$) [52]:

$$\sigma_i = M\tau_{CRSS} + K_{H-P}d^{-1/2} + \left(\sum_i B_i^{3/2}X_i\right)^{2/3} \tag{5.3}$$

K_{H-P} is the Hall-Petch constant ($K_{H-P} = 0.75\ MPa \cdot m^{1/2}$ for pure Ti) [71]. *d* is the mean grain size (calculated used EBSD grain size distributions (Fig. 5.6(b, d and f)). B_i means the solid solution strengthening coefficient. X_i is the atomic fraction of the solute element *i*. For the TMZF alloys, the σ_{SS} was estimated to be 239 MPa [71]. Therefore, intrinsic strengthening (σ_i) was estimated to be 550, 568, 501 MPa for AF-SS, AF-CS, and ST-CS TMZF alloys, respectively.

(b) Dislocation strengthening

The dislocation strengthening (σ_{DS}) was calculated using the Taylor relation as Eq. 5.4:

$$\sigma_{DS} = \alpha M \mu b \sqrt{\rho} \tag{5.4}$$

α is the dislocation interaction constant, which is 0.3 in this work [73]. *M* is the Taylor factor (*M* = 2.8) [71]. μ is the shear modulus (μ = 39 GPa) [71]. b is the magnitude of Burgers vector (b = 0.28 nm) [71]. ρ is the dislocation density which was estimated using the microstrain (ε_{micro}, Table 5.3) obtained from the XRD Rietveld method referring to the Eq. 5.5 [74]:

$$\rho = \frac{3E}{\mu b^2(1+2\nu^2)}\varepsilon_{micro}^2 \tag{5.5}$$

E is the measured Young's modulus. ν is the Poisson's ratio, ~ 0.32. The microstrain (ε_{micro}) was calculated based on the peaks broadening of XRD patterns after isolating the effects of instrument and grain size (Table 5.3). The dislocation density of the AF-SS TMZF is 2.68×10^{15} m^{-2}. This value could be overestimated because the existed ω particles can broaden the peaks of the β matrix. Furthermore, the dislocation densities were lowered evidently in AF-CS TMZF alloy due to the short scan track length of the chessboard scan. The dislocation strengthening for AF-SS, AF-CS, and ST-CS TMZF alloys are estimated to be 474, 68 and 31 MPa, respectively.

(c) Precipitation strengthening

With the intrinsic strengthening (σ_i) and dislocation strengthening (σ_{DS}) calculated, the strengthening contribution from precipitates can be derived according to Eq. 5.6:

$$\sigma_{PS} = \sigma - (\sigma_{\mathrm{i}} + \sigma_{DS}) \tag{5.6}$$

For the AF-SS TMZF, the yield strength (σ_y) was estimated according to Tabor's equation (Eq. 5.7) [75] to be 1594 MPa.

$$\sigma_y = 3H \tag{5.7}$$

Where *H* is the hardness (GPa) and σ_y can be the yield or flow stress.

Using Eqs. (5.1-5.6), strengthening contribution from different sources of the AF-SS, AF-CS, and ST-CS TMZF alloys were calculated, listed in Table 5.5 and plotted in Fig. 5.14a. The strengthening contribution from secondary phases of different samples was plotted in Fig. 5.14b, together with the volume fraction of α" phase. The secondary phases contribute about 570 MPa to the yield strength of AF-SS TMZF, which is the highest among the three groups of samples. This contribution comes from the high volume fraction of α" and ω phases. The strengthening contributions from secondary phases of the AF-CS and ST-CS TMZF alloys are reasonably close, which are 390 and 411 MPa, respectively. The AF-CS and ST-CS TMZF alloy consist of the β matrix with α" phase, in different shapes and sizes, but without ω precipitates. The dislocations slips were impeded by the α"/β interfaces during deformations, inducing substantial strengthening effects. Some work reported that the volume fraction of stress-induced martensite (SIM) α" phase has significant effects on the strength of metastable β TiAlMoVCr alloy [76]. The strength of TiNbTaZr alloy also proved to be strongly affected by the volume fraction of α" phase, controlled through isothermal ageing treatment [28]. In this work, the volume fraction of α" phase in the AF-CS is slightly lower than that of the ST-CS TMZF, which could explain the difference in strengthening contribution from α" phase between the two alloys. However, it is noted that the shape, size and distribution of α" phase in the two conditions are significantly different, which would be taken into considerations for more analysis and modelling in future works.

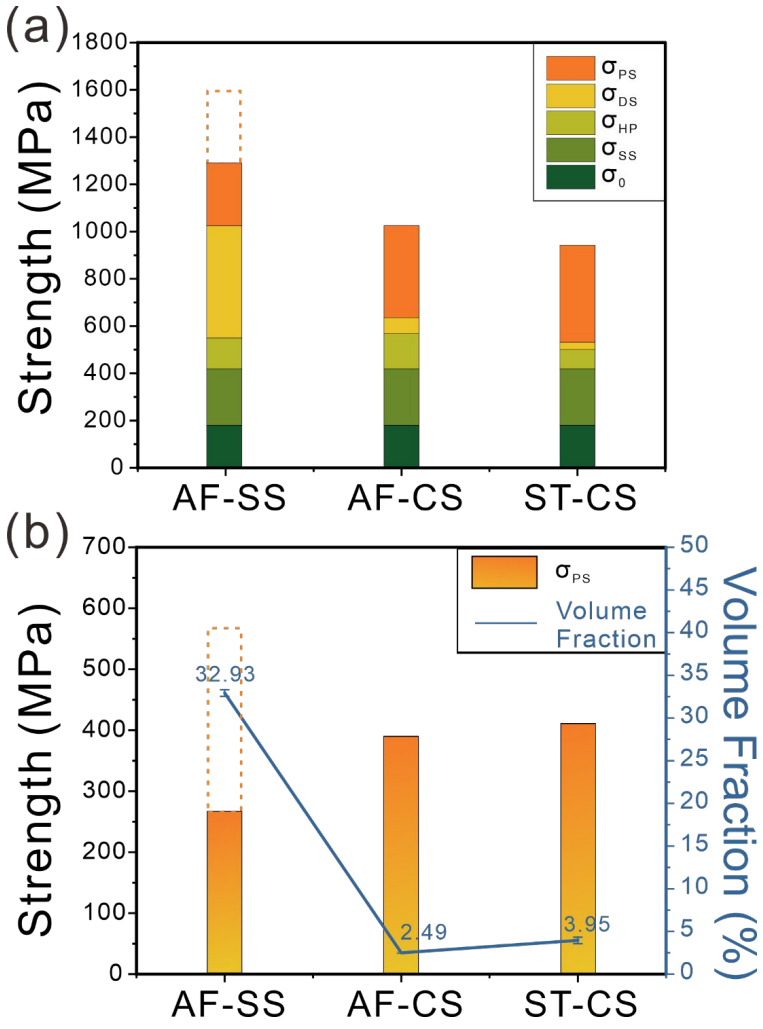


Fig. 5.14. (a) The contributions from CRSS of pure Ti (σ_0), solid solution strengthening (σ_{SS}), grain boundary strengthening (σ_{HP}), dislocation strengthening (σ_{DS}), and precipitation strengthening (σ_{PS}) of AF-SS, AF-CS and ST-CS TMZF alloys. (b) The precipitation strengthening (σ_{PS}) and the volume fraction of α" phases in AF-SS, AF-CS and ST-CS TMZF alloys.

Table 5.5. The contributions from CRSS of pure Ti (σ_0), solid solution strengthening (σ_{SS}), grain boundary strengthening (σ_{HP}), dislocation strengthening (σ_{DS}), precipitates strengthening (σ_{PS}) ,and σ_y of AF-SS, AF-CS and ST-CS TMZF alloys

TMZF	σ_0 (MPa)	σ_{SS}(MPa)	σ_{HP} (MPa)	σ_{DS} (MPa)	σ_{PS} (MPa)	σ_y (MPa)
AF-SS	180	239	131	474	570	1291 (± 25)
AF-CS	180	239	149	68	390	1026 (± 5)
ST-CS	180	239	82	31	411	943 (± 8)

5.5. Conclusions

The metastable β Ti-12Mo-6Zr-2Fe alloy with a highly dense structure was successfully fabricated by LPBF using in-situ alloying from elemental powder blends. The key findings were summarised as follows:

(1) The AF-SS TMZF alloy shows high strength of up to 1291 (± 25) MPa but fails before yielding. This alloy also demonstrates a high Young's modulus of 107.1 (± 3.3) GPa, mainly due to the strong <011> preferential orientations. The high-density sessile dislocations, heterogeneous α" phases and their interactions lead to the high strength. The embrittlement ω phase and their extended straight grain boundaries could induce intergranular fracture.

(2) The AF-CS TMZF alloy has strong {100}<001> texture, α" phase with three variants, free from ω phase. It also has heterogeneous grain size distribution with refined grains formed in the central region of the melt pool during solidification. Such a hierarchical microstructure confers an excellent combination of high yield strength of 1026 (± 5) MPa, good elongation of 12.7 (± 1.0) % and low Young's modulus of 85.7 (± 0.3) GPa.

(3) Solution treatment induces the formation of even stronger {100}<001> texture, and heterogeneous large plate-like α" precipitates in the equiaxed recrystallised β matrix. Despite a slight reduction in yield strength (943 (± 8) MPa) and elongation (12.0 (± 0.3) %), a much lower Young's modulus of 70.9 (± 0.1) GPa was achieved.

(4) Via dislocation slip system driven modelling, it is found that the nano-sized α" precipitates play an essential role in strengthening the TMZF alloys. α" phase was formed via a diffusion-driven phase transformation. The LPBF processing parameters and post-heat treatment can significantly change its size, volume fraction and distribution, hence offering a viable strategy for optimising the mechanical properties of β Ti alloys.

5.6. References

[1] C. Leyens, M. Peters, Titanium and titanium alloys: fundamentals and applications, Wiley-VCH, New York, 2003.

[2] S.B. Gabriel, L.H. de Almeida, C.A. Nunes, J. Dille, G.A. Soares, Maximisation of the ratio of microhardness to the Young's modulus of Ti–12Mo–13Nb alloy through microstructure changes, Mater. Sci. Eng., C. 33 (2013) 3319–3324. https://doi.org/10.1016/j.msec.2013.04.015.

[3] M.A.-H. Gepreel, M. Niinomi, Biocompatibility of Ti-alloys for long-term implantation, J. Mech. Behav. Biomed. Mater. 20 (2013) 407–415. https://doi.org/10.1016/j.jmbbm.2012.11.014.

[4] A. Kumar, K.C. Nune, R.D.K. Misra, Biological functionality and mechanistic contribution of extracellular matrix-ornamented three dimensional Ti-6Al-4V mesh scaffolds, J. Biomed. Mater. Res. 104 (2016) 2751–2763. https://doi.org/10.1002/jbm.a.35809.

[5] R. Huiskes, H. Weinans, B. van Rietbergen, The relationship between stress shielding and bone resorption around total hip stems and the effects of flexible materials, Clin. Orthop. Relat. Res. 274 (1992) 124–34. https://doi.org/10.1097/00003086-199201000-00014.

[6] A. Biesiekierski, J. Wang, M.A.-H. Gepreel, C. Wen, A new look at biomedical Ti-based shape memory alloys, Acta Biomater. 8 (2012) 1661–1669. https://doi.org/10.1016/j.actbio.2012.01.018.

[7] A. Cremasco, A.D. Messias, A.R. Esposito, E.A.D.R. Duek, R. Caram, Effects of alloying elements on the cytotoxic response of titanium alloys, Mater. Sci. Eng., C. 31 (2011) 833–839. https://doi.org/10.1016/j.msec.2010.12.013.

[8] L. Trentani, F. Pelillo, F.C. Pavesi, L. Ceciliani, G. Cetta, A. Forlino, Evaluation of the TiMo12Zr6Fe2 alloy for orthopaedic implants: in vitro biocompatibility study by using primary human fibroblasts and osteoblasts, Biomaterials. 23 (2002) 2863–2869. https://doi.org/10.1016/s0142-9612(01)00413-6.

[9] P. Neacsu, D.-M. Gordin, V. Mitran, T. Gloriant, M. Costache, A. Cimpean, In vitro performance assessment of new beta Ti–Mo–Nb alloy compositions, Mater. Sci. Eng., C. 47 (2015) 105–113. https://doi.org/10.1016/j.msec.2014.11.023.

[10] X. Zhao, M. Niinomi, M. Nakai, J. Hieda, Beta type Ti–Mo alloys with changeable Young's modulus for spinal fixation applications, Acta Biomater. 8 (2012) 1990–1997. https://doi.org/10.1016/j.actbio.2012.02.004.

[11] W. Sprengel, T. Yamada, H. Nakajima, Interdiffusion in Binary β-Titanium Alloys, Defect Diffusion Forum. 143–147 (1997) 431–436. https://doi.org/10.4028/www.scientific.net/ddf.143-147.431.

[12] A.B. Elshalakany, S. Ali, A.A. Mata, A.K. Eessaa, P. Mohan, T.A. Osman, V.A. Borrás, Microstructure and Mechanical Properties of Ti-Mo-Zr-Cr Biomedical Alloys by Powder Metallurgy, J. Mater. Eng. Perform. 26 (2017) 1262–1271. https://doi.org/10.1007/s11665-017-2531-z.

[13] S. Veeck, D. Lee, R. Boyer, R. Briggs, The castability of Ti-5553 alloy: Its microstructure and properties, Journal of Advanced Materials. 37 (2005) 40–45.

[14] S.L. Sing, W.Y. Yeong, F.E. Wiria, Selective laser melting of titanium alloy with 50 wt% tantalum: Microstructure and mechanical properties, J. Alloys Compd. 660 (2016) 461–470. https://doi.org/10.1016/j.jallcom.2015.11.141.

[15] W. Chen, C. Chen, X. Zi, X. Cheng, X. Zhang, Y.C. Lin, K. Zhou, Controlling the microstructure and mechanical properties of a metastable beta titanium alloy by selective laser melting, Mater. Sci. Eng., A. 726 (2018) 240–250. https://doi.org/10.1016/j.msea.2018.04.087.

[16] M. Fischer, D. Joguet, G. Robin, L. Peltier, P. Laheurte, In situ elaboration of a binary Ti-26Nb alloy by selective laser melting of elemental titanium and niobium mixed powders, Mater. Sci. Eng., C. 62 (2016) 852–859. https://doi.org/10.1016/j.msec.2016.02.033.

[17] L.C. Zhang, D. Klemm, J. Eckert, Y.L. Hao, T.B. Sercombe, Manufacture by selective laser melting and mechanical behavior of a biomedical Ti–24Nb–4Zr–8Sn alloy, Scr. Mater. 65 (2011) 21–24. https://doi.org/10.1016/j.scriptamat.2011.03.024.

[18] Y. Li, Y. Ding, K. Munir, J. Lin, M. Brandt, A. Atrens, Y. Xiao, J.R. Kanwar, C. Wen, Novel β-Ti35Zr28Nb alloy scaffolds manufactured using selective laser melting for bone

implant applications, Acta Biomater. 87 (2019) 273–284. https://doi.org/10.1016/j.actbio.2019.01.051.

[19] T. DebRoy, H.L. Wei, J.S. Zuback, T. Mukherjee, J.W. Elmer, J.O. Milewski, A.M. Beese, A. Wilson-Heid, A. De, W. Zhang, Additive manufacturing of metallic components - Process, structure and properties, Prog. Mater. Sci. 92 (2018) 112–224. https://doi.org/10.1016/j.pmatsci.2017.10.001.

[20] M. Simonelli, N.T. Aboulkhair, P. Cohen, J.W. Murray, A.T. Clare, C. Tuck, R.J.M. Hague, A comparison of Ti-6Al-4V in-situ alloying in Selective Laser Melting using simply-mixed and satellited powder blend feedstocks, Mater. Charact. 143 (2018) 118–126. https://doi.org/10.1016/j.matchar.2018.05.039.

[21] I. Yadroitsev, P. Krakhmalev, I. Yadroitsava, Titanium Alloys Manufactured by In Situ Alloying During Laser Powder Bed Fusion, J. Occup. Med. 69 (2017) 2725–2730. https://doi.org/10.1007/s11837-017-2600-7.

[22] F. Huber, T. Papke, C. Scheitler, L. Hanrieder, M. Merklein, M. Schmidt, In Situ Formation of a Metastable β-Ti Alloy by Laser Powder Bed Fusion (L-PBF) of Vanadium and Iron Modified Ti-6Al-4V, Metals-Basel. 8 (2018) 1067. https://doi.org/10.3390/met8121067.

[23] N. Kang, Y. Li, X. Lin, E. Feng, W. Huang, Microstructure and tensile properties of Ti-Mo alloys manufactured via using laser powder bed fusion, J. Alloys Compd. 771 (2019) 877–884. https://doi.org/10.1016/j.jallcom.2018.09.008.

[24] B. Vrancken, L. Thijs, J.P. Kruth, J.V. Humbeeck, Microstructure and mechanical properties of a novel β titanium metallic composite by selective laser melting, Acta Mater. 68 (2014) 150–158. https://doi.org/10.1016/j.actamat.2014.01.018.

[25] R. Martinez, I. Todd, K. Mumtaz, In situ alloying of elemental Al-Cu12 feedstock using selective laser melting, Virtual Phys Prototyp. 14 (2019) 1–11. https://doi.org/10.1080/17452759.2019.1584402.

[26] Q. Chen, G.A. Thouas, Metallic implant biomaterials, Mater. Sci. Eng. R. 87 (2014) 1–57. https://doi.org/10.1016/j.mser.2014.10.001.

[27] ASTM F1813-13, Standard Specification for Wrought Titanium-12 Molybdenum-6 Zirconium-2 Iron Alloy for Surgical Implant(UNS R58120), ASTM International, West Conshohocken.PA.USA, 2013. https://www.astm.org.

[28] H.J. Rack, J.I. Qazi, Titanium alloys for biomedical applications, Mater. Sci. Eng., C. 26 (2006) 1269–1277. https://doi.org/10.1016/j.msec.2005.08.032.

[29] C.-T. Wu, H.-T. Chang, C.-Y. Wu, S.-W. Chen, S.-Y. Huang, M. Huang, Y.-T. Pan, P. Bradbury, J. Chou, H.-W. Yen, Machine learning recommends affordable new Ti alloy with bone-like modulus, Mater Today. (2019). https://doi.org/10.1016/j.mattod.2019.08.008.

[30] M. Tane, S. Akita, T. Nakano, K. Hagihara, Y. Umakoshi, M. Niinomi, H. Nakajima, Peculiar elastic behavior of Ti-Nb-Ta-Zr single crystals, Acta Mater. 56 (2008) 2856–2863. https://doi.org/10.1016/j.actamat.2008.02.017.

[31] S.H. Lee, M. Todai, M. Tane, K. Hagihara, H. Nakajima, T. Nakano, Biocompatible low Young's modulus achieved by strong crystallographic elastic anisotropy in Ti-15Mo-5Zr-3Al alloy single crystal, J. Mech. Behav. Biomed. Mater. 14 (2012) 48–54. https://doi.org/10.1016/j.jmbbm.2012.05.005.

[32] T. Ishimoto, K. Hagihara, K. Hisamoto, S.-H. Sun, T. Nakano, Crystallographic texture control of beta-type Ti-15Mo-5Zr-3Al alloy by selective laser melting for the development of novel implants with a biocompatible low Young's modulus, Scr. Mater. 132 (2017) 34–38. https://doi.org/10.1016/j.scriptamat.2016.12.038.

[33] D. Zhang, D. Qiu, M.A. Gibson, Y. Zheng, H.L. Fraser, D.H. StJohn, M.A. Easton, Additive manufacturing of ultrafine-grained high-strength titanium alloys, Nature. 576 (2019) 91–95. https://doi.org/10.1038/s41586-019-1783-1.

[34] A. Srivastava, S. Manandhar, V. Moxson, V.A. Duz, C. Lavender, A. Devaraj, V.V. Joshi, A low-cost hierarchical nanostructured beta-titanium alloy with high strength, Nat. Commun. 6 (2016) 1–8. https://doi.org/10.1038/ncomms11176.

[35] F. Sun, J.Y. Zhang, M. Marteleur, C. Brozek, E.F. Rauch, M. Veron, P. Vermaut, P.J. Jacques, F. Prima, A new titanium alloy with a combination of high strength, high strain hardening and improved ductility, Scr. Mater. 94 (2015) 17–20. https://doi.org/10.1016/j.scriptamat.2014.09.005.

[36] S. Nag, R. Banerjee, J. Stechschulte, H.L. Fraser, Comparison of microstructural evolution in Ti-Mo-Zr-Fe and Ti-15Mo biocompatible alloys, J. Mater. Sci.: Mater. Med. 16 (2005) 679–685. https://doi.org/10.1007/s10856-005-2540-6.

[37] H. Azizi, H. Zurob, B. Bose, S.R. Ghiaasiaan, X. Wang, S. Coulson, V. Duz, A.B. Phillion, Additive manufacturing of a novel Ti-Al-V-Fe alloy using selective laser melting, Addit. Manuf. 21 (2018) 529–535. https://doi.org/10.1016/j.addma.2018.04.006.

[38] W. Chen, S. Cao, W. Kou, J. Zhang, Y. Wang, Y. Zha, Y. Pan, Q. Hu, Q. Sun, J. Sun, Origin of the ductile-to-brittle transition of metastable β-titanium alloys: Self-hardening of ω-precipitates, Acta Mater. 170 (2019) 187–204. https://doi.org/10.1016/j.actamat.2019.03.034.

[39] W. Zhu, J. Lei, C. Tan, Q. Sun, W. Chen, L. Xiao, J. Sun, A novel high-strength β-Ti alloy with hierarchical distribution of α-phase: The superior combination of strength and ductility, Mater. Design. 168 (2019) 107640. https://doi.org/10.1016/j.matdes.2019.107640.

[40] Y. Mantani, Y. Takemoto, M. Hida, A. Sakakibara, M. Tajima, Phase Transformation of α" Martensite Structure by Aging in Ti-8 mass%Mo Alloy, Mater. Trans. 45 (2004) 1629–1634. https://doi.org/10.2320/matertrans.45.1629.

[41] L. Lutterotti, S. Matthies, H.R. Wenk, A.S. Schultz, J.W. Richardson, Combined texture and structure analysis of deformed limestone from time-of-flight neutron diffraction spectra, J. Appl. Phys. 81 (1997) 594–600. https://doi.org/10.1063/1.364220.

[42] ASTM E8/E8M-16a, Standard Test Methods for Tension Testing of Metallic Materials, ASTM International, West Conshohocken, PA, 2016. https://www.astm.org.

[43] X. Yang, C.R. Hutchinson, Corrosion-wear of β-Ti alloy TMZF (Ti-12Mo-6Zr-2Fe) in simulated body fluid, Acta Biomater. 42 (2016) 429–439. https://doi.org/10.1016/j.actbio.2016.07.008.

[44] X. Zhao, M. Niinomi, M. Nakai, T. Ishimoto, T. Nakano, Development of high Zr-containing Ti-based alloys with low Young's modulus for use in removable implants, Mater. Sci. Eng., C. 31 (2011) 1436–1444. https://doi.org/10.1016/j.msec.2011.05.013.

[45] X. Zhao, M. Niinomi, M. Nakai, J. Hieda, T. Ishimoto, T. Nakano, Optimization of Cr content of metastable β-type Ti–Cr alloys with changeable Young's modulus for spinal fixation applications, Acta Biomater. 8 (2012) 2392–2400. https://doi.org/10.1016/j.actbio.2012.02.010.

[46] P.F. Santos, M. Niinomi, K. Cho, M. Nakai, H. Liu, N. Ohtsu, M. Hirano, M. Ikeda, T. Narushima, Microstructures, mechanical properties and cytotoxicity of low cost beta Ti–Mn alloys for biomedical applications, Acta Biomater. 26 (2015) 366–376. https://doi.org/10.1016/j.actbio.2015.08.015.

[47] D. Kuroda, M. Niinomi, M. Morinaga, Y. Kato, T. Yashiro, Design and mechanical properties of new β type titanium alloys for implant materials, Mater. Sci. Eng., A. 243 (1998) 244–249. https://doi.org/10.1016/s0921-5093(97)00808-3.

[48] S. Hanada, H. Matsumoto, S. Watanabe, Mechanical compatibility of titanium implants in hard tissues, Int. Congr. Ser. 1284 (2005) 239–247. https://doi.org/10.1016/j.ics.2005.06.084.

[49] W.F. Cui, A.H. Guo, Microstructures and properties of biomedical TiNbZrFe β-titanium alloy under aging conditions, Mater. Sci. Eng., A. 527 (2009) 258–262. https://doi.org/10.1016/j.msea.2009.08.057.

[50] S. Acharya, A.G. Panicker, D.V. Laxmi, S. Suwas, K. Chatterjee, Study of the influence of Zr on the mechanical properties and functional response of Ti-Nb-Ta-Zr-O alloy for orthopedic applications, Mater. Design. 164 (2019) 107555. https://doi.org/10.1016/j.matdes.2018.107555.

[51] S.A. Mantri, T. Alam, Y. Zheng, J.C. Williams, R. Banerjee, Influence of Post Deposition Annealing on Microstructure and Properties of Laser Additively Manufactured Titanium Copper Alloys, Addit. Manuf. 32 (2020) 101067. https://doi.org/10.1016/j.addma.2020.101067.

[52] G.H. Zhao, X.Z. Liang, B. Kim, P.E.J. Rivera-Díaz-del-Castillo, Modelling strengthening mechanisms in beta-type Ti alloys, Mater. Sci. Eng., A. 756 (2019) 156–160. https://doi.org/10.1016/j.msea.2019.04.027.

[53] S. Balachandran, A. Kashiwar, A. Choudhury, D. Banerjee, R. Shi, Y. Wang, On variant distribution and coarsening behavior of the α phase in a metastable β titanium alloy, Acta Mater. 106 (2016) 374–387. https://doi.org/10.1016/j.actamat.2016.01.023.

[54] Y. Ren, F. Wang, S. Wang, C. Tan, X. Yu, J. Jiang, H. Cai, Mechanical response and effects of β-to-α" phase transformation on the strengthening of Ti–10V–2Fe–3Al during one-dimensional shock loading, Mater. Sci. Eng., A. 562 (2013) 137–143. https://doi.org/10.1016/j.msea.2012.10.098.

[55] F.H. da Costa, C.A.F. Salvador, M.G. de Mello, R. Caram, Alpha phase precipitation in Ti-30Nb-1Fe alloys – phase transformations in continuous heating and aging heat treatments, Mater. Sci. Eng., A. 677 (2016) 222–229. https://doi.org/10.1016/j.msea.2016.09.023.

[56] D.D. Fontaine, N.E. Paton, J.C. Williams, The omega phase transformation in titanium alloys as an example of displacement controlled reactions, Acta Metall. 19 (1971) 1153–1162. https://doi.org/10.1016/0001-6160(71)90047-2.

[57] X.H. Min, S. Emura, L. Zhang, K. Tsuzaki, Effect of Fe and Zr additions on ω phase formation in β-type Ti–Mo alloys, Mater. Sci. Eng., A. 497 (2008) 74–78. https://doi.org/10.1016/j.msea.2008.06.018.

[58] A.M. Rubenchik, W.E. King, S.S. Wu, Scaling laws for the additive manufacturing, J. Mater. Process. Technol. 257 (2018) 234–243. https://doi.org/10.1016/j.jmatprotec.2018.02.034.

[59] R. Fabbro, Melt pool and keyhole behaviour analysis for deep penetration laser welding, J. Phys. D: Appl. Phys. 43 (2010) 445501. https://doi.org/10.1088/0022-3727/43/44/445501.

[60] B. Vrancken, S. Dadbakhsh, R. Mertens, K. Vanmeensel, J. Vleugels, S. Yang, J.-P. Kruth, Selective Laser Melting process optimization of Ti–Mo–TiC metal matrix composites, Cirp Ann. 68 (2019) 221–224. https://doi.org/10.1016/j.cirp.2019.04.120.

[61] B. Bian, Y. Liu, Y. Du, Q. Min, H. Liu, S. Wen, P. Zhou, Measurement of the Interdiffusion Coefficients in Mo-Ti and Mo- Ti-Zr Beta Phase Alloys from 1273 to 1473 K, J. Phase Equilib. Diffus. 40 (2019) 206–218. https://doi.org/10.1007/s11669-019-00715-1.

[62] M. Bönisch, A. Panigrahi, M. Stoica, M. Calin, E. Ahrens, M. Zehetbauer, W. Skrotzki, J. Eckert, Giant thermal expansion and α-precipitation pathways in Ti-alloys, Nat. Commun. 8 (2017) 1429. https://doi.org/10.1038/s41467-017-01578-1.

[63] R. Davis, H.M. Flower, D.R.F. West, Martensitic transformations in Ti-Mo alloys, J. Mater. Sci. 14 (1979) 712–722. https://doi.org/10.1007/bf00772735.

[64] L. Qi, S. He, C. Chen, B. Jiang, Y. Hao, H. Ye, R. Yang, K. Du, Diffusional-displacive transformation in a metastable β titanium alloy and its strengthening effect, Acta Mater. 195 (2020) 151–162. https://doi.org/10.1016/j.actamat.2020.05.058.

[65] R. Davis, H.M. Flower, D.R.F. West, The decomposition of Ti-Mo alloy martensites by nucleation and growth and spinodal mechanisms, Acta Metall. 27 (1979) 1041–1052. https://doi.org/10.1016/0001-6160(79)90192-5.

[66] H. Ali, H. Ghadbeigi, K. Mumtaz, Effect of scanning strategies on residual stress and mechanical properties of Selective Laser Melted Ti6Al4V, Mater. Sci. Eng., A. 712 (2018) 175–187. https://doi.org/10.1016/j.msea.2017.11.103.

[67] L. Parry, I.A. Ashcroft, R.D. Wildman, Understanding the effect of laser scan strategy on residual stress in selective laser melting through thermo-mechanical simulation, Addit. Manuf. 12 (2016) 1–15. https://doi.org/10.1016/j.addma.2016.05.014.

[68] R.P. Kolli, A. Devaraj, A Review of Metastable Beta Titanium Alloys, Metals-Basel. 8 (2018) 506. https://doi.org/10.3390/met8070506.

[69] T. Zhang, D. Wang, Y. Wang, Novel transformation pathway and heterogeneous precipitate microstructure in Ti-alloys, Acta Mater. 196 (2020) 409–417. https://doi.org/10.1016/j.actamat.2020.06.048.

[70] X. Wu, P. Jiang, L. Chen, F. Yuan, Y.T. Zhu, Extraordinary strain hardening by gradient structure, P. Natl. Acad. Sci. USA. 111 (2014) 7197–7201. https://doi.org/10.1073/pnas.1324069111.

[71] G.-H. Zhao, X. Xu, D. Dye, P.E.J. Rivera-Díaz-del-Castillo, Microstructural evolution and strain-hardening in TWIP Ti alloys, Acta Mater. 183 (2019) 155–164. https://doi.org/10.1016/j.actamat.2019.11.009.

[72] A. Mouritz, Introduction to Aerospace Materials, Woodhead Publishing Limited, Cambridge, 2012. https://doi.org/10.2514/4.869198.

[73] R. Madec, B. Devincre, L.P. Kubin, From Dislocation Junctions to Forest Hardening, Phys. Rev. Lett. 89 (2002) 255508. https://doi.org/10.1103/physrevlett.89.255508.

[74] A. Borbély, J.H. Driver, T. Ungár, An X-ray method for the determination of stored energies in texture components of deformed metals; application to cold worked ultra high purity iron, Acta Mater. 48 (2000) 2005–2016. https://doi.org/10.1016/s1359-6454(99)00457-7.

[75] D. Tabor, The hardness and strength of metals, J. Inst. Metals. 79 (1951) 1. https://ci.nii.ac.jp/naid/10029334659/en/.

[76] S. Sadeghpour, S.M. Abbasi, M. Morakabati, Deformation-induced martensitic transformation in a new metastable β titanium alloy, J. Alloys Compd. 650 (2015) 22–29. https://doi.org/10.1016/j.jallcom.2015.07.263.

Chapter 6: Deformation Mechanisms of β Ti-12Mo Alloy with High Strength and High Strain Hardening Rate Prepared by In-situ Alloying Based LPBF

The trade-off between the strength and ductility of β Titanium (Ti) alloys has been a long-standing dilemma. The metastable β Ti-12Mo (wt%) alloys usually show good ductility and high strain hardening rate (SHR), resulting from twinning-induced plasticity (TWIP), and transformation-induced plasticity (TRIP), but have low yield strength. In this work, the in-situ alloying based LPBF has been applied to produce the near fully dense and chemical homogeneous β Ti-12Mo alloy with a high yield strength of 725 MPa and excellent strain hardening rate (~2500 MPa at 4 % true strain) and 22% elongation. The deformation mechanisms controlling the mechanical performance were revealed via in-situ quantitative high energy synchrotron diffraction and advanced microstructural characterisation. The high yield strength mainly resulted from the isothermal ω nanoparticles, strengthening the alloy through the dislocation shearing mechanism. Hierarchical TWIP/TRIP effects were operative during plastic deformation. At the very early stage of plastic deformation (strain < 1.9 %), {332}<113> twinning was the dominant deformation mechanism, while the deformation-induced α" phase was only found to be activated at the later stage of deformation. The volume fraction of α" phase increased with the strain according to Olson-Cohen kinetic model, contributing to the continuous hardening of the alloy. The nanoscale composite band, consisting of the irrational {112}<751>β twin, ω lath and SIM α", was also observed at 5% tensile deformation. After that,

more secondary {112}<111> β and {130}<310> α" nano twins could confine the primary structures to nanograins, which provided continuous strain hardening behaviours.

The chapter is originated from the following manuscript:

R. Duan, F. Ren, O.V.Magdysyuk, J. H. Luan, Z. B. Jiao, M. M. Attallah, B. Cai, On the hierarchical TWIP/TRIP effects in a high strength metastable β Ti prepared by in-situ alloying based additive manufacturing. (Manuscript to be submitted Acta Materialia)

6.1. Introduction

β Ti alloy is an essential category of Ti alloys, with a wide range of applications from aerospace/aeronautical industry to biomedical implantations, due to its high specific strength, low modulus, excellent corrosion resistance and lightweight [1,2]. Laser powder bed fusion (LPBF) uses the laser to melt and fuse powders, permitting layer-by-layer construction of complicated and customised components [3–5]. A series of works have used LPBF to build high-quality β Ti alloys, including Ti-Mo, Ti-Nb, Ti-Ta, Ti-Zr and Ti-Fe systems, using either pre-alloyed powders or powder blends[2,3,6,7].

Within the last several years, enhanced ductility has been reported in several β Ti alloys, of which the deformation mechanisms, especially TWIP and TRIP, were widely studied [8,9]. The β phase stability largely governs the plastic deformation behaviour based on Mo equivalent function (Moeq). Dislocation slips dominated stabled β Ti alloys during plastic deformation[10] when Moeq >30[10]. When reducing the β phase stability to the metastable state (Moeq <30),

additional deformation mechanisms including stress-induced {332}<113> β twins, {112}<111> β twins, and SIM α" transformation can be activated[11].

To evaluate the β phase stability and develop new Ti alloys, Kuroda[12] proposed an alloying design approach established on a molecular orbital method, which is called the $\overline{Bo} - \overline{Md}$ method. $\overline{Bo}$ is the average covalent bond strength between Ti and another alloying element. $\overline{Md}$ is the mean d-orbital energy level related to the radius and electronegativity of metallic elements. In recent years, a variety of novel β Ti alloys with exceptional mechanical properties have been created based on the $\overline{Bo} - \overline{Md}$ map. By applying low $\overline{Bo}$ and high $\overline{Md}$ values [13], low modulus TiNbTaZr and TiNbSn alloys were created for biomedical applications[14–16]. Furthermore, β Ti-12Mo and Ti-9Mo-W alloys were developed with high ductility and high strain hardening capacity by triggering TWIP and TRIP simultaneously [17,18]. However, these alloys exhibit limited yield strength, typically less than 500 MPa. The low yield strength was attributed to the low critical stress (190 - 360 MPa) for triggering the martensite phase transformation, resulting in pseudo-elasticity.

For the Ti-12Mo alloy prepared by conventional methods, Sun et al. [8] found that the {332}<113> and {112}<111> β twins were activated accompanied with the β to ω/α" phases transformations at the early deformation stage of Ti-12Mo alloy. Whereas a recent work found the SIM α" phase was triggered at the initial stage of plastic deformation of Ti-12Mo alloy, followed by deformation twinning [19]. Thus, there are no consolidated conclusions of the plastic deformation sequence for the metastable β Ti alloys under solution treated state with the

same chemical compositions. Moreover, the plastic deformation behaviours were governed by composition and the initial phases constitutions. Recent works [20] proved a slightly elemental partitioning in ω phases could considerably change the mechanical behaviours from ductile to brittle. Additionally, the crystallographic orientations can also alter the sequence of TRIP/TWIP in different grains [21]. Therefore, the deformation behaviours in β Ti alloy can be varied due to a slight difference in the original microstructures.

In addition, the phases transformations (β to ω/a") in the metastable β Ti alloys were proved significantly influenced by prior processing routes [22]. Typically, materials undergo high-temperature gradients and fast cooling during LPBF, resulting in non-equilibrium microstructures inside the supersaturated matrix and the high-density dislocations [2]. These characteristics may affect the deformation sequence and hence the mechanical properties of β Ti alloys, while limited efforts have yet been paid to it. Consequently, it should be necessary to investigate the deformation mechanisms in the high-performance additive manufactured β Ti alloy.

In previous chapters/papers, we have shown that we successfully fabricated the near fully dense and largely homogeneous Ti-12Mo alloy by in-situ alloying based LPBF[3]. The samples were then solution heat-treated for further homogenisation, followed by a water quench. In this work, we have compared the microstructures and mechanical properties of the Ti-12Mo before (AF-CS) and after (ST-CS) heat treatment. The mechanical behaviours and performance were also compared with the Ti-12Mo alloy prepared via conventional methods. The ST-CS Ti-

12Mo samples show an excellent combination of high yield strength (725 ± 7 MPa), low modulus (81 ± 3 GPa), good ductility (22 ± 1 %), and high strain hardening capacities.

Moreover, the deformation mechanism of ST-CS Ti-12Mo was revealed via advanced characterisation. APT, EBSD and TEM technologies were performed to understand the microstructures of the specimens and quantify the strengthening contribution to the yield strength from various origins. The high yield strength can be attributed to the specific secondary phases of isothermal ω (ω_{iso}) and α" phases. The sequences of TWIP and TRIP was revealed using in-situ high energy synchrotron X-ray diffraction and ex-situ characterisations. These findings are essential for further optimising the microstructures and mechanical properties of metastable β Ti alloys processed using additive manufacturing.

6.2. Materials and Methods

6.2.1. Materials processing

Spherical pure Ti and Mo powders (TLS Technik GmbH, Germany), prepared by gas atomisation, were used as the base powders for Ti-12Mo (wt.%) powder blends. The Ti powder had a size in the range of 20-63 μm, and a d_{50} of 42.9 μm, while the Mo powder had a particle size in the range of 5-45 μm and a d_{50} of 20.7 μm. The mixed powders were blended for 24 h using a tumbler mixer to ensure a uniform blending under the protection of an Argon atmosphere.

All the specimens and components were then fabricated using a Concept Laser M2

Cusing® LPBF system, equipped with a 400 W Nd:YAG continuous laser source and a laser spot diameter of ~ 70 μm. The builds were carried out using a 20 μm layer thickness under a controlled argon atmosphere, where the oxygen content was ~1000 ppm. The schematic of the in situ LPBF processing can be found in Fig.6.1a. The optimised processing parameters are listed in Table 6.1. Chessboard (island) scan strategies were applied to fabricate the alloy. Using these parameters, near fully-dense (≧ 99.85%) Ti-12Mo alloys were obtained, evidently supported by the previous works [2,3]. To further homogenise the microstructure, the as-fabricated specimens were then sealed in vacuum quartz tubes and subjected to a solution treatment at 1273 K (over the β transus temperature) for 1 hour, followed by water quenching. We refer to the as-fabricated specimen as AF-CS Ti-12Mo, while the heat-treated samples are ST-CS Ti-12Mo. The specimen is highly dense and higher than theoretical density (4.88 > 4.831g/cm^3), tested using the Archimedes principle.

Table 6.1. Optimised in-situ alloying based LPBF processing parameters for the fabrication of Ti-12Mo alloy.

Parameters	Value
Laser power (W)	300
Scanning speed (mm/s)	1000
Hatch spacing (mm)	0.075
Layer thickness (mm)	0.02
Island size (mm)	5 × 5

6.2.2. In-situ X-ray diffraction and tensile tests

The tensile specimens for in-situ X-ray diffraction tests have a gauge of 4 × 1 mm (length × width), of which the total length is 42 mm. In situ synchrotron X-ray diffraction data (XRD) were recorded on a beamline I15 (Diamond, UK) using a 2D area flat panel detector Perkin Elmer. The wavelength calibration (λ= 0.22723) Å and 2D powder diffraction data reduction were performed with DAWN software [23–25] using LaB6 as a calibration standard

In situ XRD measurements were performed at various loads using the Deben CT5000 rig. The beam size of 1.1 × 1.1 mm was used during measurements. At each loading stage, the sample was rotated in steps of 10° over 180° rotation around the load direction. The resulting images were summed for every load. The Rietveld refinement of the full azimuthal integrated diffraction patterns (i.e. azimuthal integration over 360°) was performed to determine the relative amount of β Ti and α" Ti phases as a function of load. Additional azimuthal integrations of 15° (from - 7.5° till 7.5°) were performed for three directions: along the tensile (loading) direction (LD), Poisson direction (PD), and for the diagonal direction at 45° between these two directions as described on Fig.6.1b. Integration over 15° provides a good statistic for data analysis. Additional integration over 10° (from - 5° till 5°) instead of 15° showed that there is no difference in peak position or peak intensities between these two datasets.

The inter-planar distance of a given lattice plane family changes due to applied stress, known as lattice strain. The calculated lattice spacing without stress (d_0^{hkl}) and under different stress conditions (d^{hkl}), was used to quantify the lattice strain (ε^{hkl}) for all Bragg reflections,

as shown in Eq.6.1:

$$\varepsilon^{hkl} = \frac{d^{hkl} - d_0^{hkl}}{d_0^{hkl}} \tag{6.1}$$

The samples for ex-situ tensile tests were prepared based on the ASTM E8 standard [26], which have a gauge of 25 × 5 mm (length × width) and a total length of 65 mm. The tensile tests were performed at room temperature with an extensometer, of which the strain rates were 1×10^{-3} s^{-1}. The tensile direction for these samples was perpendicular to the build direction of LPBF. The ex-situ tensile tests were conducted using an MTS CMT 5000 machine. The tests were repeated three times to verify the reproducibility of the results.

6.2.3. Microstructural characterisation

The specimens were sectioned for microstructural characterisation and mechanical testing using electrical discharge machining (EDM). For scanning electron microscopy (SEM), backscattered electron (BSE) and electron backscattering diffraction (EBSD) observations, the specimens were sequentially grounded with 220 and 1200 grit SiC papers and polished by MD-Chem with OPS-H2O2 (7:3) solution (Struers, Denmark). The surface stress generated in the sample preparation process was eliminated through electrochemical polishing (6% perchloric acid + 94% methanol solution at a direct voltage of 30 V at 243 k). The transmission Kikuchi diffraction (TKD) samples and part of TEM foils were prepared using conventional grinding, polishing and ion milling (PIPS™, Gatan, Inc., Pleasanton, CA). The other TEM specimens

were lifted out from the samples' selected region, which were performed in an FEI Dual Beam FIB Helios 600i. The microstructure of the alloys was studied using SEM (TESCAN MIRA 3, Czech Republic) operated in secondary electron (SE), BSE and electron backscattering diffraction (EBSD) modes. The elemental distribution was analysed by X-MaxN Silicon Drift EDS Detector (Oxford Instruments, Oxford, UK), equipped in SEM. Before and after the deformation, the grain structure, crystallographic orientation, and martensite phase were characterised using a EBSD detector with a step size of 0.2 μm and analysed using Aztec crystal software. The TKD maps were acquired using the step size of 8 nm. The 3D EBSD maps were performed with the step size of 1 μm. Furthermore, the microstructure of the alloys was also investigated using the FEI Talos F200x TEM at 200 kV, equipped with 4 in-column SDD Super-X detectors to characterise the TEM, scanning TEM (STEM) microstructures and compositional mapping. The TEM images were processed by Image J software to determine the average diameter of ω particles. The lattice' dilatation field was studied using the geometric phase analysis (GPA) method on the Strain++ software [27].The simulations of selected area electron diffraction (SAED) patterns and the stereo-projection analysis of martensite and twinning were performed in a commercial software of SingleCrystal 4.14.

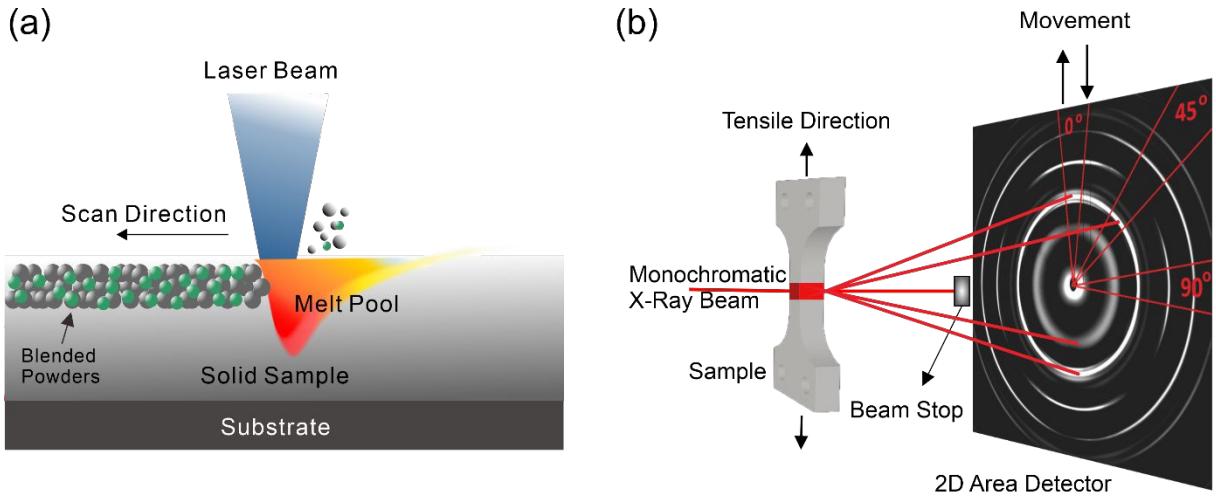


Fig. 6.1. (a) Schematic diagram shows the LPBF in-situ alloying process of Ti-12Mo blended powders. (b) schematic diagram shows the synchrotron experimental set-up of the tensile specimen, incident monochromatic X-ray beam, and the Debye-Scherrer rings represented in 2D area detector. The Debye-Scherrer ring is recorded at load 1440 N. Three 15º ranges (±7.5º) of azimuthal integration are shown: 0 º - diffraction in the tensile direction (loading direction), 90 º - diffraction in the Poisson direction, and 45 º - diffraction in the diagonal direction.

Lift-outs and annular milling in an FEI Scios focused ion beam/scanning electron microscope (FIB/SEM) were utilised to create needle-shaped specimens for atom probe tomography (APT) testing. Characterisations of APT were carried out in a local electrode atom probe (CAMEACA LEAP 5000 XR). At 70 K in voltage mode, the specimens were examined at a pulse repetition rate of 200 kHz, a pulse fraction of 20%, and an evaporation detection rate of 0.2 per cent atom per pulse. The 3D reconstructions and data analysis were carried out using Imago Visualization and Analysis Software (IVAS) version 3.8.

X-ray diffraction (XRD) patterns were recorded using a Rigaku Smartlab-9kW diffractometer (Rigaku, Tokyo, Japan) in the 2θ range of 20˚-100˚ with Cu Kα radiation (λ =

1.54056 Å, 45 kV, 200 mA). The oxygen and nitrogen content of the samples were measured using the ON736 elemental analyser (LECO, US), which were 0.236 (± 0.010) wt% and 0.091 (± 0.002) wt% in AF-CS Ti-12Mo alloy. After solution heat-treatment and water quench, the oxygen and nitrogen content were 0.189 (± 0.008) wt% and 0.123 (± 0.002) wt%, respectively.

6.3. Results

6.3.1. Tensile behaviour

As shown in Fig. 6.2a, the AF-CS and ST-CS Ti-12Mo alloys exhibit different tensile behaviours. The AF-CS Ti-12Mo alloy is brittle, which failed before the tensile yielding. While the ST-CS Ti-12Mo alloy possesses excellent ductility, as illustrated in Table 6.2. Furthermore, the stress-strain curves of in-situ and ex-situ tensile tests of ST-CS Ti-12Mo are highly consistently conducted by the same strain rate. This also supports the repeatability of the tensile results. The true stress-strain curve and its strain hardening behaviour of ST-CS Ti-12Mo specimen were compared with that of the conventional solution-treated Ti-12Mo sample, prepared by arc melting (Fig. 6.2b). The ST-CS Ti-12Mo sample shows a high yield strength (YS) of 725 (± 7) MPa, 251 MPa higher than that of conventionally made Ti-12Mo [8], as presented in Table 6.2. Its ultimate tensile strength (UTS) is also much higher than that of the conventional Ti-12Mo. Moreover, the strain hardening rate (SHR, $d\sigma_{Ture}/d\varepsilon_{Ture}$) of ST-CS Ti-12Mo is exceptionally high, especially in the early stage of plastic deformation (strain< 8 %), as shown in Fig. 6.2b. Based on the evolutions of SHR, plastic deformation can be divided into

four stages (Fig. 6.2b). The region just after yielding is assigned as stage I. Afterwards, the SHR started to decrease steadily, which is termed stage II (4 - 8%). After that, the SHR reached a small plateau and then dropped more rapidly (stage III). After 17 % true strain, the uniform plastic deformation ended and started necking.

This works also compared the strength and elongation of ST-CS Ti-12Mo with the other Ti alloys, including Ti−12Mo−6Zr−2Fe[2], Ti−24Nb−4Zr−8Sn[28], Ti−Cu[29], Ti−Ta[30], Ti5553[31], Ti−10V−2Fe−3Al[32], Ti−6Al−4V[2], CP Ti[2], which were prepared by additive manufacturing. The ST-CS Ti-12Mo specimens in this work show an excellent combination of high strength, good ductility, and high SHR, comparable to or better than the various additive manufactured β/β+α Ti alloys' mechanical performance.

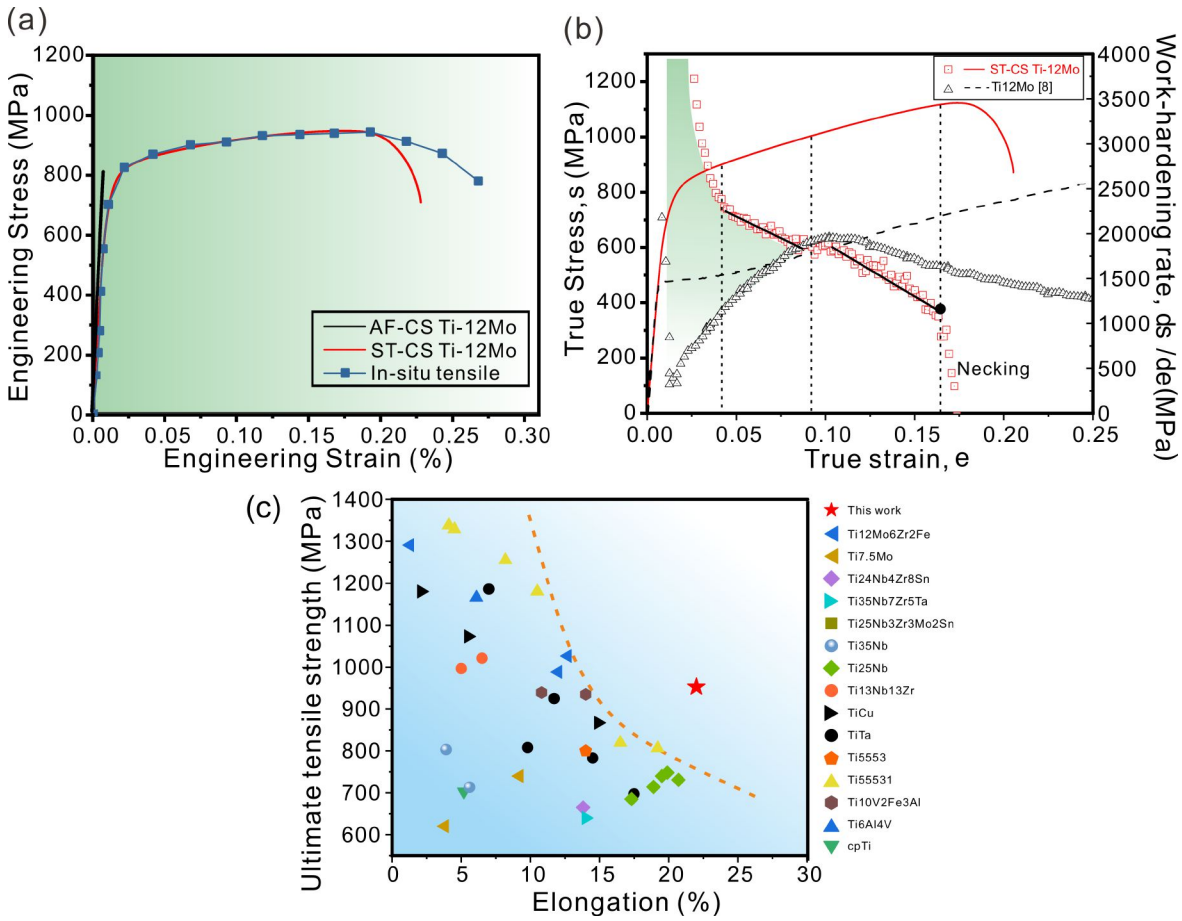


Fig. 6.2. (a) Engineering stress-strain curves of the standard tensile tests and in-situ tensile test of AF-CS and ST-CS Ti-12Mo alloy. (b) True stress-strain curves and strain-hardening rates ($d\sigma_{Ture}/d\varepsilon_{Ture}$) of the ST-CS Ti-12Mo and conventional Ti-12Mo prepared by arc melting [8]. (c) Ultimate tensile strength (UTS), accompanied with elongation of the ST-CS Ti-12Mo samples, compared with other Ti alloys prepared by additive manufacturing.

Table 6.2. The tensile mechanical properties of LPBF processed Ti-12Mo, compared with the conventional Ti-12Mo prepared by arc melting.

	Yield strength (MPa)	UTS-Engineering (MPa)	UTS-True (MPa)	Young's modulus (GPa)	Elongation (%)
AF-CS Ti-12Mo	-	773 ± 17	773 ± 17	104 ± 5	0.7 ± 0.1
ST-CS Ti-12Mo	725 ± 7	953 ± 2	1123 ± 5	81±3	22 ± 1
Ti-12Mo [8]	474	-	972	-	38
Ti-12Mo[33]	550	680	920	-	43

6.3.2. Microstructural analysis

Near fully-dense (≧ 99.85%) Ti-12Mo alloys were obtained using the optimised parameters (Table 6.1). To further homogenise the microstructure, the as-fabricated specimens were sealed in vacuum quartz tubes and subjected to a solution treatment at 1273 K (over the β transus temperature) for 1 hour, followed by water quenching. Moreover, the composition of ST-CS Ti-12Mo was homogeneous as presented via EDS elemental mapping of Ti and Mo in

Fig. 6.3a-6.3b, respectively. The weight percentage of Ti and Mo elements was acquired from six random areas, with an average of 87.5 ± 0.3 % and 12.5 ± 0.3 %, respectively (Fig. 6.3c).

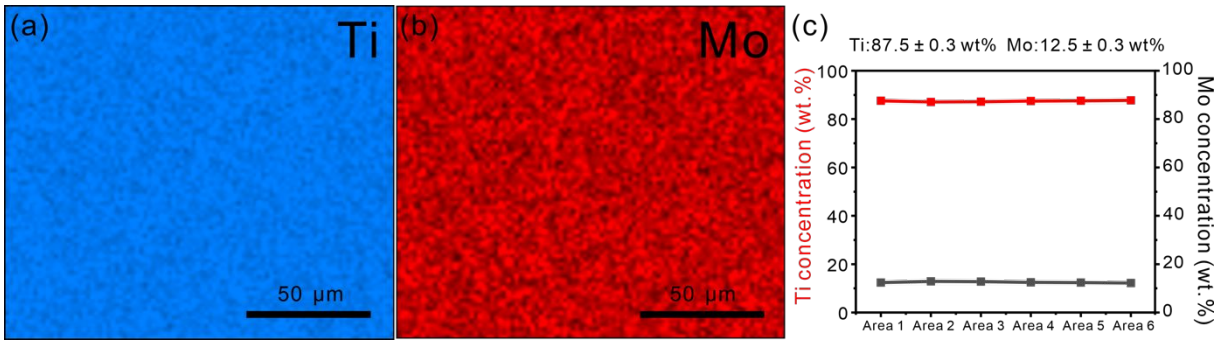


Fig. 6.3. The EDS elemental maps of Ti (a) and Mo (b). (c) The detailed weight percentage of Ti and Mo concentrations in 6 random areas.

The phase constitutions of AF-CS and ST-CS Ti-12Mo alloys were revealed, as shown in Fig. 6.4. They were composed of β, ω and α" phases. There is no apparent difference in the ω peaks of AF-CS and ST-CS Ti-12Mo alloys, implying that the similar volume fraction of ω phase. The peak intensity of α" increased apparently after solution heat-treated and water quench. Various works[34–36] have also suggested that the α" phases can form in β Ti alloys during the fast cooling from the β region.

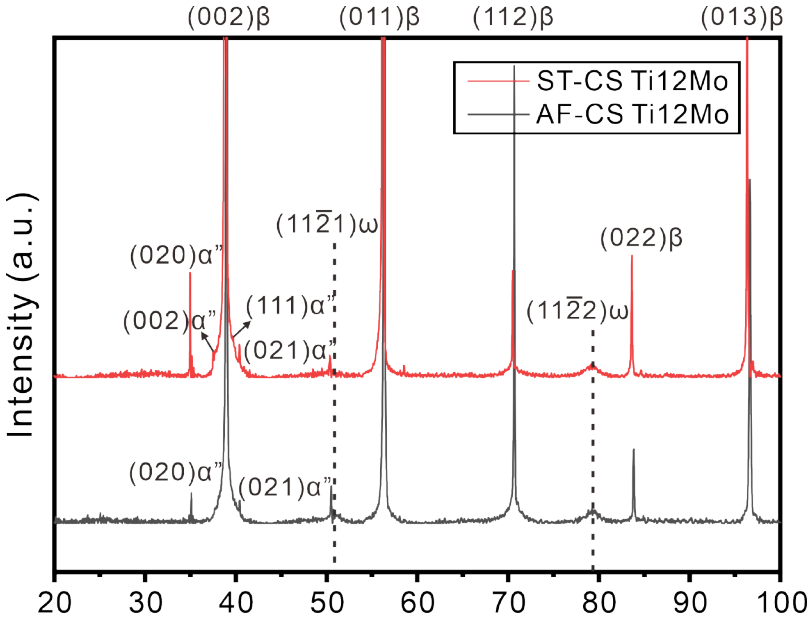


Fig. 6.4. The XRD patterns of AF-CS and ST-CS Ti-12Mo alloys

The 3D EBSD maps in Fig.6.5 show the relationship between the grain structures, the LPBF building directions, tensile direction, and incident direction of monochromatic X-Ray. The AF-CS Ti-12Mo specimen is highly textured with the strong $<001>_{\beta}$ preferential crystallographic orientation along the build and tensile directions, as shown in Fig. 6.5a and b, due to LPBF processing [2]. The average grain size of AF-CS Ti-12Mo is 33.8 μm (equivalent circle diameter). After solution heat treatment and water quench, the grain size of ST-CS Ti-12Mo alloy has increased significantly to about 114.4 μm (Fig. 6.5c). The intensity of the preferential orientation of $<001>_{\beta}$ has slightly enhanced (Fig. 6.5d).

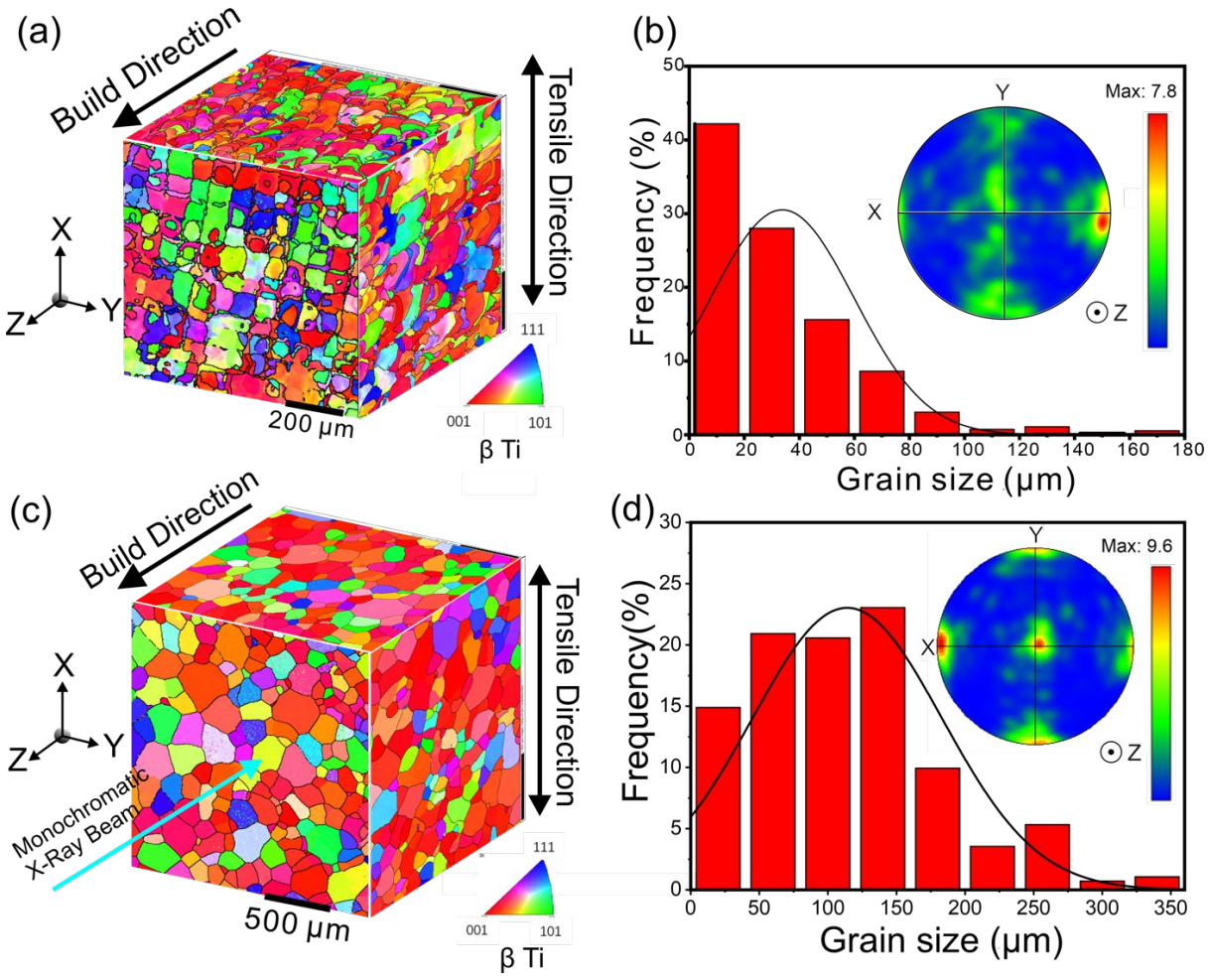


Fig. 6.5. 3D EBSD figures show the grain structure of AF-CS (a) and ST-CS (c) Ti-12Mo specimens, where the build direction, tensile direction and incident X-ray beam direction are presented; (b and c) the grain size distributions in AF-CS (b) and ST-CS (d) Ti-12Mo specimens (inserted: the (100) pole figure of X-Y plane, which is perpendicular to the build direction).

In the AF-CS Ti-12Mo sample, the precipitates in black lath shape can be found in the bright-field (BF) TEM image (Fig. 6.6a). The inserted SAED pattern only shows the β and two variants of ω phases, which confirm the black lath are ω phases. As revealed in the dark-field (DF) TEM image (Fig. 6.6b), the ellipsoid ω particles and ω laths (highlighted by yellow dotted circles) are presented, with high density. The ellipsoid ω phase has the major and minor axis

lengths of 20.8 ± 4.5 nm and 9.0 ± 1.5 nm. The ω laths have a length of 116.2 ± 17.0 nm and a width of 14.2 ± 3.3 nm. Furthermore, the HR-TEM micrograph (Fig. 6.6c) and the corresponding FFT images (Fig. 6.6d and e) have shown the dense stacking fault in the ω laths, while not in the ellipsoid ω phase. The specific stacking fault indicates the high inner stress inside the AF-CS Ti-12Mo specimens.

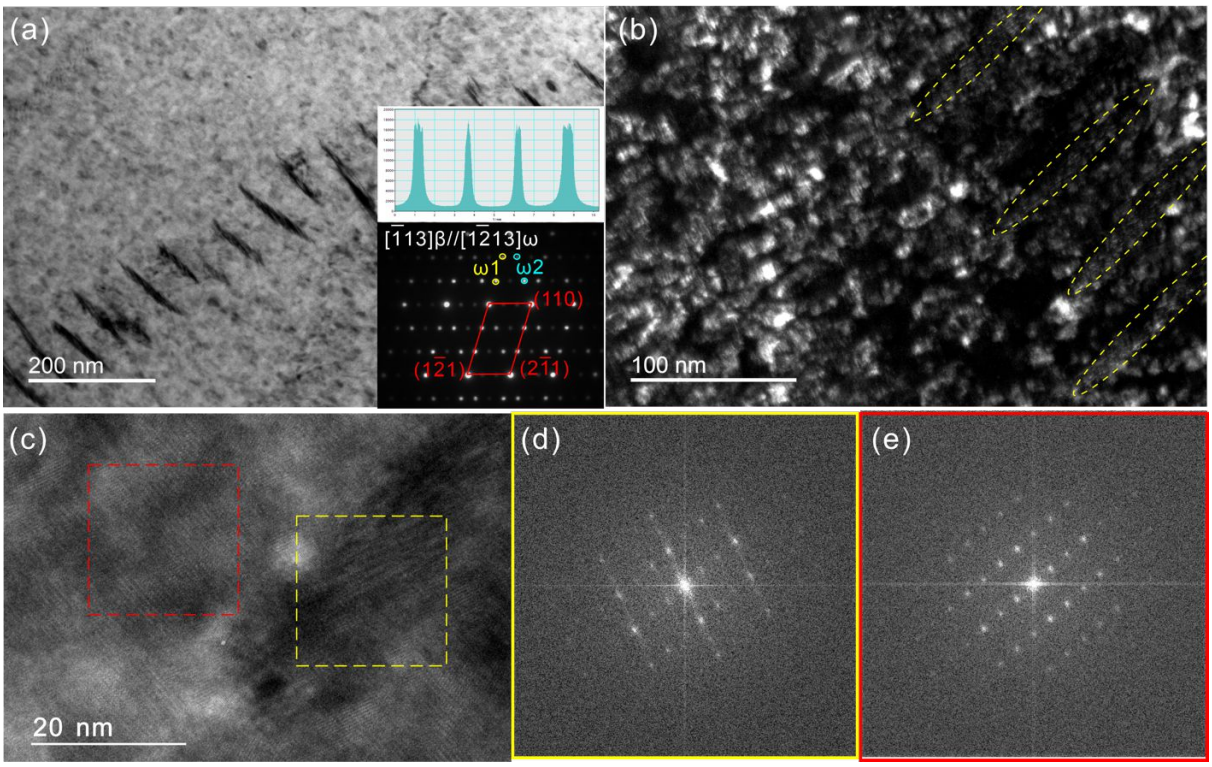


Fig. 6.6. The microstructure of AF-CS Ti-12Mo alloy: (a) the bright-field (BF) TEM micrograph (the SAED pattern and line intensity profile along the [1$\bar{2}$1] direction; (b) the dark-field (DF) TEM image of ω particles; (c) the HR-TEM image and (d-e) the corresponding inverse fast Fourier transformation (FFT). The diffraction streaks in (d) demonstrate the presence of high-density stacking faults in ω laths.

In ST-CS Ti-12Mo, the BF TEM image (Fig. 6.7b), observed along the $[\bar{1}13]_{\beta}$ zone axis

(Fig. 6.7c) shows dense ω phases in black contrast. The corresponding two variants of ω phases are observed in the DF TEM images, named ω1 (Fig. 6.7e) and ω2 (Fig. 6.7f), respectively, which were collected from the diffraction spots in the Fig. 6.7c. The area fraction of ω1 and ω2 is then measured as 2.38% and 2.56%, respectively. This suggests that the two variants of ω phases have nearly the same volume fraction in the specimen. As shown in Fig. 6.7d, the average size of ω particles is 4.1 nm (*d*), measured from over 1600 particles. According to the APT results of Fig. 6.7g, the volume fraction (*f*) and average interspacing (D) of ω particles is 3.87 % and 6.5 ± 2.4 nm, respectively. The 2D cross-sectional APT map (Fig. 6.7h) shows the distribution of the ω particles. Fig. 6.7i has quantitatively presented the elemental composition of the Mo lean region, which should be the isothermal ω phases. According to the Fig. 6.7j and Table 6.3, the Mo concentration is 5.10 ± 0.29 at% in ω particles, lower than that in β matrix (8.97 ± 0.17 at%). Moreover, it is noted that more oxygen content existed in the β matrix than in the ω phase.

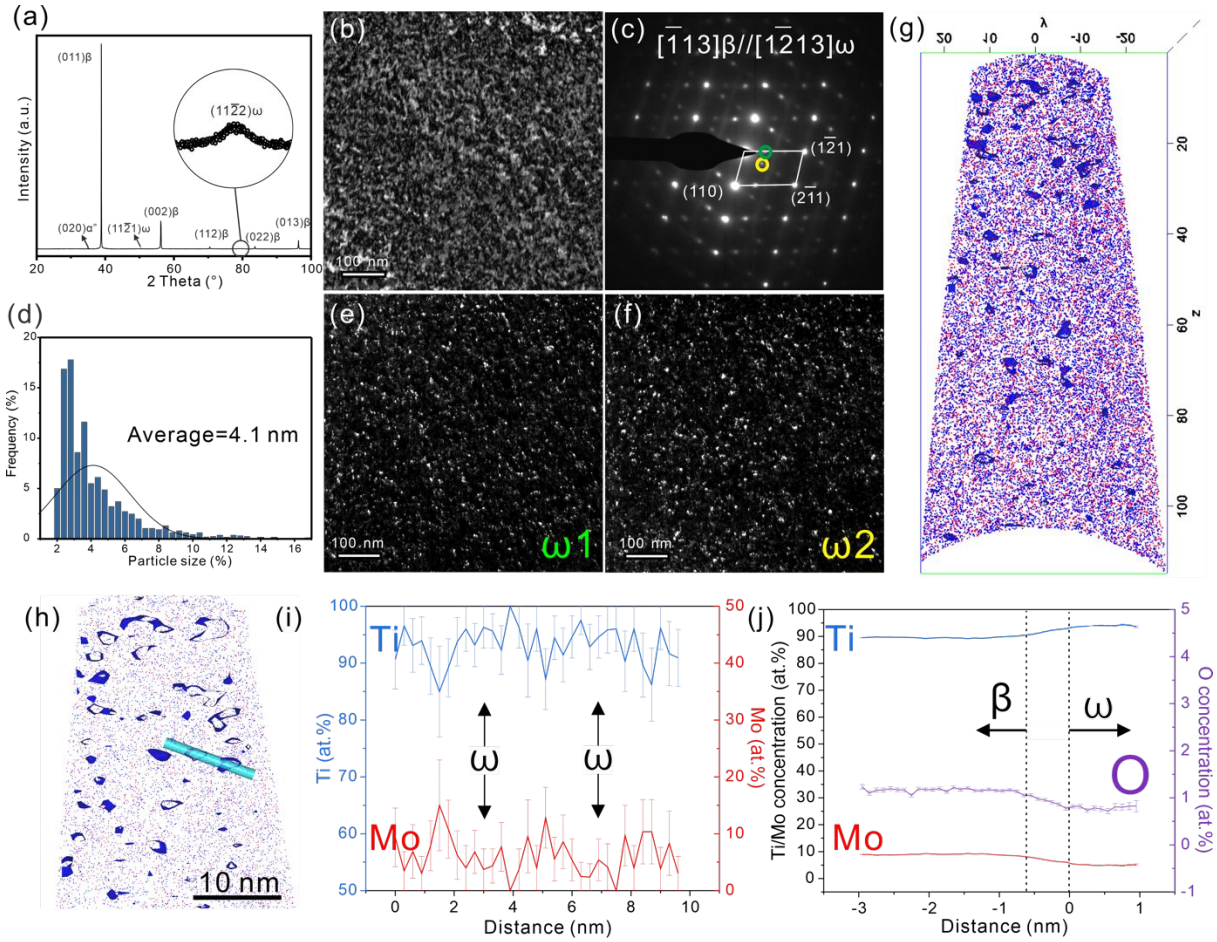


Fig. 6.7. (a) XRD pattern of the ST-CS Ti-12Mo sample. (b) The bright-field (BF) TEM micrograph and its selected area electron diffraction (SAED) pattern (c). The average size distributions of ω phase (d) and the dark-field (DF) TEM micrographs(e-f) derived from the ω diffraction spots in green and yellow circles in the SAED pattern of (c). (g) Reconstructed atom probe tomographic micrograph shows the morphology and distribution of ω particles. (h) Two-dimensional cross-sectional atom map derived from the APT with 92 at% Ti iso-concentration surfaces. (i) Concentration profiles of Ti and Mo elements with the blue arrow indicating its location in (h). (j) Proximity histograms of the mean concentrations of Ti, Mo, and O elements as a function of distance across the β/ω interface.

Table 6.3. The average Ti, Mo and O concentrations of the β matrix and ω phases， based on the APT results.

	Ti (at.%)	Mo (at.%)	O (at.%)
β	89.54 ± 0.18	8.97 ± 0.17	1.17 ± 0.04
ω	93.85 ± 0.39	5.10 ± 0.29	0.74 ± 0.11

The ω phase is shown to play a vital role in deciding the strengthening and deformation modes in various β Ti alloys, such as Ti-Mo[37], Ti-V[38], Ti-Cr[39] and Ti-Mn[40] systems. The embrittlement due to the ω phase is well documented. In the earliest studies[37,41], researchers noted that the ω phase caused embrittlement is due to the non-deformable character of these ω particles. The latest research revealed that some ω particles could be sheared by dislocations, which simultaneously induced the ω to β shear transformation [40,42]. After that, the ω-free shear bands formed. Then increased localised stress concentrated within the ω-free shear bands, which can be the crack sources and lead to premature failure [41]. Furthermore, the deformation behaviour of metastable β Ti-Mo alloys was shown to be dependent on the differences in Mo concentrations between the β and ω phases [57]. When the ω particles are fully athermal, the metastable β Ti alloys show good ductility, with the TWIP/TRIP being activated during the plastic deformation [43,44]. Moreover, the significant elemental partitioning between the β matrix and ω particles can be the reason for the brittle mechanical property of Ti-Mo alloys [20]. While in this work, such apparent difference of Mo concentrations (3.87 at%) between the β and ω, would not embrittle the ST-CS Ti-12Mo alloy. The experimental results also suggest the diffusion and lattice displacive occurred during the post heat treatment of the ST-CS Ti-12Mo. Moreover, the embrittlement reason in AF-CS Ti-

12Mo alloy can be the ω particles or high inner stress, which will need further investigations in future works

The plate-like α" phases are also shown in Fig. 6.8a, which is inhomogeneously distributed in the β matrix. There are only limited α" plates found in several β grains, whereas most of β grains are free of the precipitates. Twinning and stacking fault structures are revealed in these α" plates as shown in Fig. 6.8b. The corresponding Fast Fourier Transformation (FFT) micrograph of Fig. 6.8c has confirmed the twinning structures are the {112} type α" twins. The HRTEM image of Fig. 6.8d has revealed the incoherent phase boundaries between the α" phase and β matrix (Fig. 6.8f). The GPA map has demonstrated the high local lattice strain inside the α" phase (Fig. 6.8e). The high-angle annular dark-field (HAADF) STEM image (Fig. 6.8h) and the distribution of Ti and Mo elements (Fig. 6.8i-j) reveal constitutional modulated microstructures. Fig. 6.8k shows the long-range composition fluctuations of Ti elements, with some amplitude. Similar α" phases were reported by Davis et al.[45] in Ti-Mo alloys after low-temperature ageing and quenching. However, they did not investigate the chemical composition distribution. The formation of the α" was attributed to the spinodal decomposition during the quench [46,47]. The constitutional modulated microstructures as observed here in the α" phase in ST-CS Ti-12Mo alloy support this.

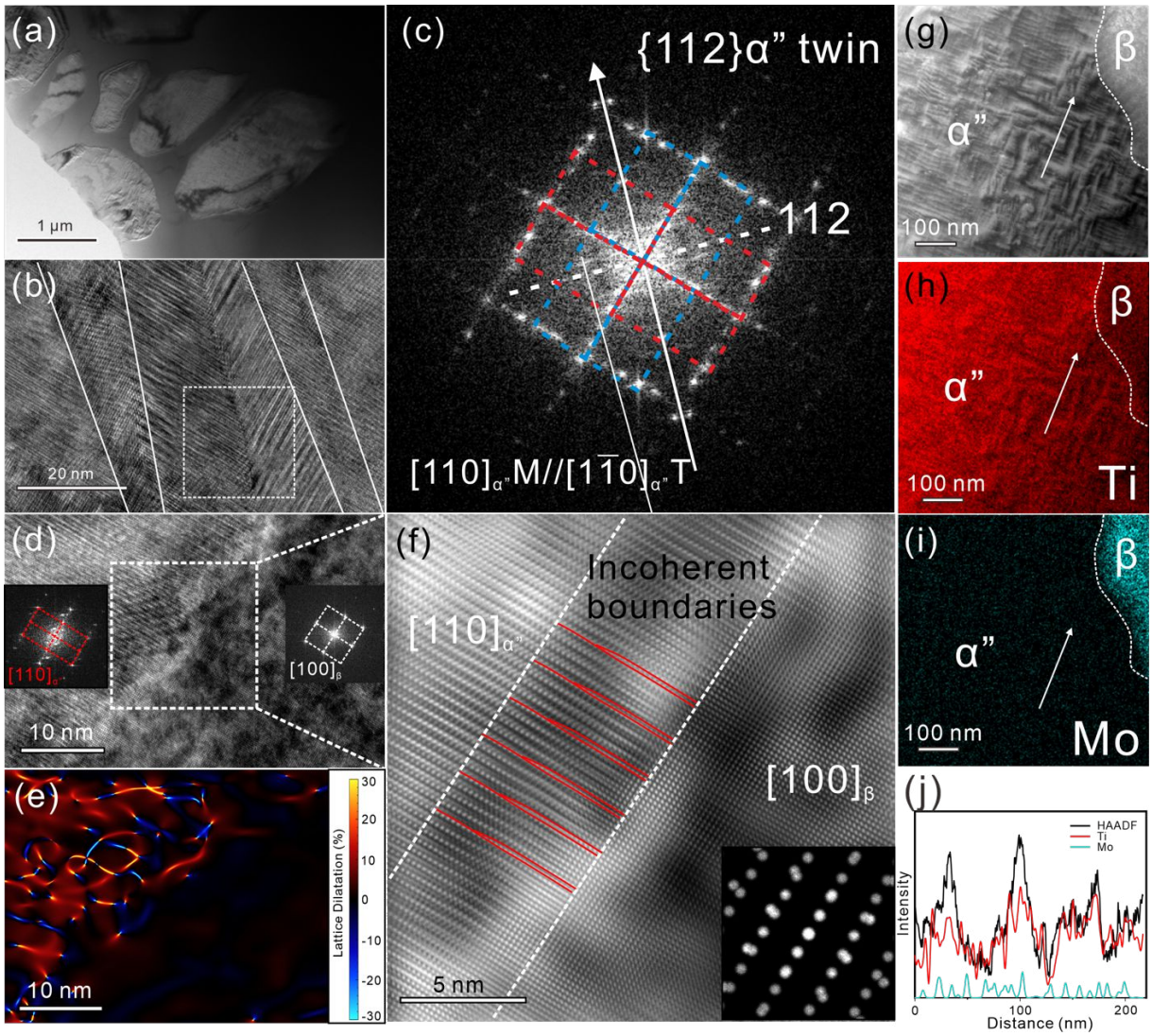


Fig. 6.8. (a) BF TEM image of the region in the ST-CS Ti-12Mo sample with some α" precipitates. (b) high-resolution TEM (HRTEM) image observed inside the α" precipitates. (c) Fast Fourier Transformation (FFT) derived from the dotted square in (b). (d) HRTEM image shows the phase boundary between the α" and β phases. (e) geometric phase analysis (GPA) conducted on the phase boundary of (d). (f) inverse FFT image derived from (d), and the applied mask was inserted. (g) high-angle annular dark-field (HAADF) STEM image and the corresponding energy dispersive spectroscopy (EDS) mapping of Ti (h) and Mo (i) elements. (j) The line intensity profiles of HAADF, Ti and Mo elements along the solid arrow lines in (g-i).

6.3.3. Synchrotron X-ray analysis

The lattice parameters of the β Ti-Mo phase were refined for the three diffraction directions (Fig. 6.9a). The average lattice parameters of β-phase are increasing with applied load. Increasing the lattice parameters along the LD with simultaneous decreasing of the lattice parameters along the PD is expected and reflects the intense strain on the cubic lattice of β-TiMo caused by the applied load.

The evolution of the lattice strain of various lattice plane families ({110}, {200}, {211}, {220}, and {031}) from the LD, 45º to LD and PD are illustrated as a function of true stress in Fig. 6.9b. The lattice strain (ε^{hkl}) of the different crystallographic planes shows a linear increase with the increase of true stress before the tensile yielding (725 MPa), whether along the LD or 45º to LD, which experienced the tensile stress. While along the PD, the lattice strain of various plane families decreases with true stress due to the compression stress. They also show a linear relationship before the yielding. After yielding, the nonlinear relationship is observed at all plane families. The stress is found to transform from the {211} plane to the others after yielding, which can be observed along the LD while not along the PD. This can be attributed to the stress-induced β to ω/α" transformations with the shearing from $\{112\}_{\beta,}$ due to the coherent boundary of $\{11\bar{2}\}_{\beta}//\{\bar{1}100\}_{\omega}$ [48] and the $\{11\bar{2}\}<111>$ shear from β to α" [49].

During the elastic deformation, the linear relationship is observed between the true stress and lattice parameters of the β phase, of which the slopes are linearly fitted to determine the elastic modulus (*E*) under the tensile or compressive stress shown in Table 6.4. Their ratios are

the Poisson's ratios (ν). Then the shear modulus (G) of the ST-CS Ti-12Mo was calculated via:

$$G = \frac{E}{2(1+\nu)} \tag{6.2}$$

Based on lattice strain evolution, the elastic constants along the LD and PD can be calculated from the linear fitting of the lattice strain during the elastic deformation. The ratios of elastic constants along the LD and PD were the Poisson's ratios, as presented in Table. 6.4. As shown in Table 6.4, the elastic constant is 73 GPa along crystallographic plane {200}, which is the lowest among all these lattice plane families. The elastic modulus of β matrix of ST-CS Ti-12Mo specimen was calculated to be 74.8 GPa, which is close to that along the {200} plane. This is due to the strong {100}<001> texture as illustrated in the EBSD pole figure of Fig. 6.5d and XRD patterns in Fig. 6.10a-b. Furthermore, Young's modulus, obtained from the ex-situ tensile stress-strain curve in Fig. 6.2a, is slightly higher than the elastic modulus of β matrix (74.8 GPa). This may be because of the high stiffness of the secondary phase ω, which were proved to increase the modulus of the metastable β Ti alloys [2].

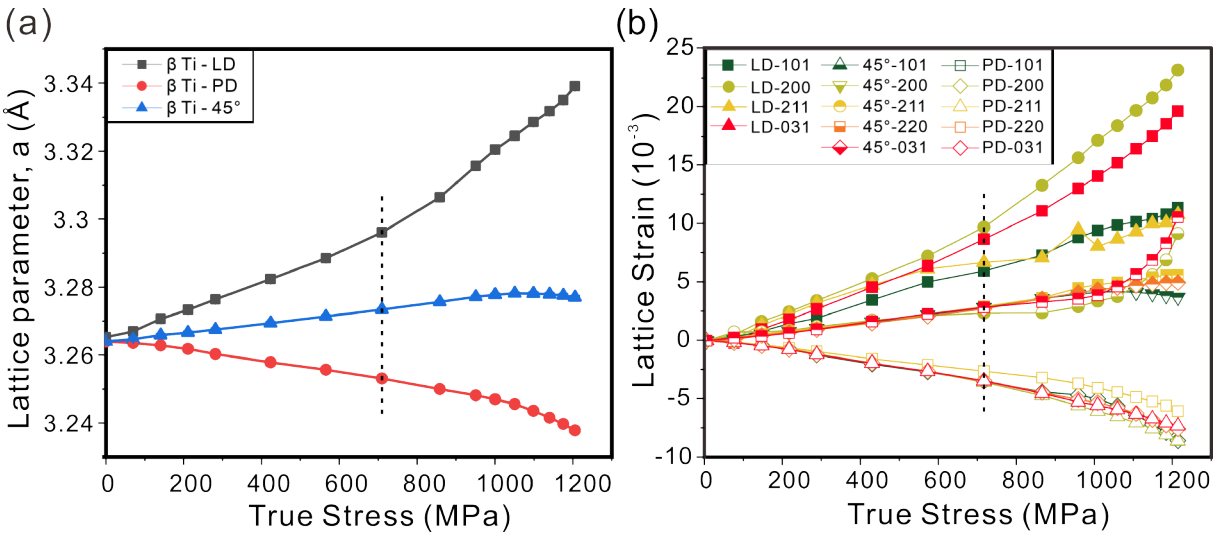


Fig. 6.9. (a) Evolution of lattice strain along the LD, 45 º to LD and PD. (b) Evolution of lattice parameter of β Ti along the LD, 45 º to LD and PD.

Table 6.4. The Young's modulus of the ST-CS Ti-12Mo alloy and the elastic modulus and Poisson ratio (ν) along the different crystallographic families.

	Young's modulus (GPa)	*E* (GPa)	*E101* (GPa)	*E200* (GPa)	*E211* (GPa)	*E031* (GPa)
ST-CS Ti-12Mo	81±3	74.8	111	73	95	77
	ν	$\nu 101$	$\nu 200$	$\nu 211$	$\nu 031$	G_β (GPa)
	0.37	0.572	0.380	0.367	0.386	27.3

At 0 N load, the sample consists of mainly β phase with some α" and ω phases, as shown in Fig. 6.11a, which is consistent with the microstructures in Fig. 6.7 and Fig. 6.8. The volume fraction of α" phase is estimated to be less than 1 %. The $(002)_{\alpha''}$ phase peak appeared to be disappeared during the early stages of elastic deformation, which can be attributed to the reorientation of α" during tensile loading, as suggested in previous studies [50]. Furthermore, there is no SIM α" formed loading to 1.9 % true strain.

After 1.9 % true strain, additional peaks belonging to α" phase can be identified, signalling α" phase transformation during deformation, according to Fig. 6.11. Moreover, the SIM α" phase transformation is highly anisotropic. There is apparent SIM α" during the deformation along the LD (Fig. 6.10a), while not along the PD (Fig. 6.10b). Considering the preferential crystallographic orientations are the {100} along the LD and PD, the only difference is that the

stress along the LD is tensile while that along the PD is compression during the deformation. Some research works [51] also revealed this phenomenon and concluded that the strain-induced β to α" phase transformation would favour the tensile stress, while the compressive stress in the PD would suppress the phase transformation.

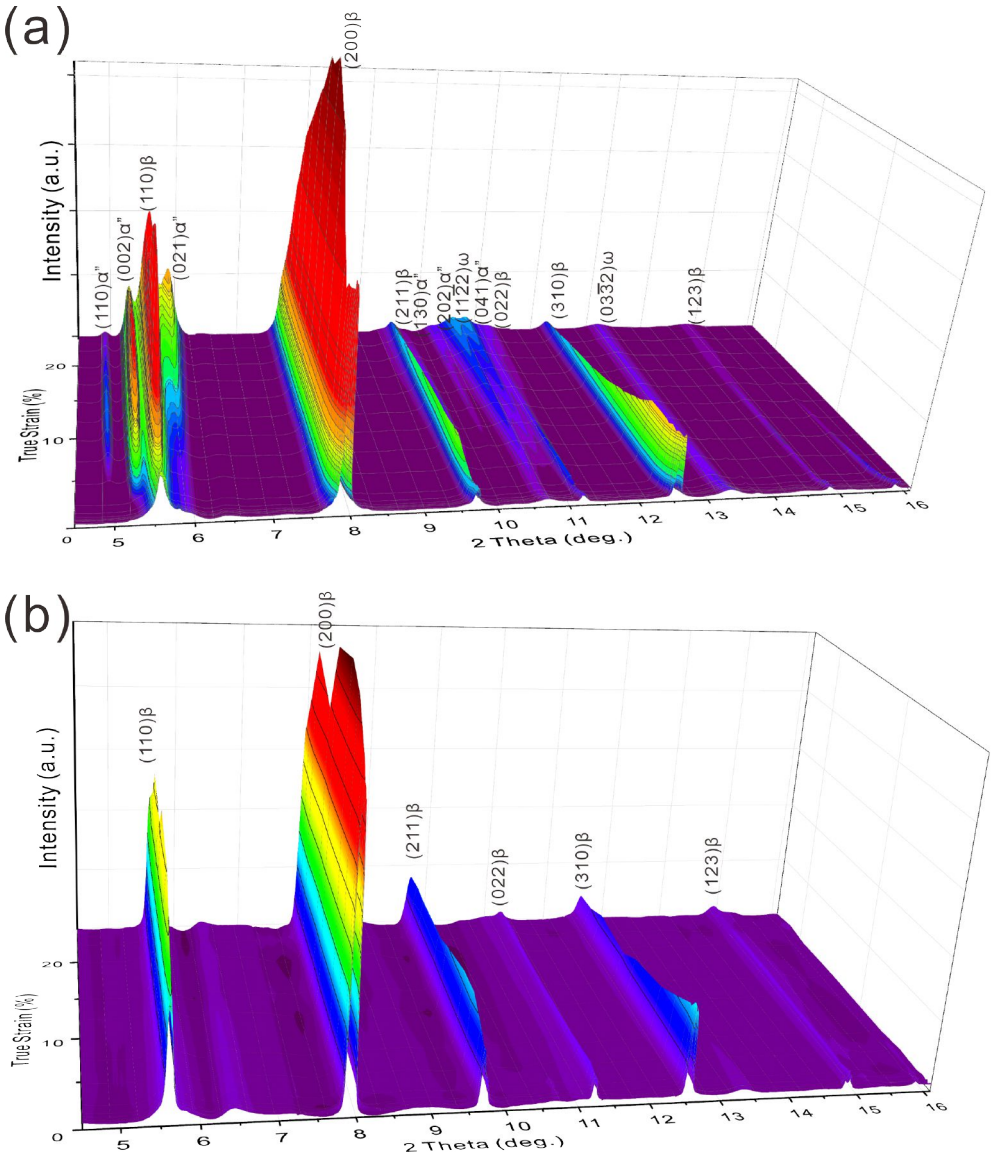


Fig. 6.10. Color-coded 3D plots derived from the XRD patterns during the deformation: (a) Loading direction (LD); (b) Poisson direction (PD).

The evolution of α" phase volume fraction is presented in Fig. 6.11c, which was fitted based on the sigmoidal Olson-Cohen model during the plastic stages. The model [52] was proposed to reveal the relationship between the martensite volume fraction and macro strain during the stress-induced austenite to martensite transformations, expressed as:

$$f_{\alpha''} = 1 - \exp\{-B[1 - \exp(-A\varepsilon_T)]^n\} \quad (6.3)$$

where ε_T is the true strain, A is the parameter that defines the course of the deformation bands formation and is related to stacking fault energy (SFE). Parameter B corresponds to the probability of the deformation bands intersection forming α"-martensite embryo. The parameter n is related to the shear band orientations and geometry. After fitting with the in-situ experimental results of α" volume fraction, the parameters of the Kinetic model of A, B and n were obtained as 0.17, 44.4, 1.72 respectively. The R square is 0.98, which means the relationship between the volume fraction of martensite α" and true strain fit well with the Olson-Cohen kinetic model. The volume fraction of the SIM α" phase finally increased to about 10 % when reaching the end of uniform deformation.

The intensity of the peaks of the ω phase, especially the $(11\bar{2}2)\omega$, continuously increased with the progress of plastic deformation (Fig. 6.11a), indicating the reorientation or increased volume fraction of ω phases. This is different from the ω phases' evolution during plastic deformation of the conventional Ti-12Mo alloy[8]. For the conventional Ti-12Mo alloy, the ω phases gradually disappeared with the strain increased.

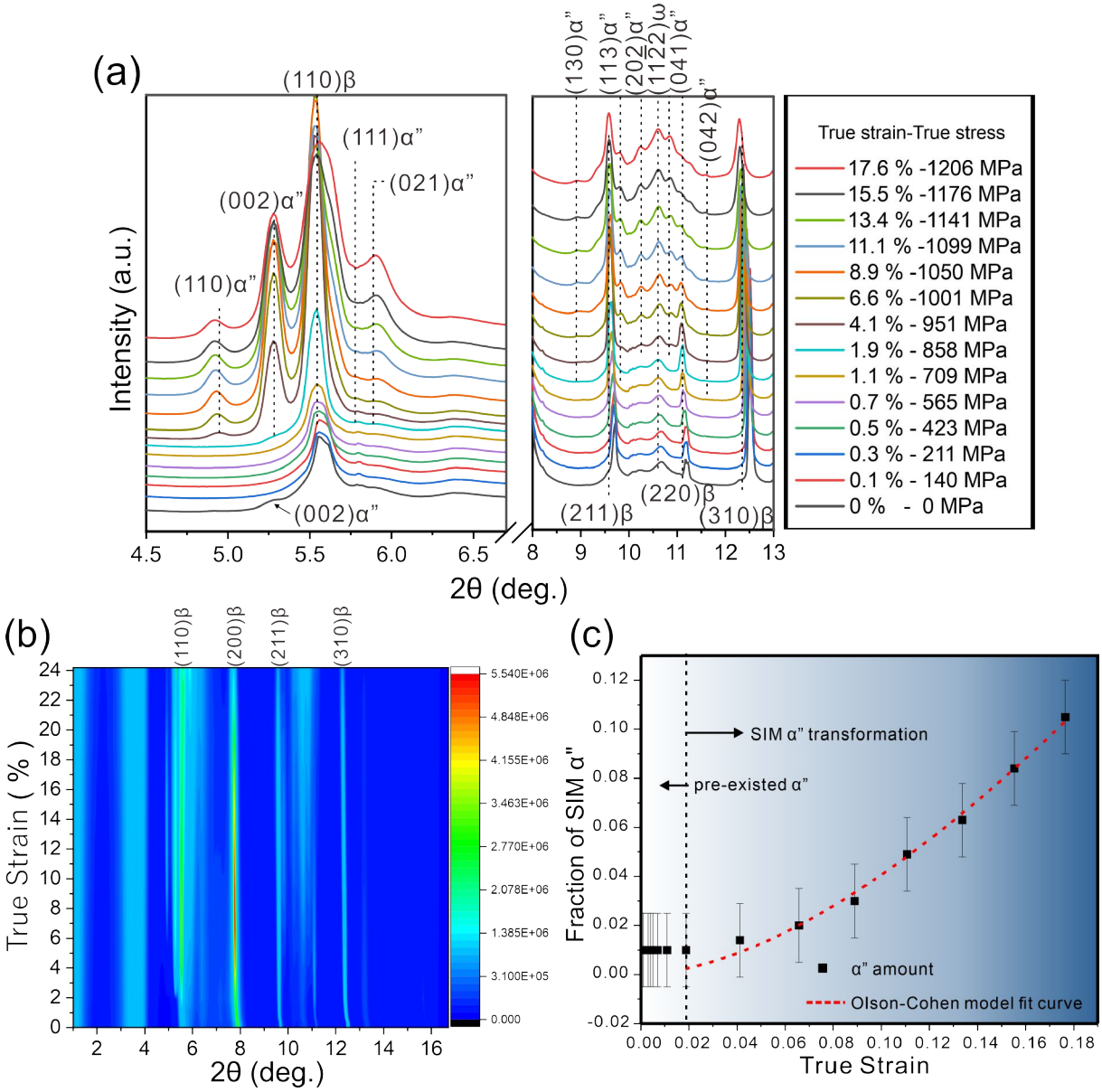


Fig. 6.11. (a) XRD patterns maximised from selected two theta range show the reflections' evolution of β, α" and ω phases. (b) Color-coded 2D plots are corresponding to the reflections of β and α" phases. (c) Evolution of the volume fraction of SIM α" phase during the tensile deformation.

6.3.4. Microstructural investigations after 1.4 % strain

The specimen tensile deformed to 1.4 % strain was chosen to investigate the deformation

microstructures between the yielding and 1.9 % true strain. As shown in Fig. 6.12a, some fine parallel structures are found in some grains of the sample, where a FIB lamellar was lifted out. In Fig. 6.12b, the structure is revealed to be the twins whose width is 765 ± 18 nm. Three SAED patterns, along the zone axis of $[01\bar{1}]_{\beta}$, are obtained from different positions. Fig. 6.12c of the SAED ① clearly shows the {332}<113> twin relationship. As shown in Fig. 6.12d, which was derived from SAED ② region, shows the β phase with two variants of ω phases ($[11\bar{2}0]_{\omega1}$ and $[2\bar{1}\bar{1}0]_{\omega2}$). Fig. 6.12e presents the microstructure of the matrix and the twin boundary. As illustrated in Fig. 6.12f, some ω1 phases are decorated along the twin boundary with a thickness of 6.5 nm. Moreover, there is no ω2 phase formed along the twin boundaries (Fig. 6.12g). Further observation from the SAED ③, shown in Fig. 6.12h, illustrates the strong diffraction intensity of ω1 and weak diffraction intensity of ω2 inside the twin structure. The BF TEM (Fig. 6.12i) image shows the parallel slip trace (along the $\{11\bar{2}\}<111>_{\beta}$ direction), and high-density dislocations inside the twin structure. The ω1 phases are homogeneously distributed in the β twin (Fig. 6.12j), while the ω2 phase is absent in some slip traces (Fig. 6.12k). Among these ω variants, only the $[0001]_{\omega2}$ direction is parallel to the particular $[111]_{\beta}$ direction. At the same time, the $\{11\bar{2}\}_{\beta}//\{\bar{1}100\}_{\omega2}$ interface is highly coherent [3]. Therefore, when they move along the slipe traces, the dislocations may shear the ω2 phases and force the phases to transform back to the β matrix [53,54]. Then the ω2 free channels formed in some slip traces.

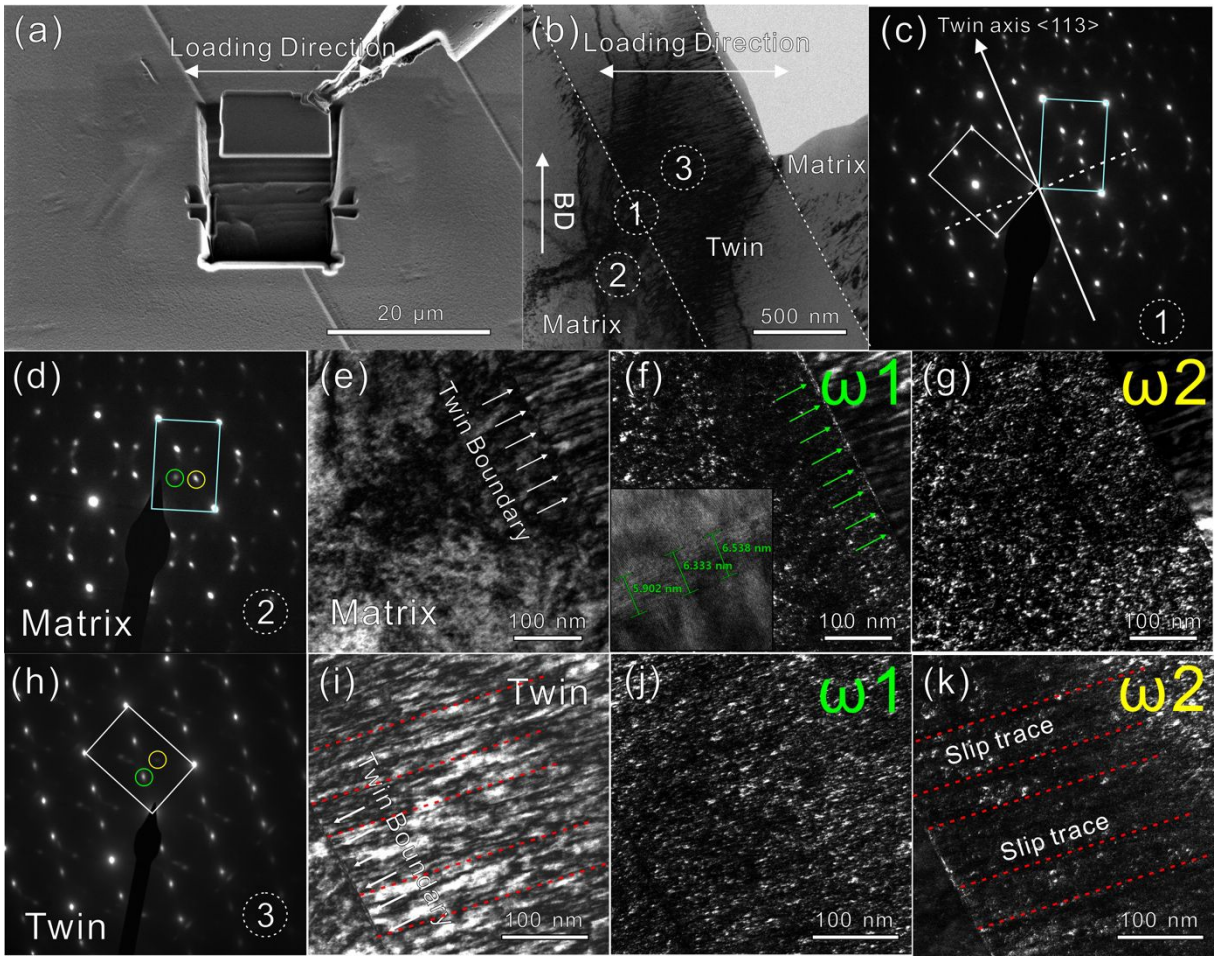


Fig. 6.12. Microstructures of the tensile specimen at 1.4 % true strain (just after yielding): (a) SEM image shows the position where the FIB lamellar was lifted out. (b) BF TEM image. (c) SAED pattern from the selected area 1. (d) SAED pattern from the selected area 2. (e) BF TEM image of matrix and twin boundary. (f-g) DF TEM micrograph derived from the ω diffraction spots in green and yellow circles in the SAED pattern of (d), where the HRTEM was inserted. (h) SAED pattern from the selected area 3. (i) BF TEM image of twin and twin boundary, where the slip traces were marked by red dotted lines. (j-k) DF TEM micrograph derived from the ω diffraction spots in green and yellow circles in the SAED pattern of (h).

In summary, there was no SIM α" formed before 1.9 % true strain according to the X ray synchrotron results (Fig. 6.11). At the same time, no SIM α" phase was observed from the

microstructure of 1.4 % true strain (just after yielding) (Fig. 6.12), where we only observed {332}<113>β twins and ω variants. Moreover, the interfacial twin boundary (ITB) ω phase was revealed decorated along the {332}<113>β twins. The significant variants reordering of ω phases happened in the {332}<113>β twin. This means the ITB ω phases were transformed from the reorientation of pre-existed ω phases, which was recently reported by Chen et al.[55].

6.3.5. Microstructural investigations after 5 % strain

To investigate the deformation microstructures in stage II of the strain hardening curve, the EBSD maps were used to characterise a single β grain (solid red square) and multiple β grains (green dotted square), respectively as shown in the Fig. 6.13a. Inside the single β grain, the boundaries of the twin structures are the CSL $\sum 11$ boundaries (50.5º <110> misorientation), equivalent to the {332}<113> twin boundaries. The twin boundaries are indicated using red lines in Fig. 6.13a. The EBSD IPF map of β phases (Fig. 6.13b) reveals the crossed twinning structures. As shown in Fig. 6.13c, the SIM α" phases are mainly formed along the twin structures. The stereo projection analysis of the $\{332\}_{\beta}$ pole figure (Fig. 6.13d) confirmed that the mass of the bands are the {332}<113> β twins. The two crossed twinning structures of {332}<113> should correspond to two varied {332} planes of the β matrix (the two common poles circled in $\{332\}_{\beta}$ pole figure of Fig. 6.13d). The stereo projection analysis (Fig. 6.13d) indicates that the SIM α" phases are originated from the β matrix, or the crossed β twins. The classical crystallographic orientation relationship of β and SIM α" phases follow the {112}β //{110}α".

Fig. 6.13e illustrate the microstructure of grains and twin bands from the selected area of Fig. 6.13a. As shown in Fig. 6.13f, the intensity of red colour indicates the Schmid factor of the {332}<113> twining range from 0.4 to 0.5. With higher SF, the grains are more likely to form the {332}<113> β twins. Fig. 6.13g demonstrated that only the {332}<113> twin boundaries are observed across multiple grains. The Grain Reference Orientation Deviation (GROD) map (Fig. 6.13h) shows that the intersections of twin/twin and twin/grain boundaries are highly deformed. Fig. 6.13i defines the Schmid factor of SIM α" transformation using the habit plane of the martensite phase. Fig. 6.13j presents that α" phases were mainly decorated along the twin boundaries. Some of them may be formed during heat treatment as observed in Fig. 6.4, but it is difficult to distinguish between SIM α" and heat-treatment-induced α"[21].

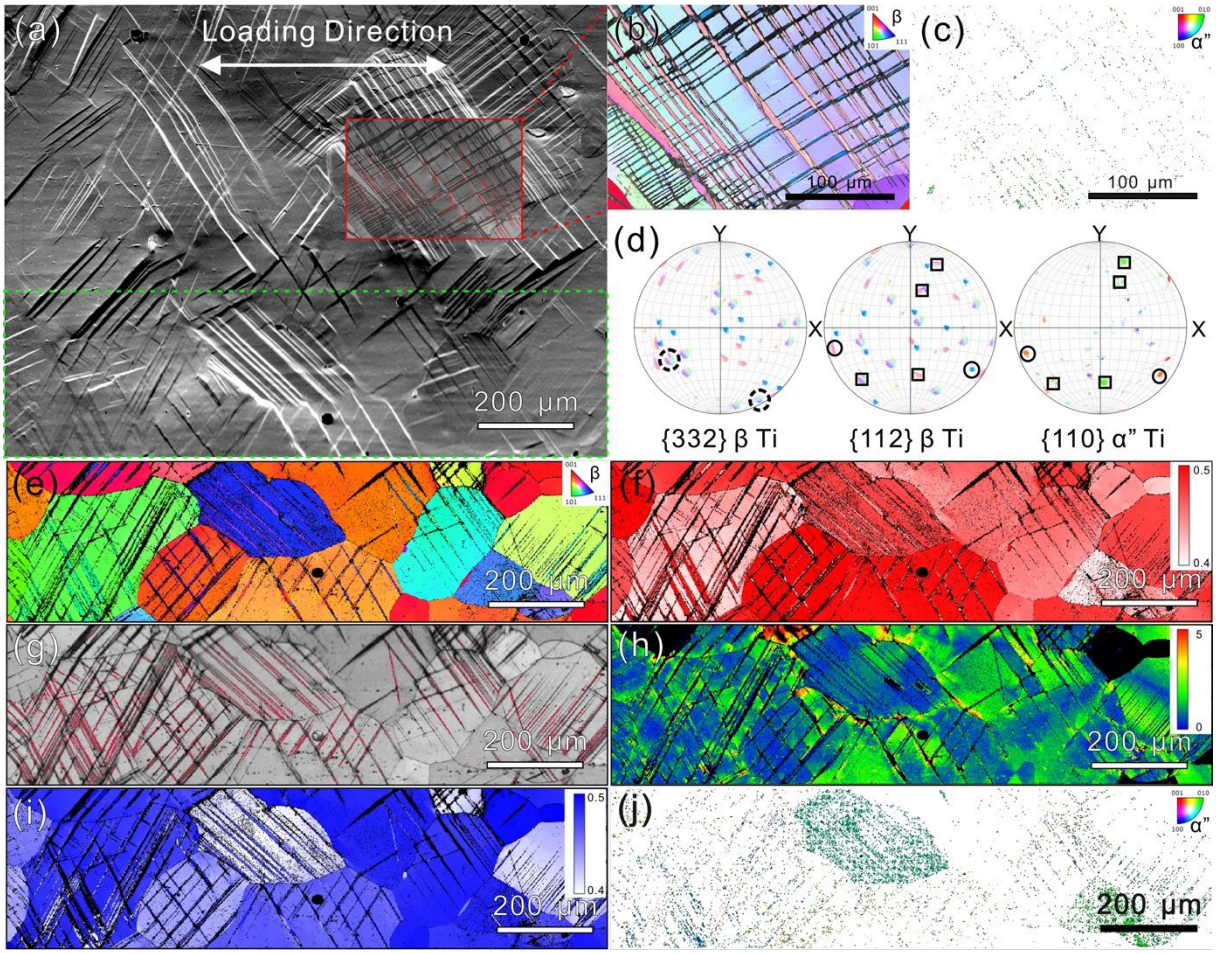


Fig. 6.13. Microstructures of the tensile specimen at 5 % true strain: (a) SEM image (the inserted figure is the band contrast image superimposed with CSL $\sum 11$ boundaries). (b) EBSD inverse pole figure (IPF) of β Ti matrix from the red square in (a) and corresponding IPF map showing the distribution of SIM α" phase (c). (d) pole figures of β matrix and SIM α" in (b) and (c) (dotted circle means the common poles in selected pole figures, and the solid square and circle represents the several corresponding poles in the selected pole figures of β and α" phases). (e) EBSD IPF map of β Ti matrix from the green dotted square in (a). (f) Schmid factor ($0.4 < SF < 0.5$) distribution of {332}<113> twinning system along tensile direction. (g) The band contrast image superimposed with CSL $\sum 11$ boundaries. (h) The GROD (grain-based misorientation parameter) map. (i) Schmid factor ($0.4 < SF < 0.5$) distribution of SIM α" transformation along tensile direction. (j) IPF map shows the distribution of SIM α" phase

To further understand the fine twins and SIM α" structures, TEM thin films were lifted out from different positions of the 5% strained specimen. Fig. 6.14b shows the complex twinning structures where the Pt was deposited on two selected areas. In area 1 (Fig. 6.14a), the microstructures consist of mainly the coarse primary twins and unconfirmed plate-like structures. In area 2 (Fig. 6.14c), the TEM thin lamella shows the fine and crossed twins.

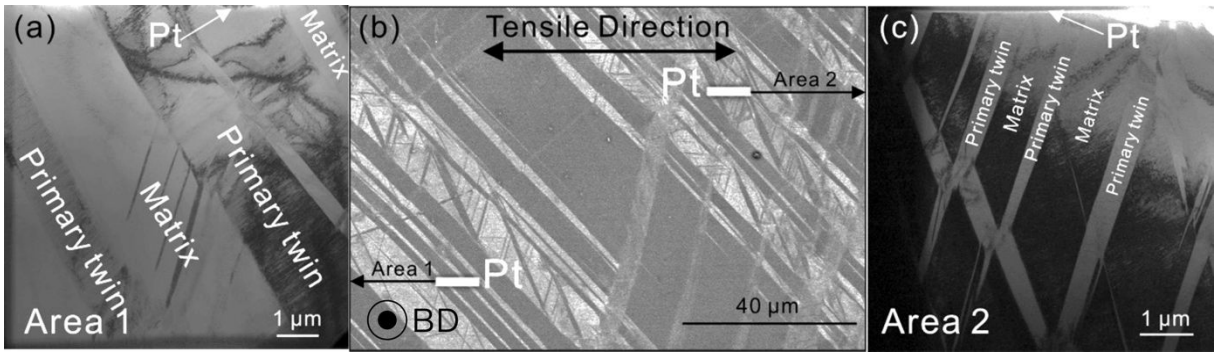


Fig. 6.14. Microstructures of the tensile specimen at 5 % true strain: (a) BF TEM image of the FIB lamellar lift out from Area 1 in (b). (b) Backscattered electron (BSE) micrograph of the ST-CS Ti-12Mo sample at the true strain of 5 % (the squares in white contrast show the locations of FIB lift-out). (c) BF TEM image of the FIB lamellar lift out from Area 2 in (b).

Furthermore, Fig. 6.15a displays the microstructure of area 1 with the inner band edge-on (the low Miller index plane of the band is parallel to the electron beam), where two SAED patterns were collected. Fig. 6.15b shows a magnified region from Fig. 6.15a. The dark band is composed of complex structures, which is termed the composite band. Fig. 6.15c illustrate SAED of the phase composition of β matrix and SIM α" in the region ①. Some variants of ω phases, with a high lattice plane index, were also shown in Fig. 6.15c. Fig. 6.15d is the diffraction pattern of area 2 (inside the composite band), and the simulated diffraction pattern

of the area ② can be found in Fig.6.15h. Inside the composite band, β, SIM α" and ω phases coexisted. As illustrated in Fig. 6.15d, the angle between the two (110) diagonal spots is 64.3º, which demonstrate the phase is SIM α". The DF TEM of Fig. 6.15e shows the ω lath in the composite band. Fig. 6.15f presents the secondary β twin and β lath structures. The phases between these β laths are the SIM α" phases. Fig. 6.15g reveals the pile-up of high-density dislocations along the slip traces in the primary β twins, which means a high strain field in the twinning structures.

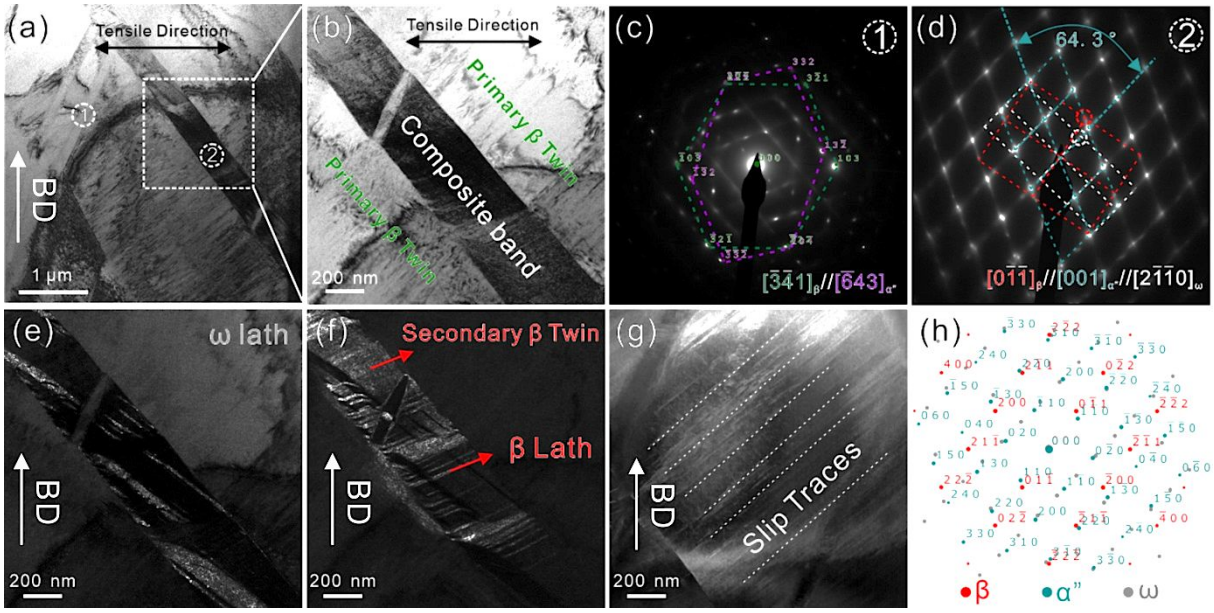


Fig. 6.15. Microstructures of area 1 in Fig.9b: (a) BF TEM micrograph shows the primary β twin. (b) BF TEM micrograph magnified from (a). (c) SAED pattern collected from region 1 in (a). (d) SAED pattern collected from region 2 in (a), and the corresponding DF TEM images showing the location of ω lath (e), secondary β twin and lath (f) inside the composite band. (g) The DF STEM image shows the slip traces inside the primary β twin, where the high-density dislocations were observed. (h) Simulated SAED pattern of (d).

As shown in Fig. 6.16a, the microstructure of area 2 shows the crossed twinning structures,

of which the thin bands (marked by the white arrows) decorated the twin boundaries. One β twin structure is magnified and edge-on (Fig. 6.16b). The SAED was performed in the twin boundary. The Fig. 6.16c reveal the microstructure is composed of the β matrix, β twin, SIM α" phase and ω phase. Moreover, The DF-TEM obtained from the diffraction spots of ω and SIM α" phases are shown in Fig. 6.16d and Fig. 6.16e respectively. The SIM α" phases (the white bands in Fig. 6.16e) decorated the twin boundaries, while some other work [56] also reported similar findings. There is only one variant of the ω phase that exists in the β twin. The simulation of the SAED pattern can be seen in Fig. 6.16f, which fit well with the SAED pattern of Fig.6.16c.

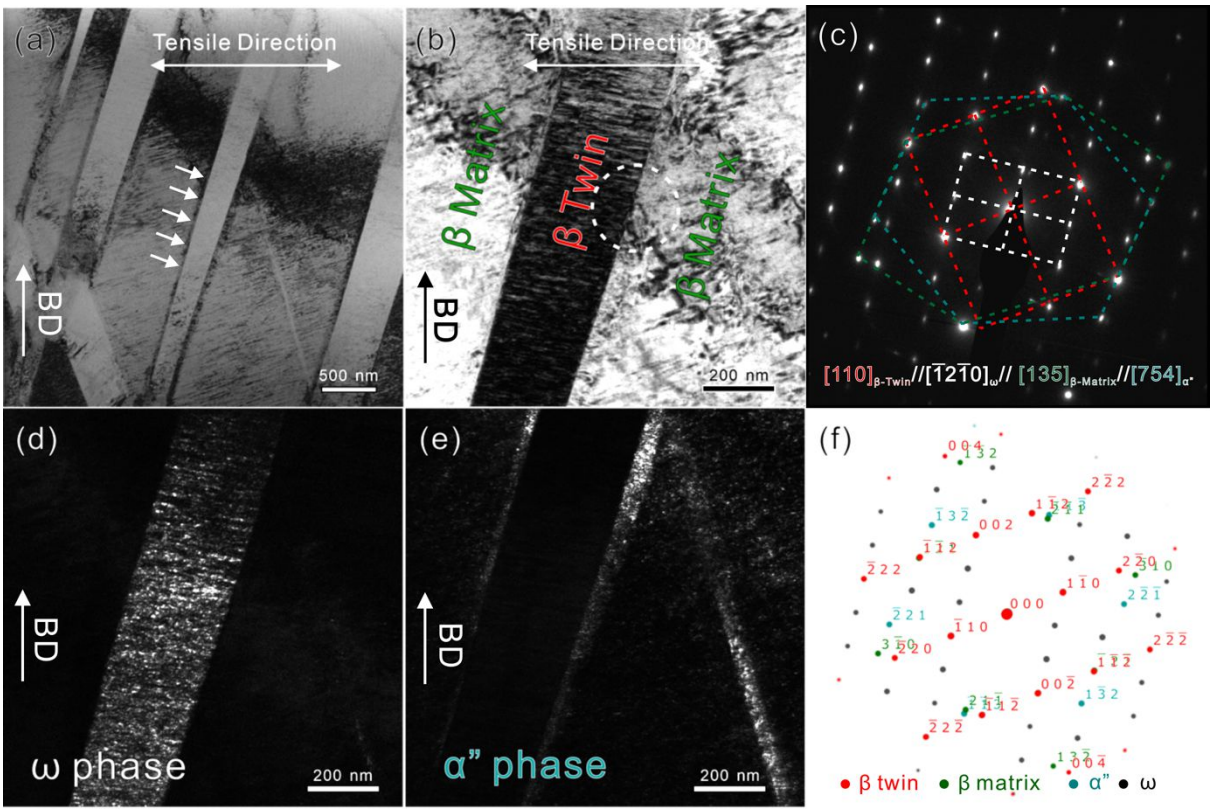


Fig. 6.16. Microstructures of area 2 in Fig.9b: (a) BF TEM image. (b) BF TEM image magnified from (a). (c) SAED pattern collected from a dotted circle in (b), and the corresponding DF TEM

images showing the ω phases (d) in the primary β twin, and the boundary SIM α" phase (e). (f) simulated SAED pattern of (c).

At the deformation stage of 5 % true strain, no other twin systems were found except {332}<113> β (Fig. 6.13). This twin system was frequently observed in the plastic deformation of metastable β Ti alloys [57]. Due to the lattice instability [58], the {112}<111> (the main twin system in stable BCC structured alloys) is unlikely to happen at the early stage of deformation.

Accompanied by the {332}<113>β twins, the SIM martensite α" phase was also detected decorating along the twin structures. To understand the transformation sequences of the secondary structures of twins and martensite, the crystallographic orientations relationship between the β and SIM α" was investigated by TEM. Based on the simulations of diffraction patterns, the crystallographic orientations of primary β twin, secondary β twin, SIM α" in primary β twin and SIM α" in composite bands derived from SAED patterns, are depicted in Fig. 6.17a-b as the stereographic projections. The Burgers orientation relationship between the primary β twin and SIM α" is as below, which follows the classical burgers orientation relationship (BOR):

$$(2\bar{1}\bar{1})_{\beta} \parallel (101)_{\alpha"}$$
$$(100)_{\beta} \parallel (100)_{\alpha"}$$
$$(01\bar{1})_{\beta} \parallel (010)_{\alpha"}$$

This demonstrates that SIM α" phases could originate from the primary β twin. In the composite band (Fig. 6.17c-d), the secondary β twin and SIM α" also have the same classical

BOR, indicating the SIM α" phases in the composite bands were transformed from the secondary β twins.

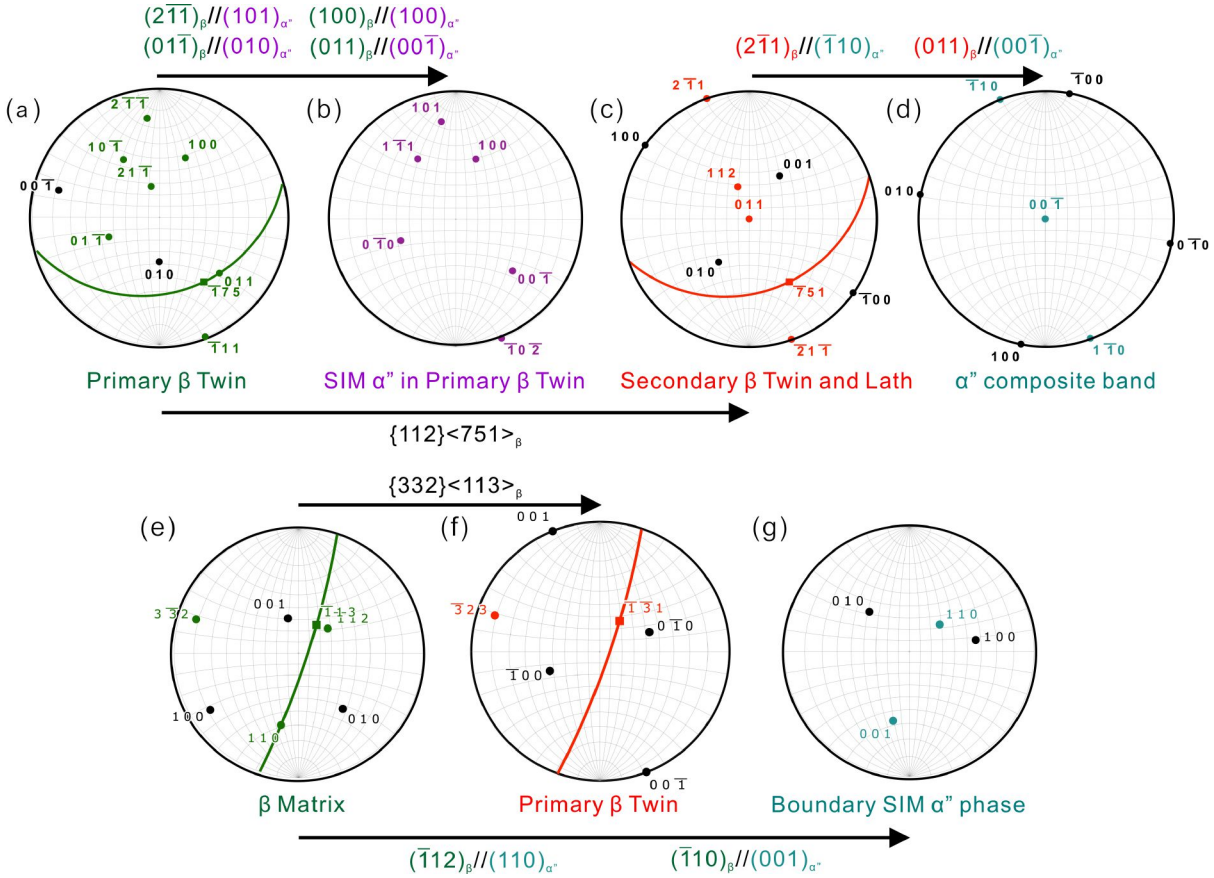


Fig. 6.17. Crystallographic orientations of β and α" phases represented using the stereographic projections to analyse the burgers orientation relationship (BOR) between the primary β matrix, β twin, secondary β twin and SIM α" phases in area 1 (a-d) and 2 (e-g) from Fig.6.15 and Fig.6.16, respectively.

The primary β twins and the secondary β twins in the composite band follow an unconventional twin relationship of {112}<751>β. Some other unconventional deformation twin systems, such as {5 8 11} < 135 >β [59], {013} < 531 >β, and {541}<111>β[9] were also reported to be decorated along the interfaces of primary and secondary twins, which highlight

that the irrational twin systems can relieve the local misfit stresses created by the intersection of different twinning systems. In our work, when the specimens deformed at the true strain of 1.4 %, only {332}<113>$_\beta$ twins are present, with no secondary internal twinning. According to Ref.[9,60,61], twins cannot occur within the main twin without altering the primary twin's level of stress. The primary twin's initial habit plane is significantly distorted, as shown Fig. 6.13i, resulting in the primary twin's initial twinning relationship with the matrix being lost. Therefore, the secondary structures can be viewed as the means of reducing the strain energy between the matrix and the distorted twin boundaries.

In area 2, the matrix and primary twin obviously follow a common {332} β pole and <113> β direction, emphasizing the {332}<113>β twin relationship (Fig. 6.17e-g). Indeed, the orientation of the primary twin is determined by a reflection on the (332) β plane or by a 180-degree rotation around the matrix $[\overline{1}\overline{1}3]$ direction. As a result, the matrix and primary twin are twinning in the {332}<113>$_\beta$ relationship, where the SIM α" were found decorated along the twin boundaries. These SIM α" phases have the classical BOR with the β matrix, which means they were transformed from β matrix.

Furthermore, we have noticed some plate-like α" phases in some regions of the sample after 5 % strain. Fig. 6.18a shows the apparent bright and dark contrast, representing the different elemental concentrations in the matrix and precipitates. The α" phases have a different composition as the matrix (α" phases are lean in Mo, which is 2.07 wt%), according to Fig. 6.18b and Fig. 6.18c.

The composition difference indicates that these are α" phases formed during heat treatment, rather than SIM α". These plate-like α" phases are surrounded by high-density dislocations as shown in Fig. 6.18d, under the two-beam conditions of g = $[1\bar{1}0]$. In the weak beam dark field condition (Fig. 6.18e), the morphology of sessile dislocations can be clearly observed. Fig. 6.18f shows the microstructure magnified from a region in Fig. 6.18e. Similar sessile interfaces were previously reported in Ti-Cr systems[62], composed of pure screw dislocations.

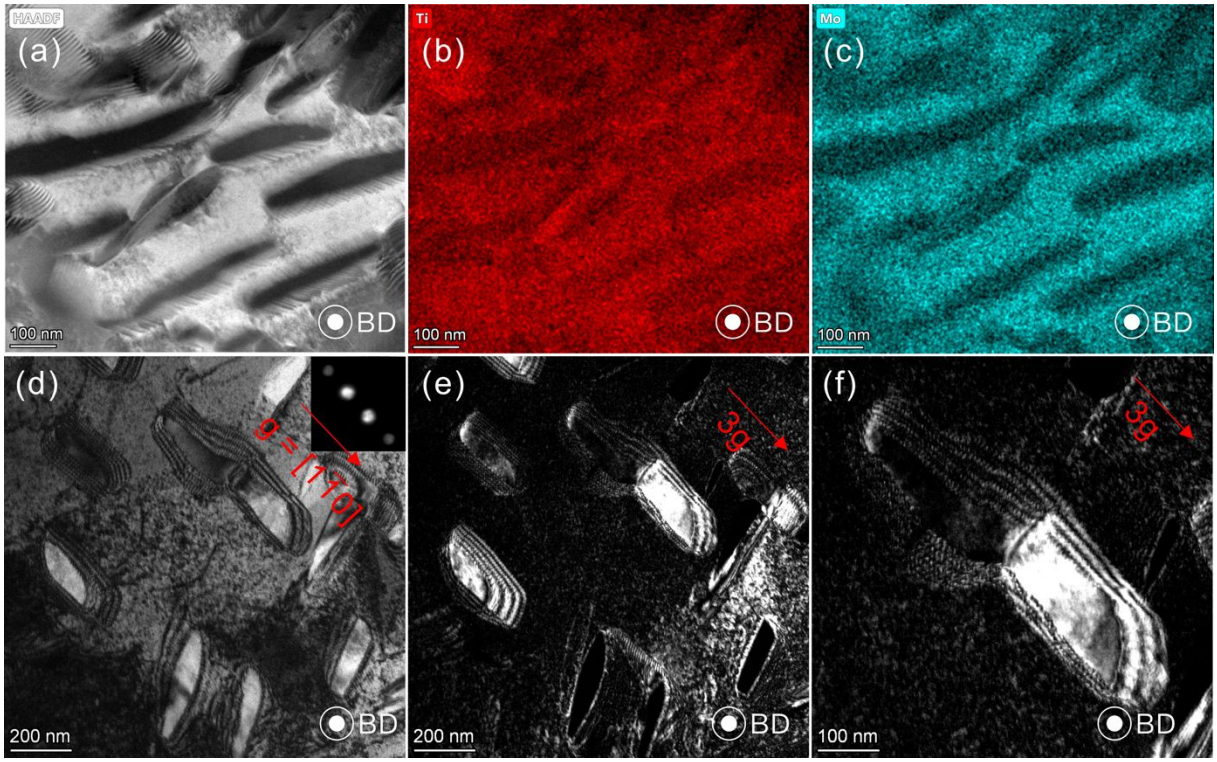


Fig. 6.18. Microstructures of the tensile specimen at 5 % true strain: (a) HAADF-STEM image, EDS mapping of Ti (b) and Mo elements (c). (d) BF TEM image under the two-beam condition of g = $[1\bar{1}0]$. (e) weak beam dark field (WBDF) image (g-3g). (f) The magnified WBDF image.

6.3.6. Microstructural investigations after 11 % strain

In stage III of the plastic deformation, many refined structures were formed by the

interaction of TWIP/TRIP in ST-CS Ti-12Mo. It is hard to obtain the high-precision micrograph by the traditional EBSD technology due to the limitations of the technology and the high inner stress in the SIM α" phases. Instead, we performed TKD characterisations on the samples after 11% strain. As shown in Fig. 6.19a, the β matrix, the primary β twins and the secondary β twins can be observed, most of which followed some specific twin relationship based on the 3D crystallographic cells. In Fig. 6.19b, the SIM α" phases were formed along the twin boundaries or cross the primary twins. The amount of the α" phases taken account of 14.1%, which is much higher than 5%, that calculated from synchrotron diffraction results (Fig. 6.11c). This means the SIM α" transformation was inhomogeneous across the samples. As shown in Fig. 6.19c, high-density secondary twinning structures, including {332} and {112} typed β twins, were revealed in the large cross primary twinning. The {112}<111>β twin boundaries (**Σ**3 boundaries in Fig.6.19c) were observed distributed around the intersection of primary {332}<113>β twins. The intersected primary twins were seriously distorted.

After subletting a single primary β twin (Fig. 6.19d) from Fig.6.19a, primary (green) and secondary (red) β twins were clearly observed. The misorientation along the black line (Fig. 6.19d) is 50.5º, as presented in Fig. 6.19e, and the common poles of the primary β twin and secondary β twin were circled in $\{332\}_{\beta}$ pole figure of Fig. 6.19g, which confirmed the {332}<113> twin relationship. Furthermore, two variants (pink and yellow) of SIM α" phases are found decorated the boundaries of secondary β twins (red). In Fig.6.19f, the secondary α" phases are revealed in the primary α" band, which correspond to the two variants of SIM α".

For the two α" variants, the pink variants (primary α” bands) follow the orientation relationship of $\{112\}_{\beta}$ //$\{110\}_{\alpha''}$ with the primary β twin, while the yellow ones (secondary α” phases) have the orientation relationship of $\{112\}_{\beta}$//$\{110\}_{\alpha''}$ with the secondary β twin. These findings reveal the two α" variants are transformed from primary β twin and secondary β twin respectively. According to the stereo projection analysis of the $\{130\}_{\alpha''}$ plane , the two variants have the common poles, as circled in Fig.6.19g, which indicated the twin relationship of {130}<310> α”. The {130}<310>α” twin system in the SIM α”, decorated along the {332}<113>β twin boundaries, was also reported in the tensile deformed Ti12Mo3Zr [11], Ti25Ta20Nb [63], and single-crystal Ti-27Nb alloy [64]. The results here demonstrate the hierarchical TWIP/TRIP effects during the deformation of ST-CS Ti-12Mo specimens.

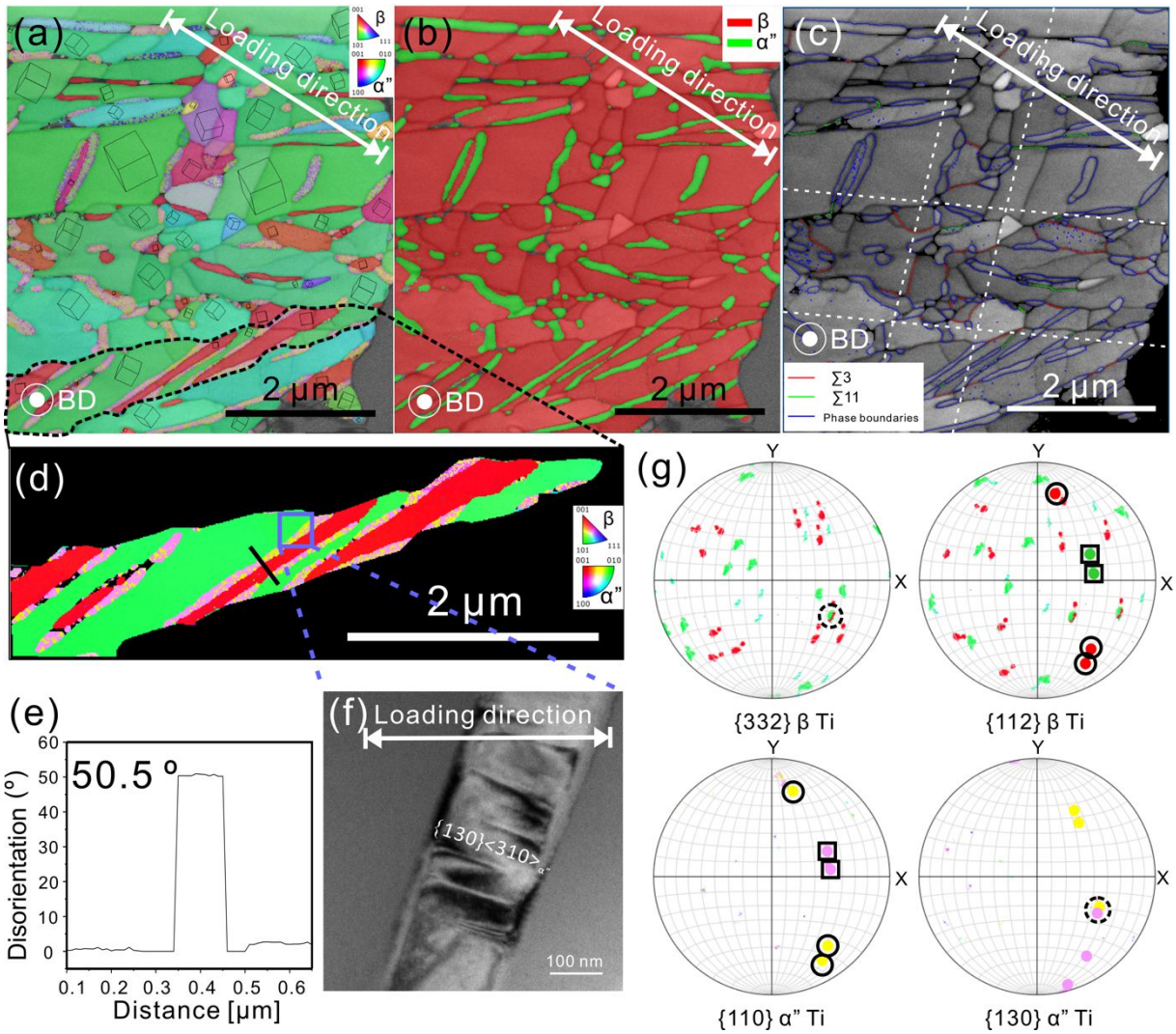


Fig. 6.19. TKD micrographs show the microstructure of ST-CS Ti-12Mo at 11 % true strain: (a) IPF EBSD map of β and α" phases; (b) the distributions of β and α" phases;(c) band contrast (BC) map superimposed with the twin boundaries of CSL $\sum 3$ and $\sum 11$. (d) IPF EBSD map of a single primary β twin and the corresponding line intensity profile (e) across the solid black line. (f) BF TEM image shows the boundary α" phases. (g) pole figures of β and SIM α" phases (dotted circle means the common poles in selected pole figures, and the solid square and circle represent the several corresponding poles in the selected pole figures of β and α" phases).

6.3.7. Microstructural investigations after 17 % strain

When the deformation propagates to 17 % strain, some large composite bands are formed due to the synergistic effect of TWIP/TRIP, as shown in EBSD maps (Fig. 6.20 (a-c)). Large regions were not indexed in Fig. 6.20 (a-c) due to the high inner stress in the severely deformed microstructures. The β primary twins in the large composite band were also following the {332}<113> twin relationship with the β matrix, as illustrated in $\{332\}_{\beta}$ pole figure of Fig. 6.20d. The variant of α" phase, in blue, has the orientation relationship of {112}β//{110}α" with β matrix. While the variant in pink follows the orientation relationship of {112}β//{110}α" with β twins. Therefore, the blue and pink variants of α" phases were originated from the β matrix and β twin, respectively. Moreover, there is another variant of α" (in yellow) (Fig. 6.20c), which have the {130}<310> twin relationship with the α" (in pink) in large composite bands.

By performing the TKD on the specimens, although some regions are non-indexed, the severely refined nano-sized grains are observed in Fig. 6.20 (e-g). With the synergistic effects of TWIP/TRIP, the nano-sized β grains and α" phases can be finally achieved. In another work [33], the grain size of the Ti-12Mo alloy prepared by the conventional method was also dynamically reduced by the high-density stress-induced twins and martensite, which was finally refined to only 50-100 nm.

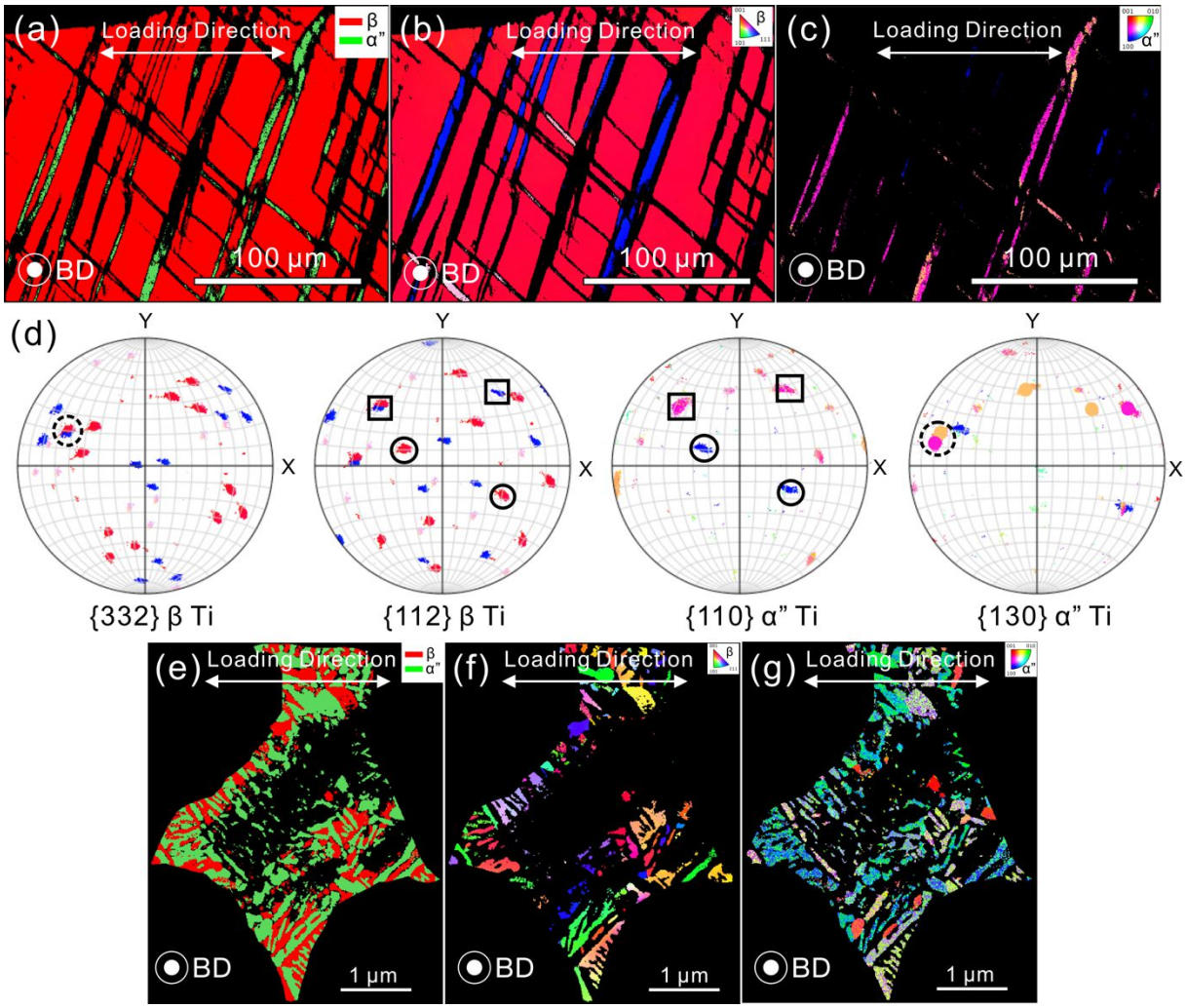


Fig. 6.20. Microstructures of ST-CS Ti-12Mo at 17 % true strain (the endpoint of uniform deformation): (a) phase map shows the distributions of β and α" phases; (b) IPF EBSD map of β phases; (c) IPF EBSD map of α" phase. (d) pole figures of β and SIM α" phases (dotted circle means the common poles in selected pole figures, and the solid square and circle represent the several corresponding poles in the selected pole figures of β and α" phases). (e to g) TKD micrographs show the microstructures in unindexed region: (e) distributions of β and α" phases; (f) IPF EBSD map of β phases; (g) IPF EBSD map of α" phase.

6.4. Discussion

To understand the excellent mechanical behaviours of the ST-CS Ti-12Mo samples, this

work first discussed the contributions from different strengthening effects and then determined the sequence of TWIP/TRIP behaviours during the tensile deformation.

6.4.1. Strengthening contribution to the yield strength

Based on the previous demonstration of the microstructures of the ST-CS Ti-12Mo alloy, the dislocation slip system driven modelling is used to quantify the strengthening mechanisms of this material. The high yield strength of 725 ± 7 MPa, is composed of the lattice friction stress of pure Ti (σ_0), solid solution strengthening effect (σ_{SS}), grain boundary strengthening effect (σ_{HP}), dislocation strengthening effect (σ_{DS}) and precipitation strengthening effect (σ_{PS}), which can be calculated as below:

$$\sigma_y = \sigma_0 + \sigma_{SS} + \sigma_{HP} + \sigma_{DS} + \sigma_{PS} \tag{6.4}$$

The lattice friction stress of pure Ti (σ_0) is equal to 180 MPa in this work [44]. The solid solution strengthening effect can be calculated using Eq.6.5 [65]:

$$\sigma_{SS} = \left(\sum_i B_i^{3/2} X_i \right)^{2/3} \tag{6.5}$$

Bi means the solid solution strengthening coefficient. *Xi* is the atomic fraction of the solute element *i*. Therefore, σ_{SS} is 94 MPa for the ST-CS Ti-12Mo specimens with Mo concentrations of 12.5 wt%.

The grain boundary strengthening effect will be calculated using the Hall-Petch equation:

$$\sigma_{HP} = K_{H-P} d^{-1/2} \tag{6.6}$$

The K_{H-P} is the Hall-Petch constant ($K_{H-P} = 0.75\ MPa \cdot m^{1/2}$ for Ti alloys)[2]. d is the mean grain size. According to Fig. 6.5d, the grain size (d) is 114.35 μm. Thus, the strengthening contribution from grain boundaries is 70 MPa.

Furthermore, the strengthening effect from the dislocations (σ_{DS}) is calculated using the Taylor relation as follow:

$$\sigma_{DS} = \alpha M G b \sqrt{\rho} \tag{6.7}$$

α is the dislocation interaction constant (0.3 used in this work[2]). M is the Taylor factor (M = 2.8) [2]. G is the shear modulus (G = 27.3 GPa from Table 6.4). b is the magnitude of Burgers vector (b = 0.28 nm)[44]. Geometrically necessary dislocation (GND) map and distribution of GND are shown in Fig. 6.21. The average GND density (ρ_{GND}) is denoted as the dislocation density (ρ) of this work. As shown in Fig. 6.21, the dislocation density (ρ) is estimated to be 1.04 × 10^{14} m^{-2}. Therefore, the σ_{DS} is calculated as 65 MPa.

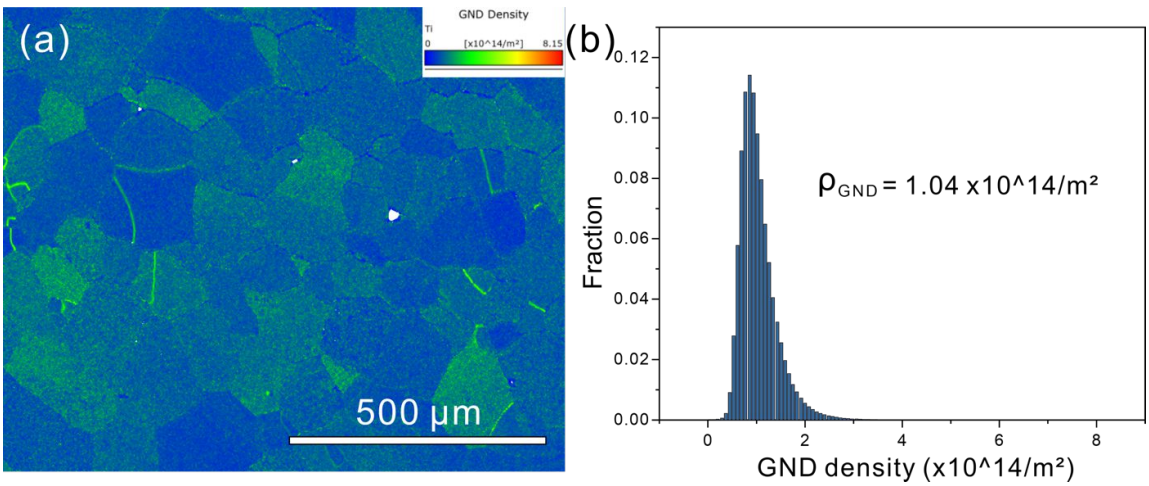


Fig. 6.21. (a) GND map and (b) distribution of GND density.

Due to the limited amount of α" phases (< 1%) in the initial microstructure (Fig. 6.4 and 6.11a), the strengthening contribution from α" is neglected. We mainly discuss the strengthening effects of ω particles. Given the minimal misfit between the ω and β lattices and the coherent nature of the $\{11\bar{2}\}_\beta//\{\bar{1}100\}_\omega$ interface promotes the slip transfer of dislocations from β to ω [3,48,66]. Lai et al.[67] concluded the dislocation movement through the coherent plane of ω phase to be the shearing mode. It can be described as the motion of a 1/2 <111>β dislocation ***b*** on the $\{11\bar{2}\}_\beta$ plane dissociates into three partials, 1/12 $<111>_\beta$, 1/12 $<111>_\beta$, and 1/3 $<111>_\beta$, when shearing the ω phase. These partial dislocations enable the ω phase to revert to β matrix form [48]. Applying Gleiter and Hornbogen's [68] theoretical treatment of misfit-free ordered particles and correcting for the movement of single dislocations, the coherent particle-induced rise in shear stress ($\Delta\tau_s$) is given by:

$$\Delta\tau_s = 1.02\gamma^{3/2}G^{-1/2}b^{-2}r^{1/2}f^{1/2} \quad (6.8)$$

γ, antiphase-boundary energy. *r* and *f* are the radius and volume fraction of ω particles. Gysler et al.[42] estimated the γ of Ti-11wt%Mo alloy according to the plot of $\sigma_{0.1}$ vs $r^{1/2}f^{1/2}$, which is 0.3 J/m^2. The $\Delta\tau_s$ is then estimated to be 115 MPa. In a polycrystalline system, the strengthening effects from ω phases can be calculated using the Eq.6.9:

$$\sigma_\omega = M\Delta\tau \quad (6.9)$$

Therefore, the strengthening increment from particle shearing (σ_s) is 322 MPa. Then, dominating strengthening effect from the ω particles should be the particle shearing in this work.

The total contribution from various origins is 731 MPa, which is close to the yield strength of the material (725 MPa).

6.4.2. Mechanisms and sequence of plastic deformation

The deformation twinning traverses the grains, resulting in a decrease in the mean free path of the dislocation, a phenomenon known as the dynamic Hall-Petch effect. Then, dislocations are disrupted when arriving at the twin/matrix interfaces, allowing internal stress fields (back stress) to obstruct slip. Moreover, the SIM α" formed at β twins, can also provide the additional β/α" interface, providing additional barriers to impede dislocation movements [69].

Fig. 6.22a illustrates changing of the twin fraction and morphology at different strain levels. At 1.4 % true strain, the black region illustrates the location of primary twins as shown in Fig.6.12. The regions were non-indexed due to the high inner stress and thin width. With the increase of plastic deformation to 5 % true strain, the size and fraction of primary β twins have grown significantly. After that, the size of β twins expanded further. The twins formed at 17% strain were not considered for calculations, where the large region is unindexed, because of the severely refined grains and high-density SIM α" as shown in Fig.6.20 e-g. Moreover, the nano-sized hierarchical structures observed from TEM or TKD micrographs were also not considered for present calculations due to the structure's complex nature and inhomogeneous distributions. Then, using Fullman's volumetric analysis, the volume fraction (F) of twins can be determined as [70]:

$$\frac{1}{l} = \frac{1}{2e}\frac{F}{1-F} \tag{6.10}$$

where l means the average intertwin spacing, and e denotes the twins' thickness. Using the TEM and EBSD micrographs, l and e were determined for the samples after 1.4 %, 5%, and 11% strain, as shown in Table 6.5. F was calculated as 7 %, 60%, and 71 % with the increase of true strain, as shown in Table 6.5 and Fig. 6.22b.

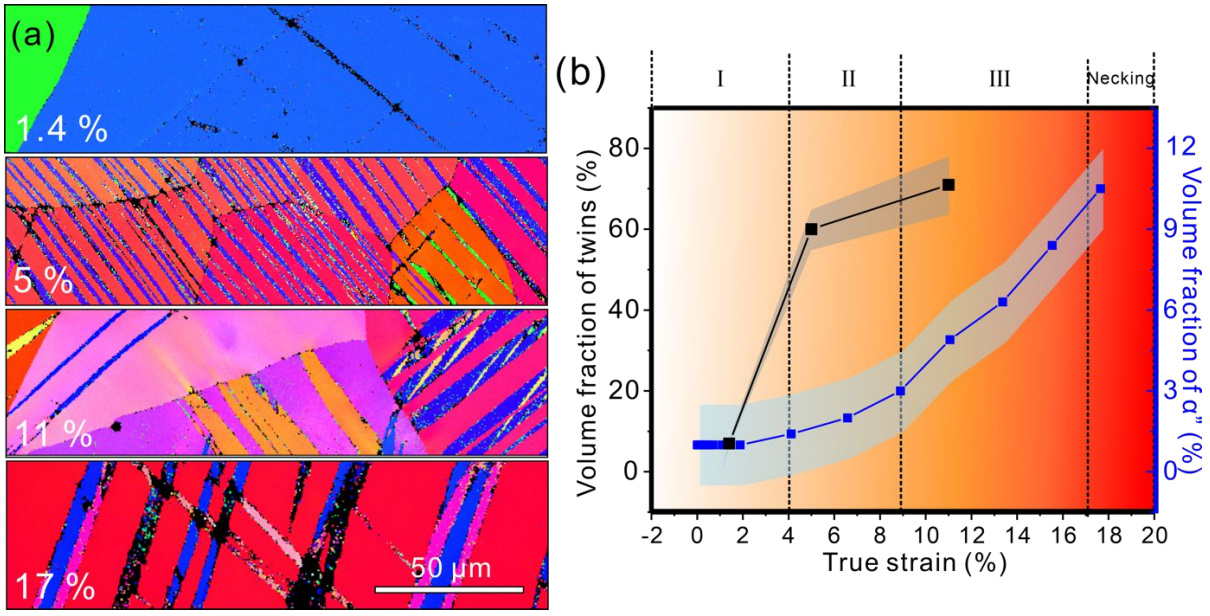


Fig. 6.22. (a) EBSD IPF maps of the twinning structures after different levels of true strain. (b) The relationship between the true strain with the volume fraction of twins and α".

Table 6.5. The measured *l, e* and the calculated *F* after several true strains of the ST-CS Ti-12Mo samples.

True strain	*l* (μm)	*e* (μm)	*F* (%)
1.4 %	20.1 ± 0.2	765 ± 18 nm	7 %
5 %	2.4 ± 0.9	1.8 ± 0.4	60 %

11 %	4.1 ± 2.6	5.0 ± 0.8	71%

This work believes that the strain hardening comes from the hierarchical TRIP and TWIP effects. The nano-sized secondary structures, such as the composite band, twins, boundary α", and {130}<310> α" martensite twins, all contributed to the strain hardening. Compared to other β Ti alloys that only exhibit TWIP effects, TWIP/TRIP alloys exhibit an improved strain-hardening rate due to the collaborative activation of deformation twinning and SIM transformation[8,71].

The activation sequence of TWIP/TRIP effects in ST-CS Ti-12Mo alloy can be concluded in Fig. 6.23. The specimens show a high strain hardening performance just after yielding, which is due to the strain field around the boundaries of specific phase constitutions of β + ω + α". The phase boundaries impede dislocations' movement which providing extensive interfacial hardening. In stage I, the $\{332\}\langle 113\rangle_{\beta}$ twins were firstly activated, increasing rapidly from 7% at strain level of 1.4% to about 57% at the strain level of 4% (Fig.6.22a), whereas the α" phase only increased slightly during this stage. Hence, the high strain hardening capacity maintained at stage I can be attributed to $\{332\}\langle 113\rangle_{\beta}$ deformation twinning. In stage II, the SHR of ST-CS Ti-12Mo as shown in Fig. 6.2, steadily dropped. There is not enough space for more primary twins in the stage. Thus, the increase of primary twins became stable in this stage and reached about 60 % volume fraction, as shown in Fig. 6.22. The SIM α" located along the {332}<113> twin boundaries and the nano-sized composite band were formed, which was composed of {112}<751>β twin, ω lath and SIM α". According to the previous analysis of the

crystallographic relationship between α" and β phases (Fig. 6.17), the SIM α" could transform from the β matrix or β twins, which partly occupied the regions. Therefore, these hierarchical microstructures, including the boundary α" and composite bands, can effectively confine the primary and secondary β Twins. Then they provide extra barriers for the dislocations' movement and additional composite effects. In stage III, some secondary structures, such as {112}<111>β twins and {130}<310>α" twins, could confine the primary microstructures even further. In addition, the grains were continuously refined under the crossed hierarchical TWIP/TRIP effects until reaching the nano-sized grains. With the refinement of β and α" grains, the strain hardening rate dropped more rapidly in the stage. Although ultrafine grains can provide high local flow stress, they limit the operation of dislocations and twinning's activity [72]. Thus, the refinement effects could be detrimental to the strain-hardening capacity. This is why the strain hardening rate decreased rapidly during stage III.

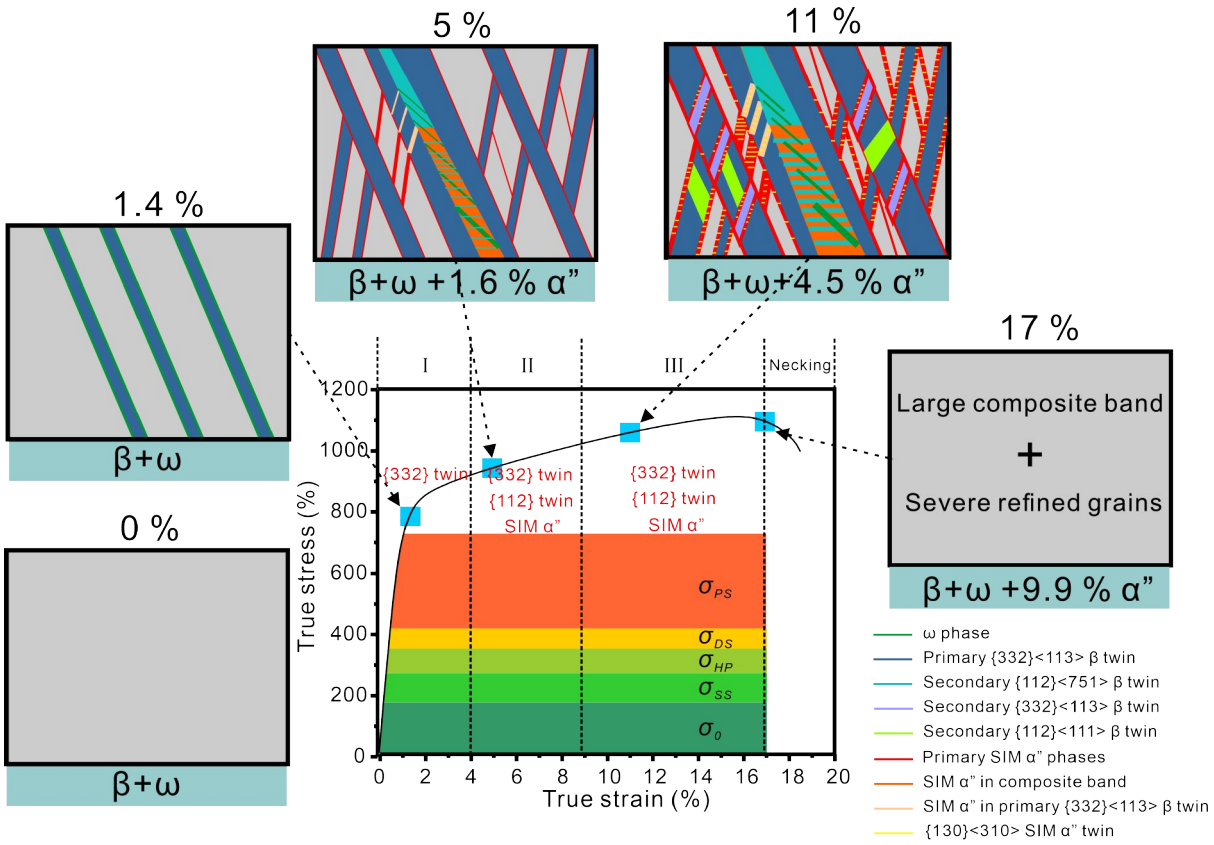


Fig. 6.23. Schematic shows the evolution of the microstructure of ST-CS Ti-12Mo alloy during the tensile deformation.

In the ST-CS Ti-12Mo alloy, the excellent mechanical performance originated from four contributions, the ω phase, the stress-induced hierarchical twinning structures, the stress-induced hierarchical martensite structures, and the stress-induced composite bands (ω lath + β twin + α" band). Combining these effects enhanced the efficiency of the dynamic Hall-Petch effect, raising the inter-grain and trans-grain slip resistance, thus contributing to the high strength, high SHR and good ductility.

6.5. Conclusion

In this study, the microstructural and mechanical properties of as-fabricated and solution treated Ti-12Mo were detailly investigated. Furthermore, the deformation mechanisms and sequence of TWIP/TRIP effects in ST-CS Ti-12Mo were also studied. The main findings can be summarised as follows:

(1) The near fully dense and chemical homogeneous AF-CS Ti-12Mo alloy, with {100} crystallographic preferential orientations along the tensile and build directions, was successfully fabricated by LPBF. However, the tensile specimens are brittle, which failed before the yielding.

(2) After solution heat treatment, the solution treated Ti-12Mo shows an excellent combination of high yield strength (725 ± 7 MPa), high UTS of 1123 ± 5 MPa, low modulus (81 ± 3 GPa), a high strain hardening rate (~2500 MPa at 4% true strain) and good ductility (22 ± 1 %). According to the dislocation slip system driven modelling, the high yield strength is mainly attributed to nano-sized ω particles (contributing 322 MPa). The ω particles have an average diameter of 4.1 nm and the Mo concentrations of 5.10 at.%. They strengthen the materials by the dislocations shearing mechanism.

(3) At the early stage of plastic deformation at 1.4 % strain level, the SIM α" transformation and pseudo-elasticity were suppressed, while the {332}<113> twins decorated with ITB ω phases were found to be dominant.

(4) With the increase of deformation to 5% true strain, massive twins formed in the specimens, which led some primary and secondary twins to lose the {332}<113> relationship. Then some unconventional structures formed, such as the composite bands, consisting of secondary β twins, SIM α" phases, and ω laths, where the secondary β twins have an irrational twin relationship of $\{112\}\langle 751\rangle_{\beta}$ with the primary β twins. Furthermore, SIM α" phases were found decorated along the {332}<113> β twins, which transformed from β matrix.

(5) At the higher strain of 11%, nano-sized secondary {112}<111> β twins, {130}<310>α" twins are revealed in the primary β twins and the primary SIM α" respectively. After that, the grains were continuously refined during the interaction of hierarchical twinning and martensite structures until reaching the nano-sized grains.

(6) The main deformation mechanisms are revealed to be the propagation of hierarchical twining and martensite structures with the increase of plastic deformation. Various primary and secondary twins and martensite structures form hierarchical structures, enhancing the dynamic Hall-Petch effect and resulting in a high strain hardening rate.

6.6. References

[1] C. Leyens, M. Peters, Titanium and titanium alloys: fundamentals and applications, Wiley-VCH, New York, 2003.

[2] R. Duan, S. Li, B. Cai, W. Zhu, F. Ren, M.M. Attallah, A high strength and low modulus metastable β Ti-12Mo-6Zr-2Fe alloy fabricated by laser powder bed fusion in-situ alloying, Addit Manuf. 37 (2021) 101708. https://doi.org/10.1016/j.addma.2020.101708.

[3] R. Duan, S. Li, B. Cai, Z. Tao, W. Zhu, F. Ren, M.M. Attallah, In situ alloying based laser powder bed fusion processing of β Ti–Mo alloy to fabricate functionally graded composites, Compos Part B Eng. 222 (2021) 109059. https://doi.org/10.1016/j.compositesb.2021.109059.

[4] A.E.-M.A. Mohamed, J. Zou, R.S. Sheridan, K. Bongs, M.M. Attallah, Magnetic Shielding Promotion via the Control of Magnetic Anisotropy and Thermal Post Processing in Laser Powder Bed Fusion Processed NiFeMo-based Soft Magnet, Addit Manuf. 32 (2020) 101079. https://doi.org/10.1016/j.addma.2020.101079.

[5] S. Li, H. Hassanin, M.M. Attallah, N.J.E. Adkins, K. Essa, The development of TiNi-based negative Poisson's ratio structure using selective laser melting, Acta Mater. 105 (2016) 75–83. https://doi.org/10.1016/j.actamat.2015.12.017.

[6] M.H. Mosallanejad, B. Niroumand, A. Aversa, A. Saboori, In-Situ Alloying in Laser-Based Additive Manufacturing Processes: A Critical Review, J. Alloys Compd. 872 (2021) 159567. https://doi.org/10.1016/j.jallcom.2021.159567.

[7] Y.J. Liu, S.J. Li, H.L. Wang, W.T. Hou, Y.L. Hao, R. Yang, T.B. Sercombe, L.C. Zhang, Microstructure, defects and mechanical behavior of beta-type titanium porous structures manufactured by electron beam melting and selective laser melting, Acta Mater. 113 (2016) 56–67. https://doi.org/10.1016/j.actamat.2016.04.029.

[8] F. Sun, J.Y. Zhang, M. Marteleur, T. Gloriant, P. Vermaut, D. Laillé, P. Castany, C. Curfs, P.J. Jacques, F. Prima, Investigation of early stage deformation mechanisms in a metastable β titanium alloy showing combined twinning-induced plasticity and transformation-induced plasticity effects, Acta Materialia. 61 (2013) 6406–6417. https://doi.org/https://doi.org/10.1016/j.actamat.2013.07.019.

[9] Y. Yang, P. Castany, Y.L. Hao, T. Gloriant, Plastic deformation via hierarchical nano-sized martensitic twinning in the metastable β Ti-24Nb-4Zr-8Sn alloy, Acta Mater. 194 (2020). https://doi.org/10.1016/j.actamat.2020.04.021.

[10] M. Li, X. Min, K. Yao, F. Ye, Novel insight into the formation of α″-martensite and ω-phase with cluster structure in metastable Ti-Mo alloys, Acta Mater. 164 (2019) 322–333. https://doi.org/10.1016/j.actamat.2018.10.048.

[11] B. Qian, J. Zhang, Y. Fu, F. Sun, Y. Wu, J. Cheng, P. Vermaut, F. Prima, In-situ microstructural investigations of the TRIP-to-TWIP evolution in Ti-Mo-Zr alloys as a function of Zr concentration, J Mater Sci Technol. 65 (2020) 228–237. https://doi.org/10.1016/j.jmst.2020.04.078.

[12] D. Kuroda, M. Niinomi, M. Morinaga, Y. Kato, T. Yashiro, Design and mechanical properties of new β type titanium alloys for implant materials, Mater. Sci. Eng., A. 243 (1998) 244–249. https://doi.org/10.1016/s0921-5093(97)00808-3.

[13] T. Ozaki, H. Matsumoto, S. Watanabe, S. Hanada, Beta Ti Alloys with Low Young's Modulus, Mater Trans. 45 (2004) 2776–2779. https://doi.org/10.2320/matertrans.45.2776.

[14] M. Niinomi, T. Akahori, S. Katsura, K. Yamauchi, M. Ogawa, Mechanical characteristics and microstructure of drawn wire of Ti–29Nb–13Ta–4.6Zr for biomedical applications, Mater Sci Eng C. 27 (2007) 154–161. https://doi.org/10.1016/j.msec.2006.04.008.

[15] P. Laheurte, F. Prima, A. Eberhardt, T. Gloriant, M. Wary, E. Patoor, Mechanical properties of low modulus β titanium alloys designed from the electronic approach, J Mech Behav Biomed. 3 (2010) 565–573. https://doi.org/10.1016/j.jmbbm.2010.07.001.

[16] T.-K. Jung, S. Semboshi, N. Masahashi, S. Hanada, Mechanical properties and microstructures of β Ti–25Nb–11Sn ternary alloy for biomedical applications, Mater Sci Eng C. 33 (2013) 1629–1635. https://doi.org/10.1016/j.msec.2012.12.072.

[17] F. Sun, T. Gloriant, P. Vermaut, P. Jacques, F. Prima, Beta Titanium Alloys with Very High Ductility Induced by Complex Deformation Mechanisms: a New Material Perspective for Coronary Stent Applications, Solid State Phenomen. 172–174 (2011) 129–134. https://doi.org/10.4028/www.scientific.net/ssp.172-174.129.

[18] M. Marteleur, F. Sun, T. Gloriant, P. Vermaut, P.J. Jacques, F. Prima, On the design of new β-metastable titanium alloys with improved work hardening rate thanks to simultaneous TRIP and TWIP effects, Scripta Materialia. 66 (2012) 749–752. https://doi.org/https://doi.org/10.1016/j.scriptamat.2012.01.049.

[19] K. Cho, R. Morioka, S. Harjo, T. Kawasaki, H.Y. Yasuda, Study on formation mechanism of {332}<113> deformation twinning in metastable β-type Ti alloy focusing on stress-induced α" martensite phase, Scripta Mater. 177 (2020) 106–111. https://doi.org/10.1016/j.scriptamat.2019.10.011.

[20] M.J. Lai, T. Li, F.K. Yan, J.S. Li, D. Raabe, Revisiting ω phase embrittlement in metastable β titanium alloys: Role of elemental partitioning, Scr. Mater. 193 (2021) 38–42. https://doi.org/10.1016/j.scriptamat.2020.10.031.

[21] L. Lilensten, Y. Danard, C. Brozek, S. Mantri, P. Castany, T. Gloriant, P. Vermaut, F. Sun, R. Banerjee, F. Prima, On the heterogeneous nature of deformation in a strain-

transformable beta metastable Ti-V-Cr-Al alloy, Acta Mater. 162 (2019) 268–276. https://doi.org/10.1016/j.actamat.2018.10.003.

[22] E.M. Hildyard, L.D. Connor, L. Owen, D. Rugg, N. Martin, H.J. Stone, N.G. Jones, The influence of microstructural condition on the phase transformations in Ti-24Nb (at.%), Acta Mater. 199 (2020) 129–140. https://doi.org/10.1016/j.actamat.2020.08.004.

[23] M. Basham, J. Filik, M.T. Wharmby, P.C.Y. Chang, B.E. Kassaby, M. Gerring, J. Aishima, K. Levik, B.C.A. Pulford, I. Sikharulidze, D. Sneddon, M. Webber, S.S. Dhesi, F. Maccherozzi, O. Svensson, S. Brockhauser, G. Náray, A.W. Ashton, Data Analysis WorkbeNch (DAWN), J Synchrotron Radiat. 22 (2015) 853–858. https://doi.org/10.1107/s1600577515002283.

[24] J. Filik, A.W. Ashton, P.C.Y. Chang, P.A. Chater, S.J. Day, M. Drakopoulos, M.W. Gerring, M.L. Hart, O.V. Magdysyuk, S. Michalik, A. Smith, C.C. Tang, N.J. Terrill, M.T. Wharmby, H. Wilhelm, Processing two-dimensional X-ray diffraction and small-angle scattering data in DAWN 2, J Appl Crystallogr. 50 (2017) 959–966. https://doi.org/10.1107/s1600576717004708.

[25] M.L. Hart, M. Drakopoulos, C. Reinhard, T. Connolley, Complete elliptical ring geometry provides energy and instrument calibration for synchrotron-based two-dimensional X-ray diffraction, J Appl Crystallogr. 46 (2013) 1249–1260. https://doi.org/10.1107/s0021889813022437.

[26] A. E8/E8M-16a, Standard Test Methods for Tension Testing of Metallic Materials, ASTM International, West Conshohocken, PA, 2016. https://www.astm.org.

[27] M.J. Hÿtch, E. Snoeck, R. Kilaas, Quantitative measurement of displacement and strain fields from HREM micrographs, Ultramicroscopy. 74 (1998) 131–146. https://doi.org/10.1016/s0304-3991(98)00035-7.

[28] C.L. Yang, Z.J. Zhang, S.J. Li, Y.J. Liu, T.B. Sercombe, W.T. Hou, P. Zhang, Y.K. Zhu, Y.L. Hao, Z.F. Zhang, R. Yang, Simultaneous improvement in strength and plasticity of Ti-24Nb-4Zr-8Sn manufactured by selective laser melting, Mater Design. 157 (2018) 52–59. https://doi.org/10.1016/j.matdes.2018.07.036.

[29] D. Zhang, D. Qiu, M.A. Gibson, Y. Zheng, H.L. Fraser, D.H. StJohn, M.A. Easton, Additive manufacturing of ultrafine-grained high-strength titanium alloys, Nature. 576 (2019) 91–95. https://doi.org/10.1038/s41586-019-1783-1.

[30] S.L. Sing, W.Y. Yeong, F.E. Wiria, Selective laser melting of titanium alloy with 50 wt% tantalum: Microstructure and mechanical properties, J. Alloys Compd. 660 (2016) 461–470. https://doi.org/10.1016/j.jallcom.2015.11.141.

[31] H. Schwab, M. Bönisch, L. Giebeler, T. Gustmann, J. Eckert, U. Kühn, Processing of Ti-5553 with improved mechanical properties via an in-situ heat treatment combining selective laser melting and substrate plate heating, Mater Design. 130 (2017) 83–89. https://doi.org/10.1016/j.matdes.2017.05.010.

[32] C. Qiu, Q. Liu, R. Ding, Significant enhancement in yield strength for a metastable beta titanium alloy by selective laser melting, Mater Sci Eng. 816 (2021) 141291. https://doi.org/10.1016/j.msea.2021.141291.

[33] L. Choisez, L. Ding, M. Marteleur, H. Idrissi, T. Pardoen, P.J. Jacques, High temperature rise dominated cracking mechanisms in ultra-ductile and tough titanium alloy, Nat Commun. 11 (2020) 2110. https://doi.org/10.1038/s41467-020-15772-1.

[34] S. Bahl, S. Suwas, K. Chatterjee, Comprehensive review on alloy design, processing, and performance of β Titanium alloys as biomedical materials, Int Mater Rev. 66 (2020) 1–26. https://doi.org/10.1080/09506608.2020.1735829.

[35] W. Elmay, S. Berveiller, E. Patoor, T. Gloriant, F. Prima, P. Laheurte, Texture evolution of orthorhombic α″ titanium alloy investigated by in situ X-ray diffraction, Materials Science and Engineering: A. 679 (2017) 504–510. https://doi.org/10.1016/j.msea.2016.10.072.

[36] F.H. da Costa, C.A.F. Salvador, M.G. de Mello, R. Caram, Alpha phase precipitation in Ti-30Nb-1Fe alloys – phase transformations in continuous heating and aging heat treatments, Mater. Sci. Eng., A. 677 (2016) 222–229. https://doi.org/10.1016/j.msea.2016.09.023.

[37] A.W. Bowen, Omega phase embrittlement in aged Ti-15%Mo, Scripta Metall Mater. 5 (1971) 709–715. https://doi.org/10.1016/0036-9748(71)90258-4.

[38] J.C. Williams, B.S. Hickman, H.L. Marcus, The effect of omega phase on the mechanical properties of titanium alloys, Metall Trans. 2 (1971) 1913–1919. https://doi.org/10.1007/bf02913423.

[39] C.W. Phillips, D.N. Frey, Isothermal Transformation Characteristics, Jom-Us. 4 (1952) 381–385. https://doi.org/10.1007/bf03397700.

[40] E. Levine, S. Hayden, H. Margolin, Deformation behavior of an omega hardened alpha-beta titanium alloy, Acta Metall Mater. 22 (1974) 1443–1448. https://doi.org/10.1016/0001-6160(74)90045-5.

[41] J.C. Williams, B.S. Hickman, D.H. Leslie, The effect of ternary additions on the decompositon of metastable beta-phase titanium alloys, Metall Trans. 2 (1971) 477–484. https://doi.org/10.1007/bf02663337.

[42] A. Gysler, G. Lütjering, V. Gerold, Deformation behavior of age-hardened Ti-Mo alloys, Acta Metall Mater. 22 (1974) 901–909. https://doi.org/10.1016/0001-6160(74)90057-1.

[43] L. Ren, W. Xiao, C. Ma, R. Zheng, L. Zhou, Development of a high strength and high ductility near β-Ti alloy with twinning induced plasticity effect, Scripta Mater. 156 (2018) 47–50. https://doi.org/https://doi.org/10.1016/j.scriptamat.2018.07.012.

[44] G.-H. Zhao, X. Xu, D. Dye, P.E.J. Rivera-Díaz-del-Castillo, Microstructural evolution and strain-hardening in TWIP Ti alloys, Acta Mater. 183 (2019) 155–164. https://doi.org/10.1016/j.actamat.2019.11.009.

[45] R. Davis, H.M. Flower, D.R.F. West, Martensitic transformations in Ti-Mo alloys, J. Mater. Sci. 14 (1979) 712–722. https://doi.org/10.1007/bf00772735.

[46] R. Davis, H.M. Flower, D.R.F. West, The decomposition of Ti-Mo alloy martensites by nucleation and growth and spinodal mechanisms, Acta Metall. 27 (1979) 1041–1052. https://doi.org/10.1016/0001-6160(79)90192-5.

[47] M. Bönisch, M. Stoica, M. Calin, Routes to control diffusive pathways and thermal expansion in Ti-alloys, Scientific Reports. 10 (2020) 3045. https://doi.org/10.1038/s41598-020-60038-x.

[48] M.J. Lai, C.C. Tasan, J. Zhang, B. Grabowski, L.F. Huang, D. Raabe, Origin of shear induced β to ω transition in Ti–Nb-based alloys, Acta Mater. 92 (2015) 55–63. https://doi.org/10.1016/j.actamat.2015.03.040.

[49] Y. Zheng, R.E.A. Williams, S. Nag, R. Banerjee, H.L. Fraser, D. Banerjee, The effect of alloy composition on instabilities in the β phase of titanium alloys, Scripta Mater. 116 (2016) 49–52. https://doi.org/10.1016/j.scriptamat.2016.01.024.

[50] W. Ma, S. Guo, G. Liu, Q. Meng, R. Luo, D. Li, C.-T. Peng, X. Cheng, Tensile deformation behavior of a solution-treated Ti–33Nb–4Sn alloy with a dual β and α" phases under cyclic loading-unloading, Prog Nat Sci Mater Int. (2020). https://doi.org/10.1016/j.pnsc.2020.01.008.

[51] S. Cai, J.E. Schaffer, Y. Ren, Deformation of a Ti-Nb alloy containing α"-martensite and omega phases, Appl Phys Lett. 106 (2015) 131907. https://doi.org/10.1063/1.4916960.

[52] G.B. Olson, M. Cohen, Kinetics of strain-induced martensitic nucleation, Metallurgical Transactions. 6 (1974) 791. https://doi.org/10.1007/bf02672301.

[53] S.A. Mantri, F. Sun, D. Choudhuri, T. Alam, B. Gwalani, F. Prima, R. Banerjee, Deformation Induced Hierarchical Twinning Coupled with Omega Transformation in a Metastable β-Ti Alloy, Scientific Reports. 9 (2019) 1334. https://doi.org/10.1038/s41598-018-37865-0.

[54] W. Kou, Q. Sun, L. Xiao, J. Sun, Coupling effect of second phase and phase interface on deformation behaviours in microscale Ti-55531 pillars, J. Alloys Compd. 820 (2020) 153421. https://doi.org/10.1016/j.jallcom.2019.153421.

[55] W. Chen, S. Cao, J. Zhang, Y. Zha, Q. Hu, J. Sun, New insights into formation mechanism of interfacial twin boundary ω-phase in metastable β-Ti alloys, Mater Charact. 164 (2020) 110363. https://doi.org/10.1016/j.matchar.2020.110363.

[56] Y. Danard, R. Poulain, M. Garcia, R. Guillou, D. Thiaudière, S. Mantri, R. Banerjee, F. Sun, F. Prima, Microstructure Design and in-situ investigation of TRIP/TWIP effects in a forged dual-phase Ti–10V–2Fe–3Al alloy, Materialia. 8 (2019) 100507. https://doi.org/10.1016/j.mtla.2019.100507.

[57] M.J. Lai, C.C. Tasan, D. Raabe, On the mechanism of 332 twinning in metastable β titanium alloys, Acta Materialia. 111 (2016) 173–186. https://doi.org/https://doi.org/10.1016/j.actamat.2016.03.040.

[58] H. Tobe, H.Y. Kim, T. Inamura, H. Hosoda, S. Miyazaki, Origin of 332 twinning in metastable β-Ti alloys, Acta Mater. 64 (2014) 345–355. https://doi.org/https://doi.org/10.1016/j.actamat.2013.10.048.

[59] J. Zhang, F. Sun, Z. Chen, Y. Yang, B. Shen, J. Li, F. Prima, Strong and ductile beta Ti–18Zr–13Mo alloy with multimodal twinning, Mater Res Lett. 7 (2019) 251–257. https://doi.org/10.1080/21663831.2019.1595763.

[60] Q. Yu, J. Wang, Y. Jiang, R.J. McCabe, N. Li, C.N. Tomé, Twin–twin interactions in magnesium, Acta Mater. 77 (2014) 28–42. https://doi.org/10.1016/j.actamat.2014.05.030.

[61] P. Müllner, A.E. Romanov, Internal twinning in deformation twinning, Acta Mater. 48 (2000) 2323–2337. https://doi.org/10.1016/s1359-6454(00)00025-2.

[62] D. Qiu, M.-X. Zhang, P.M. Kelly, T. Furuhara, Crystallography of surface precipitates associated with shape change in a Ti–5.26wt.% Cr alloy, Acta Mater. 61 (2013) 7624–7638. https://doi.org/10.1016/j.actamat.2013.08.067.

[63] E. Bertrand, P. Castany, Y. Yang, E. Menou, T. Gloriant, Deformation twinning in the full-α″ martensitic Ti–25Ta–20Nb shape memory alloy, Acta Mater. 105 (2016) 94–103. https://doi.org/10.1016/j.actamat.2015.12.001.

[64] M. Tahara, N. Okano, T. Inamura, H. Hosoda, Plastic deformation behaviour of single-crystalline martensite of Ti-Nb shape memory alloy, Sci Rep-Uk. 7 (2017) 15715. https://doi.org/10.1038/s41598-017-15877-6.

[65] G.H. Zhao, X.Z. Liang, B. Kim, P.E.J. Rivera-Díaz-del-Castillo, Modelling strengthening mechanisms in beta-type Ti alloys, Mater. Sci. Eng., A. 756 (2019) 156–160. https://doi.org/10.1016/j.msea.2019.04.027.

[66] L.M. Hsiung, D.H. Lassila, Shock-induced deformation twinning and omega transformation in tantalum and tantalum–tungsten alloys, Acta Mater. 48 (2000) 4851–4865. https://doi.org/10.1016/s1359-6454(00)00287-1.

[67] M.J. Lai, C.C. Tasan, D. Raabe, Deformation mechanism of ω-enriched Ti–Nb-based gum metal: Dislocation channeling and deformation induced ω–β transformation, Acta Mater. 100 (2015) 290–300. https://doi.org/10.1016/j.actamat.2015.08.047.

[68] H. Gleiter, E. Hornbogen, Theorie der Wechselwirkung von Versetzungen mit kohärenten geordneten Zonen (I), Phys Status Solidi B. 12 (1965) 235–250. https://doi.org/10.1002/pssb.19650120122.

[69] F. Sun, J.Y. Zhang, C. Brozek, M. Marteleur, M. Veron, E. Rauch, T. Gloriant, P. Vermaut, C. Curfs, P.J. Jacques, F. Prima, The Role of Stress Induced Martensite in Ductile Metastable Beta Ti-alloys Showing Combined TRIP/TWIP Effects, Mater Today Proc. 2 (2015) S505–S510. https://doi.org/10.1016/j.matpr.2015.07.336.

[70] R.L. Fullman, Measurement of Particle Sizes in Opaque Bodies, Jom-Us. 5 (1953) 447–452. https://doi.org/10.1007/bf03398971.

[71] C. Brozek, F. Sun, P. Vermaut, Y. Millet, A. Lenain, D. Embury, P.J. Jacques, F. Prima, A β-titanium alloy with extra high strain-hardening rate: Design and mechanical properties, Scripta Materialia. 114 (2016) 60–64. https://doi.org/https://doi.org/10.1016/j.scriptamat.2015.11.020.

[72] S. Zhao, R. Zhang, Q. Yu, J. Ell, R.O. Ritchie, A.M. Minor, Cryoforged nanotwinned titanium with ultrahigh strength and ductility, Science. 373 (2021) 1363–1368. https://doi.org/10.1126/science.abe7252.

Chapter 7：Conclusions & Future Work

7.1. Summary and Conclusions

This study used LPBF technology to resolve the challenging issues such as high cost of using the conventional methods to produce β Ti alloys containing refractory elements. It has demonstrated that in-situ alloying based LPBF processing can be used to fabricate high-quality β Ti-12Mo, Ti-12Mo-6Zr-2Fe (TMZF), and Ti-Mo functional gradient composites (FGCs). The influences of energy density, scanning strategies and post-treatments on the alloys' microstructural evolutions and mechanical performances were summarised, which advanced our understanding of the essential relationship between the processing, microstructures, and mechanical properties of additive manufactured β Ti alloys.

7.1.1. Parametrical studies for densification and homogenisation

Due to the high melting point of Mo and the low interdiffusion rate between Mo and Ti, conventional processing of Ti-Mo alloys, such as arc melting, usually requires several remelting cycles, followed by long-term homogenisation heat treatment. For the powder metallurgy route, preparing pre-alloyed powders through atomisation is also expensive and time-consuming.

This work has applied the cost-effective, in-situ alloying based LPBF to process the Ti-Mo binary alloying system from powder blends. It is found that the Mo particles can be melted and dissolved into the Ti matrix using high laser energy input (e.g. 4 J/mm^2 or higher), attributed to the repeated remelts on each powder layer. Due to excessively high energy input, keyhole-

induced defects were formed but can be eliminated by optimising the laser beam delay (LBD) and island spacing (IS) settings of LPBF processing.

By applying the optimised parameters of 4 J/mm^2 area energy density, with low LBD and IS values of 0.1 ms and 0.06 mm respectively, the highly dense (>99.9%) Ti-12Mo alloy was successfully fabricated. The optimised scanning parameters were also verified in processing the high-quality TMZF alloys with near fully dense microstructures (>99.8%). Although some chemical inhomogeneities, across different scales, could be found in both as-fabricated Ti-12Mo and TMZF alloys, the actual chemical compositions were closed to the nominal composition.

Therefore，in-situ alloying based LPBF processing is demonstrated to be a promising manufacturing route for new alloy fabrication when pre-alloyed powders are challenging to produce.

7.1.2. Influence of energy density and the FGC material

It is found that the input energy density can significantly influence the specimen's microstructure, including the grain structure, the inner stress, and the phases constitutions during the parametrical studies of Ti-12Mo alloy. At a low AED of 1.6 J/mm^2, the microstructure contained refined grains, high inner stress and β + α" phases. At a high AED of 4 J/mm^2, the microstructure consisted of the larger grains and reduced inner stress, where the phases constitutions were mainly β and ω phases, with a small amount of α" phase along the

grain boundaries. The grain, composed of β and α" phases, showed high strength and large strain hardening capacity. In contrast, the grain with β and ω phases showed substantial strain bursts without apparent strain hardening.

The highly dense Ti-Mo functional gradient composites (FGCs) were successfully prepared by controlling the energy input for the LPBF processing of the powder blends. A gradient distribution of α" phase with varied sizes and quantities across the designed layer boundaries was produced. The Ti-Mo FGCs illustrated a higher compressive yield strength of 1173 (± 15) MPa, with improved strain hardening capacity than the mechanical performance of Ti-12Mo alloy processed by a high AED of 4 J/mm^2.

This finding opens a new opportunity to design and engineer high-performance biomimetic FGCs components with gradient composition and microstructure through controlling the laser energy density of in situ alloying based LPBF.

7.1.3. Influence of scanning strategies

The scanning strategies have been verified as a viable way to control the elastic modulus of β Ti alloys processed by LPBF using pre-alloyed powders. However, the influence of the scanning strategies on the mechanical performance of β Ti alloys processed by in-situ alloying based LPBF is still unclear. In this work, the near fully-dense TMZF alloys have been processed by simple and chessboard scanning strategies, of which the microstructure-property relations were understood.

By applying the simple scanning strategy, the TMZF alloy showed a high strength of up to 1291 (± 25) MPa but failed before yielding. This alloy also demonstrated a high elastic modulus of 107.1 (± 3.3) GPa, mainly due to the mixture of strong <011> and <111> preferential orientations. The high-density sessile dislocations, heterogeneous α" phases and their interactions led to the high strength. The embrittlement ω phase and their extended straight grain boundaries could induce intergranular fracture.

By applying the chessboard scanning strategy, we obtained the TMZF alloy with strong {100}<001> texture, α" phase, but was free from ω phase. It also exhibited heterogeneous grain size distribution with refined grains formed in the central region of the melt pool during solidification. Such a hierarchical microstructure confered an excellent combination of high yield strength of 1026 (± 5) MPa, good elongation of 12.7 (± 1.0) % and lower elastic modulus of 85.7 (± 0.3) GPa.

Via dislocation slip system driven modelling, it is found that the α" precipitates play an essential role in strengthening the TMZF alloys. The α" phase was formed via a diffusion-driven phase transformation, of which the size, volume fraction and distribution could be altered by different LPBF scanning strategies.

This demonstrates that grain structure, crystallographic orientation, and phase constitution can be controlled through changing the scanning strategies, offering a viable strategy for optimising the mechanical properties of β Ti alloys processed by in-situ alloying based LPBF.

7.1.4. Influence of solution heat treatments

Additive manufactured β Ti components might require a heat treatment process, such as solution treatment, for the chemical homogenization or inner stress releasing, during which recrystallisation and non-equilibrium phases transformations might occur. It is unclear whether the high strength of the printed alloy could maintain after such heat treatment.

For TMZF alloy, solution heat treatment at 1000 ℃ followed by water quench (ST) could induce the formation of stronger {100}<001> texture, and heterogeneous large plate-like α" precipitates in the equiaxed recrystallised β matrix. Despite a slight reduction in yield strength (943 (± 8) MPa) and elongation (12.0 (± 0.3) %), a much lower elastic modulus of 70.9 (± 0.1) GPa was achieved.

For Ti-12Mo alloy, as-fabricated Ti-12Mo alloys were brittle, failed before the yielding. After ST, the Ti-12Mo alloy showed an excellent combination of high yield strength (725 ± 7 MPa), low modulus (81 ± 3 GPa), and good ductility (22 ± 1 %), due to the strong {100}<001> texture and nano-sized ω particles, strengthening the materials by the dislocations shearing mechanism.

Thus, the additional ST can regulate the texture and precipitations in the additive manufactured TMZF and Ti-12Mo alloys to obtain the combination of high strength and low modulus. The findings advanced our understanding of the influence of post heat treatments on the microstructure-properties relations of β Ti alloys.

7.1.5. The deformation mechanisms

After ST, Ti-12Mo tensile specimens exhibited high UTS of 1123 ± 5 MPa and a high strain hardening rate, contributing to good ductility. The mechanism and sequence of twinning-induced plasticity (TWIP) and transformation-induced plasticity (TRIP) during the plastic deformation of the Ti12Mo alloy were investigated as well. The main findings are summarized below:

At the early stage of plastic deformation, the stress-induced martensite (SIM) α" transformation was suppressed, while the {332}<113> twins decorated with interfacial twin boundary ω phases were found to be dominant. With the increase of deformation to 5% true strain, massive twins formed in the specimens. Some unconventional structures were revealed, such as the composite bands, consisting of secondary β twins, SIM α" phases, and ω laths. The secondary β twins had an irrational twin relationship of {112}<751>β with the primary β twins, which could be perceived as the way to minimise the energy between the matrix and distorted twin boundaries. Furthermore, SIM α" phases were found decorated along the {332}<113> β twins, which were transformed from β matrix. At the higher strain of 11%, nano-sized secondary {112}<111>β twins, {130}<310>α" twins were revealed in the primary β twins and the primary SIM α" respectively. After that, the grains were continuously refined during the interaction of hierarchical twinning and martensite structures until reaching the nano-sized grains.

The main deformation mechanisms are revealed to be the propagation of hierarchical twining and martensite structures with increased plastic deformation. Various primary and

secondary twins, and martensite structures formed hierarchical structures, enhancing the dynamic Hall-Petch effect and resulting in a high strain hardening rate and good ductility of additive manufactured β Ti alloy.

7.2. Future Works

This work has provided fundamental contribution to reveal the processing-microstructure-properties development in additive manufactured β Ti alloys, including parametrical studies, functionally graded structure design, and structure-properties relations. At the same time, the influence of laser processing parameters and post heat treatments were also considered. Future work should be directed to more fundamental research topics through combining the advanced in-situ and ex-situ techniques and exploring the actual applications in biomedical/aerospace by using the in-situ alloying based LPBF processing. This would include the following aspects:

- This work has observed some α" precipitates formed in Ti-12Mo and TMZF alloys after ST. It suggested that the precipitates were formed through spinodal decomposition. However, the mechanisms of the phase transformation are still not clear. In-situ synchrotron XRD (SXRD) characterisation at different solution treatment temperatures and cooling rates would be ideal for verifying the spinodal decomposition mechanism and for determining the dynamics of α" phase transformation, which will be correlated to TEM, EBSD and APT works to establish a comprehensive map connecting dynamics with the structure and composition of α" phase.

- Through SXRD in-situ tensile deformation and TEM characterisation of Ti-12Mo alloy, we have observed the transformation and reorientation of ω phase. However, ω phase transformations cannot be clearly demonstrated by SXRD, whereas Small-Angle X-ray scattering (SAXS) is an ideal technique to confirm the evolution of nano-sized ω phase. The combined use of SXRD and SAXS will allow the correlation between work-hardening effects, TRIP/TWIP effects, and ω phase evolutions during tensile testing to be revealed.
- The components' inhomogeneity and reproducibility constitute a major challenge due to the random nature of the powder quality and the particle size distributions. Further evaluation of the mechanical properties of the printed samples, especially the fracture and fatigue properties, from different batches and across scales are needed to verify the consistency of properties upon scale up and from batch to batch. Therefore, further work should be required to ensure quality control before the industrial applications of the components prepared by in-situ alloying based LPBF.
- The blends used in the in-situ alloying based LPBF processing contain particles with different thermophysical properties. The influence of the size, distribution, and content of the residual particles on the mechanical properties of solid samples is not clear, especially for the FGCs. The rules for the material selection of FGCs also need investigations systematically. More in-depth studies also need to be performed to achieve precise control of the microstructure of FGCs.
- High-quality solid β Ti alloys can be successfully prepared in this work. Future work

can be extended to fabricate the complex porous structure with precise control and optimisations. When the porous structures are optimised, the biocompatibility and high cycle fatigue properties can be investigated for biomedical applications in future.

- In this work, the embrittlement reasons and mechanisms are still unclear in as-fabricated Ti-12Mo alloys and TMZF alloys, and the brittle to ductile transformation mechanisms when performing different scanning strategies. There is a need to investigate the underlying mechanisms through the combined use of atom probe tomography and high-resolution transmission electron microscopy.